

AD No. 1
DDC FILE COPY

ADA 049037

RADC-TR-77-389
Final Technical Report
November 1977



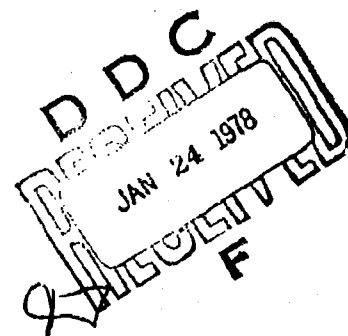
22

BISTATIC CLUTTER DATA MEASUREMENTS PROGRAM

Environmental Research Institute of Michigan

Sponsored by
Defense Advanced Research Projects Agency (DoD)
ARPA Order No. 3071

Approved for public release; distribution unlimited.



The views and conclusions contained in this document are those of the authors and should not be interpreted as necessarily representing the official policies, either expressed or implied, of the Defense Advanced Research Projects Agency or the U. S. Government.

ROME AIR DEVELOPMENT CENTER
Air Force Systems Command
Griffiss Air Force Base, New York 13441

This report contains a large percentage of machine-produced copy which is not of the highest printing quality but because of economical consideration, it was determined in the best interest of the government that they be used in this publication.

This report has been reviewed by the RADC Information Office (OI) and is releasable to the National Technical Information Service (NTIS). At NTIS it will be releasable to the general public, including foreign nations.

RADC-TR-77-389 has been reviewed and is approved for publication.

APPROVED:

Richard A. Schneible
RICHARD A. SCHNEIBLE
Project Engineer

If your address has changed or if you wish to be removed from the RADC mailing list, or if the addressee is no longer employed by your organization, please notify RADC (OCSA) Griffiss AFB NY 13441. This will assist us in maintaining a current mailing list.

Do not return this copy. Retain or destroy.

BISTATIC CLUTTER DATA MEASUREMENTS PROGRAM

R. W. Larson, et al.

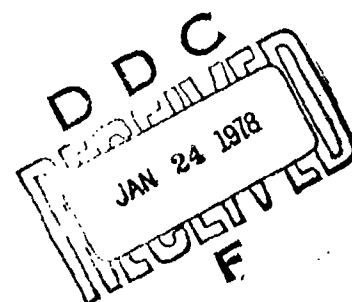
Contractor: Environmental Research Institute of Michigan
Contract Number: F30602-76-C-0037
Effective Date of Contract: 10 September 1975
Contract Expiration Date: 30 September 1976
Short Title of Work: Bistatic Clutter Data Measurements
Program
Program Code Number: 6E20
Period of Work Covered: Oct 75 - Sep 76

Principal Investigator: R. W. Larson
Phone: 313 994 1200 x237

Project Engineer: Richard A. Schneible
Phone: 315 330 2814

Approved for public release; distribution unlimited.

This research was supported by the Defense Advanced
Research Projects Agency of the Department of
Defense and was monitored by Richard A. Schneible (OCSA),
Griffiss AFB NY 13441 under Contract F30602-76-C-0037.



UNCLASSIFIED

SECURITY CLASSIFICATION OF THIS PAGE (When Data Entered)

REPORT DOCUMENTATION PAGE		READ INSTRUCTIONS BEFORE COMPLETING FORM
1. REPORT NUMBER RADC-TR-77-389	2. GOVT ACCESSION NO.	3. RECIPIENT'S CATALOG NUMBER
4. TITLE (and Subtitle) BISTATIC CLUTTER DATA MEASUREMENTS PROGRAM	5. TYPE OF REPORT & PERIOD COVERED Final Technical Report 1 Oct 75-30 Sep 76	6. PERFORMING ORG. REPORT NUMBER 118200-14-Y
7. AUTHOR(s) R. W. Larson et al R.C. Heimiller	8. CONTRACT OR GRANT NUMBER(s) F30602-76-C-0037	9. PROGRAM ELEMENT, PROJECT, TASK AREA & WORK UNIT NUMBERS 62301E C0710103
10. PERFORMING ORGANIZATION NAME AND ADDRESS Environmental Research Institute of Michigan P.O. Box 618 Ann Arbor MI 48107	11. CONTROLLING OFFICE NAME AND ADDRESS Defense Advanced Research Projects Agency 1400 Wilson Boulevard Arlington VA 22209	12. REPORT DATE November 1977
13. MONITORING AGENCY NAME & ADDRESS (if different from Controlling Office) Rome Air Development Center (OCSA) Griffiss AFB NY 13441	14. SECURITY CLASS. (of this report) UNCLASSIFIED	15. DECLASSIFICATION/DOWNGRADING SCHEDULE N/A
16. DISTRIBUTION STATEMENT (of this Report) Approved for public release; distribution unlimited.		
17. DISTRIBUTION STATEMENT (of the abstract entered in Block 20, if different from Report) Same		
18. SUPPLEMENTARY NOTES RADC Project Engineer: Richard A. Schneible (OCSA)		
19. KEY WORDS (Continue on reverse side if necessary and identify by block number) Bistatic Radar Cross-Section Density Reflection Coefficient 85 deg.		
20. ABSTRACT (Continue on reverse side if necessary and identify by block number) Empirical data have been obtained from which estimates of the bistatic reflection coefficient, σ_0 , have been determined. Measurements were made on two terrain types (grassy terrain and an area of tall weeds and rough ground) at bistatic angles of 70, 75, 80, and 85° low grazing angles and 0 to 180° azimuth angle. The terrain was irradiated at wavelengths of 3 cm and 23 cm with horizontal polarization. Both like and orthogonal polarizations were received at each wavelength; four channels of data were recorded.		

DD FORM 1 JAN 73 1473

EDITION OF 1 NOV 65 IS OBSOLETE

UNCLASSIFIED

SECURITY CLASSIFICATION OF THIS PAGE (When Data Entered)

407903

JP

UNCLASSIFIED

SECURITY CLASSIFICATION OF THIS PAGE(When Data Entered)

The measurement technique utilized an aircraft with the 3 cm and 23 cm transmitters on board; the receivers were mounted on a tower. The transmissions were pulsed, and coherent signals were recorded by utilizing a separate air-to-ground link for the receiver local oscillator signal.

This report presents the design considerations of the experiment, the complete experimental results, the results of the data analysis as well as a detailed documentation of the instrumentation and the data analysis procedures.

ACCESSION for

White Section ☒

Buff Section ☐

NTIS

DDC

UNCLASSIFIED

DISSEMINATION

BY

DISTRIBUTION/AVAILABILITY CODES

DIS

SPECIAL

A

UNCLASSIFIED

SECURITY CLASSIFICATION OF THIS PAGE(When Data Entered)

PREFACE

This technical report describes the experimental program for the measurement of bistatic reflection coefficients funded under Contract F30602-76-C-0037. The research reported herein was carried out by members of the Radar and Optics Division, Environmental Research Institute of Michigan (ERIM) during the period 1 October 1975 to 30 September 1976.

This contract was monitored by Mr. Richard Schneible of Rome Air Development Center, Rome, New York. The DARPA Program Director was Dr. D. Walsh, ARPA, STO.

The Principal Investigators for the program at ERIM were Messrs. R.W. Larson and R.C. Heimiller. In addition, the following persons contributed to the project: (1) Dr. M. Hidayet, Dr. E.L. Johansen, and Prof. A.L. Maffett in the analysis phase, (2) Mr. J.L. Auterman, Mr. J.E. Ferris, Mr. A.F. Fromm, and Mr. R.F. Rawson in the instrumentation design phase, (3) Mr. B. DiTullio, Mr. J. Ferris, Mr. A.F. Fromm, Mr. F.L. Smith, and Mr. D.E. Wertz in the fabrication phase and instrumentation test phase, (4) Mr. B. DiTullio, Mr. A.F. Fromm, Mr. R.F. Rawson, Mr. F.L. Smith, and Mr. D.E. Wertz in the data-gathering phase, as well as (5) Mr. A. Gillies, Mr. H.W. Klimach, and Prof. A.L. Maffett in the data analysis phase. Mr. R.E. Hamilton served as technical editor while Mrs. C. Randazzo and Mrs. A. Sadlowski typed the entire report. This effort was conducted in ERIM's Electromagnetics and Electronics Department, which is directed by Dr. A. Kozma.

CONTENTS

FOREWORD	iii
LIST OF FIGURES	vii
LIST OF TABLES	xiv
1. INTRODUCTION AND SUMMARY	1
1.1 Introduction	1
1.2 Summary	10
2. MEASUREMENT THEORY AND REQUIREMENTS	17
2.1 Experimental Approach	19
2.2 Geometry	20
2.3 System Requirements	26
2.3.1 Antenna Parameters	26
2.3.2 Transmitter and Receiver Parameters	28
2.3.3 Power Calculations	32
2.4 Independent Samples for Bistatic Data	34
2.4.1 Receiving Antenna Selectivity	34
2.4.2 Doppler Shift	35
2.4.3 Wired Fluctuations	41
2.5 Summary of Advantages of Spotlight Scanning Technique	42
3. INSTRUMENTATION	44
3.1 Transmitter System	45
3.2 Receivers	47
3.3 Bistatic Receiving Antennas	50
3.4 Tracker	51
3.5 Bistatic Scan and Tracker Angle Calibration	53
4. DATA GATHERING	54
4.1 Preparation and Calibration	54
4.2 Data Gathering Phase	60
4.3 Data Evaluation	63
4.4 Preparation of Data for Analysis	68
5. DATA REDUCTION	69
5.1 Definition of σ_o and Associated Parameters	70
5.2 Evolution of Method for Approximating σ_o	75
5.3 Pattern Approximations for Receiving and Transmitting Antennas	77
5.4 Scattering Element A_{gd} ; Final Form of Equation for σ_o	84
5.4.1 Formulas for Footprint and Range Ellipses	88
5.4.2 Modification of I by Receiver Impulse Response	91
5.4.3 Final Form for σ_o	91

5.5	Ensemble Statistics of a Set of Scattering Elements; Parameter Variation	93
5.6	Data Processing: $\bar{\sigma}_0$ vs Azimuth ϕ_s	109
5.7	Results: Plots of σ_0 vs ϕ_s Over a Set of Parameter Values	110
5.7.1	Flight 7/17/76	111
5.7.2	Flight 7/9/76	125
5.7.3	Flight 7/2/76	132
5.8	Summary of Experimental Conditions and Results	138
5.8.1	System Operation	138
5.8.2	System Parameters	146
5.8.3	Monostatic Measurements	150
6.	ERROR ANALYSIS	152
6.1	Instrumentation Errors	152
6.2	Receiving Antenna Pattern Errors	162
6.2.1	Sidelobe Effects on Data	166
6.2.2	Polarization Isolation	167
6.3	Error Analysis Conclusions	168
6.3.1	Instrumentation Errors	168
6.3.2	Sampling Error	169
7.	CONCLUSIONS AND RECOMMENDATIONS	170
7.1	Conclusions	170
7.2	Recommendations	172
	REFERENCES.....	174
	LIST OF SYMBOLS.....	176
APPENDIX A:	THEORETICAL ANALYSIS AND DESIGN	A-1
	CONSIDERATIONS.....	A-1
APPENDIX B:	INSTRUMENTATION.....	B-1
APPENDIX C:	DATA COLLECTION.....	C-1
APPENDIX D:	DATA PROCESSING.....	D-1
APPENDIX E:	RESULTS.....	E-1

LIST OF ILLUSTRATIONS

1. Basic Bistatic Geometry.....	3
2. Complete Receiving Instrumentation.....	4
3. Interior of Receiving Equipment Van.....	5
4. Tracking Antennas and Local Oscillator Receiving Antenna.....	6
5. Transmitting Antennas, Transmitters, and Aircraft..	7
6. Example of 3 cm Wavelength Imagery.....	9
7. Functional Block Diagram of Complete System.....	11
8. Spotlight Measurement Geometry.....	18
9. Bistatic and Specular Time Delays vs. SCAN.....	23
10. Receiver Antennas and Pedestal.....	29
11. Transmitting System Block Diagram.....	46
12. Block Diagram of Bistatic Receiving Systems.....	49
13. Bistatic Receiving Antennas.....	52
14. Photograph of Site 1.....	55
15. Photograph of Site 2.....	56
16. Aircraft Flight Paths for 2 July 1976.....	57
17. Aircraft Flight Paths for 9 July 1976.....	58
18. Aircraft Flight Paths for 17 July 1976.....	59
19. Example Chart Record: Calibration.....	61
20. Sample Data Chart Record.....	62
21. Coordinate Systems.....	72
22. Detail of Parameters for Clutter Area Element dA... 74	74
23. Receiver Antenna Patterns at $f = 1.315$ GHz.....	82
24. Receiver Antenna Patterns at $f = 9.45$ GHz.....	83
25. Footprint and Range Ellipses.....	87
26. Receiver Impulse Response $h[t(A)]$	92
27. 3 cm Wavelength Histograms, ERIM SAR Data.....	94
28. Width of 95% Confidence Interval vs. Number of Samples.....	96
29. A_{gd} for SCAN = TRACK = 90° ($\phi_s = 0^\circ$).....	101
30. A_{gd} for SCAN = TRACK = 120° ($\phi_s = 0^\circ$).....	102

LIST OF ILLUSTRATIONS (continued)

31.	A_{gd} for SCAN = TRACK = 150° ($\phi_s = 0^\circ$).....	103
32.	A_{gd} for SCAN = TRACK = 60° ($\phi_s = 0^\circ$).....	104
33.	A_{gd} for SCAN = 90° , TRACK = 60° ($\phi_s = 30^\circ$).....	105
34.	A_{gd} for SCAN = 120° , TRACK = 60° ($\phi_s = 60^\circ$).....	106
35.	A_{gd} for SCAN = 60° (Back), TRACK = 60° ($\phi_s = 180^\circ$).....	107
36.	A_{gd} for SCAN = 120° (Back), TRACK = 60° ($\phi_s = 120^\circ$).....	108
37.	$\bar{\sigma}_o$ vs. ϕ_s for Passes 4 and 7, Flight 7/17/76, at 23 cm.....	112
38.	$\bar{\sigma}_o$ vs. ϕ_s for Passes 4 and 7, Flight 7/17/76, at 3 cm.....	113
39.	$\bar{\sigma}_o$ vs. ϕ_s for Passes 5 and 6, Flight 7/17/76, at 23 cm.....	114
40.	$\bar{\sigma}_o$ vs. ϕ_s for Passes 5 and 6, Flight 7/17/76, at 3 cm.....	115
41.	$\bar{\sigma}_o$ vs. ϕ_s for Passes 3 and 9, Flight 7/17/76, at 23 cm.....	116
42.	$\bar{\sigma}_o$ vs. ϕ_s for Passes 3 and 9, Flight 7/17/76, at 3 cm.....	117
43.	$\bar{\sigma}_o$ vs. ϕ_i for Flight 7/17/76.....	119
44.	Comparison of σ_o Scatter With One Standard Deviation About $\bar{\sigma}_o$ Using Log-Normal Distribution of σ_o	121
45.	Comparison, at 3 cm, of $\bar{\sigma}_o$ from Pass 3, Flight 7/17/76, with $\bar{\sigma}_o$ from Pass 7, Flight 7/9/76.....	122
46.	Comparison, at 23 cm, of $\bar{\sigma}_o$ from Pass 3, Flight 7/17/76, with $\bar{\sigma}_o$ from Pass 7, Flight 7/9/76.....	124
47.	Comparison of ERIM and OSU Data.....	127
48.	$\bar{\sigma}_o$ vs. ϕ_s for Passes 2, 5, and 7, Flight 7/9/76, at 23 cm (Averages Over All Passes).....	128

LIST OF ILLUSTRATIONS (continued)

49.	$\bar{\sigma}_o$ vs. ϕ_s for Passes 2, 5, and 7, Flight 7/9/76, at 3 cm (Averages Over All Passes).....	129
50.	$\bar{\sigma}_o$ vs. ϕ_s for Passes 2, 5, 6, and 7, Flight 7/9/76, at 23 cm (Averages Over All Passes).....	130
51.	$\bar{\sigma}_o$ vs. ϕ_s for Passes 2, 5, 6, and 7, Flight 7/9/76, at 3 cm (Averages Over All Passes).....	131
52.	$\bar{\sigma}_o$ vs. ϕ_s for Passes 2, 5, and 7, Flight 7/9/76, at 23 cm (Separate Averages for Each Pass).....	133
53.	$\bar{\sigma}_o$ vs. ϕ_s for Passes 2, 5, and 7, Flight 7/9/76, at 3 cm (Separate Averages for Each Pass).....	134
54.	$\bar{\sigma}_o$ vs. ϕ_s for Passes 2, 5, 6, and 7, Flight 7/9/76, at 23 cm (Separate Averages for Each Pass).....	135
55.	$\bar{\sigma}_o$ vs. ϕ_s for Passes 2, 5, 6, and 7, Flight 7/9/76, at 3 cm (Separate Averages for Each Pass).....	136
56.	σ_o vs. ϕ_{TRACK} for Site 1, Flight 7/2/76, and $\lambda = 23$ cm.....	137
57.	View from Receiving Antenna at Site 1.....	140
58.	View of Grassy Area at Site 1.....	141
59.	Close-Up View of Grass at Site 1.....	142
60.	View from Base of 100 ft Tower at Site 2.....	143
61.	Close-Up View of Weeds at Site 2.....	144
62.	σ_o vs. ϕ_s for 7/17/76, Pass 4, and 23 cm Wavelength.....	148
63.	Estimates of Signal-to-Noise Ratio.....	149
64.	Imagery from Pass 9, Flight 7/2/76.....	151
65.	Simplified Block Diagram of a Bistatic Measurement Channel.....	157
66.	One-Dimensional Model of σ_o and Calculated Values.....	165

LIST OF ILLUSTRATIONS (continued)

A-1.	Bistatic Geometry.....	A-9
A-2.	Scattering Geometry for Relative Doppler.....	A-16
A-3.	Side-Looking Geometry.....	A-22
A-4.	Constant Range Ellipses.....	A-23
A-5.	Receiving System with Narrow Fixed Beams.....	A-25
A-6.	Receiving System with Narrow Scanning Beam	A-27
A-7.	Theoretical Estimate of $\sigma_o(\psi)/\sigma_o(0)$ for Short Grass at $\lambda = 3$ cm.....	A-31
B-1.	Simplified Block Diagram of Bistatic Receiver System.....	B-9
B-2.	Video Amplifier Circuit Diagram.....	B-10
B-3.	Parallel Receiver Circuit Diagram.....	B-11
B-4.	Crossed Receiver Circuit Diagram for $\lambda = 3$ cm...B-12	
B-5.	Crossed Receiver Circuit Diagram for $\lambda = 23$ cm...B-13	
B-6.	Sample-Hold Output Response Vs. Sample-Hold Gate Delay.....	B-17
B-7.	Received STALO Powers Vs. 3 and 23 cm L.O. Power.	B-19
B-8.	Conversion Losses Vs. L.O. Power.....	B-21
B-9.	Board 1: Sync Generator and PRF Instrumentation..	B-22
B-10.	Board 2: Calibration PRF Generator.....	B-24
B-11.	Board 3: AR Instrumentation Generator.....	B-26
B-12.	Boards 4 and 5: 3 and 23 cm Wavelength Video Instrumentation.....	B-28
B-13.	Board 6: Data Logic and Angle Instrumentation....	B-29
B-14.	Board 7: Dual-Band Offset Frequency Generators...	B-31
B-15.	Board 8: Calibration Step Generator.....	B-33
B-16.	Board 9: Step Driver.....	B-34
B-17.	Boards 10 and 11: Antenna Demodulator-Servo Amplifier Driver.....	B-36
B-18.	Board 12: Interface Scan Generator to Antenna Drive.....	B-38
B-19.	Board 13: Scan Generator.....	B-39
B-20.	Board 14: Scan Generator.....	B-40

LIST OF ILLUSTRATIONS (continued)

B-21.	Board 15: Relay Board.....	B-42
B-22.	Block Diagram of 3 or 23 cm Calibration System..	B-43
B-23.	Map from 16-Bit Word to 7-Track Tape.....	B-47
B-24.	Tape Format.....	B-46
B-25.	Format of Tape Records.....	B-49
C-1.	Data Gathering Flight Path for Bistatic Measurements.....	C-2
C-2.	Calculated Transmitting Antenna Pointing Errors.	C-5
C-3.	Pre-Flight Calibration Checklist.....	C-7
C-4.	Ground Check and Operate Checklist.....	C-11
C-5.	In-Flight Calibration Checklist.....	C-13
C-6.	Measurement Log Form.....	C-14
D-1.	Digitization System.....	D-2
D-2.	Digitization Timing Diagram.....	D-3
D-3.	Example of Scan Angle Divisions.....	D-5
D-4.	Flow Chart for Procedure FIRST.....	D-8
D-5.	Program Listing for Procedure FIRST.....	D-11
D-6.	Flow Chart for Procedure SECOND.....	D-13
D-7.	Source Listing for Procedure SECOND.....	D-16
D-8.	Flow Chart for Procedure THIRD.....	D-18
D-9.	Example Output Plots from Procedure THIRD.....	D-19
D-10.	Source Listing for Procedure THIRD.....	D-20
D-11.	Source Listing for BSMAIN Program and Its Subroutines.....	D-26
E-1.	σ_o vs ϕ_s for Pass 3, Flight 7/17/76 at 23 cm Wavelength, Horizontal Polarization.....	E-2
E-2.	σ_o vs ϕ_s for Pass 9, Flight 7/17/76 at 23 cm Wavelength, Horizontal Polarization.....	E-3
E-3.	σ_o vs ϕ_s for Pass 4, Flight 7/17/76 at 23 cm Wavelength, Horizontal Polarization.....	E-4
E-4.	σ_o vs ϕ_s for Pass 7, Flight 7/17/76 at 23 cm Wavelength, Horizontal Polarization.....	E-5

LIST OF ILLUSTRATIONS (continued)

E-5.	σ_o vs ϕ_s for Pass 5, Flight 7/17/76 at 23 cm Wavelength, Horizontal Polarization.....	E-6
E-6.	σ_o vs ϕ_s for Pass 6, Flight 7/17/76 at 23 cm Wavelength, Horizontal Polarization.....	E-7
E-7.	σ_o vs ϕ_s for Pass 10, Flight 7/17/76 at 23 cm Wavelength, Horizontal Polarization.....	E-8
E-8.	σ_o vs ϕ_s for Pass 11, Flight 7/17/76 at 23 cm Wavelength, Horizontal Polarization.....	E-9
E-9.	σ_o vs ϕ_s for Pass 12, Flight 7/17/76 at 23 cm Wavelength, Horizontal Polarization.....	E-10
E-10.	σ_o vs ϕ_s for Pass 3, Flight 7/17/76 at 3 cm Wavelength, Horizontal Polarization.....	E-11
E-11.	σ_o vs ϕ_s for Pass 9, Flight 7/17/76 at 3 cm Wavelength, Horizontal Polarization.....	E-12
E-12.	σ_o vs ϕ_s for Pass 4, Flight 7/17/76 at 3 cm Wavelength, Horizontal Polarization.....	E-13
E-13.	σ_o vs ϕ_s for Pass 7, Flight 7/17/76 at 3 cm Wavelength, Horizontal Polarization.....	E-14
E-14.	σ_o vs ϕ_s for Pass 5, Flight 7/17/76 at 3 cm Wavelength, Horizontal Polarization.....	E-15
E-15.	σ_o vs ϕ_s for Pass 6, Flight 7/17/76 at 3 cm Wavelength, Horizontal Polarization.....	E-16
E-16.	σ_o vs ϕ_s for Pass 10, Flight 7/17/76 at 3 cm Wavelength, Horizontal Polarization.....	E-17
E-17.	σ_o vs ϕ_s for Pass 11, Flight 7/17/76 at 3 cm Wavelength, Horizontal Polarization.....	E-18
E-18.	σ_o vs ϕ_s for Pass 12, Flight 7/17/76 at 3 cm Wavelength, Horizontal Polarization.....	E-19

LIST OF ILLUSTRATIONS (concluded)

E-19.	σ_o vs ϕ_s for Pass 2, Flight 7/9/76 at 23 cm Wavelength, Horizontal Polarization.....	E-20
E-20.	σ_o vs ϕ_s for Pass 5, Flight 7/9/76 at 23 cm Wavelength, Horizontal Polarization.....	E-21
E-21.	σ_o vs ϕ_s for Pass 6, Flight 7/9/76 at 23 cm Wavelength, Horizontal Polarization.....	E-22
E-22.	σ_o vs ϕ_s for Pass 7, Flight 7/9/76 at 23 cm Wavelength, Horizontal Polarization.....	E-23
E-23.	σ_o vs ϕ_s for Pass 2, Flight 7/9/76 at 3 cm Wavelength, Horizontal Polarization.....	E-24
E-24.	σ_o vs ϕ_s for Pass 5, Flight 7/9/76 at 3 cm Wavelength, Horizontal Polarization.....	E-25
E-25.	σ_o vs ϕ_s for Pass 6, Flight 7/9/76 at 3 cm Wavelength, Horizontal Polarization.....	E-26
E-26.	σ_o vs ϕ_s for Pass 7, Flight 7/9/76 at 3 cm Wavelength, Horizontal Polarization.....	E-27

LIST OF TABLES

1. Summary of Bistatic Measurement Angles	14
2. Summary of Bistatic Data	16
3. Four Typical Geometries	22
4. Antenna Parameters	27
5. Transmitter Parameters	30
6. Receiver Parameters	31
7. Bistatic Measurements Flight Parameters for 2 July 1976	36
8. Bistatic Measurements Flight Parameters for 9 July 1976	37
9. Bistatic Measurements Flight Parameters for 17 July 1976	38
10. Independent Samples per Receiver Beam Position Caused by Doppler Spread	40
11. Receiver Channels and Antennas	48
12. Data Evaluation, 2 July 1976	64
13. Data Evaluation, 9 July 1976	65
14. Data Evaluation, 17 July 1976	66
15. 23-cm Wavelength Antenna Characteristics (Measured)	80
16. 3-cm Wavelength Antenna Characteristics (Measured)	81
17. Variations in A_{gd} and KI Values	100
18. Behavior of A_{gd} and KI for Forward and Back- Scattering Cases	100
19. Comparison of ERIM and OSU Backscattering ($\phi_s = 180^\circ$) σ_o Data	126
20. Description of Test Areas	139
21. Summary of Digitized Bistatic Data	145
22. Recorded Parameters with Applications and Accuracies	153
23. Estimates of Systematic Errors	158
24. Estimates of Random Errors	160

LIST OF TABLES (concluded)

A-1.	Bandwidth vs. θ_{limit}	A-6
A-2.	Bandwidth Required for $\Delta\theta = 5^\circ$, $y_1 = 100$ ft.....	A-11
A-3.	$\Delta\theta$ vs. θ_s for Bandwidth of 30 MHz and $y_1 = 100$ ft.....	A-12
A-4.	Change in Doppler vs. Change in Squint Angle Complement.....	A-14
A-5.	Change in Doppler vs. ϕ_s	A-18
A-6.	Ratios of Mainlobe to Sidelobe Return.....	A-33
B-1.	3 cm Wavelength Receiving Antenna Data.....	B-5
B-2.	23 cm Wavelength Receiving Antenna Data.....	B-5
B-3.	Spurious Cross-Polarized Component Caused by an Error Between Transmitting and Receiving Antenna Axes.....	B-7
D-1.	Procedure FIRST Output.....	D-10
D-2.	Procedure SECOND Output.....	D-16
D-3.	BSMAIN Program Output.....	D-25

1

INTRODUCTION AND SUMMARY

1.1 INTRODUCTION

In the design of radar detection systems, an often-used measure of system performance is the probability of detection for a target of specified cross section. For most radar applications, cultural objects are the targets of interest. However, the energy scattered to the radar antenna from the target must compete with energy scattered from the terrain that is included within the resolution element surrounding the target. The latter energy is referred to as clutter signal return and the probability of detection is a function of the magnitude and the statistics of this clutter return. Considerable (although not always adequate) empirical clutter data are available from the literature for backscatter radar geometry. However, very few radar clutter data are available for the bistatic radar situation. It is therefore the objective of the present effort to obtain estimates of the bistatic scattering coefficient.

The empirical data resulting from this effort are used to determine estimates of the bistatic scattering coefficient σ_0 for 3 and 23 cm wavelength radiation, for like and cross polarization at each of the wavelengths (a total of four simultaneous data channels), as well as for a variety of bistatic angles and two terrain types.

Calibration signals are used to obtain an accurate measure of the absolute value of received power; also, system and geometrical parameters are measured to permit the received power data to be used to calculate values of σ_0 as a function of the bistatic angles. The basic bistatic

geometry used for the measurements is shown in Figure 1. Note that the transmitting antenna is flown in a straight line path; the receiving antenna is located on a tower and scans in order to obtain a suitable number of data samples.

A four-channel receiving system provides simultaneous measurements at two wavelengths and two polarization states. Figure 2 shows a photograph of the complete receiving installation. The system consists of two dual-polarization antennas, two receivers for each operating wavelength, and four recorder channels. Also, calibration signals are provided for each receiver. Figure 3 shows the interior of the receiving equipment van.

Coherent operation is required in order to measure the Doppler signal history. The instrumentation therefore includes a separate transmitter-to-receiver link for the receiver local oscillator source; the receiving antenna for this link (along with tracking horn antennas) is shown in Figure 4. Local oscillator power for each receiver mixer is obtained using power received from the transmitter via this direct link. The signal radiated from the bistatic transmitter is obtained from the basic stable frequency source used to drive the transmitter. Thus, the complete bistatic system is coherent and the residual Doppler signal relative to the scattering area is recorded. The Doppler shift due to the transmitter illumination angle ϕ_{TRACK} in Figure 1 is cancelled out since this shift also appears in the local oscillator signal.

The transmitter antenna system for the two wavelengths and for the local oscillator link is shown in Figure 5a; the transmitter itself is shown in Figure 5b. The aircraft in which the bistatic transmitter and a synthetic aperture radar (SAR) are carried is shown in Figure 5c. SAR imagery

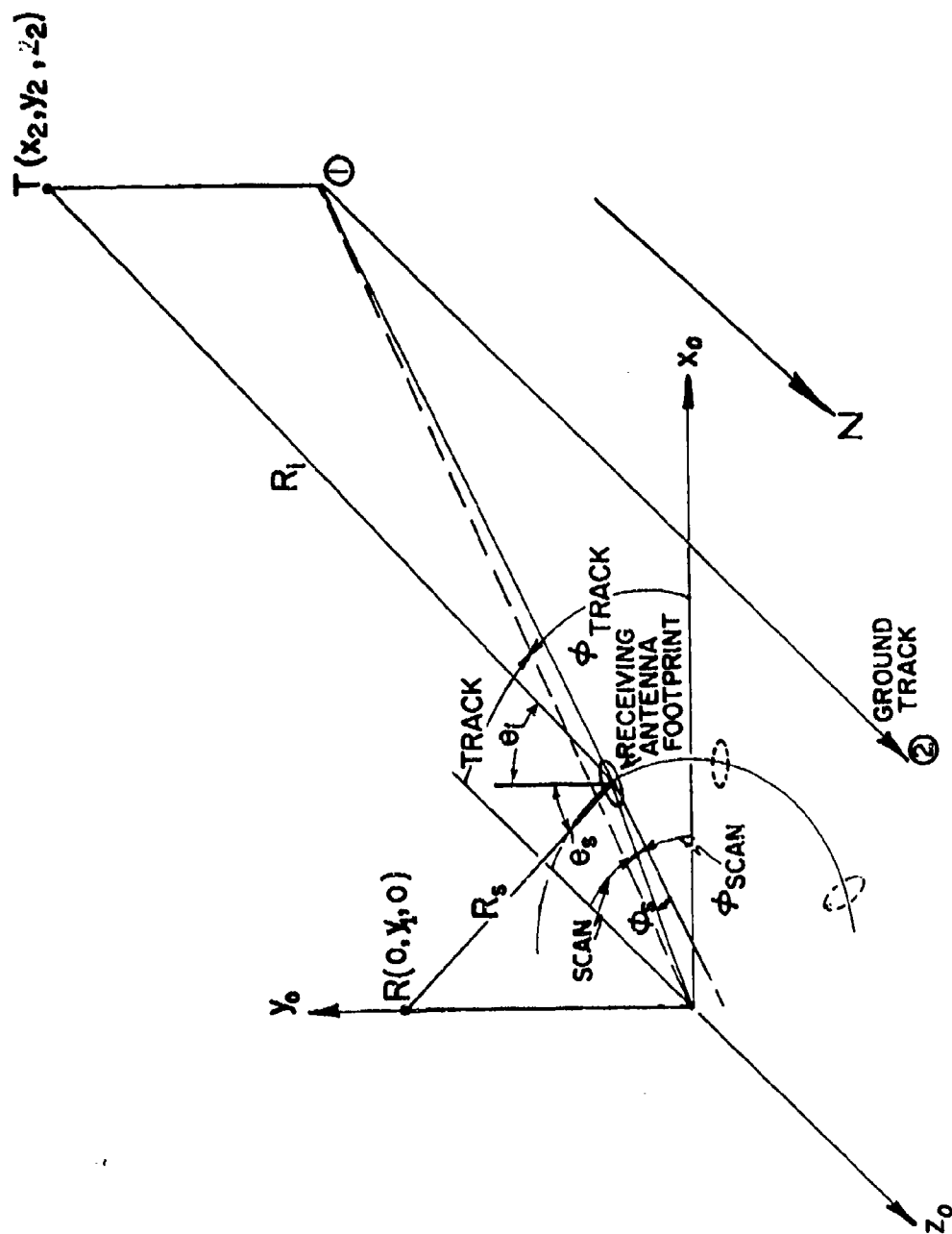


Figure 1. Basic Bistatic Geometry

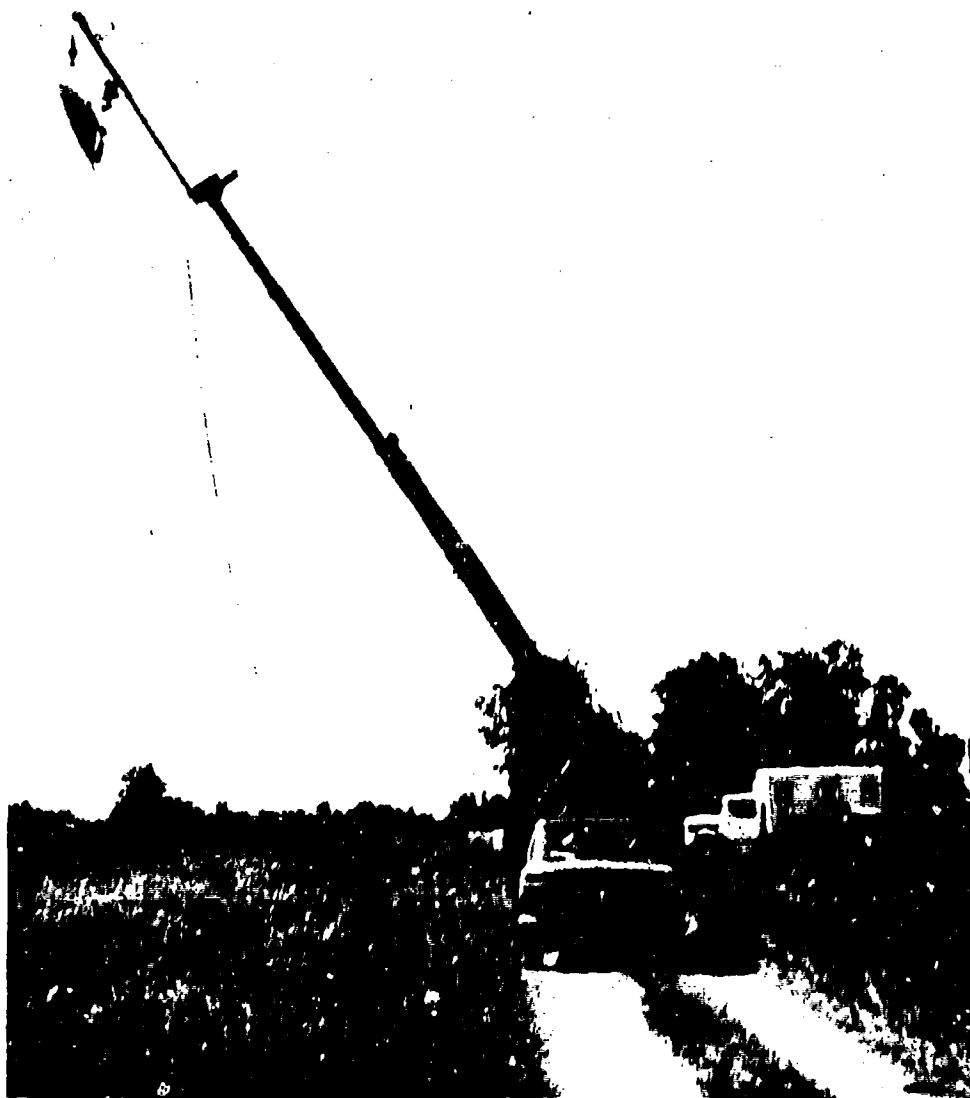


Figure 2. Complete Receiving Instrumentation

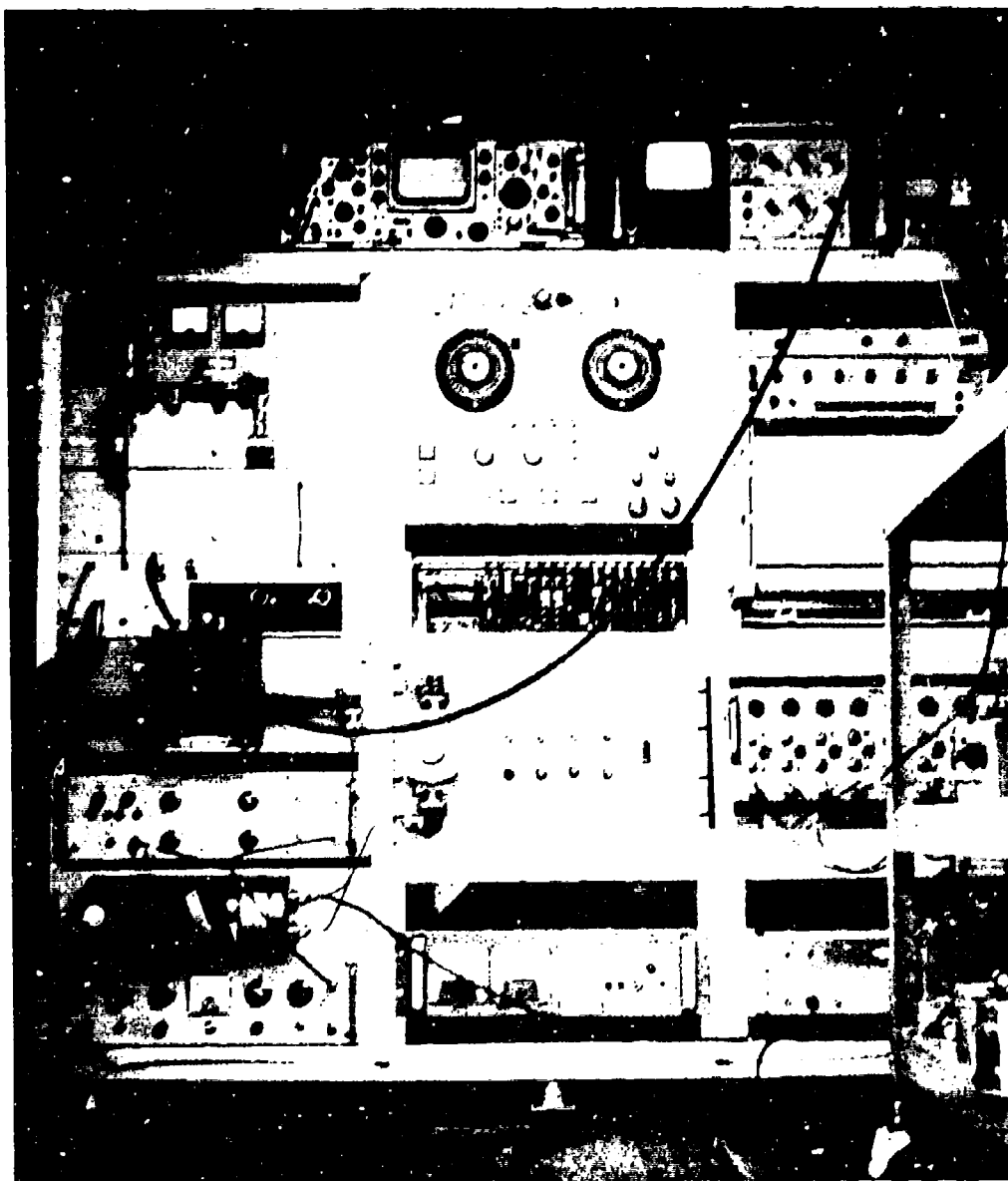
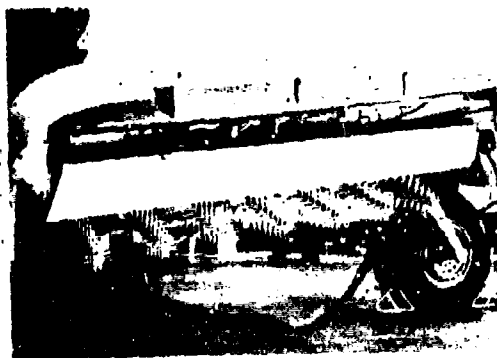


Figure 3. Interior of Receiving Equipment Van



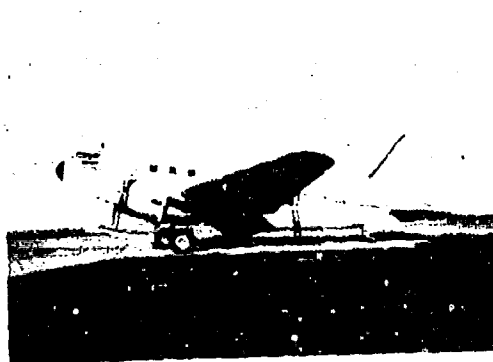
Figure 4. Tracking Antennas and Local Oscillator Receiving Antenna



(a) 3 cm and 23 cm
Transmitting
Antennas



(b) Transmitting
Equipment
Installation



(c) C-46 Instrumenta-
tion Aircraft

Figure 5. Transmitting Antennas, Transmitters, and Aircraft

at both 3 and 23 cm wavelengths was obtained as a reference from which an estimate of backscattering coefficient can be made. Calibration reflectors can be seen in the 3 cm imagery shown in Figure 6.

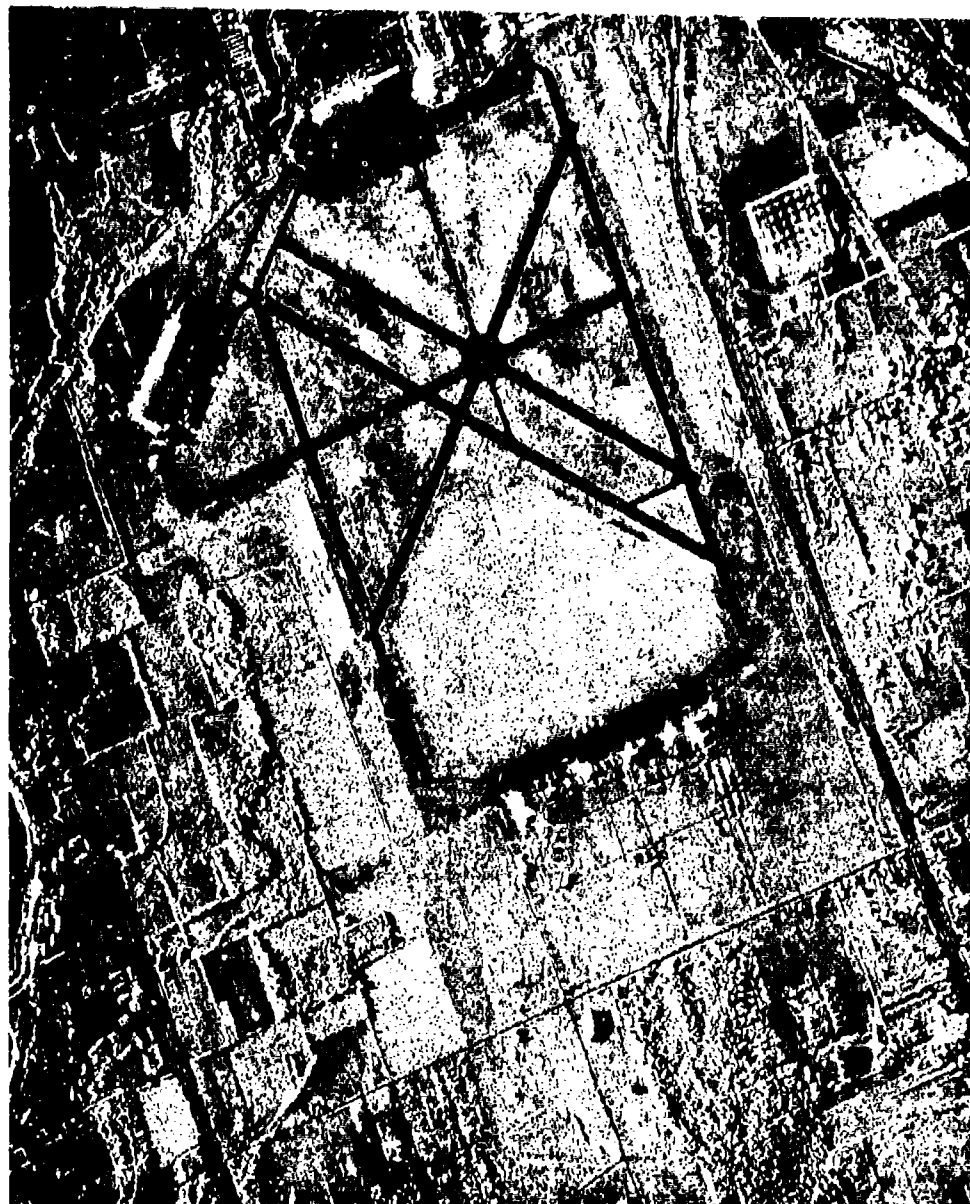


Figure 6. Example of 3 cm Wavelength Imagery

1.2 SUMMARY

This report describes work which was performed during the period from 1 October 1975 through 30 September 1976. The objective of this program was to collect empirical data from which to obtain an accurate estimate of bistatic clutter statistics. Instrumentation was used which matches, as closely as practicable, the configuration expected in a typical operational bistatic system (except that, here, an aircraft and a ground tower were used for transmitting and receiving, respectively, instead of two aircraft). A block diagram of the complete system is shown in Figure 7. The program was conducted in four phases:

1. analysis of the bistatic clutter measurements experiment,
2. design and construction of necessary equipment,
3. performance of the data-gathering experiments, and
4. reduction of the empirical data.

Simultaneous empirical data were obtained at 3 cm and 23 cm wavelengths, with like and orthogonal polarizations at each wavelength. The experiment provided coherent data, sampled and recorded on a pulse-by-pulse basis, from each of the four channels. The following tasks were completed during the program:

1. An analysis of the bistatic coherent measurement system for two wavelengths and two polarizations.
2. An analysis describing the empirical data expected and the calibration requirements; also, a system error analysis.
3. The specification of measurement geometry,

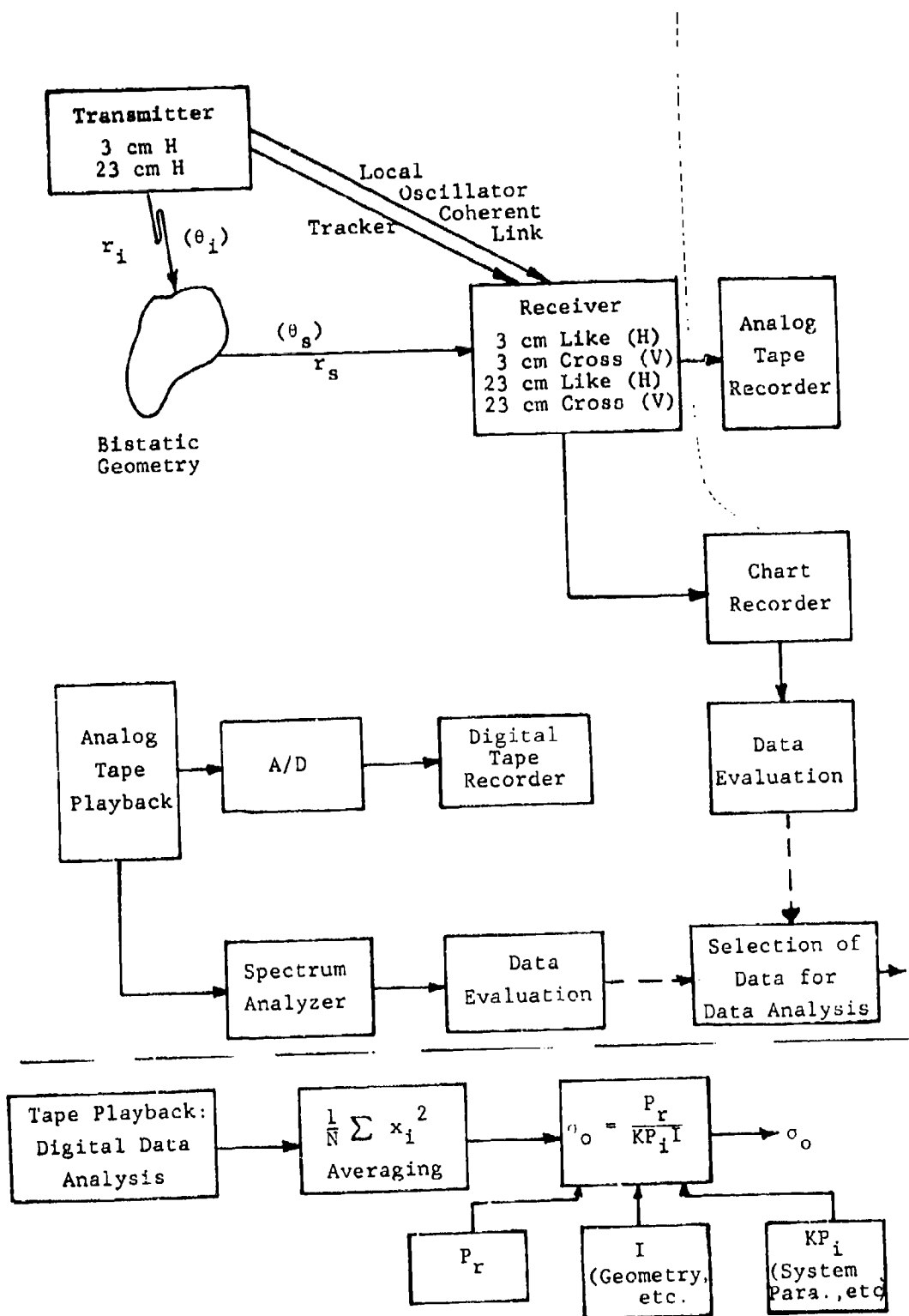


Figure 7. Functional Block Diagram of Complete System

system operating parameters, and instrumentation requirements.

4. Using the results from (3), the design and fabrication of the four-channel measurements instrumentation, the coherence and synchronization link, and the calibration system; also, the measurement of total system response.
5. The writing of computer programs for data digitization and analysis; also, the implementation and testing of these programs.
6. System test and data gathering at two test sites.
7. Data evaluation and digitization; also the delivery of digital data tapes to General Research Corporation (GRC) and to Radio Corporation of America (RCA) for analysis.
8. An analysis of the empirical data to determine values of the bistatic reflection coefficient as a function of the bistatic angles.
9. Documentation of the instrumentation.
10. Documentation of the data analysis technique and the computer programs.
11. Graphical presentation of the bistatic scattering coefficients; also, an estimate of the error.
12. The collection of radar imagery of the test sites and the determination of backscattering coefficient values.

The measurement technique utilized is illustrated in

Figure 1. Receiving apertures are mounted on a tower and their field of view is scanned through an azimuth angular interval Δ SCAN. The scattering area is illuminated using the radar transmitters in ERIM's C-46 radar aircraft as sources. Radiation at two wavelengths is transmitted simultaneously and horizontal polarization is used in both transmitter channels. As the aircraft flies along a path 1-2 (Figure 1), the transmitter antennas are scanned so as to spotlight the scattering area. The receiving antenna scan rate is adjusted so that one scan is completed during a period in which the transmitted illumination angle changes by approximately 5 degrees. Measurements were made for the bistatic angles listed in Table 1; priorities for the selection of angles θ_i and θ_s were determined by GRC.

To obtain estimates of the values of σ_o , empirical values of received power are substituted into the bistatic equation (see equation 3) along with the experimental geometrical parameters, and the equation is solved for σ_o as a function of bistatic angle. During data analysis, values of received power are averaged over approximately 5 degrees of azimuth angle. It is assumed that the function σ_o is a slowly-varying function of azimuth angle and that therefore the 5-degree truncation does not obscure any fine-scale structure in the σ_o characteristics. This assumption is based on a consideration of available data [1].

The aircraft carrying the transmitter was tracked during each data pass and the nominal illumination angle (that is, the ϕ_{TRACK} angle) at the receiver site was recorded.

1. W.H. Peake and T.L. Oliver, The Response of Terrestrial Surfaces at Microwave Frequencies, Report No. AFAL-TR-70-301, Electrosience Laboratory, Ohio State University, Columbus, May 1971.

TABLE 1. SUMMARY OF BISTATIC
MEASUREMENT ANGLES

<u>Terrain</u>	θ_s (deg)	θ_i (deg)	ϕ_s (deg)
Site 1 (flat grass and cement taxiway; dry)	85	80	0-105
		75	0-105
		65	0-105
		50	0-105
Site 2 (tall weeds and scrub trees; dry)	80	80	0-180
		75	0-180
		70	0-180
	70	80	0-105
		75	0-105
		70	0-105

Similarly, the receiving antenna azimuth angle SCAN was recorded. The difference between these two angles is the bistatic azimuthal, or out-of-plane, angle ϕ_s . Based on the results of an error analysis (discussed in Section 6), the estimated error in σ_o values obtained is 6 dB.

Reviews of the system analysis are included in Section 2 and in Appendix A. Descriptions of the instrumentation are included in Section 3 and in Appendix B. Data analysis procedures and computer programs are presented in Section 5 and in Appendix D. The results obtained are discussed in Section 5.7; the results of the analysis of all data that were determined to be usable are presented in Appendix E. A summary of the bistatic data obtained is given in Table 2.

TABLE 2. SUMMARY OF BISTATIC DATA

<u>Data Gathering Flight</u>	<u>Data on Analog Tape</u>	<u>Digitized Data</u>
7/2/76	All passes, 1-10 2 calibrations	2 calibrations
7/9/76	All passes, 1-7 2 calibrations	passes 2,5,6,7 2 calibrations
7/17/76	All passes, 1-12 4 calibrations	passes 3,4,5,6, 7,9,10,11,12 4 calibrations

2 MEASUREMENT THEORY AND REQUIREMENTS

The quantity to be measured in this program is the value of the bistatic scattering cross section density $\sigma_o(\theta_i, \theta_s, \phi_s)$ for a range of bistatic angles θ_i , θ_s and ϕ_s , as defined in Figure 1. The basic conceptual block diagram for the measurement system (Figure 8) shows that the measure of received power after processing is proportional to the value of σ_o . Using the generalized geometry shown in Figure 1, the relationship between σ_o and the measurement parameters (both system and geometrical) is derived in the following paragraph. The mathematical terminology used throughout this report is defined in the List of Symbols provided at the back of the report.

Power incident on a scattering area A_{gd} is given as

$$P'_i = P_i \frac{G_{OT}}{4\pi r_i^2} f_T, \quad (1)$$

and the power incident on the receiving antenna aperture is given by

$$P'_r = P'_i A_{gd} \sigma_o \frac{1}{4\pi r_s^2} \quad (2)$$

Utilizing Eqs. (1) and (2) and the fact that $P_r = (P'_r G_{OR} f_R)/4\pi$, the received power can be written

$$P_r = P_i \frac{G_{OT} G_{OR}}{(4\pi)^3 r_i^2 r_s^2} \sigma_o A_{gd} f_T f_R \quad (3)$$

Solving Eq. (3) for σ_o in terms of the antenna responses and

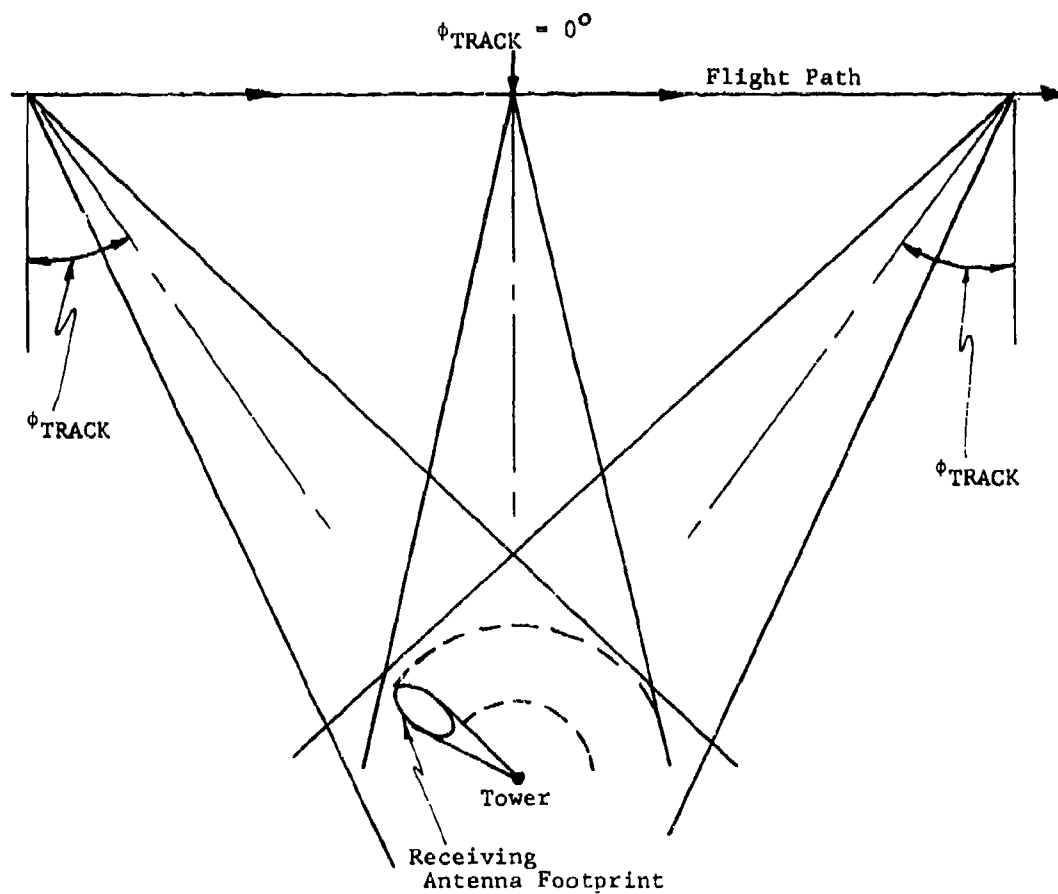


Figure 8. Spotlight Measurement Geometry

the total scattering area to account for total antenna (including sidelobe) contributions, gives

$$\sigma_o = \frac{P_r}{P_i KI} \quad (4)$$

where

$$K = \frac{\lambda^2 G_{OT} G_{OR} L}{(4\pi)^3}$$

and

$$I = \int_{A_{gd}} \frac{f_T f_R W_{\rho\phi}}{r_i^2 r_s^2} h[t(A)] dA$$

The parameter K includes the fixed value of wavelength, receiving and transmitter maximum gains, as well as total system losses. The integral I includes the angle- and time-dependent parameters of antenna angular response, along with range, transmitter waveform, and scattering area.

The parameters on the right side of Eq. (4) are measured during the data gathering. Data reduction then involves the computation of σ_o using these parameter values.

2.1 EXPERIMENTAL APPROACH

There are several measurement techniques that can be utilized to obtain an estimate of the bistatic scattering coefficient σ_o . Clearly, the measurement technique used must satisfy the following basic requirements:

1. the geometry must be defined,
2. the scattering area, A_{gd} , must be determined,
3. the system parameters must be measured, and
4. the parameters must be calibrated.

The spotlight measurement technique utilized in the work described is illustrated in Figure 8. Other measurement techniques were considered; these are discussed in Appendix A along with the reasons for rejecting them.

In the bistatic terrain measurement system, 3 and 23 cm power is radiated from the C-46 aircraft to the ground, and a ground-based system receives and records the scattered signals from the terrain to provide a measure of scattered power P_r . An analysis of these data then provides information on bistatic terrain scattering. As a result of planning studies, the aircraft is flown along a straight line past the crane holding the receiving antennas. The aircraft has wide-beam antennas which illuminate the ground in the vicinity of the receiver, and the receiving antenna scans the same terrain as the aircraft passes. The receiving antenna provides selectivity to isolate terrain patches. A pulse signal provides range gating to isolate the direct and scattered signals. Doppler information has not been used for azimuth beam sharpening, although this could be done using the raw data obtained from these measurements. The output consists of σ_0 values as a function of the bistatic angles. Measurement priorities* have indicated that the low grazing angles (large incidence and scattering angles) are the most important. Data were obtained at the angles indicated in Table 1.

2.2 GEOMETRY

Figure 1 is a sketch of the measurement geometry and the nomenclature adopted. The maximum aircraft height did not exceed 14,000 ft, and the receiver height was 45 ft at Site 1 and 100 ft at Site 2. To obtain large values of θ_s

*Based on discussions with Dr. David Walsh, DARPA and with Mr. J. Belyea and Dr. G. Ackinson of GRC.

and to maximize the received power, the aircraft should fly near to the receiver; however, the receiving antenna must then slew rapidly at short ranges. The distance to the aircraft is thus a compromise.

Table 3 lists the ground distance x_2 and the aircraft height y_2 for four typical geometries with $\theta_i = 20, 40, 60$, and 75° . Figure 9 presents curves of ΔT versus SCAN, where ΔT is the difference in path length between the direct and scattered signals. As the incidence angle θ_i increases, ΔT decreases; this makes separation of the direct and scattered fields more difficult. A pulse system is used to isolate the direct signal from the bistatic; a 90 nsec pulse width (Section 5.8) corresponding to a theoretical resolution of 90 ft is used throughout. Since the path-length difference is only 90 ft when θ_i is 60° , it is not possible to separate the direct and scattered signals at greater incidence angles. It is, in fact, difficult to separate these signals at 60° , because the received signals do not have a rectangular envelope. Thus, an additional delay δ is provided; the minimum δ value of 30 nsec is used to insure that the direct signal is rejected. Figure 9 also indicates that range gating will be ineffective for discriminating against particular signals entering through the sidelobes. With a 90 ft range gate, signals for a wide θ_s interval are time-coincident; however, with antenna sidelobe levels of -24 dB or less and with thresholding in the receiver, the sidelobe response is minimal.

The contours of constant time delay are closer together when ϕ_s is not zero, and time discrimination will be more effective. However, time discrimination still cannot be counted on to gate sidelobe energy out of the receiver completely.

TABLE 3. FOUR TYPICAL GEOMETRIES

$$\left[\begin{array}{ll} y_1 = 100 \text{ ft} & V = 250 \text{ fps} \\ \beta_t = 12^\circ & \phi_s = 0^\circ \end{array} \right]$$

<u>Geometry</u>	$\frac{x_2}{(\text{ft})}$	$\frac{y_2}{(\text{ft})}$	$\frac{\Delta R_{\min}}{(\text{ft})}$	$\frac{\theta_i = \theta_s}{(\text{deg})}$	$\frac{\text{Scan Time}}{(\text{sec})}$
I	3,676	10,000	188	20	7.4
II	8,476	10,000	153	40	9.1
III	17,493	10,000	99	60	14.0
IV	25,373	6,698	51	75	18.1

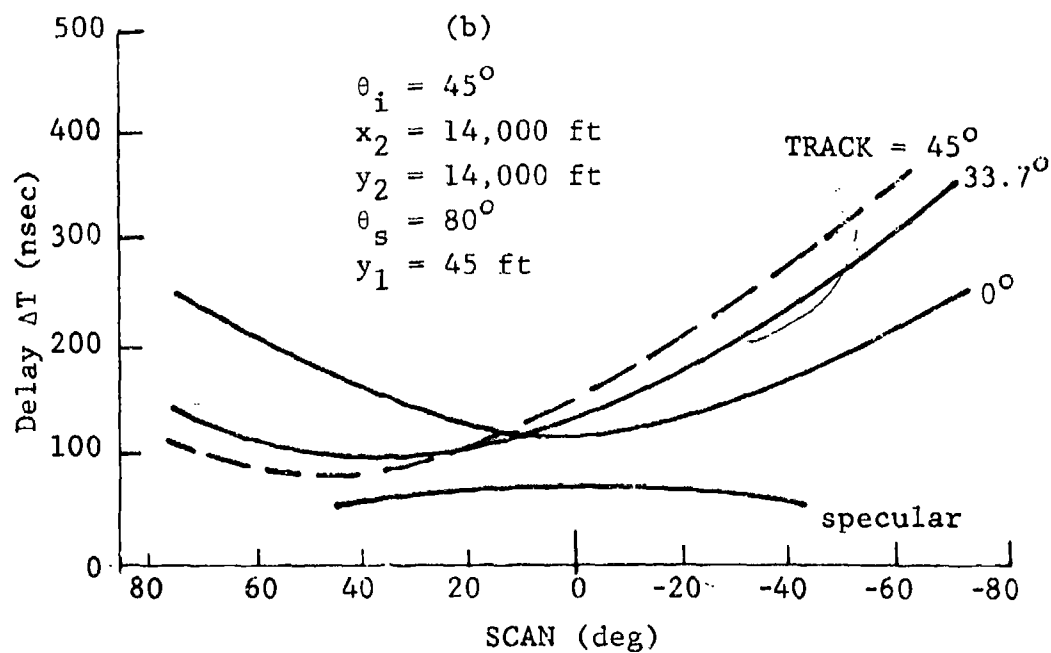
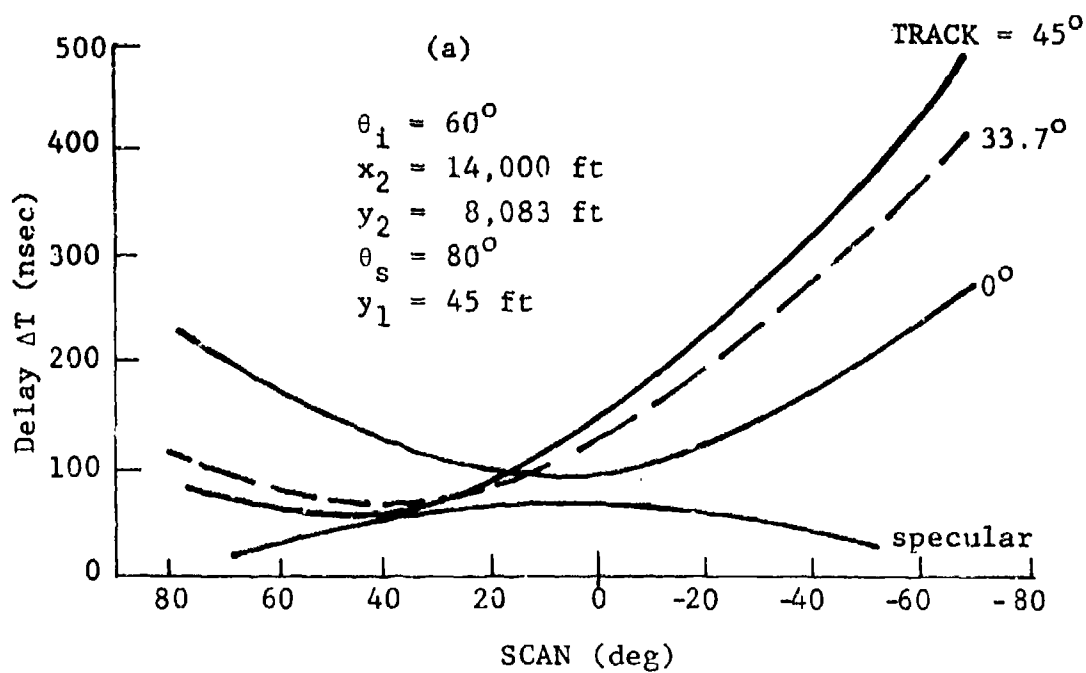


Figure 9. Bistatic and Specular Time Delays vs. SCAN

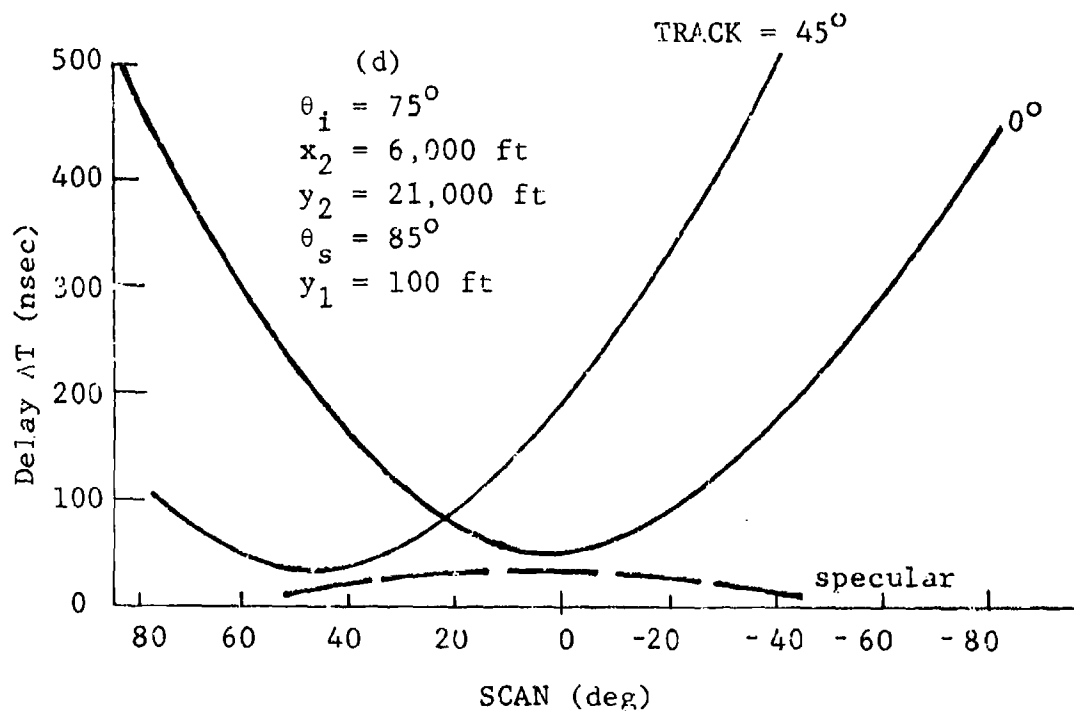
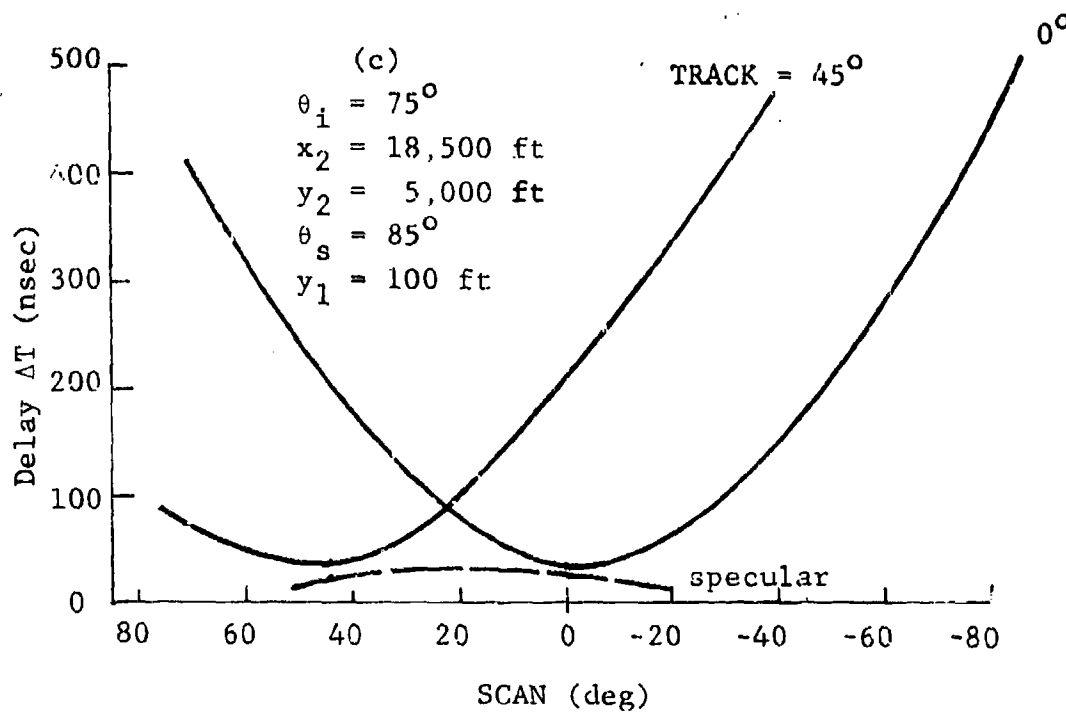


Figure 9. Bistatic and Specular Time Delays vs. SCAN (Continued)

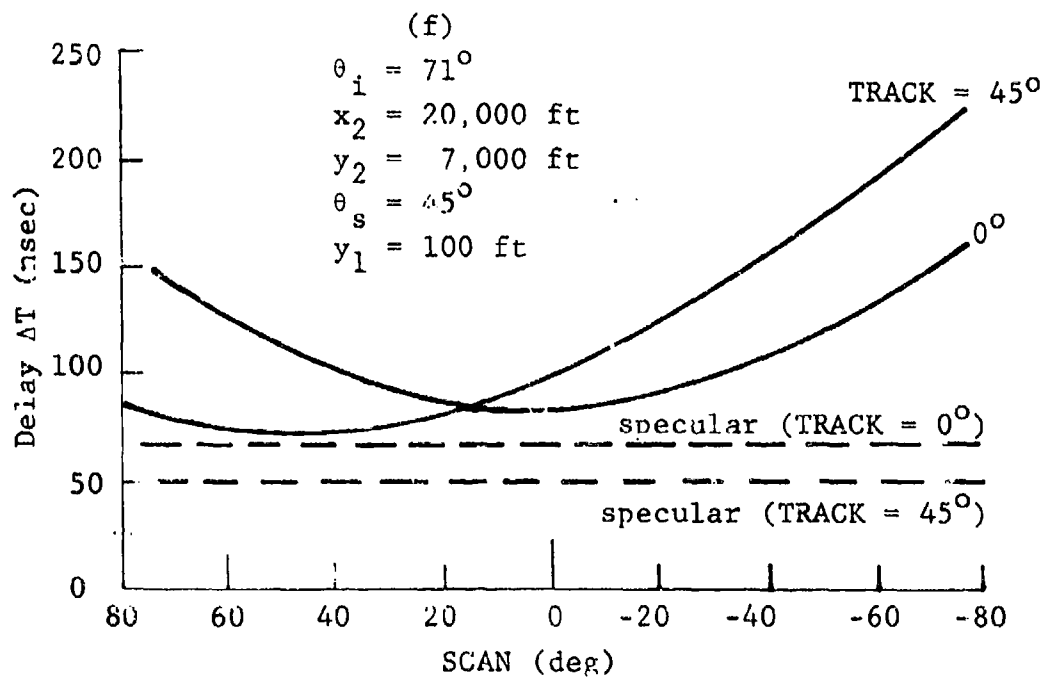
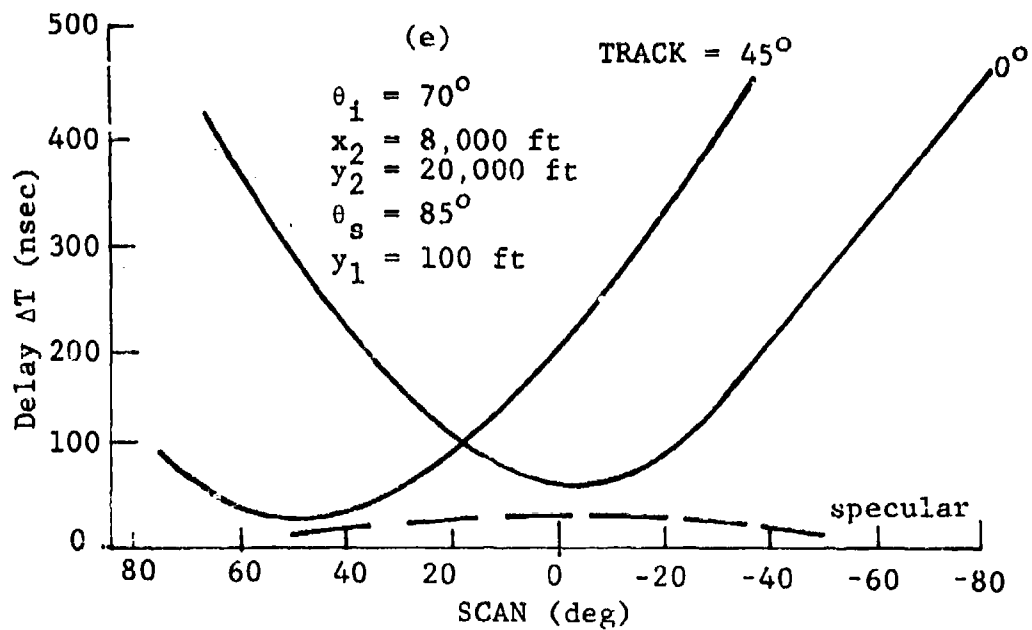


Figure 9. Bistatic and Specular Time Delays vs. SCAN (Concluded)

Table 3 also lists the receiver antenna scan times for the four geometries with a 10° transmitter beam; the scan time varies from 7.45 to 18 seconds. The receiving antenna must have a slew rate commensurate with 7.45 seconds to collect data from all ground patches of interest before the transmitter illumination angle changes by 5° .

With a receiver antenna beamwidth of 5° , the values of $\Delta\theta_s$ and $\Delta\phi_s$ will be approximately 5° . The geometry determines the spread $\Delta\theta_i$. Calculations using the four geometries in Table 3 show that $\Delta\theta_i < 0.7^\circ$ in all cases during each antenna scan. With a scanning antenna, the change in $\Delta\phi_s$ during the time when data are being collected from a resolution patch will be small; if data are collected from 30 patches during a pass, $\Delta\phi_i$ will be about $1/3^\circ$.

2.3 SYSTEM REQUIREMENTS

2.3.1 ANTENNA PARAMETERS

Table 4 lists the major parameters for the transmitting antennas in the aircraft and the receiving antenna on the tower. There are two transmitting antennas, one for 23 cm and one for 3 cm wavelength, which have dual-polarization capability; these permit collecting data with both horizontal and vertical transmitted polarizations on different flights.

The receiving antennas are more complicated than the transmitting antennas. They must have dual-frequency and dual-polarization capabilities, that is, they must receive both horizontal and vertical polarizations at 23 and 3 cm wavelengths. Also, there must be adequate isolation (25 dB or more) between the vertically and horizontally-polarized feeds for accurate simultaneous measurements of like and cross-polarized σ_o values.

TABLE 4. ANTENNA PARAMETERS

A. Transmitter	Wavelength	
	22.8 cm	3.17 cm
Polarization (Capabilities: V or H)	H	H
Cross-Polarization Isolation	>20 dB	>25 dB
Center Frequency	1.315 GHz	9.450 GHz
Maximum Bandwidth (3 dB)	100 MHz	100 MHz
Horizontal Beamwidth (3 dB)	12°	12°
Vertical Beamwidth (3 dB)	90°	13°
Peak Antenna Gain (referred to isotropic)	16 dB	22.2 dB
B. Receiver		
Polarization	V & H	V & H
Cross-Polarization Isolation	>31 dB	>27 dB
Center Frequency	1.315 GHz	9.450 GHz
Maximum Bandwidth (3 dB)	100 MHz	100 MHz
Beamwidth (3 dB; Horizontal and Vertical)	5°	5°
Peak Gain	30 dB	31 dB
Aperture Diameter	3.1 m	46 cm
Gain (Sidelobe Region)	0 dB	0 dB
Highest Sidelobe	<-25 dB	<-25 dB
Mount	Inverted elevation over azimuth	
Minimum Scanning Speed	25°/sec	
Time to Reach Speed	≈2 sec	
Position Readout Accuracy	<1°	
Azimuth Scan Angle	0-360° (in segments)	
Elevation Scan Angle	0-90°	
Maximum Safe Wind Loading During Operation	10 mph	

The 5° antenna beam requirement determines the sizes of the receiving dishes. (A narrower beam would be preferable, but there are mechanical problems associated with the correspondingly larger physical size at 23 cm.) The 23 cm wavelength antenna is therefore about 305 cm in diameter while the 3 cm wavelength antenna is about 46 cm in diameter. The gain in the sidelobe region is approximately unity. Aperture weighting is used to lower all sidelobes 25 dB or more below the mainlobe. An elevation-over-azimuth type of pedestal is employed; this is mounted in an inverted position as sketched in Figure 10. With this type of pedestal, θ_s is constant and ϕ_s is variable during a data run. The geometry with the smallest incidence angle requires the fastest antenna slew rate; here, the antenna must scan all data points within $7\frac{1}{2}$ seconds, requiring a rotation speed of about $25^\circ/\text{sec}$. The antenna must also reach maximum scanning speed quickly once the scan has started. A position readout accuracy of about 1° or better is needed.

2.3.2 TRANSMITTER AND RECEIVER PARAMETERS

Tables 5 and 6 list the transmitter and receiver parameters for the two frequencies. The transmitter uses components presently in ERIM's C-46, the major change being the transmission of a 50 nsec pulse instead of the chirp pulse normally used for synthetic aperture mapping. Because of the narrow pulse width, the average power transmitted is low. During any one pass, the transmitters can be connected for either horizontal or vertical polarization. However, only horizontal polarization was transmitted during this data gathering program.

The receiver needs to be coherent in order to permit the recording of Doppler history and th a coherent local

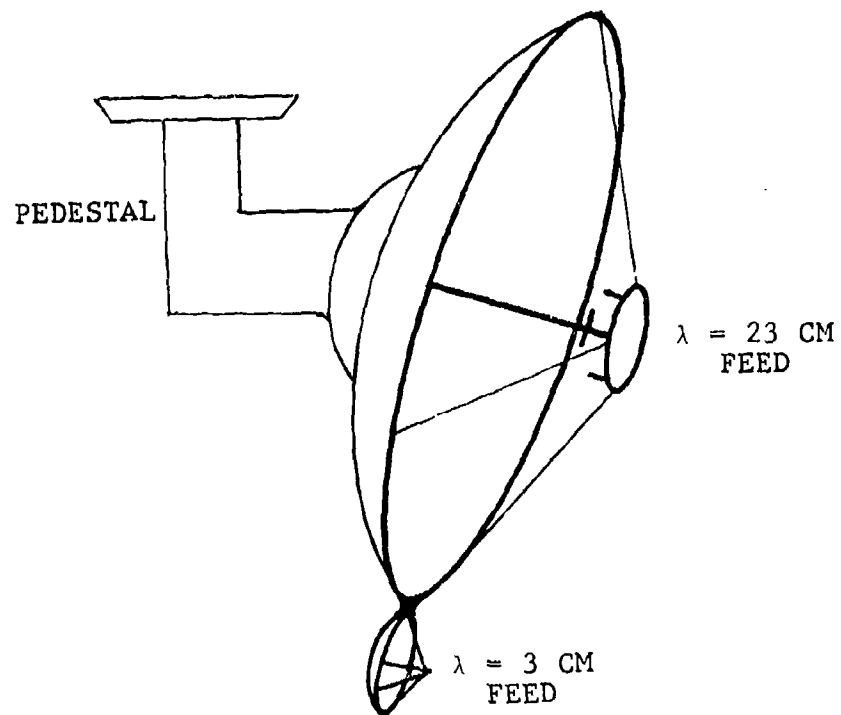


Figure 10. Receiver Antennas and Pedestal

TABLE 5. TRANSMITTER PARAMETERS

	<u>Wavelength</u>	
	<u>22.8 cm</u>	<u>3.17 cm</u>
Center Frequency	1.315 GHz	9.450 GHz
Bandwidth (3 dB)	>100 MHz	>100 MHz
Peak Power Output	5 kW	0.5 kW
Average Power Output	1.8 W	0.14 W
Pulse Width	90 ns	70 ns
PRF	4000	4000
Losses	0.5 dB	1.9 dB

TABLE 6. RECEIVER PARAMETERS

	<u>Wavelength</u>	
	<u>22.8 cm</u>	<u>3.17 cm</u>
Mode	Coherent	Coherent
Channels	2 (V&H)	2 (V&H)
Bandwidth (3 dB)	30 MHz	30 MHz
Noise Figure	4 dB	5 dB
Losses	2 dB	2 dB
Range Gate Width	1.6 μ sec	1.6 μ sec
Minimum Detectable Signal	-78 dBm	-75 dBm

oscillator link is required; however, no Doppler processing is anticipated during the present program. There are two channels in each receiver, one for horizontal and one for vertical polarization. Since it is not feasible to record pulses as narrow as 50 nanoseconds, there is a sample-and-hold circuit in each channel to simplify recording; the width of the sampling time is 10 nanoseconds. The outputs of the four channels are recorded on magnetic tape together with other information necessary to associate the data recorded with the pass number and time during the pass.

2.3.3 POWER CALCULATIONS

The signal-to-noise (S/N) ratio at the input to the receiver must be high enough for adequate measurement accuracy. The starting point for this calculation is the bistatic radar equation [2]

$$\frac{S}{N} = \frac{P_i G_T G_R L \lambda^2 \sigma}{(4\pi)^3 k T_N B R_i^2 R_s^2} \quad (5)$$

For a distributed target, the cross section equals the area the receiving beam illuminates times σ_0 ; thus,

$$\sigma = \sigma_0 (R_s^2 \beta_r^2 \sec \theta_s) \quad (6)$$

This equation assumes that the range gate is wider than the width of the ground patch which the receiving antenna illuminates. The S/N equation now becomes

-
2. F.E. Nathanson, Radar Design Principles, McGraw-Hill Book Co., New York, 1969, Ch. 2.

$$\frac{S}{\tilde{N}} = \frac{P_i G_T G_R L \lambda^2 \sigma_o \beta_r^2 \sec \theta_s}{(4\pi)^3 kT_N B R_i^2} \quad (7)$$

which is independent of the distance R_s .

With the coherent addition of \tilde{N} pulses, the S/N ratio will increase by a factor of \tilde{N} . Now \tilde{N} is equal to the product of the time the transmitting antenna illuminates the receiver and the PRF divided by the number n of patches for which data are collected:

$$\tilde{N} = \frac{\beta_t R_i (\text{PRF})}{nV} \quad (8)$$

After coherent integration, the S/N equation becomes

$$\frac{S}{\tilde{N}} = \frac{P_{av} G_T G_R L \lambda^2 \sigma_o \beta_t \beta_r \sec \theta_s}{(4\pi)^3 kTR_i nV} \quad (9)$$

assuming the pulse width is the reciprocal of the bandwidth B . Note that the S/N ratio varies only with the inverse transmitter distance R_i .

Actual S/N ratios have been computed based on the experimental data gathered under this program. Computer printouts of these results are presented in Appendix C.

Another pertinent quantity is the ratio of the direct power to the scattered power (P_d/P_s). The direct power enters through the sidelobes of the receiving antenna and the scattered power through the mainlobe. Using the bi-static radar equation and the free space transmission formulas between two antennas, the following equation can be derived:

$$\frac{P_d}{P_s} = \frac{4\pi G_{Rs} \ell}{\sigma_o \beta_r^2 \sec \theta_s G_R} \quad (10)$$

2.4 INDEPENDENT SAMPLES FOR BISTATIC DATA

One of the problems which must be considered in this program is that of obtaining a sufficient number of data samples. Since the statistics of σ_o can be considered as random variables, adequate sampling is required for an accurate average value of σ_o . Independent samples can be obtained by means of the following mechanisms:

1. receiving antenna selectivity,
2. Doppler shift because of transmitter motion, and
3. motion of wind-blown clutter.

There are two possible modes of operation when the aircraft passes the receiver. The transmitting antennas can be aimed normal to the ground track of the aircraft, or they can spotlight the receiver area. The spotlight mode of operation has the advantage of increasing the data collection time and hence the number of samples obtained. Therefore, this mode of operation is used in the present program.

2.4.1 RECEIVING ANTENNA SELECTIVITY

Independent samples are measured when the receiving antenna is pointed at different spots on the ground. The receiving antenna has a 5° beamwidth at the half power points. Assuming that the antenna will scan over an angular interval of 140° , there are about $140/5 = 28$ independent samples taken during each pass if the transmitter beam is aimed normal to the ground track.

With spotlight operation, the time on target is much greater, and it is possible for the receiving antenna to scan several times during each pass. Because the receiving antenna beamwidth is 5° , the samples on successive scans will be independent if the transmitter moves 5° between scans. Assuming that it will be possible to make 8 or 9 independent scans during each spotlight pass, the number of independent samples will increase by a factor of 8 or 9 to a total of 224 or 252.

Increasing the number of independent samples improves the σ_0 average considerably. As a result of making several scans per pass, there are more data to be processed, and the processing is more complicated. For example, it should be noted that θ_i will change during a spotlight pass as shown in Tables 7, 8, and 9.

2.4.2 DOPPLER SHIFT

Because the transmitter is moving, there will be a Doppler gradient across the patch which the receiving antenna illuminates. From Skolnik [3], the correlation function between sample measurements of the return from the patch will be down to 0.2 for a sampling time interval T_i where

$$T_i = \frac{0.65}{\Delta f_d} \quad (11)$$

The Doppler shift Δf_d across the footprint is

$$\Delta f_d = \frac{V}{\lambda} (\sin \phi_{i1} - \sin \phi_{i2}) \quad (12)$$

-
3. M.I. Skolnik ed., Radar Handbook, McGraw-Hill Book Co., New York, 1970, Chap. 25, p. 15.

TABLE 7. BISTATIC MEASUREMENTS FLIGHT PARAMETERS FOR 2 JULY 1976

Pass	x ₁ (ft)	y ₁ (ft)	x ₂ (ft)	y ₂ (ft)	TRACK*			θ_s	θ_i		
					Start	Mid	End		Start	Mid	End
1	0	45	15100	8000	-	-	-	85°	--	62.1°	69.4°
2	0	45	14300	8000	-	85°	140°	85°	--	60.1°	68°
3	0	45	16600	13300	-	-	-	85°	--	51.8°	60.4°
4	0	45	13100	13300	-	87°	140°	85°	48.6°	44.5°	54.3°
5	0	45	13600	13300	-	85°	145°	85°	49.2°	45.6°	55.3°
6	0	45	13600	13300	66°	90°	145°	85°	49.2°	45.6°	55.3°
7	0	45	14700	8000	-	-	-	85°	57.8°	61.4°	68.9°
8	0	45	13300	8000	66°	86°	146°	85°	56.1°	59°	67°
9	-	-	12100	8000	-	-	-	mapping	--	56.5°	-
10	0	45	13000	8000	-	85°	110°	85°	55.2°	58.4°	66.5°

*Correction of 5° added due to boresight error of tracker antenna reference angle

TABLE 8. BISTATIC MEASUREMENTS FLIGHT PARAMETERS FOR 9 JULY 1976

Pass	x_1 (ft)	y_1 (ft)	x_2 (ft)	y_2 (ft)	TRACK			θ_s (deg)	θ_1		
					Start (deg)	Mid (deg)	End (deg)		Start (deg)	Mid (deg)	End (deg)
1	0	45	15,300	3,200	---	---	---	85.0	---	78.0	---
2	0	45	14,700	3,200	40.0	85.0	110.0	85.0	81.0	77.7	80.0
3	0	45	14,900	4,200	72.0	98.0	---	85.0	---	74.3	---
4	0	45	15,400	4,200	50.0	92.0	---	85.0	---	74.7	---
5	0	45	15,500	3,200	80.0	94.0	94.0	85.0	79.5	78.3	81.4
6	0	45	14,850	3,400	45.0	---	125.0	85.0	79.0	77.1	80.5
7	0	45	16,400	2,200	45.0	75.0	130.0	85.0	84.1	92.4	84.0

TABLE 9. BISTATIC MEASUREMENTS FLIGHT PARAMETERS FOR 17 JULY 1976

Pass	x_1 (ft)	y_1 (ft)	x_2 (ft)	y_2 (ft)	TRACK			θ_s (deg)	ϕ_1			7-Channel Digital Tape Record	Number of Records
					Start (deg)	Mid (deg)	End (deg)		Start (deg)	Mid (deg)	End (deg)		
2	0	100	21,120	4,000	43	82	116	80	82.7	79.3	80.0	---	---
3	0	100	21,120	4,000	40	76	115	80	82.7	78.8	80.0	---	---
4	0	100	20,060	6,000	38	82	112	80	77.0	73.0	74.5	File 2, Tape 2	461
5	0	100	18,480	8,000	40	79	130	80	75.0	67.0	74.0	File 3, Tape 1	562
6	0	100	18,480	8,000	32	75	129	80	75.0	67.0	74.0	File 4, Tape 1	618
7	0	100	18,740	6,000	38	77	125	80	78.6	72.2	75.5	File 1, Tape 2	712
9	0	100	18,480	4,000	38	78	125	80	82.5	78.0	80.0	---	---
10	0	100	18,740	4,000	38	82	130	70	82.0	78.0	80.6	---	---
11	0	100	18,480	6,000	38	82	124	70	79.0	72.4	75.5	---	---
12	0	100	18,480	8,000	36	82	135	70	75.0	67.0	74.0	---	---

It can be shown that

$$\sin \phi_{i1} - \sin \phi_{i2} \approx \frac{\beta_r R_s}{R_i} \quad (13)$$

Thus,

$$\Delta f_d = \frac{v \beta_r R_s}{\lambda R_i} \quad (14)$$

and

$$T_i = \frac{0.65 \lambda R_i}{\beta_r R_s v} \quad (15)$$

The number of uncorrelated samples n per beam position equals the ratio of the time on a patch, T_p , to T_i . For a fixed transmitting antenna (assuming 28 beam positions per scan), it can be shown that

$$n = \frac{T_p}{T_i} \approx \frac{\beta_t R_i}{28 v T_i} \approx \frac{\beta_t \beta_r R_s}{18 \lambda}.$$

For the 90° spotlight case, the total T_p at one of the 28 beam positions is

$$T_p = \frac{2 R_i}{28 v} \quad (16)$$

and

$$n = \frac{\beta_r R_s}{9 \lambda}, \quad (17)$$

assuming only one receiver scan per pass. The number of independent samples from the footprint is obviously much greater with the spotlight mode of operation.

Table 10 lists some values from these formulas. For

TABLE 10. INDEPENDENT SAMPLES PFR RECEIVER BEAM
POSITION CAUSED BY DOPPLER SPREAD

Wavelength (λ) (cm)	Scattering Angle (θ_s) (deg)	Number of Independent Samples	
		Fixed Transmitter Beam $n = \frac{\beta_t \beta_r R_s}{18\lambda}$	Spotlight $n = \frac{\beta_r R_s}{9\lambda}$
22.7	0	0.10	1.28
	60	0.20	2.56
3.17	0	0.96	9.14
	60	1.92	18.29

These values are for one receiver scan per pass.

a fixed beam transmitter antenna, there is less than one independent sample per receiver beam position at 23 cm; hence, the Doppler shift does not increase the number of independent samples over that obtained from the receiving antenna selectivity. For the spotlight case, a couple of independent samples occur per beam position for values of $\theta_s \geq 45^\circ$. At 3 cm, the values of n are higher by a factor of about 7. Except for the spotlight case at 3 cm, the Doppler spread does not add many independent samples beyond the single sample resulting from the receiving antenna selectivity.

What the Doppler shift does is give more independent samples from each terrain patch being measured. With more samples, the median value of the return from the patch is determined more accurately, but the number of independent patches measured does not itself increase.

2.4.3 WIND FLUCTUATIONS

The wind changes the orientation and position of vegetation, causing land echo to fluctuate. The width of the clutter spectrum depends to a small degree on wind speed and on the terrain.

There are no wind-fluctuation data which apply specifically to the type of terrain which has been measured in the bistatic experiment. Some clutter spectra have been measured at 3 cm for trees in a 12-knot wind; here, the clutter power was down 3 dB at 7 Hz [4]. For a Gaussian clutter spectrum, the time between independent samples is approximately

-
4. M.W. Long, Radar Reflectivity of Land and Sea, Lexington Books, D.C. Heath and Co., Lexington, Mass., 1975, Fig. 5-9.

$$T = \frac{1}{4f_{1/2}} \quad (18)$$

At 3 cm, therefore, a decorrelation time of approximately 36 milliseconds might be expected. If the total scan time is 7 or 15 seconds, the number of independent samples at each beam position will be about 194 and 388, respectively.

The clutter spectral width is roughly proportional to center frequency, according to Ref. 5. Based on this, the decorrelation time at 23 cm is approximately 7 times as long and there are only about 1 or 2 independent samples at this wavelength.

Decorrelation because of wind motion gives a better average value for the return from one ensemble point. If the terrain were a uniform area such as a wheat field, the decorrelated samples from one patch might give the same statistics as would samples taken from different ensemble points. In general, however, ensemble sampling yields different results.

2.5 SUMMARY OF ADVANTAGES OF SPOTLIGHT SCANNING TECHNIQUE

The area near the receiver is spotlighted to increase the time on target, and the receiving antenna is scanned back and forth several times during a pass. A given terrain patch is sampled at different ϕ_s values during each scan; hence, samples are obtained from many different ensemble points during a single pass. Data from an ensemble of patches is preferable to several independent samples from a single patch, unless the terrain is very uniform.

5. M.W. Long, Radar Reflectivity of Land and Sea, Lexington Books, D.C. Heath and Co., Lexington, Mass., 1975, Chap. 5.

Since the receiving antenna is scanned several times during each fly-by, Doppler spread and wind motion do not increase the number of independent samples from a single ensemble point. If the receiving antenna were to scan only once during a fly-by, these factors would significantly increase the number of independent samples at 3 cm but not at 23 cm. More independent samples at one ensemble point give a more accurate mean value of the cross section density for that point.

3
INSTRUMENTATION

All of the instrumentation described in this section was designed, constructed, and tested as a part of the dual-frequency, bistatic-scattering-coefficient measurements program. This instrumentation consists of:

- (a) two-channel receivers for 3 cm,
- (b) two-channel receiver for 23 cm,
- (c) aircraft-to-ground data link for local oscillator to permit coherent operation,
- (d) automatic monopulse tracking system,
- (e) control circuitry,
- (f) recording interface for analog and chart recorders,
- (g) automatic calibration system,
- (h) two-wavelength, dual-polarization antenna system, including automatic sector scan,
- (i) analog-to-digital data conversion system,
- (j) digital data averaging program, and
- (k) digital data analysis program to accept experimental parameters and calculate σ_0 values.

In this section that part of the instrumentation used to obtain and record the basic bistatic signal data is described; this description includes items (a) through (h) of the above list. Data analysis (items i, j, and k) is discussed in Section 5.

A functional block diagram of the complete instrumentation used (1) for obtaining measurements of the bistatic terrain clutter data and (2) for analyzing the data to determine values of σ_0 is shown in Figure 7. A summary of the instrumentation parameters is provided in Tables

4, 5, and 6. Detailed drawings of the instrumentation are given in Appendix B.

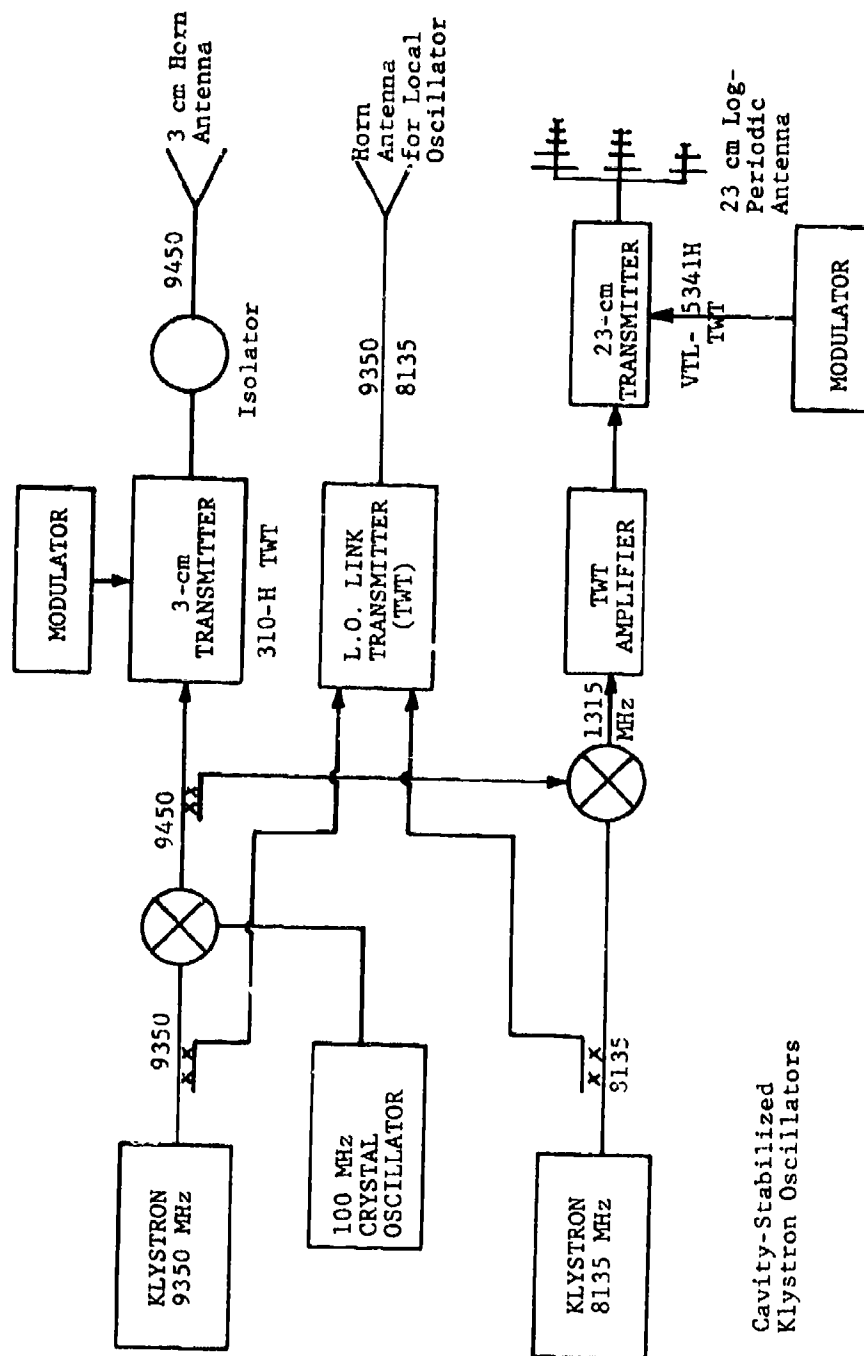
3.1 TRANSMITTER SYSTEM

The bistatic transmitter consists of the transmitter portion of the ERIM X-L synthetic aperture radar (SAR) system. This system is installed in ERIM's C-46 aircraft as shown in Figure 5b. A block diagram of the complete transmitter system, including the local-oscillator transmitter for the coherent link, is shown in Figure 11.

The antenna system used with the bistatic instrumentation consists of (1) a seven-element array with log-periodic elements for the 23 cm wavelength band (Figure 5a), (2) a 22 dB standard gain horn (Scientific Atlantic Model 12-8.2) for the 3 cm wavelength band, and (3) an antenna for the air-to-ground local oscillator link. The parameters for the bistatic antennas are listed in Table 4. The complete antenna system is mounted on a pedestal to permit 360° rotation of the antennas. A synchro angular read-out is provided to accurately point the antennas with respect to the airframe.

Two cavity stabilized klystron oscillators are used to provide drive power for the bistatic traveling-wave-tube power amplifiers. The bistatic transmitter outputs are summarized in Table 5.

For the L.O. data link, a portion of the power from each of the bistatic klystrons is frequency offset by 100 MHz and amplified by a TWT to a level of +37 dBm at the L.O. antenna input. This antenna is a 20-degree horn having a gain of about 17 dB; it transmits to the ground receiving site via a direct-path link in order to provide local oscillator power for the receiver. In addition to the



Cavity-Stabilized
Klystron Oscillators

Figure 11. Transmitting System Block Diagram

frequency shift, filtering is used to provide isolation between the bistatic and the local oscillator signals.

3.2 RECEIVERS

Seven receiver channels and associated antennas are included in the ground receiving instrumentation, as shown in Table 11. Photographs of the receiving installation are shown in Figures 2 and 3; a block diagram of the receiving system is provided in Figure 12. Each of the four bistatic receiver signal channels consists of conventional low-noise front end design followed by linear amplification up to the detector stage. Table 6 lists the minimum detectable signal and the bandwidth for each channel.

The detector circuit in the bistatic receiver is a sample-and-hold device, designed to attain bandwidth reduction and to permit each sample pulse to be recorded on the Ampex 1300 analog tape recorder. A detailed operational description of the complete receiving system is provided in Appendix B; this description includes detailed diagrams and schematics.

The L.O. data link receiving antenna has a gain of 30 dB and the L.O. receivers have minimum detectable signal levels of -85 dBm. During the data-gathering period (when the aircraft transmitter is tracked), the L.O. S/N ratio is greater than 25 dB.

Local-oscillator power is provided from the radiation received from the transmitter aircraft; it is then amplified and mixed to the desired frequency. There were occasions during the experiment when the receiver local-oscillator power was low, due to tracking error and/or to great distance between the ground station and the aircraft; at these times, inadequate power was available for the receiver

TABLE 11. RECEIVER CHANNELS AND ANTENNAS

<u>Receiver Channel</u>	<u>Antenna</u>
23 cm wavelength, like polarization }	3.1 m dish
23 cm wavelength, cross polarization }	dual feed
3 cm wavelength, like polarization }	46 cm dish
3 cm wavelength, cross polarization }	dual feed
Local oscillator (high) }	46 cm dish
Local oscillator (low) }	
Tracker signal	dual horns

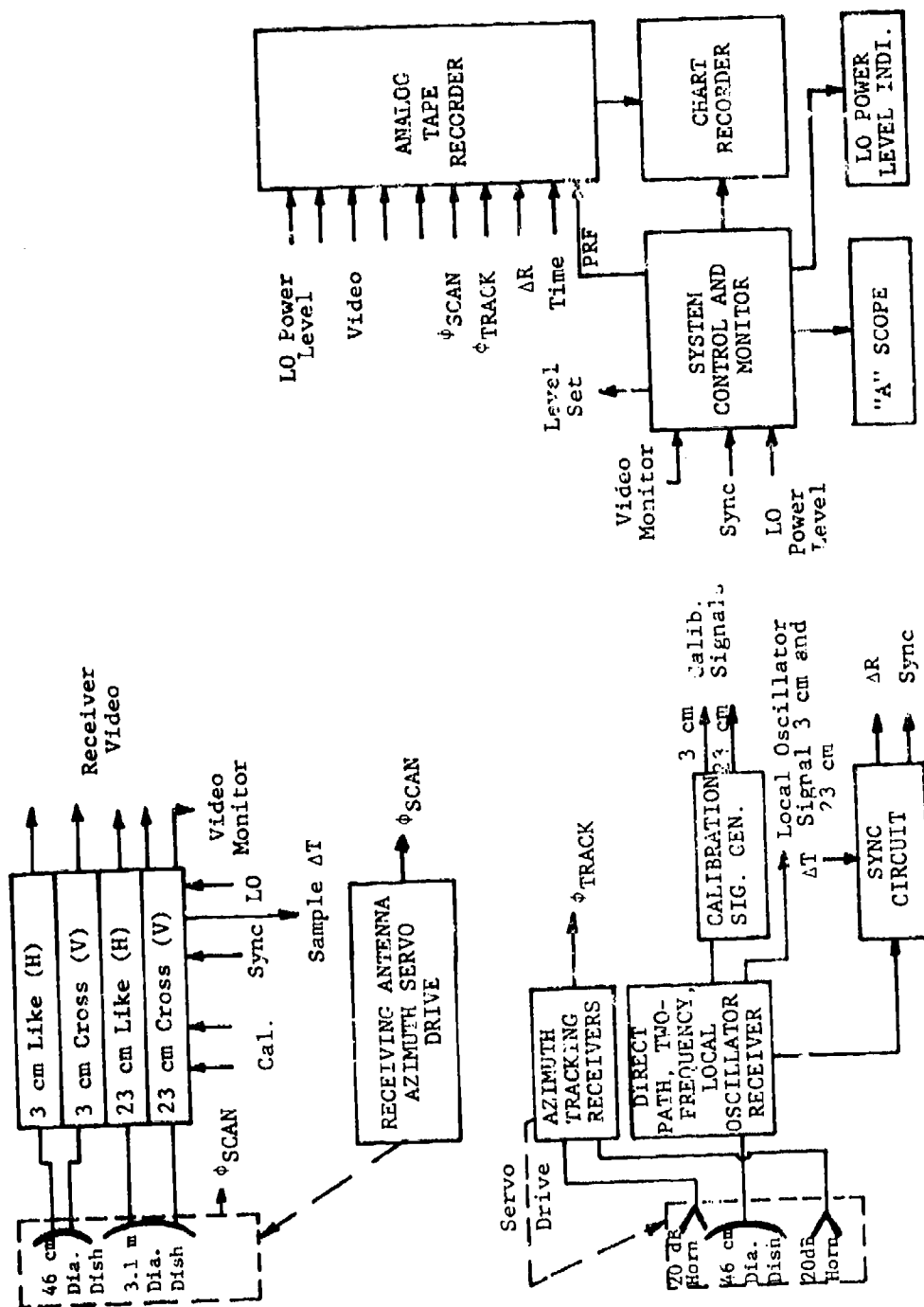


Figure 12. Block Diagram of Bistatic Receiving Systems

mixers. This condition was indicated by a power-level meter on the operating panel and by a trace on the chart recorder record. Receiver gain variations as a function of local-oscillator power are given in Appendix B.

3.3 BISTATIC RECEIVING ANTENNAS

Two antennas, one each for 9.45 GHz and 1.315 GHz have been designed, fabricated, and tested for use with the dual-frequency bistatic receiving system. The design goals for the antennas were as follows:

1. 3 dB beamwidth = 5° ,
2. first sidelobe level ≤ -25 dB,
3. polarization: vertical and horizontal with respect to the local ground,
4. polarization isolation = 25 dB, and
5. minimum cost.

To meet the above goals, a conventional parabolic reflector with its feed mounted in a plane parallel to the aperture plane at the focal point of the parabola was chosen for each of the antennas. Such a feed obviously blocks part of the antenna aperture.

In the design of the receiving antennas, it was necessary to consider illumination taper and aperture blocking. Properly tapering the illumination from the center to the edge of the dish decreases the height of the first sidelobe [6]. However, as the taper is increased, the aperture blockage increases, and this latter factor degrades sidelobe performance [7]. As a result, a compromise

6. Microwave Journal Technical and Buyer's Guide, February 1, 1968, p. 132.

7. Op. cit., p. 133.

was made between these two factors in evolving the final antenna designs; these designs are discussed in Appendix B.

A close-up of the three-meter-diameter and the 46-cm-diameter parabolic dishes is shown in Figure 13. The tracker's dual-horn antenna system is pictured along with the 46 cm dish used in the local oscillator link in Figure 4. Also included in the receiving instrumentation are two pedestals; one is for the two dishes used with the bistatic data channels and the other is for the tracker and local oscillator antennas. Angular synchro read-outs are provided for both antenna pedestals. An automatic angular sector scan is provided for the data channel antenna system and an automatic tracking antenna system is used with the local oscillator link.

3.4 TRACKER

An automatic monopulse tracker (Fig. 4) system provides a continuous monitoring of the track angle as measured from the receiver site to the airborne transmitter. The monopulse tracker receives the high-frequency local-oscillator signal transmitted from the aircraft and uses this signal to track the aircraft during the entire data-gathering run; the S/N ratio of the tracking receiver exceeds 15 dB during the run. The tracker utilizes basic dual-antenna, dual-channel techniques to generate an error signal from a comparison of the two signals. This error signal is used to drive the antenna pedestal to complete the feedback loop. The receiving antenna for the local-oscillator channel is also mounted on the tracking pedestal to ensure a maximum and constant local oscillator power level for the bistatic receiver channels.

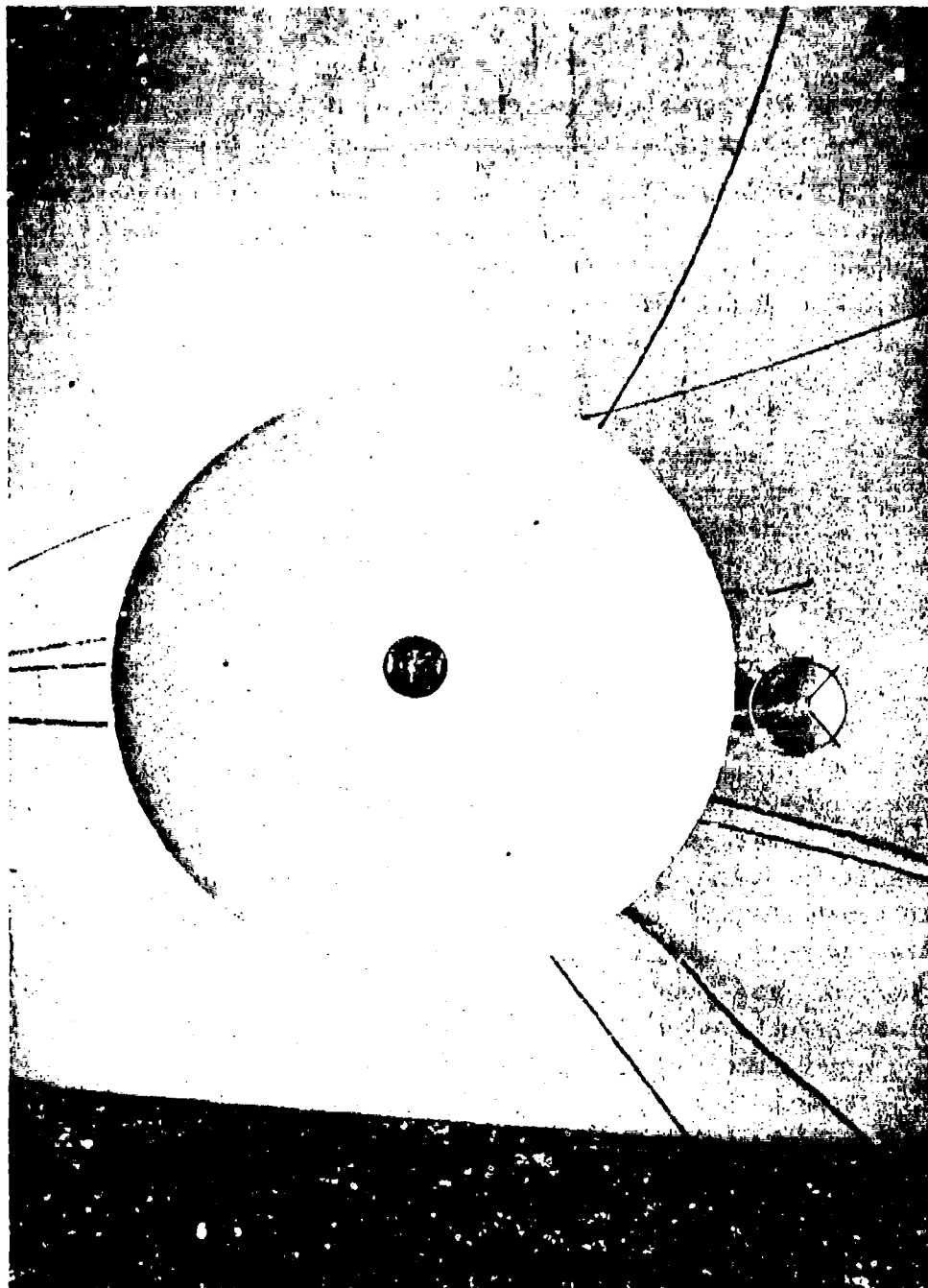


Figure 13. Bistatic Receiving Antennas

3.5 BISTATIC SCAN AND TRACKER ANGLE CALIBRATION

The bistatic antenna scan and tracker angles are calibrated with reference to a precision angle indicator (PAI). A DC voltage corresponding to the PAI readout is recorded on the tape and analog recorders. The recorders are run for several seconds at incremental angle readouts of 10° whenever possible from 0° to 180° . In addition to the absolute calibration of the angles, the same staircase voltages used for the RF calibration are recorded. These step voltages serve as an indication of any voltage drift problems which may occur during operation. The step angle calibrations are recorded at the same time that the RF calibration is carried out.

4 DATA GATHERING

Operation of the bistatic measurements system was divided into four phases for each data gathering problem:

- (1) preparation and calibration,
- (2) data gathering,
- (3) data evaluation, and
- (4) preparation of data for analysis.

Each phase involves several procedures to insure that best accuracy is achieved for the final data output product.

4.1 PREPARATION AND CALIBRATION

Site selection is the first consideration in the preparation for data gathering. Two test sites were used; views of the terrain as seen by the receiving antennas are given in Figure 14 for Site 1 and in Figure 15 for Site 2. Site 1 consists of a very flat section of cement taxiway and an adjacent grassy area. Site 2 consists of an area of tall weeds and scrub trees. The basic characteristics and "ground truth" describing the two test sites are given in Section 5.8. The flight paths selected for the aircraft are shown in Figures 16, 17, and 18. These same paths were flown for the measurements at both test sites.

The range of angles SCAN over which the receiving antenna will scan are selected during the preparation phase and set into the automatic scan control. All angular calibrations are referenced to magnetic directions so as to be compatible with aircraft headings. The calibrations for the bistatic receiver channels, angle channels, and ΔR channel are recorded on both magnetic tape and on the chart recorder. Calibrations are recorded before and after



Figure 14. Photograph of Site 1



Figure 15. Photograph of Site 2

BEST AVAILABLE COPY

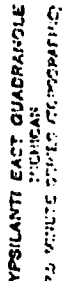


Figure 16. Aircraft Flight Paths for 2 July 1976

This figure is of poor quality. However, it is included because the relevant information is sufficiently clear to the reader.

BEST AVAILABLE COPY

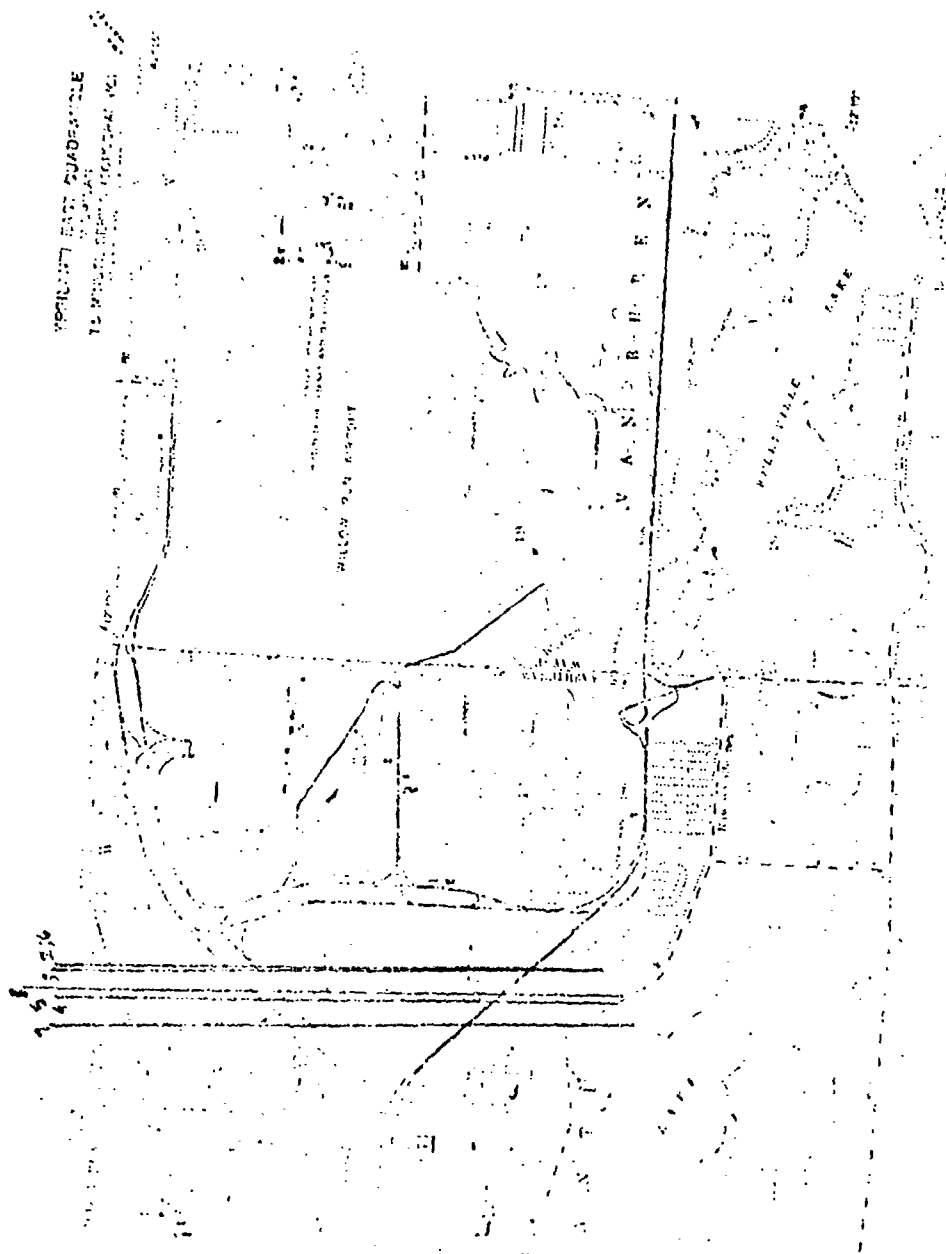


Figure 17. Aircraft Flight Paths for 9 July 1976

This figure is of poor quality. However, it is included because the relevant information is sufficiently clear to the reader.

BEST AVAILABLE COPY

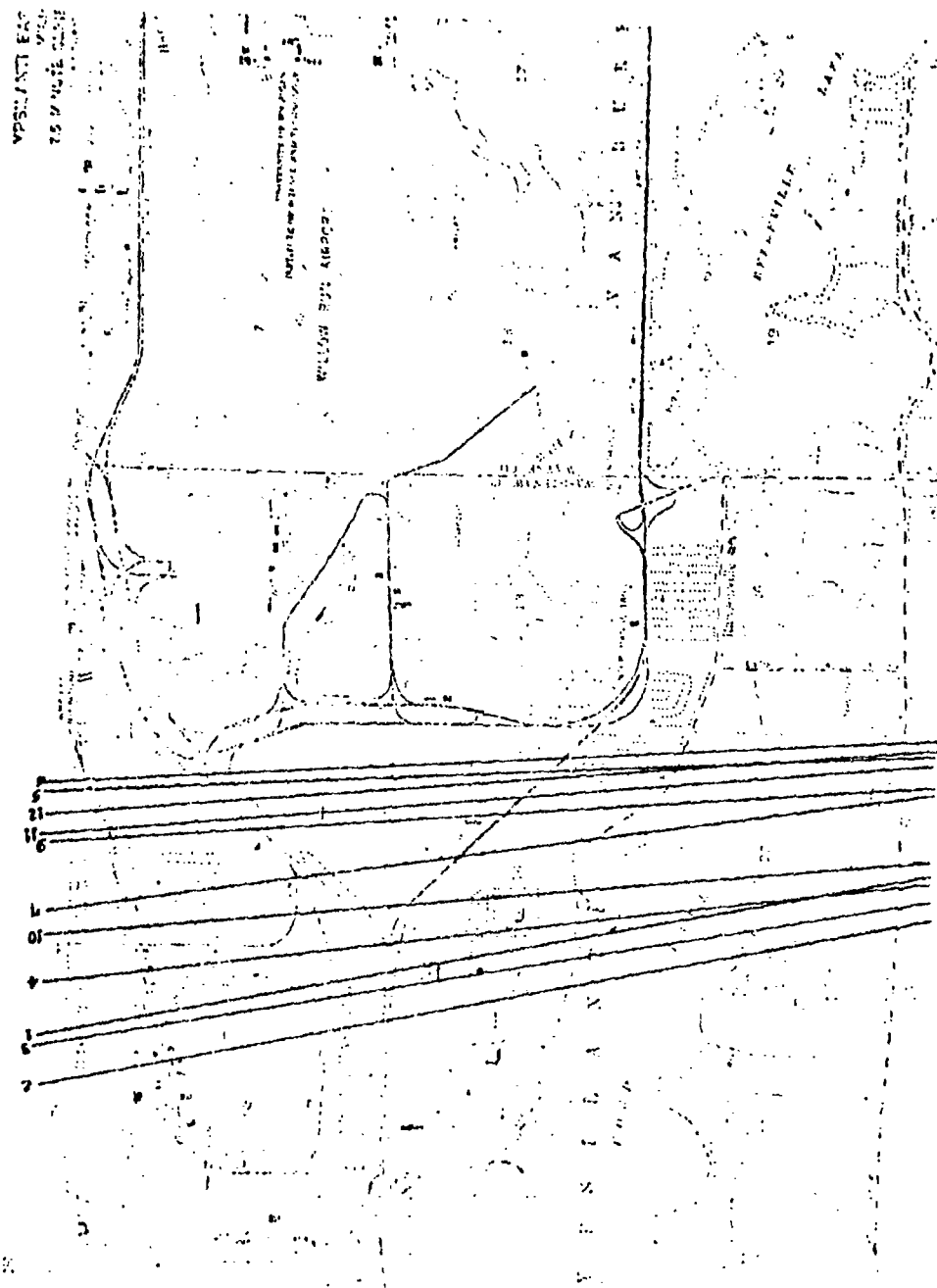


Figure 18. Aircraft Flight Paths for 17 July 1976

This figure is of poor quality. However, it is included because the relevant information is sufficiently clear to the reader.

each flight; an example of the chart recorder calibration read-out is shown on Figure 19. During the preparation phase, an instrumentation checklist is employed; this list is shown in Appendix B.

4.2 DATA GATHERING PHASE

The procedures followed during the gathering of bistatic data are illustrated in Figure 1. Each data gathering flight consists of a number of passes flown as illustrated in Figures 16, 17, and 18. Variations in the incident angle θ_i are obtained by varying the flight altitude and/or the offset distance from the receiver.

Summaries of the measurement parameters for the three data gathering flights are given in Tables 7, 8, and 9; a total of 9 hours of flying time was involved in these flights. A summary of the bistatic angles for which data were obtained is given in Table 1. All data are averaged over 5° intervals of the bistatic scattering angles, as discussed in Section 5. Figure 2 is a photograph of the complete bistatic receiver instrumentation in operation during the data gathering flight of 17 July 1976.

A sample of the chart record made in real time during each data gathering pass is given in Figure 20. This example shows about 50 seconds of data. Note the scan record of the receiving antenna; about 6 complete scans are shown. The receiver-to-aircraft tracker angle is also recorded. The ΔR channel is integrated for the chart recorder, but is fed on a pulse-by-pulse basis to the analog tape recorder. The lower four chart-recorder channels are received power signals; these signals are passed through a logarithmic amplifier prior to being fed to the chart recorder, but are recorded linearly on the analog tape.

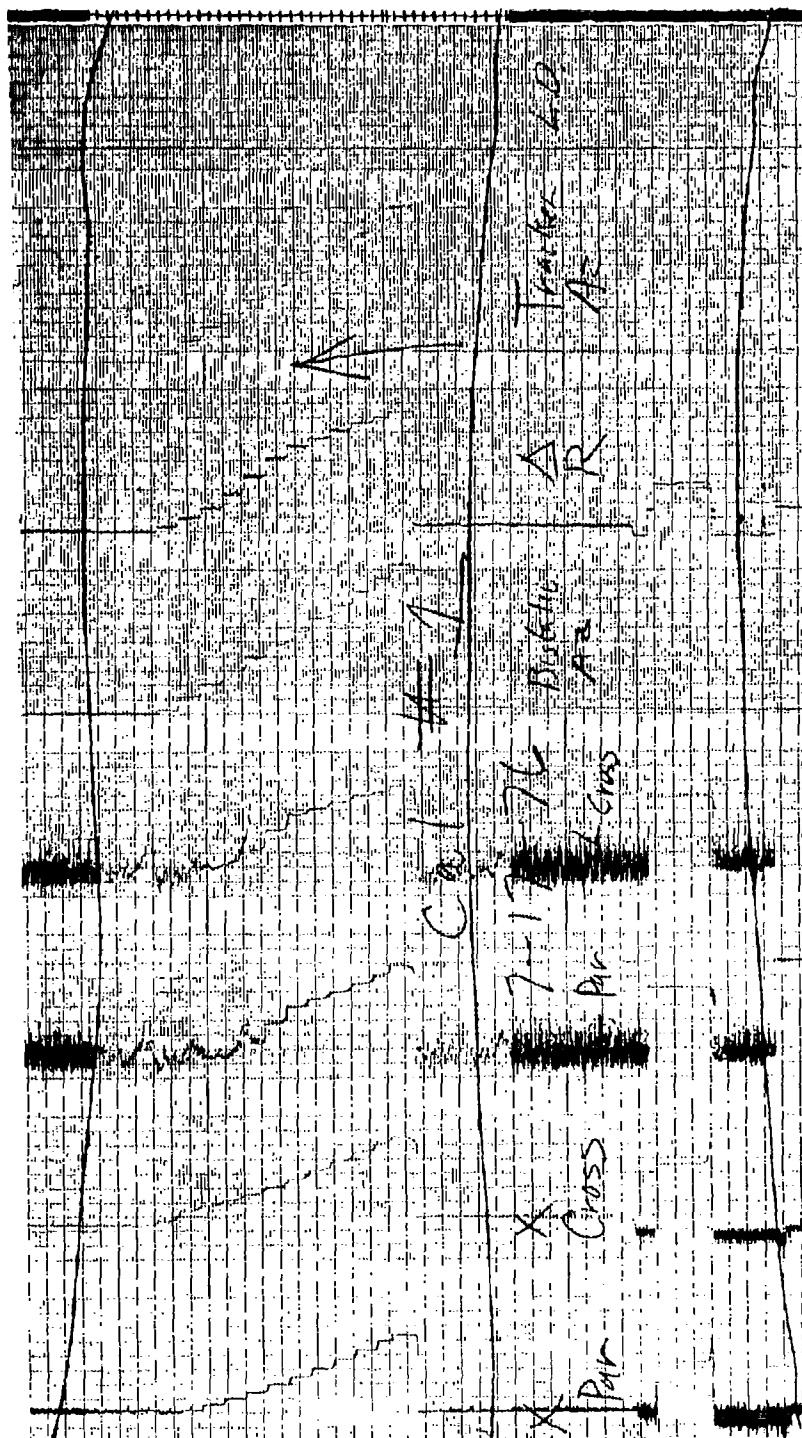


Figure 19. Example Chart Record: Calibration

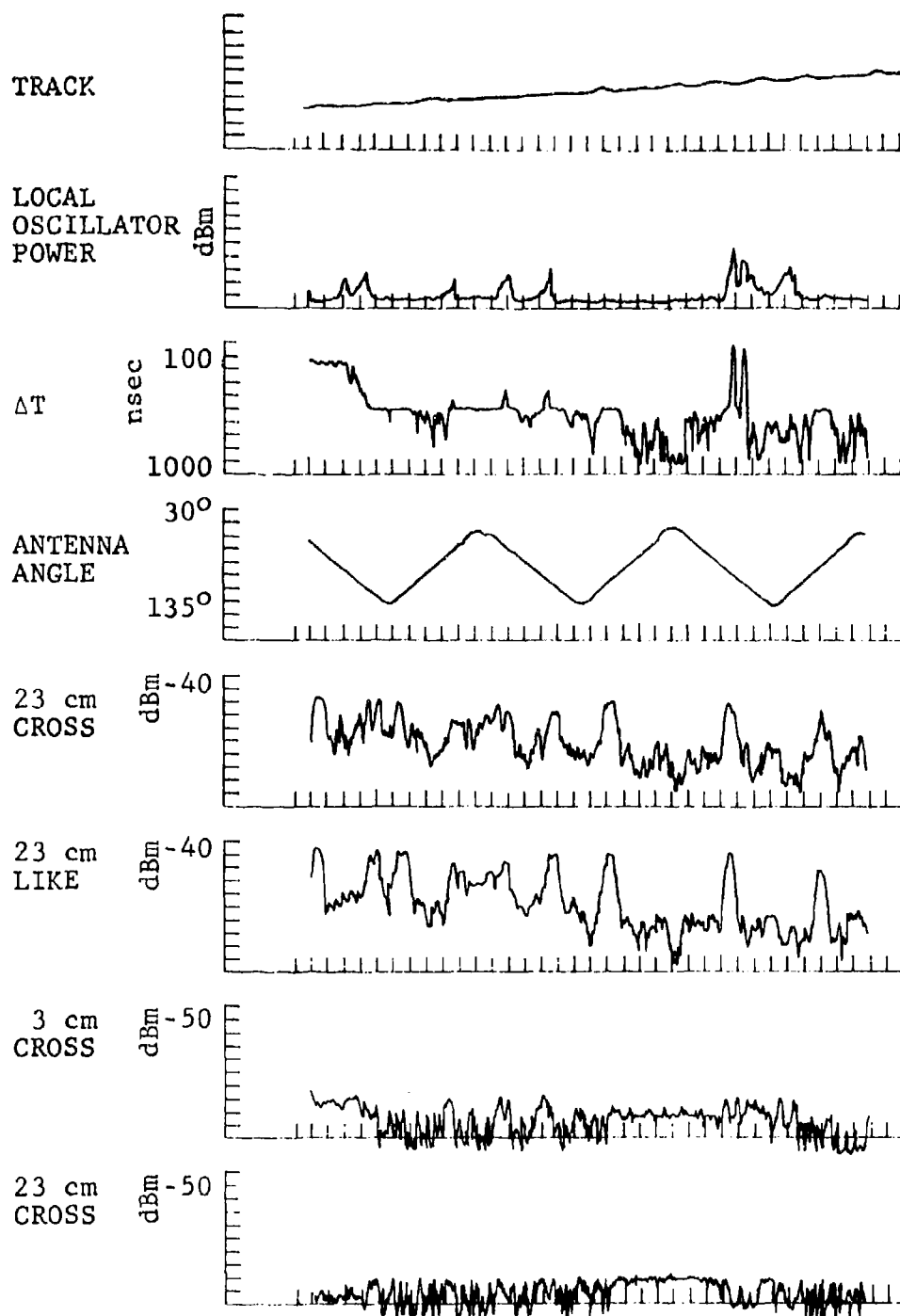


Figure 20. Sample Data Chart Record

Over 40 dB of instantaneous dynamic range are realized in the analog tape channels.

Complete logs are kept during each measurement pass of each flight; examples of these logs are included in Appendix C.

4.3 DATA EVALUATION

Since the data are to be digitized before processing, a two-step data evaluation procedure is used. The first step uses the chart record obtained during the data gathering; the received signal-level, local-oscillator-power, tracking, antenna-scan, and aircraft-operating parameters are evaluated for proper operation on each pass. The data evaluations for the three data flights are summarized in Tables 12, 13, and 14. Certain passes in each table are marked to indicate that they provide acceptable data for computing σ_0 values.

The second step of the evaluation is carried out during digitization. Since the PRF is required for synchronizing the digitization of the data, this signal is included in the local oscillator air-to-ground data link. Thus, a low signal-to-noise ratio in the PRF/L.O. channel will result in unusable data by producing (1) a weak PRF signal which makes the above-mentioned synchronization difficult and (2) low local oscillator power which reduces the overall system sensitivity.

As indicated in Tables 12, 13, and 14, the data are usable for 4 of 9 passes from the first flight (2 July) and 5 of 7 passes from the second flight (9 July). Both the first and second flights covered Test Site 1, giving usable data from a total of 9 passes for this site. A total of 10 of the 12 passes made on the third data-gathering flight covering Site 2 have provided usable data.

TABLE 12. DATA EVALUATION, 2 JULY 1976

Pass	S/N	L.O. Power	ΔR	Signal Level		Antenna		Transmitter Antenna Weighting, $\lambda = 3$ cm			Evaluation
				$\lambda = 23$ cm	$\lambda = 3$ cm	SCAN	TRACK	Start	Mid	End	
1	Low	Low	--	Low	---	Fixed	---	---	---	---	Test
2	Low	Good	--	Good last half	Low	Fixed	Manual from Broadside to 45°	0	0	0	Test Tracker operating, good 23 and 3 cm, 22 sec -- 90 sec
3	---	Low	--	---	---	Fixed	Marginal	0	0	0	Some data good, center of pass
4*	---	15 dB Low	--	Good last half	Good	Fixed	Auto 90°-140°	0	0	0	Good data complete pass
5*	---	10 dB Low	--	Good last half	Good	Fixed	Auto 90°-140°	0	0	0	~30 sec from start, good 23 and 3 cm, to 120 sec
6*	---	10 dB Low	--	Good 45° past broadside	Good	Fixed	Auto 90°-140°, possible tracking or sidelobe	0	0	0	Good sections of data only
7	---	Low	--	Low	Low	Fixed	Manual	0	0	0	Poor, perhaps some good sections
8*	---	Good	--	TRACK = 68° - 100° Good last half	Good	Fixed	Auto 90°-140°	0	0	0	Good, ~20 sec to 80 sec
9	---	---	--	---	---	---	Radar imaging	0	0	0	Mapping
10*	---	-11 dB	--	TRACK = 65° - 115° Good last half	Good	Fixed	Auto 80°-120°	0	0	0	Good, ~30 sec to 120 sec

*Usable for computing ϕ_0 .

TABLE 13. DATA EVALUATION, 9 JULY 1976

Pass	S/N	L.O. Power	AR	Signal Level		Antenna		Transmitter Antenna Weighting, $\lambda = 23$ cm			Evaluation
				$\lambda = 3$ cm	$\lambda = 23$ cm	TRACK	SCAN	Start	Mid	End	
1	---	Low	---	Marginal	---	Manual	---	---	---	---	Low signals
2*		Last half	Partially	Last half of pass of moderate strength TRACK = $55^\circ - 110^\circ$	---	Manual	Last half	-4 -1	-3 0	-6 -3	Good last half pass
3	---	Low	---	---	---	No track	---	---	---	---	Nothing
4	---	None	---	---	---	---	---	---	---	---	Nothing
5*	---	Adequate	Good	Good last half of pass	Good last half of pass	No track	Scan	---	---	---	Last half OK
6*	---	Good	Good	Good Low in first half of pass	Good Good	Track	Scan	-5 -2	-6 -3	-3 0	Good all passes
7*	---	Adequate	Good	Good last third of pass	TRACK = $74^\circ - 130^\circ$	Track	Scan	-9 -6	-3 0	-3 0	Acceptable last half

* Usable for computing σ_0 .

TABLE 14. DATA EVALUATION, 17 JULY 1976

Pass	S/N	L.G. Power	ΔR	Signal Level		Antenna		Transmitter Antenna			Evaluation
				$\lambda = 23$ cm	$\lambda = 3$ cm	TRACK	SCAN	Start	Mid	End	
1	---	---	---	---	---	---	---	---	---	---	No good data
2*	---	Start 1/4 OK, low rest of pass	?	Start 1/4 OK, other- wise OK	OK	---	OK?	-16 -13	-7 -4	-3 0	Fixed SCAN -20 sec, poor data after
3*	---	Good	OK	---	---	fixed SCAN first 1/4 of pass	OK	-11 -9	-3 0	-3 0	Fixed SCAN 14 sec, fix- ed SCAN 8 sec, Good 48 sec to end
4*	---	Good, last 1/4 slight- ly low	OK	OK	OK	Fixed SCAN during start of pass		-2 -2	-13 -13	-15 -15	Complete pass good
5*	---	Good	OK	OK	OK	Fixed SCAN during early start		-4 -1	-14 -10	-3 0	Fixed SCAN 60 sec, good -60 sec to end
6*	---	Good	OK	Question peaks during first 1/4 of pass		Scanning SCAN complete pass		-3 0	-7 -4	-5 -2	Fixed SCAN 20 sec, good to end
7*	---	Good	OK?	?		Several power outs		0 0	-13 -13	-10 -10	Good, some low P/R
8	---	---	---	---		---	---	Aborted, A/C in area			A/C in area
9*	---	Good	?	First 1/8 question- able OK	OK	Wind affecting SCAN several power outs		-6 -3	-16 -13	-8 -5	Good with some bad sections

TABLE 14. DATA EVALUATION, 17 JULY 1976 (Continued)

Pass	S/N	L.O. Power	AR	Signal Level		Antenna		Transmitter Antenna Weighting, $\lambda = 23$ cm			Evaluation
				$\lambda = 23$ cm	$\lambda = 3$ cm	TRACK	SCAN	Start	Mid	End	
10*	---	Good	Good	First 1/4?		---	Windy	-6 -3	-3 0	-16 -13	Fixed SCAR start, best data after 60 sec
11*	---	Good	Good	Good last 1/2 pass OK		---	Windy	-2 -2	-2 -2	-2 -2	Best data after 60 sec
12*	---	Good	??	Bad first half		---	---	-6 -3	-16 -13	-3 0	Best data after 70 sec

*Usable for computing σ_o .

4.4 PREPARATION OF DATA FOR ANALYSIS

After evaluation and selection of the data for analysis, each analog tape is converted to a 9-track digital format*; a detailed description of the digital data tape format used is given in Appendix D. The data (on the basic analog tape and on the digitized tape) include measures of received power on a pulse-by-pulse basis for four receiver channels. Since the data analysis is performed on received power values averaged over the 5° beamwidth of the receiver antenna (as discussed in Section 5), the next data preparation step is the summing and averaging operation described by the relation

$$S_n = \frac{1}{N} \sum_{i=1}^N x_i^2 \quad (19)$$

Here, the value of N over which the data are averaged corresponds to the number of samples obtained in a 5° azimuth interval.

*Special digital tapes are also generated on a 7-track format to be compatible with the GRC computation facility.

5 DATA REDUCTION

This section contains definitions of all parameters (Section 5.1) and descriptions of all processes which are used to obtain the terrain scattering cross section per unit area, σ_0 , from a particular set of recorded power and aspect data. Various physical and measurement constraints make it necessary to approximate σ_0 . Section 5.2 gives the steps by which this approximation method evolved. In particular, approximations for the gain patterns of the transmitting and receiving antennas (especially the latter) are considered in Section 5.3.

The geometry of the terrain scattering area A_{gd} presents a rather interesting aspect of the problem since it may be bounded by several (at most four) elliptical arcs. Two of these elliptical boundaries are defined by the pulse length, over which a weighting corresponding to the receiver impulse response must be applied. The final weighted area so obtained is described in Section 5.4 and the results are used to describe the form used in this program for σ_0 . Since this quantity is actually a random variable it is necessary to take some pains to insure an adequate and independent sample set from the terrain region being examined. This aspect of the data reduction provisions of the program is considered in Section 5.5.

A brief discussion of the data processing scheme is given in Section 5.6. A more detailed discussion of the processing, including all computer programs prepared, can be found in Appendix D. In Section 5.7, the reduced data (σ_0 versus the azimuth angle ϕ_s) are presented for 23 cm and 3 cm wavelengths at several transmitter and receiver elevations and for various terrain conditions. Finally,

Section 5.8 presents a discussion of the data; calibration curves are included.

5.1 DEFINITION OF σ_0 AND ASSOCIATED PARAMETERS

The terrain scattering cross section per unit area, σ_0 , is defined [8,9] as

$$\sigma_0 = \frac{4\pi r_s^2 dS_s}{S_i dA} \quad (20)$$

The incident power density S_i is expressible in terms of transmitted power P_i , transmitting antenna maximum gain G_{OT} , and normalized power pattern function f_T as

$$S_i = \frac{1}{4\pi r_i^2} P_i G_{OT} f_T \quad (21)$$

(Since G_{OT} is constant, and f_T is a normalized function of aspect, the product $G_{OT} f_T$ represents the antenna gain as a function of aspect.) The scattered power density dS_s may be written in terms of the incremental power dP_r received by an antenna of aperture A_R , which in turn is expressible in terms of receiving antenna gain G_{OR} and power pattern function f_R . The result is

$$dS_s = \frac{dP_r}{A_R} = dP_r / \frac{\lambda^2 G_{OR} f_R L}{4\pi} \quad (22)$$

8. D.E. Barrick, Normalization of Bistatic Radar Return, Report No. 1388-13, Ohio State University Research Foundation, Columbus, January 1964.
9. W.H. Peake and T.L. Oliver, The Response of Terrestrial Surfaces at Microwave Frequencies, Report No. AFAL-TR-70-301, Electrosience Laboratory, Ohio State University, Columbus, May 1971.

Equations (20) (21), and (22) may be assembled to yield the increment of received power dP_r as

$$dP_r = \frac{P_i \lambda^2 G_{OT} G_{OR} L}{(4\pi)^3} \cdot \frac{f_T f_R \sigma_o}{r_i^2 r_s^2} dA \quad (23)$$

The total power received from the entire illuminated surface A_{gd} is then

$$P_r = P_i K \int_{A_{gd}} \frac{f_T f_R \sigma_o}{r_i^2 r_s^2} dA \quad (\text{mW}), \quad (24)$$

where constant terms have been collected as

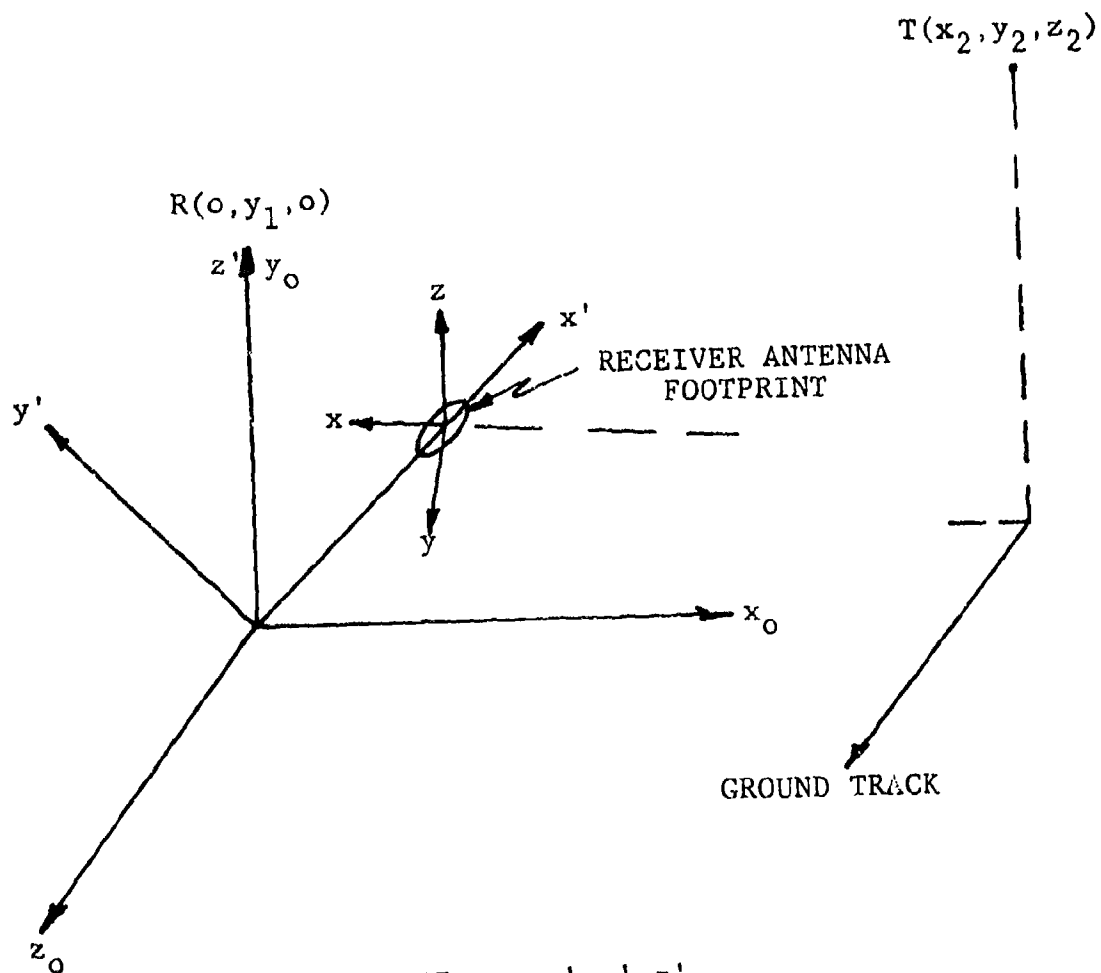
$$K = \frac{\lambda^2 G_{OT} G_{OR} L}{(4\pi)^3} \quad (\text{m}^2). \quad (25)$$

The integral

$$I = \int_{A_{gd}} \frac{f_T f_R \sigma_o}{r_i^2 r_s^2} dA \quad (\text{m}^{-2}) \quad (26)$$

is discussed in detail in Sections 5.2 and 5.4 below.

The coordinate system and aspect parameters of the scattering area A_{gd} are shown in Figures 1 and 21. The origin for the range-curve (x_o, y_o, z_o) and footprint (x', y', z') coordinate systems is placed at the foot (nadir) of the receiver R. The y_o -axis is vertical, through the receiver, and the z_o -axis is taken in the direction of, and parallel to, the ground track of the transmitter. Then the x_o -axis is chosen to form a right-hand system.



FOOTPRINT: x', y', z'

RANGE CURVE: x_0, y_0, z_0
(system in which R and T are defined)

INTEGRATION: $x, y, z; \rho, \phi, z$

Figure 21. Coordinate Systems

In the (x_0, y_0, z_0) system, the receiver is fixed at $(0, y_1, 0)$ and the transmitter is located at the variable point (x_2, y_2, z_2) . The distance from the receiver to the scattering area center is R_s and from the transmitter to the patch center is R_i . Corresponding to these radiation paths the angles of incidence and scattering at the scattering area center are, respectively, θ_i and θ_s . The azimuth angle between the ground-plane projection of R_s and the extension of the ground-plane projection of R_i through the scattering area is ϕ_s .

The quantities r_i and r_s (Eq. 26) describe the respective distances from transmitter and receiver to the integration point of the scattering area A_{gd} . They can be described (See Figure 22)* in terms of the distances R_i and R_s and the angle ϕ_s in a polar coordinate system with its origin at the center of A_{gd} :

$$r_i^2 = R_i^2 + \rho^2 + 2R_i\rho \sin \theta_i \cos \phi \quad (27)$$

and

$$r_s^2 = R_s^2 + \rho^2 - 2R_s\rho \sin \theta_s \cos(\phi_s - \phi). \quad (28)$$

The transmitter and receiver power pattern functions f_T and f_R are assumed to have rotational symmetry about their respective beam axes. Thus, the behavior of each is describable in terms of a single variable, namely the angle from the beam axis. Therefore,

$$f_R \equiv f_R(\psi_s) \quad \text{and} \quad f_T \equiv f_T(\psi_i) ,$$

*These descriptions have been adapted from Ref. 8 which considers only the case $R_i = R_s$

where ψ_s is implicitly defined by

$$\sin \psi_s = \frac{\rho \sqrt{1 - \sin^2 \theta_s \cos^2(\phi_s - \phi)}}{\sqrt{R_s^2 + \rho^2 - 2R_s \rho \sin \theta_s \cos(\phi_s - \phi)}} \quad (29)$$

In Section 5.3, an analytic approximation for the power pattern function $f_R(\psi_s)$ is given and the gain quantities G_{OT} and G_{OR} are discussed. Corrections for $f_T(\psi_i)$ are discussed in Appendix C.

Since σ_o , the quantity to be determined, appears as a factor of the integrand in Eq. (24), it is clear that either the integral must be inverted, or an approximation treatment must be developed. It is worthwhile to look, briefly, at some of the steps by which the latter approach evolved from the former.

5.2 EVOLUTION OF METHOD FOR APPROXIMATING σ_o

In the development of a solution for any problem, the fewer the approximations used in the method of solution, the fewer the uncertainties (at least in number if not size) in the result. This precept encouraged the initial viewpoint that Eq. (24) should be inverted. Even though the inversion method itself would require an approximation of the integral I by a system of linear equations, no assumptions would be required concerning the behavior of σ_o within the scattering area A_{gd} . This approach would necessitate the division of area A_{gd} into a set of small cells in each of which the received power P_r would be known. The power pattern functions and ranges form the kernel of I , and their form is such that their characteristics at an arbitrary point are dependent on all other integration points of the region A_{gd} . Thus, the kernel relates the power received from a point in A_{gd} to the effect of σ_o at all other points of A_{gd} . Consider a simple example where

the region A_{gd} may be approximated by only four cells or subdivisions, with received power and radar cross section per unit area σ_o evaluated at only one point a_{ij} within each cell. (All points a_{ij} could, of course, be related to directions defined by some θ_s , θ_i , and ϕ_s in the fashion of Eqs. 27 and 28). The integral I can then be approximated by a sum and Eq. (24) can be written

$$P_r(a_{ij}) = \sum_{k=1}^4 \sum_{\ell=1}^4 K_o(a_{ij}, a_{k\ell}) \sigma_o(a_{k\ell}) \Delta A, \quad i, j = 1, \dots, 4, \quad (30)$$

where the kernel K_o incorporates the range and power pattern factors (as well as the constants P_i and K). Then, presuming $P_r(a_{ij})$ to be measurable at each a_{ij} and K_o to be a known function, the system of four equations can be solved, thus giving σ_o at the four points $a_{k\ell}$, ($k, \ell=1, \dots, 4$) of A_{gd} .

The feasibility of this approach rests on two requirements: (1) the capability of reducing each cell to a size fine enough to make a sum like Eq. (30) a good approximation of Eq. (24) and (2) the capability of making a measurement of received power P_r for each such small cell. Initially, these two requirements appeared to be entirely realizable for a cell configuration formed by range and Doppler lines. However, some study soon showed that range ellipses with sufficiently close spacing were incommensurate with the pulse length and receiver height (≤ 100 ft) available to this program, particularly the latter.

With the above approach unavailable, it is then necessary to make some assumptions concerning the behavior of σ_o over the illuminated area A_{gd} , so as to be able to bring σ_o outside of the integral I in Eq. (24). It may be

reasonably valid to assume that σ_0 is constant over a portion of the region A_{gd} , and that it may take on different constant values over different portions of A_{gd} . This type of approximation can be handled by moving σ_0 to the outside of the integral I and replacing it in the integrand by a weight function $W_{\rho\phi}$. The values that $W_{\rho\phi}$ takes on in different portions of A_{gd} may be fixed (1) by appeal to previous studies, (2) by an examination of the data themselves (to determine, for instance, whether or not the specular point lies inside of A_{gd}), or (3) by estimating the nature of $W_{\rho\phi}$ by the presence or absence of the specular point from portions of A_{gd} (or from regions nearby that may be within the receiver sidelobes).

When σ_0 is replaced in I by the weight function $W_{\rho\phi}$, the solution for σ_0 now depends on simple algebraic manipulation (although the quantities to be manipulated are themselves not so simple). Insofar as the data analysis for this program has been concerned, $W_{\rho\phi}$ has been set equal to unity over the entire region A_{gd} . This choice is tantamount to assuming that σ_0 is constant over A_{gd} .

As a result of these approximations, the forms of Eq. (26) for I and of Eq. (24) for P_r can be modified to yield an explicit expression for σ_0 . Following additional modifications (in Section 5.4 below) of I to include the effect of receiver impulse response, a final form is given for σ_0 in Section 5.4.3.

5.3 PATTERN APPROXIMATIONS FOR RECEIVING AND TRANSMITTING ANTENNAS

Both power patterns and gain were measured for the 3 and 23 cm wavelength receiving antennas. Each agrees well with the desired theoretical behavior.

Descriptions of the antennas and feed configurations appear elsewhere (Section 3.3). Here, suffice it to say that the 23 cm wavelength paraboloidal dish is 3 meters in diameter and operates at a center frequency of 1.315 GHz. The 3 cm wavelength dish is 46 centimeters in diameter and operates at a center frequency of 9.45 GHz.

The desired theoretical pattern is presumed to arise from a tapered illumination given by $a^2 - r^2$, where $D = 2a$ is dish diameter and $0 \leq r \leq a$. The resulting normalized power pattern is then [10,11]

$$f_R = [\Lambda_2(u)]^2 = \left[\frac{8J_2(u)}{u^2} \right]^2 \quad (31)$$

At 23 cm, half of the 1/2 and 1/10 power beamwidths of Eq. (31) are, respectively, $5.46^\circ/2$ and $9.36^\circ/2$. The first sidelobe occurs at 8.74° and has a level of -24.6 dB with respect to the mainlobe peak. The second sidelobe occurs at 13.45° and has a level of -33.6 dB/mainlobe.

At 3 cm, half of the 1/2 and 1/10 power beamwidths of Eq. (31) are, respectively, $5.06^\circ/2$ and $8.70^\circ/2$. The first and second sidelobes occur at 8.11° and 12.46° with the same levels as for 23 cm.

The theoretical peak gain G_0 is calculated to be 28.2 dB at 23 cm and 28.9 dB at 3 cm. The measured values of these quantities are 27.7 (VV) and 25.1 (HH) for 23 cm and 30.5 (HH) for 3 cm — (VV) for 3 cm.

10. S. Silver, Microwave Antenna Theory and Design, MIT Radiation Lab. Series, No. 12, Boston Technical Lithographers, Inc., Lexington, Mass., 1963.
11. E. Jahnke and F. Emde, Tables of Functions with Formulae and Curves, Dover Publications, New York, 1945.

Patterns for each dish were measured for rotations of the dish about its axis by multiples of 30° (with corresponding rotations of the transmitting antenna about its axis). The results are given in Table 15 for the 23 cm case and in Table 16 for the 3 cm case. The results in each case demonstrate a very satisfactory symmetry of the pattern about the dish axis.

Averages and standard deviation have also been taken over the data set for the beamwidth and the levels of the first and second sidelobes. The conclusions to be drawn are as follows. For 23 cm, Eq. (31) makes a satisfactory approximation for the actual pattern through the first sidelobe. Thereafter, for the second sidelobe, the first sidelobe could be repeated with its peak at -29 dB/mainlobe. For 3 cm, Eq. (31) also makes a satisfactory approximation through the first sidelobe. Similarly, its second sidelobe should be given a peak 3 dB below the first sidelobe.

Figures 23 and 24 give comparisons of the experimental and theoretical curves for 23 and 3 cm wavelengths. In Figure 23, the theoretical and several experimental curves are overlaid. In Figure 24, since the pattern is so narrow, the theoretical and experimental curves are placed side by side.

In actual fact, the above discussion concerning sidelobes is somewhat moot, since it was decided to limit the receiver antenna footprint size by the -10 dB/mainlobe level. For both the 23 and 3 cm cases, this level occurs well inside the mainlobe where the experimentally-measured patterns are almost indistinguishable from the theoretical ones.

The 3 dB beamwidth for the transmitter antenna in the

TABLE 15. 23 cm WAVELENGTH ANTENNA CHARACTERISTICS (MEASURED)

Measurement Number	Frequency (GHz)	Sidelobes (dB/mainlobe)				B (deg)	Orientation (deg)	Range (ft)
		1st(right)	2nd(right)	1st(left)	2nd(left)			
21	1.315	-22.5	-29.4	-24.6	-24.5	5.9	+30	300
22	1.315	-21.7	-28.0	-25.0	-25.0	6.0	-60	300
23	1.315	-25.7	-26.6	-25.4	-28.6	5.9	-30	300
24	1.315	-22.2	-25.0	-25.0	-24.6	6.8	+60	300
25	1.315	-18.6	-25.4	-19.0	-23.8	7.0	0	70
27	1.315	-22.4	-22.4	-19.0	-26.6	6.8	90	70
37	1.315	-20.4	-26.6	-20.4	-27.6	7.2	-60	70
36	1.315	-20.0	-24.4	-20.0	-22.4	6.7	+30	70
35	1.315	-22.5	-23.5	-19.8	-24.6	7.1	-30	70
34	1.315	-19.4	-24.6	-21.6	-24.2	6.8	+60	70
33	1.300	-18.0	-24.6	-19.0	-24.0	6.7	0	70
32	1.330	-21.0	-25.0	-20.6	-26.0	7.1	0	70
31	1.330	-22.0	-22.8	-19.0	-27.6	6.5	90	70
30	1.300	-22.0	-22.0	-19.0	-24.6	6.4	90	70
15	1.330	-23.4	-26.0	-23.0	-32.4	5.9	90	300
14	1.315	-24.9	-26.2	-25.2	-30.2	6.0	90	300
13	1.300	-27.8	-26.2	-25.0	-29.2	5.7	90	300
9	1.330	-22.3	-25.8	-19.5	-26.0	6.0	0	300
8	1.315	-21.6	-26.3	-19.8	-26.2	5.8	0	300
7	1.300	-22.5	-30.0	-21.3	-30.0	5.8	0	300
av(arith)	1.315	-21.4	-25.3	-21.3	-25.2	6.0*		
av(geom)**	1.315	-21.8	-25.7	-22.1	-25.7			
s	1.315	6.4	7.4	6.6	7.4	1.9		

* Theoretical value of 5.5° is within s/4 of mean value of 6.

** Note that there is very little difference here between average power and dB average.

TABLE 16. 3-cm WAVELENGTH ANTENNA CHARACTERISTICS (MEASURED)

Measurement Number	Frequency (GHz)	Sidelobes (dB/mainlobe)				BW (deg)	Orientation (deg)
		1st(right)	2nd(right)	1st(left)	2nd(left)		
1	9.45	-22.4	-25.6	-22.7	-24.2	5.0	VV
2	9.45	-26.1	-28.0	-24.0	-25.6	5.0	HH
3	9.45	-23.4	-27.4	-24.4	-28.4	5.0	HH +30
4	9.45	-24.3	-26.6	-23.6	-25.6	5.0	VV +30
5	9.45	-24.0	-28.1	-26.6	-29.1	5.0	VV +60
6	9.45	-21.0	-27.9	-24.1	-24.9	5.0	HH +60
7	9.45	-25.2	-29.3	-23.8	-28.2	5.0	HH -30
8	9.45	-23.8	-26.6	-24.4	-29.2	5.0	VV -30
9	9.45	-28.2	-28.4	-24.8	-29.0	5.0	VV -60
10	9.45	-25.8	-28.3	-21.8	-28.9	---	HH -60
13	9.35	-22.7	-27.2	-22.4	-25.2	5.5	VV
14	9.55	-21.6	-26.0	-21.4	-24.4	5.5	VV
15	9.55	-25.6	-28.0	-26.8	-26.4	5.0	HH
16	9.35	-27.6	-27.2	-25.4	-26.6	5.0	HH
av(arith)	9.45	-24.0	-27.5	-23.9	-26.9	5.0	(agrees exactly
av(geom)	9.45	-24.4	-27.6	-24.0	-27.3	---	with theory)
s	9.45	2.3	1.6	1.6	2.1	0	

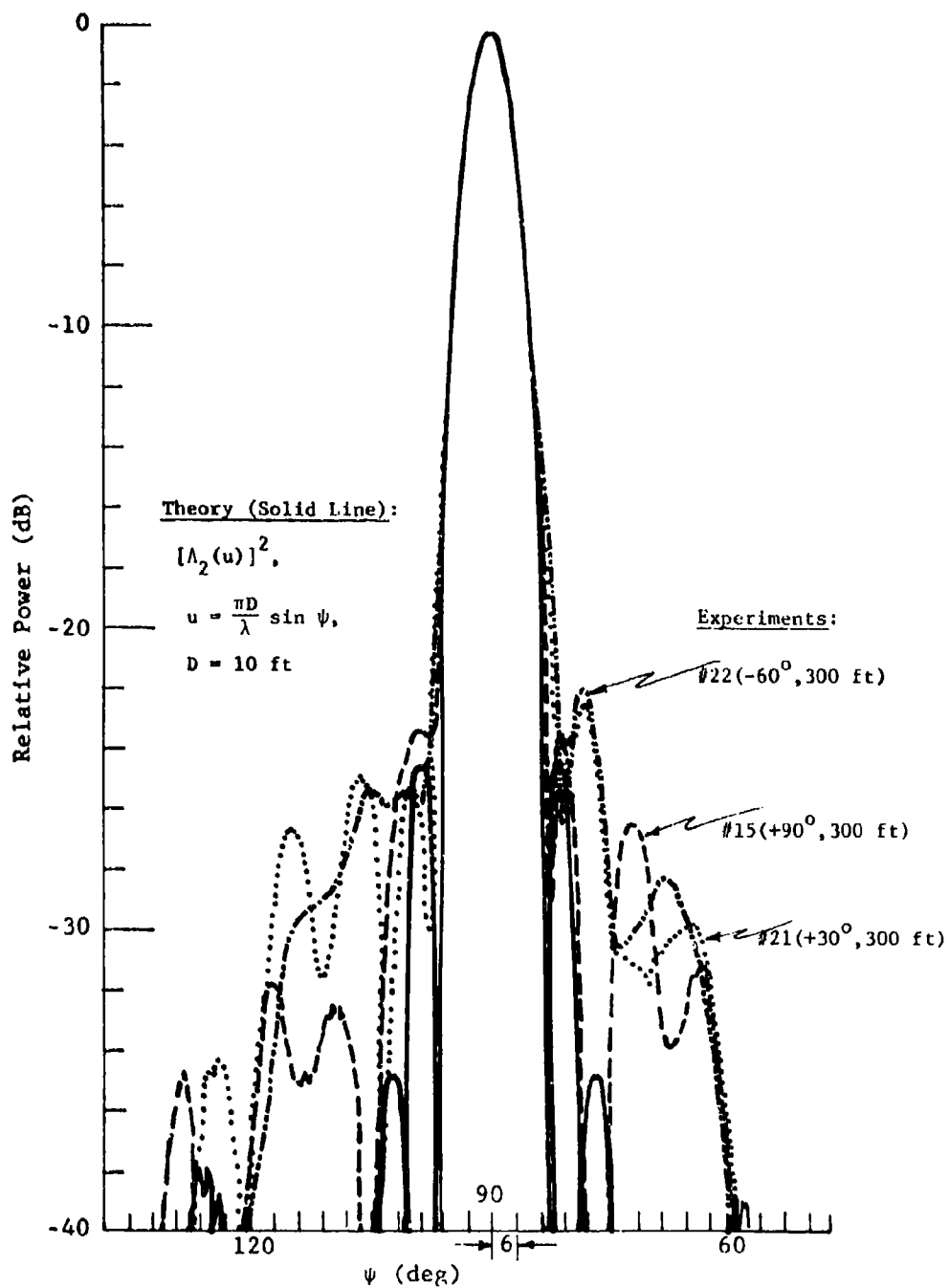


Figure 23. Receiver Antenna Patterns at $f = 1.315$ GHz

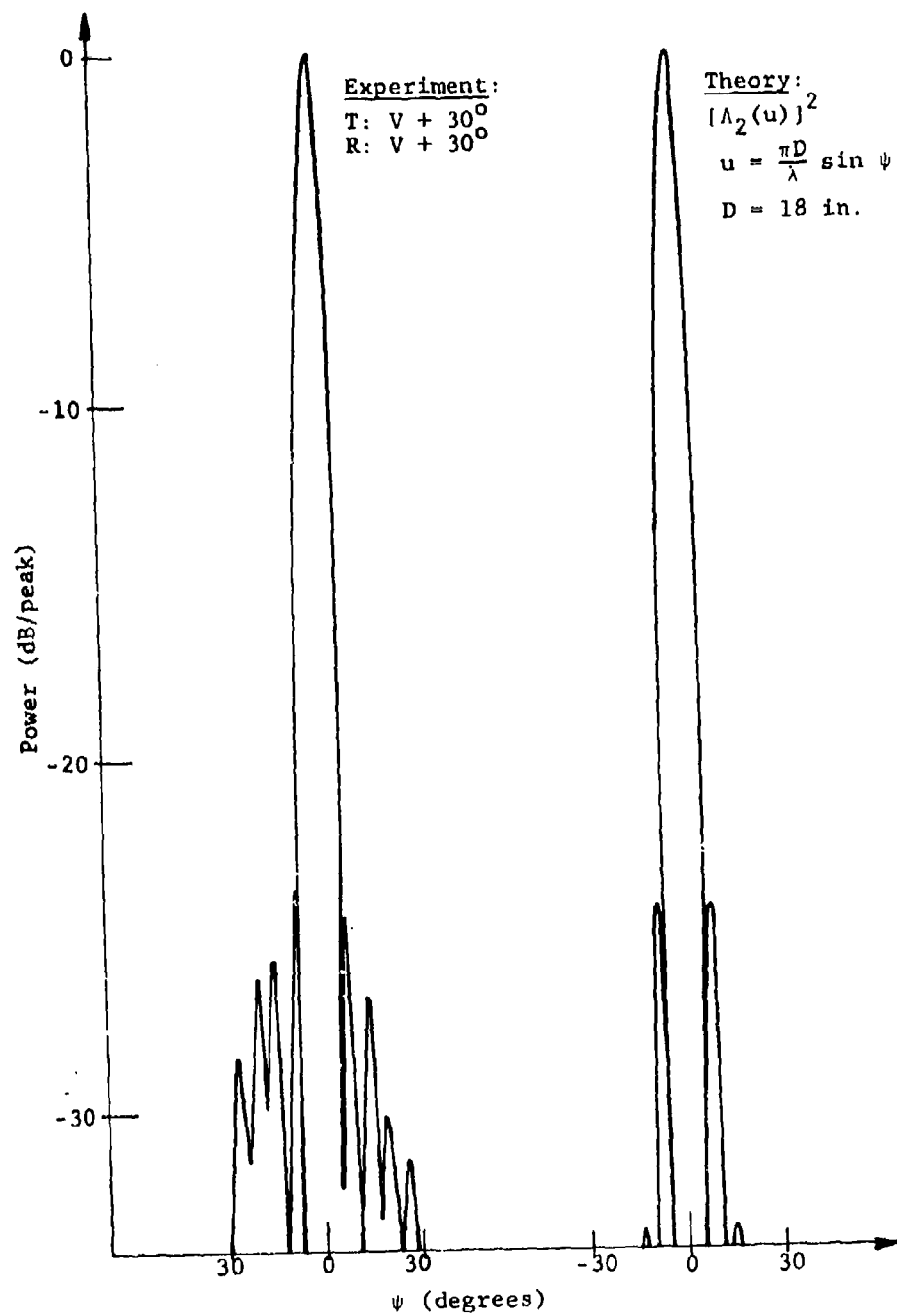


Figure 24. Receiver Antenna Patterns at $f = 9.45 \text{ GHz}$

horizontal plane is 12° at both the 3 cm and 23 cm wavelengths. The vertical 3 dB beamwidth for the 23 cm antenna is 90° , and for the 3 cm antenna is 13° . Since the distance from the transmitter to the scattering area was never less than 14,000 ft (4.27 km) during the measurements, the illuminated ground area always exceeded 3000 ft (915 m) in the z_o and x_o directions; also, the diameter of the receiver scan arc never exceeded 1000 ft (305 m). Therefore, the receiver antenna footprint is always well within the transmitter antenna footprint. Furthermore, the angle subtended by A_{gd} at the transmitter is always $<3^\circ$; therefore, the variation of incident power over the receiver antenna footprint is so small that the transmitter antenna power pattern can be taken to be approximately unity over the entire area A_{gd} , that is, $f_T \approx 1$.

5.4 SCATTERING ELEMENT A_{gd} ; FINAL FORM OF EQUATION FOR σ_o

Let a vector be denoted by \vec{v} [or by (x_o, y_o, z_o)], or by \hat{v} if its length $|\vec{v}|$ is unity. The receiver position has already (Section 5.1) been defined by

$$\vec{p}_1 = (0, y_1, 0).$$

The receiver antenna beam can be defined as a set of pattern cones

$$\hat{w} \cdot \hat{s} = \cos \alpha_c \quad (32)$$

concentric about an axis

$$\hat{w} = \frac{\vec{v} - \vec{p}_1}{|\vec{v} - \vec{p}_1|}, \quad (33)$$

where \vec{v}_c is a fixed vector to some arbitrary point on the beam axis; \vec{s} ($\hat{s} = \vec{s}/|\vec{s}|$) is a variable vector which traces out a cone of half-angle α_c . The angle α_c is chosen to fix some particular power level of the antenna pattern. In all of the results to be given below, α_c is chosen to define the -10 dB power level (with respect to the peak).

The "footprints" of the pattern cones on the ground plane are obtained by intersecting the cones (Eq. 32) with the x_0z_0 -plane ($y_0 = 0$). These intersections are nested ellipses (neither concentric nor confocal).

The integration area A_{gd} does not include an entire receiving antenna footprint if that footprint is limited by range curves. These range curves (curves of constant range from transmitter-to-ground-to-receiver) are nested ellipses (again, neither concentric nor confocal) defined in the following paragraph.

Nested ellipsoids having foci at the receiver \vec{P}_1 and transmitter \vec{P}_2 are traced by the vector \vec{P} so that

$$|\vec{P} - \vec{P}_1| + |\vec{P} - \vec{P}_2| = 2q, \quad (34)$$

where $2q$ is a constant distance defined by the time for a signal to get from transmitter to receiver by way of the ellipsoid; the factor of 2 is included for convenience. (Different values of $2q$ yield confocal ellipsoids.) Let these ellipsoids be intersected with the ground plane $y_0 = 0$. The resulting curves are constant range ellipses (which are not confocal). If two of these ellipses which are defined by the receiver sampling time* and the transmitter pulse length intersect the receiver antenna footprint, the area A_{gd} is

* See Appendix B for a description of the circuitry which samples the peak value of the received bistatic pulse.

modified accordingly**. Figure 25 illustrates both cases where a footprint is and is not cut by the bounding range ellipses.

To summarize, the integration area A_{gd} is defined as follows: Let the receiver footprint area of interest be fixed by the 10 dB pattern contour:

$$E_f \leq 1, \quad (35)$$

where $E_f = 1$ is the ellipse (see also Eq. (40) for the canonical form) described by

$$\begin{cases} \hat{w} \cdot \hat{s} = \cos \alpha, \\ y_0 = 0. \end{cases} \quad (36)$$

Now, let $E_{r_1} = 1$ and $E_{r_2} = 1$ be successive range ellipses defined by the receiver sampling time and the transmitter pulse length where each $E_r = 1$ is an ellipse given by (see also Eq. (46))

$$\begin{cases} |\vec{P} - \vec{P}_1| + |\vec{P} - \vec{P}_2| = 2q, \\ y_0 = 0. \end{cases} \quad (37)$$

Then, A_{gd} is the integration area given by

$$A_{gd} = (E_f \leq 1) \cap (E_{r_1} \geq 1) \cap (E_{r_2} \leq 1), \quad (38)$$

where the symbol \cap stands for "intersected with" and means all points common to the three sets (that is, all points

** In general, it would be possible for the integration area A_{gd} to be modified by the transmitting antenna footprint. However, in this program, the transmitting antenna footprint is so large as to always encompass the entire receiving antenna footprint. (See Section 5.3.)

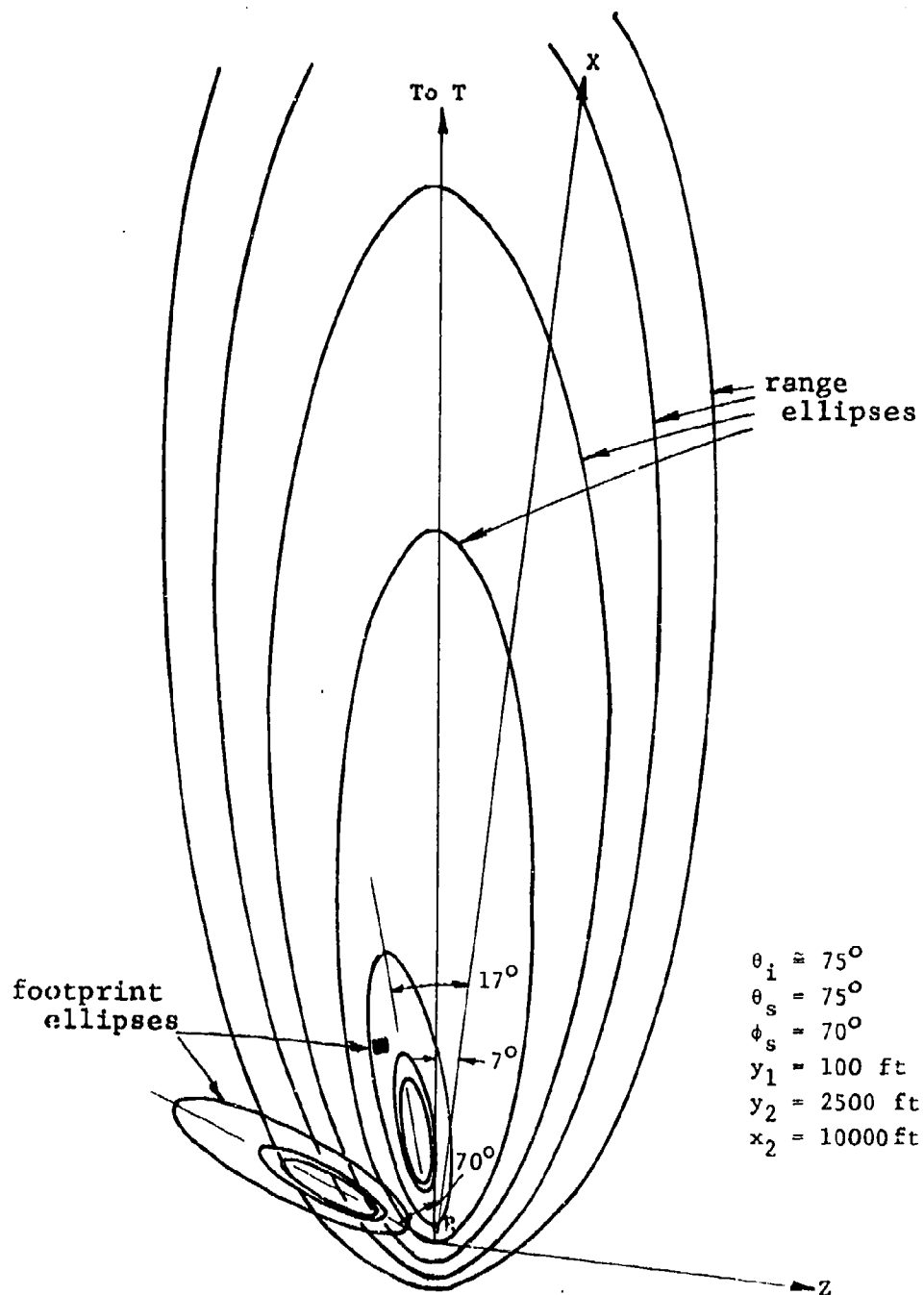


Figure 25. Footprint and Range Ellipses

common to the interior of the receiver footprint ellipse, the exterior of the first range ellipse, and the interior of the second range ellipse).

Thus, it is easy to determine from Eq. (38) whether an integration point P [or perhaps the specular point

$$P_s = \left(\frac{x_2 y_1}{(y_1 + y_2) \sqrt{x_2^2 + z_2^2}}, 0, \frac{z_2 y_1}{(y_1 + y_2) \sqrt{x_2^2 + z_2^2}} \right)$$

lies inside A_{gd} : the procedure is simply to test whether $E_f(P) \leq 1$ at the same time that $E_{r_1}(P) \geq 1$ and $E_{r_2}(P) \leq 1$.

5.4.1 FORMULAS FOR FOOTPRINT AND RANGE ELLIPSES

Footprint Ellipses:* Suppose the beam size of interest to be specified by (See Eq. 31)

$$\psi_s \leq \eta \quad (39)$$

Then, the receiving antenna footprint ellipse (Eq. 36) can be written in canonical form as

$$E_f \equiv \frac{(x' - \text{ctr } x)^2}{a'^2} + \frac{(y' - \text{ctr } y)^2}{b'^2} = 1. \quad (40)$$

Taking a' to be the semi-major axis, the x', y', z' -system can be oriented accordingly by placing the x' -axis along the intersection of the plane of the earth with the vertical plane determined by the receiver antenna beam axis and the y_0 -axis, using the same origin as for the x_0, y_0, z_0 -system (See Figure 21). The parameters for the elliptical footprint are

*Because of the conditions set by Section 5.3, only the receiver antenna footprint need be considered.

$$a' = \frac{1}{2} y_1 \left[\tan(\theta_s + \eta) - \tan(\theta_s - \eta) \right], \quad (41)$$

$$b'^2 = \frac{a'^2 z_{oo}^2}{a'^2 - x_{oo}^2}, \quad (42)$$

and

$$\begin{aligned} \text{ctr } x &= y_1 \tan(\theta_s - \eta) + a', \\ \text{ctr } y &= 0, \end{aligned} \quad (43)$$

where

$$x_{oo} = \frac{1}{2} y_1 \left[\tan(\theta_s + \eta) + \tan(\theta_s - \eta) \right] - y_1 \tan \theta_s, \quad (44)$$

and

$$z_{oo} = \frac{y_1 \tan \eta}{\cos \theta_s}. \quad (45)$$

(The quantities y_1 and θ_s are measured quantities and are defined in Figure 21.) When the area A_{gd} is defined by the footprint alone, it is given by $E_f \leq 1$.

Range Ellipses: A range ellipse (Eq. 37) can be written in canonical form* as

*The eccentricity of the range ellipse is given by

$$e = \frac{\sqrt{x_2^2 + z_2^2}}{2q} = \frac{\text{ground range}}{\text{total range}}.$$

$$E_r \equiv \frac{\left[x_o - \frac{(4q^2 - r_2^2 + y_1^2)(x_2^2 + z_2^2)^{1/2}}{2(4q^2 - x_2^2 - z_2^2)} \right]^2}{\frac{q^2 \left[(4q^2 - r_2^2 - y_1^2)^2 - 4y_1^2 y_2^2 \right]}{(4q^2 - x_2^2 - z_2^2)^2}} + \frac{\frac{z_o^2}{(4q^2 - r_2^2 - y_1^2)^2 - 4y_1^2 y_2^2}}{4(4q^2 - x_2^2 - z_2^2)} = 1, \quad (46)$$

where $r_2^2 = x_2^2 + y_2^2 + z_2^2$

(x_2 being the minimum distance from the foot of receiver to the transmitter ground track). The parameter $2q$ is defined** following Eq. (34).

If the integration area A_{gd} is to be defined with the help of two range ellipses $E_{r1} = 1$ and $E_{r2} = 1$, then the distance $(2q)_1$ for the first ellipse is determined by the elapsed time ΔT between the end of the received direct pulse and the sampling time. Thus,

$$(2q)_1 = c\Delta T + d, \quad d = \sqrt{x_2^2 + z_2^2 + (y_2 - y_1)^2}. \quad (47)$$

The second range ellipse $E_{r2} = 1$ is then given by

$$(2q)_2 = (2q)_1 + p, \quad (48)$$

where p is the distance corresponding to the transmitter pulse length τ (p is taken in this study to be 90 ft).

**Note that $(2q)_{\min} = \sqrt{x_2^2 + z_2^2 + (y_1 + y_2)^2}$, the specular distance from transmitter to receiver.

5.4.2 MODIFICATION OF I BY RECEIVER IMPULSE RESPONSE

The amplitude response for a pulse, between the ellipses $E_{r_1} = 1$ and $E_{r_2} = 1$, is not uniform; so, this fact should be accounted for in the integral I. To determine this response, measurement was made at the output of the instrumentation when a pulse similar to the transmitted pulse was fed into the receiver. The amplitude response, called $h[t(A)]$, is shown in Figure 26. Between the two bounding ellipses $E_{r_1} = 1$ and $E_{r_2} = 1$, a continuum of ellipses can be envisioned corresponding to the time continuum between those curves. Then, the amplitude response can be represented implicitly as a function of area A. This idea is applied in the computational work by taking h to be constant over strips between successive ellipses in the continuum between the bounding ellipses $E_{r_1} = 1$ and $E_{r_2} = 1$. For this reason, h has been approximated in Figure 26 by the staircase function actually used in the computation of I, which is now modified to be

$$I = \int_{A_{gd}} \frac{f_T f_R W_{\rho\phi} h[t(A)] dA}{r_i^2 r_s^2} \quad (m^{-2}). \quad (49)$$

5.4.3 FINAL FORM FOR σ_o

Now that the interaction of the scattering properties of the illuminated terrain region A_{gd} with the incident pulse have been replaced by suitable weight functions, the quantity σ_o can be brought out of the integral I to make possible the explicit solution. Using Eqs. (26) and (24),

$$\sigma_o = \frac{P_r}{P_i KI} \quad (50)$$

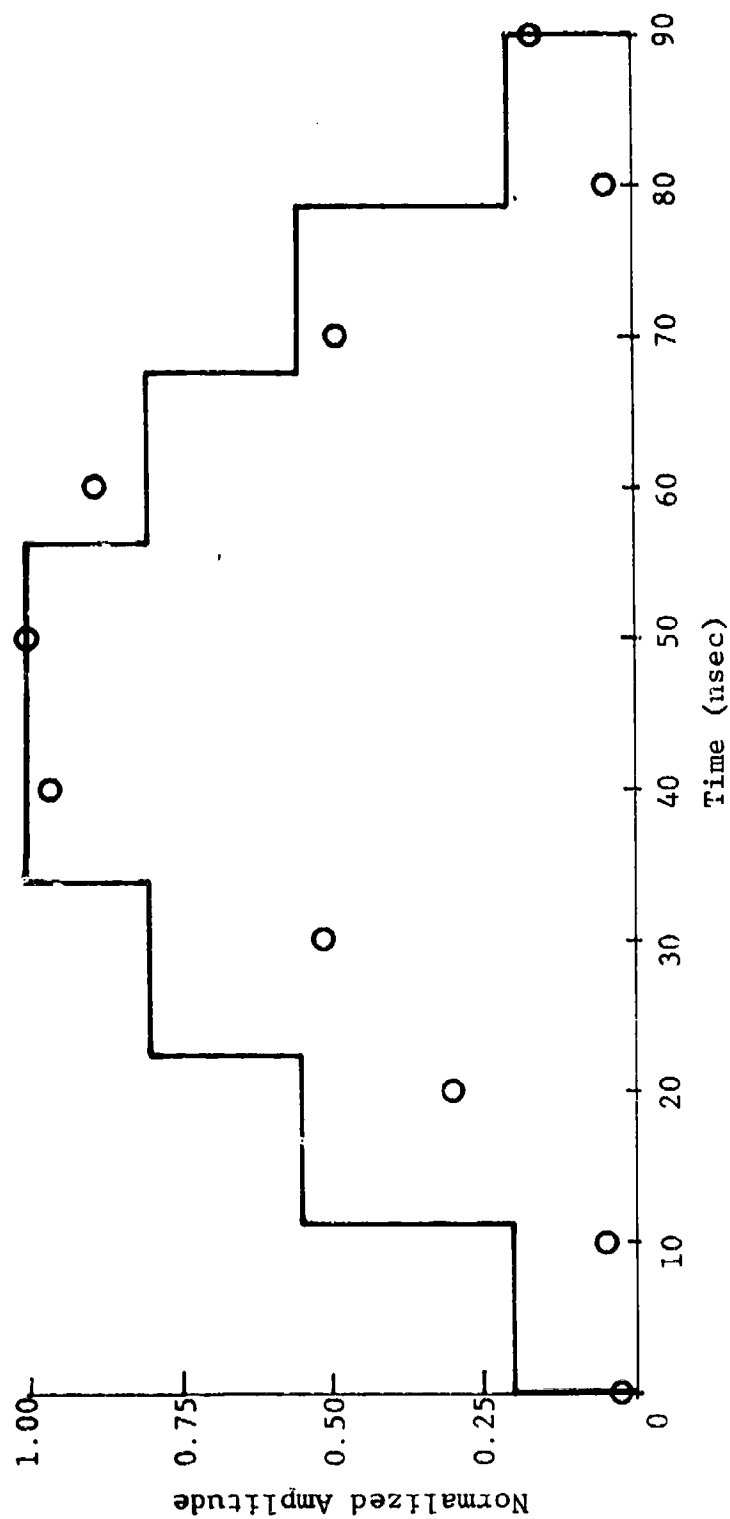


Figure 26. Receiver Impulse Response $h[t(A)]$

Since both powers P_i and P_r have the same dimensions, K has dimensions of area, and I has dimensions of inverse area, then the quantity σ_0 is dimensionless.

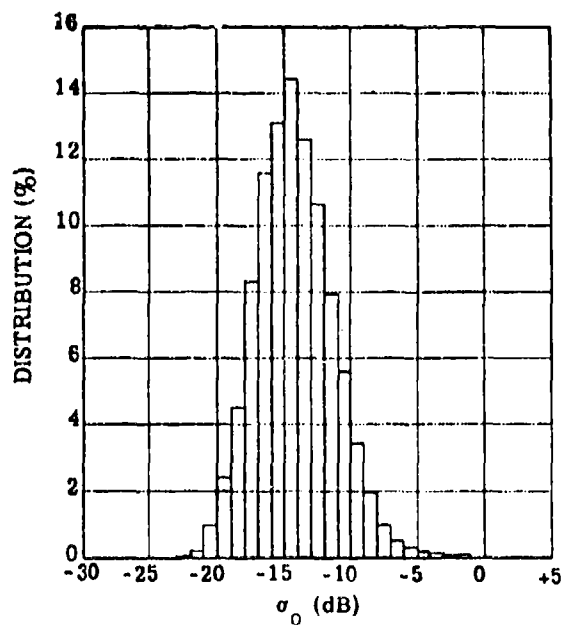
Remarks concerning power and angle calibration and their incorporation into the determination of σ_0 are given in Section 5.7

5.5 ENSEMBLE STATISTICS OF A SET OF SCATTERING ELEMENTS; PARAMETER VARIATION

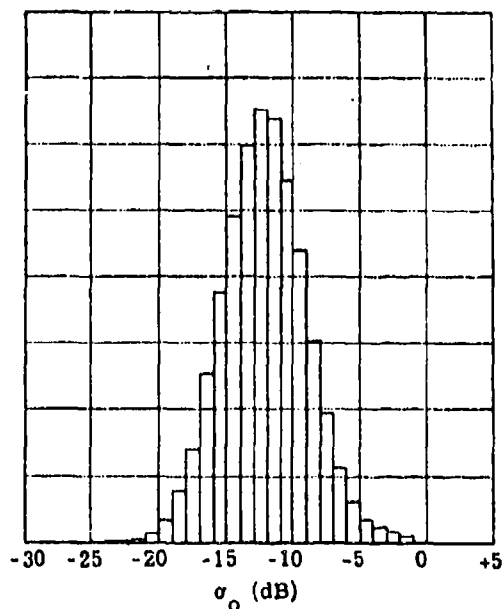
The quantity σ_0 is a random variable whose distribution is governed by the type and condition of the terrain it describes. Thus, in order to estimate the statistics of the terrain being measured, the number of samples taken at a fixed set of parameters must be sufficiently large. Unfortunately, the number of samples required is based on the distribution of the terrain clutter σ_0 that must be approximated with the sample statistics. Since such distributions are unavailable, estimates must be made.

Long [12] gives the probability distribution for monostatic backscattering from terrain. For homogeneous terrain, the distribution tends to be Rayleigh, but distributions for urban and mountainous areas have long tails typical of log-normal distributions. Figure 27 shows histograms of monostatic return data taken with the ERIM synthetic aperture radar. These distributions are reasonably close to being log-normal. Since the distribution of clutter return often becomes log-normal as the area of the resolution cell

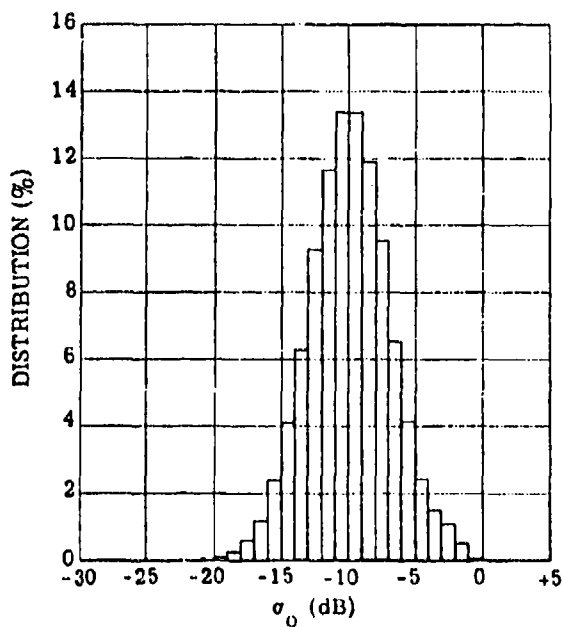
-
12. M.W. Long, Radar Reflectivity of Land and Sea, Lexington Books, Lexington, Mass., 1975, p. 156.



(a) Grazing Angle 11°
 $(\bar{\sigma}_0 = 0.048 = -13.2 \text{ dB})$



(b) Grazing Angle 15°
 $(\bar{\sigma}_0 = 0.079 = -11.0 \text{ dB})$



(c) Grazing Angle 19°
 $(\bar{\sigma}_0 = 0.128 = -8.9 \text{ dB})$

Figure 27. 3 cm Wavelength Histograms, ERIM SAR Data
 (Ohio Farmland, 10 ft Resolution, Single Look)

decreases, fine-resolution SARs are more likely to measure log-normal distributions than conventional radars.

For the data of Figure 27, the standard deviation s of $\log \sigma_0$ is in the order of 3 or 4 dB. For a Rayleigh distribution, the standard deviation is 5.6 dB, so that the log-normal distribution makes a fair approximation of the Rayleigh. Thus, the log-normal provides a good approximation of ground clutter returns no matter whether they are actually log-normal or Rayleigh distributed. So it is assumed here, for purposes of estimating desired sample size, that terrain clutter, both monostatic and bistatic, is log-normally distributed.

From standard statistical theory, the 95% confidence interval for the population mean is given by

$$\bar{\sigma}_0 - \frac{1.96s}{\sqrt{n}} < \mu < \bar{\sigma}_0 + \frac{1.96s}{\sqrt{n}}, \quad (51)$$

where $\bar{\sigma}_0$ is the mean of n samples, while μ and s are the mean and standard deviation of the terrain clutter population. The 95% confidence interval for μ is therefore $3.92s/\sqrt{n}$ dB in width. Figure 28 shows plots of $3.92s/\sqrt{n}$ for s equal to 3 and 5 dB for sample numbers n ranging from 4 to 20 (which is representative of the range of σ_0 samples obtained in this program).

To achieve the desired number of samples, the receiving antenna is made to rotate from side to side as the transmitting antenna travels along a straight-line course. The angles defining the direction of look of the receiving antenna and the direction of the transmitter from the receiver are each measured clockwise from the negative z_0 -axis of Figure 1; they are called SCAN and TRACK, respectively.

For the forward scattering case (scattering area

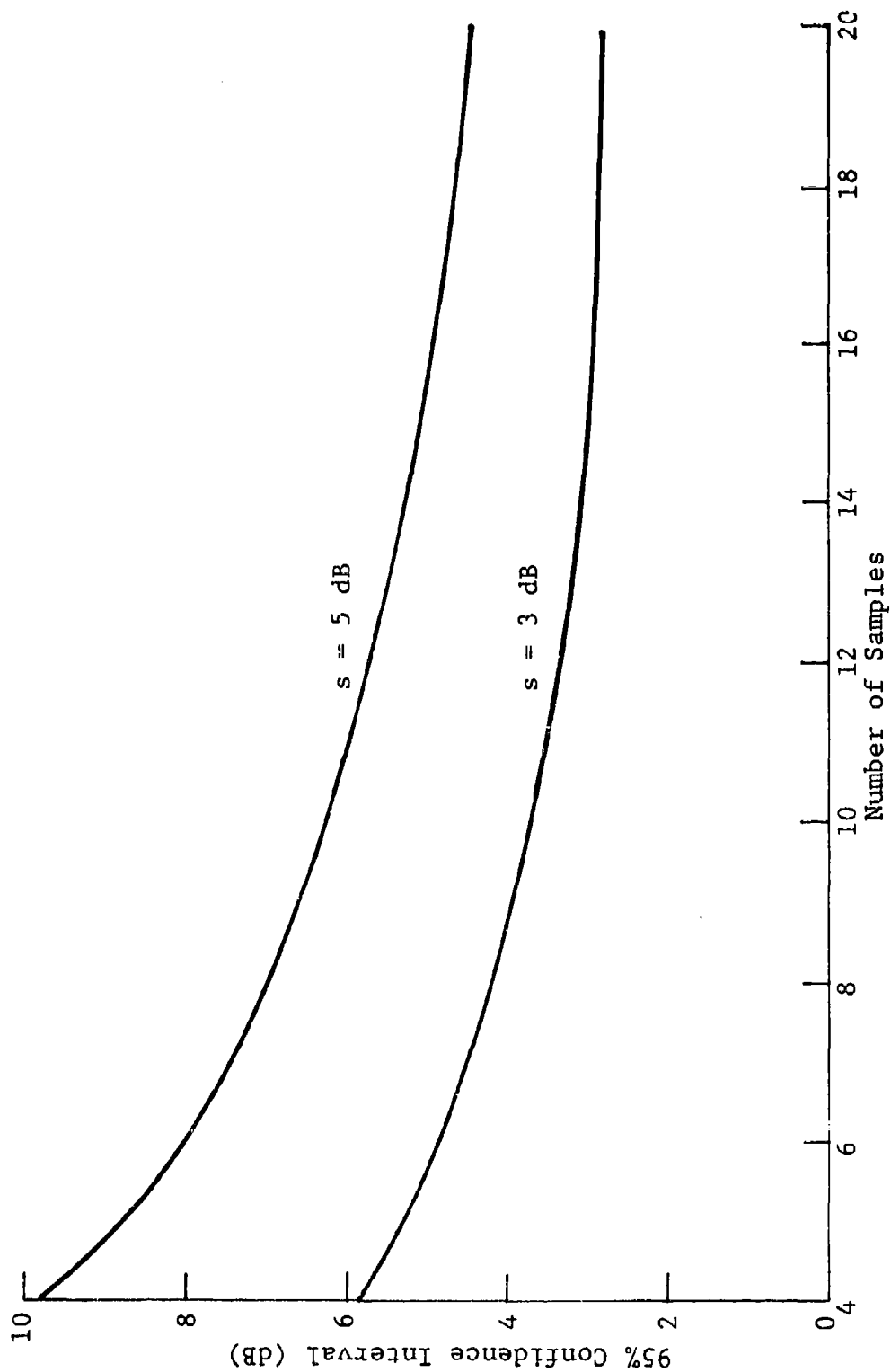


Figure 28. Width of 95% Confidence Interval vs. Number of Samples

between transmitter and receiver), the azimuth angle ϕ_s is given approximately* by

$$\phi_s = |\text{SCAN} - \text{TRACK}|. \quad (52)$$

Since SCAN moves through its range (typically 65° through 155°) many times (typically 20) during a pass of the transmitter (TRACK range typically 45° through 135°), ϕ_s takes on the same (largely acute) value many times. Each of these ϕ_s values occurs for a different terrain scattering element in an essentially homogeneous field or region of terrain; in this way, the sought-after set of scattering element (or σ_o) samples is obtained. If values of SCAN and TRACK are approximated to the nearest multiple of 5° , then a typical sample number range of 4 to 20 can be expected.

For the backscattering case (receiver between scattering area and transmitter), the azimuth angle ϕ_s is given approximately by

$$\phi_s = ||\text{SCAN} - \text{TRACK}| - 180| \quad (53)$$

since, in this case, SCAN is measured clockwise from the positive z_o -axis while TRACK is measured clockwise from the negative z_o -axis as above. (In other words, the receiver is rotated through 180° and the SCAN angle measurement relative to the receiver itself is unchanged.) SCAN and TRACK move through essentially the same ranges as above, and so ϕ_s takes on mainly obtuse values. Once again, each ϕ_s value is repeated many times, each time for a different terrain

*The precise value is
$$\phi_s = |\text{SCAN} - \text{TRACK}| + \arcsin \frac{y_1 \tan \theta_s \sin |\text{SCAN} - \text{TRACK}|}{y_2 \tan \theta_i}$$

However, since the denominator is much larger than the numerator in the arcsine argument, the arcsine value is close to zero.

scattering element. Typical numbers of samples are in the same range as for the forward scattering case.

Actually, for a given value of ϕ_s to be repeated, special provisions would be required. As has been documented elsewhere in this report (Appendix D), angle digitization is done on the basis of a number of voltage intervals whose total encompasses the total angular excursion (of either SCAN or TRACK) for a pass. Each voltage interval thus corresponds to an angular interval; for this interval, the median value is digitized. If, instead, the digitized angle were always placed at an integer multiple of 5° , then $|\text{SCAN} - \text{TRACK}|$ would give exact repetitions of ϕ_s . In this case, σ_o would be averaged over the number of repetitions of ϕ_s . Since the special assignments of SCAN and TRACK values are not made, no repetitions of ϕ_s are guaranteed.

However, an arrangement essentially equivalent to the above is obtained by striking an average of all σ_o values over a range of ϕ_s values within $2\frac{1}{2}^\circ$ on either side of integer multiples of 5° . In this interval of ϕ_s , samples may come from any portion of the pass and so the incidence angle θ_i may vary by the maximum amount possible in the total pass. The incidence angle is given approximately* by

$$\theta_i = \arctan \frac{x_2 \csc(\text{TRACK})}{y_2} \quad (54)$$

and so varies directly as $\csc(\text{TRACK})$. In a pass with, say,

*The exact expression is

$$\theta_i = \arctan \frac{1}{y_2} \sqrt{x_2^2 \csc^2[\text{TRACK}] + 2x_2 y_1 \tan \theta_s (1 + \cos[\text{SCAN}]) + y_1^2 \tan^2 \theta_s (1 + \cos^2[\text{SCAN}])}$$

$x_2 = 18,000$ ft, $y_2 = 6,000$ ft, and TRACK between 65° and 155° , the incidence angle θ_i may change by as much as 9° for samples at the beginning and end of the pass. This is the most serious change in any parameter over any set of samples; it may or may not occur in any particular sample set depending on the portions of the pass for which SCAN and TRACK combine to give a particular ϕ_s value. The scattering angle θ_s , of course, remains fixed throughout a given pass.

Since σ_0 samples may come from any part of a pass, the sizes of A_{gd} and values of KI may vary correspondingly. Consider a 23 cm wavelength example for which $y_1 = 100$ ft, $\theta_s = 80^\circ$, $x_2 = 20,000$ ft, and $y_2 = 6,000$ ft. Then, for all of the (SCAN, TRACK) pairs $(90^\circ, 90^\circ)$, $(120^\circ, 120^\circ)$, and $(150^\circ, 150^\circ)$, ϕ_s is 0° . Assuming that the first limiting range ellipse passes through the intersection of the receiver antenna beam axis with the earth and the second limiting range ellipse occurs 90 nanoseconds later, there are pronounced differences in A_{gd} and KI values because of the range changes involved. Table 17 illustrates these differences. Graphs of A_{gd} for the three sets of conditions covered in the table are shown in Figures 29, 30, and 31, respectively.

As the values of ϕ_s change, A_{gd} can vary over a much wider range; but, due again to the changing ranges from A_{gd} to transmitter and receiver, the values of KI seldom suffer more than 4 to 6 dB excursions. Illustrations of this behavior of A_{gd} and KI are afforded by the five illustrations (using the above values of y_1 , θ_s , x_2 , and y_2), three for forward and two for backscattering, given in Table 18. The areas A_{gd} corresponding, respectively, to the five sets of conditions covered in the table are shown in Figures 32, 33, 34, 35, and 36.

TABLE 17. VARIATIONS IN A_{gd} AND KI VALUES

$\frac{\text{SCAN}}{(\text{deg})}$	$\frac{\text{TRACK}}{(\text{deg})}$	$\frac{\phi_s}{(\text{deg})}$	$\frac{A_{gd}}{(\text{m}^2)}$	$\frac{\text{KI}}{(\text{dB})}$
90	90	0	4387	-97.6
120	120	0	4475	-99.2
150	150	0	4855	-103.0

TABLE 18. BEHAVIOR OF A_{gd} AND KI FOR FORWARD AND BACKSCATTERING CASES

$\frac{\text{SCAN}}{(\text{deg})}$	$\frac{\text{TRACK}}{(\text{deg})}$	$\frac{\phi_s}{(\text{deg})}$	$\frac{A_{gd}}{(\text{m}^2)}$	$\frac{\text{KI}}{(\text{dB})}$
60	60	0	4475	-99.2
90	60	30	4065	-95.2
120	60	60	1579	-96.5
60 (back)	60	180	468	-101.1
120 (back)	60	120	614	-100.2

AREA = 4366.8

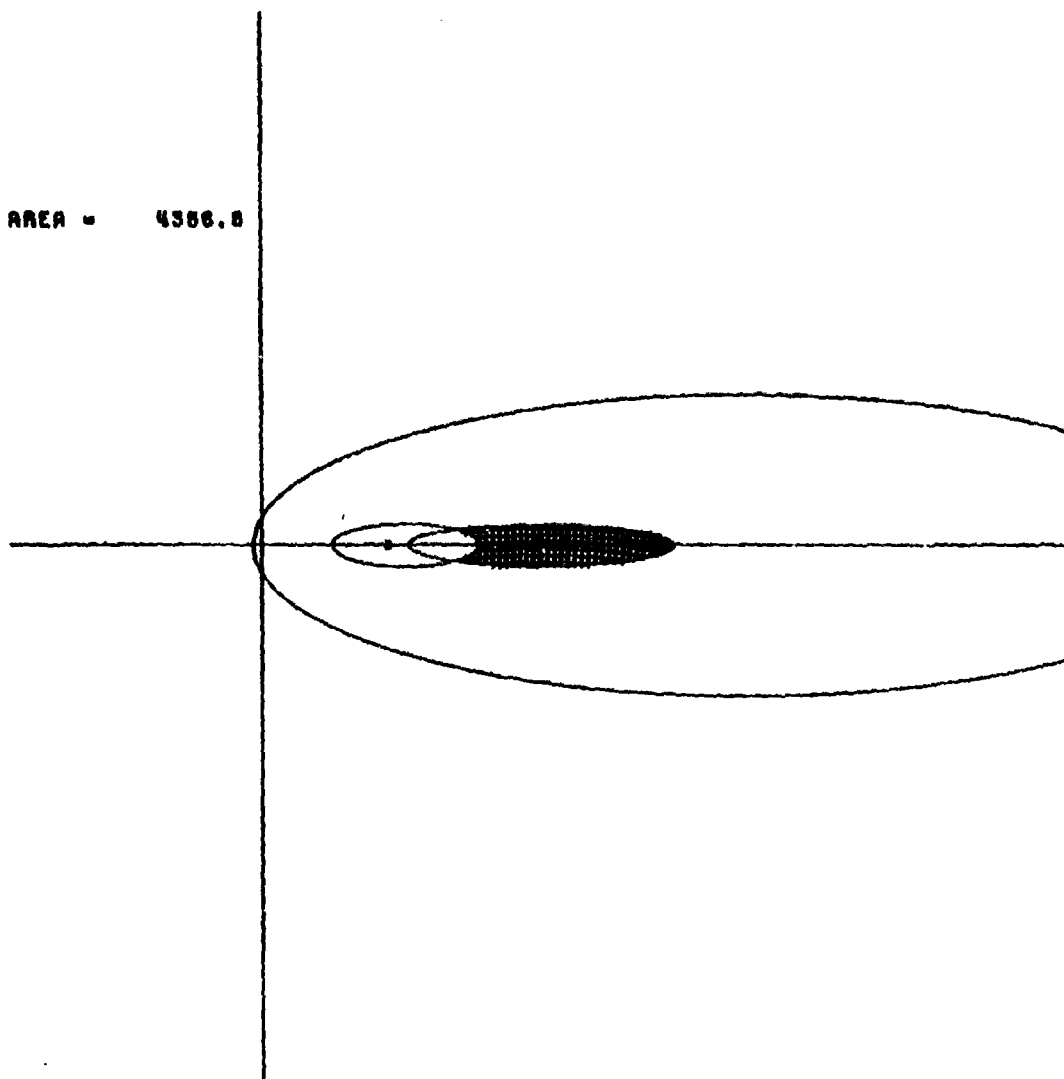


Figure 29. A_{gd} for SCAN = TRACK = 90° ($\phi_s = 0^\circ$)

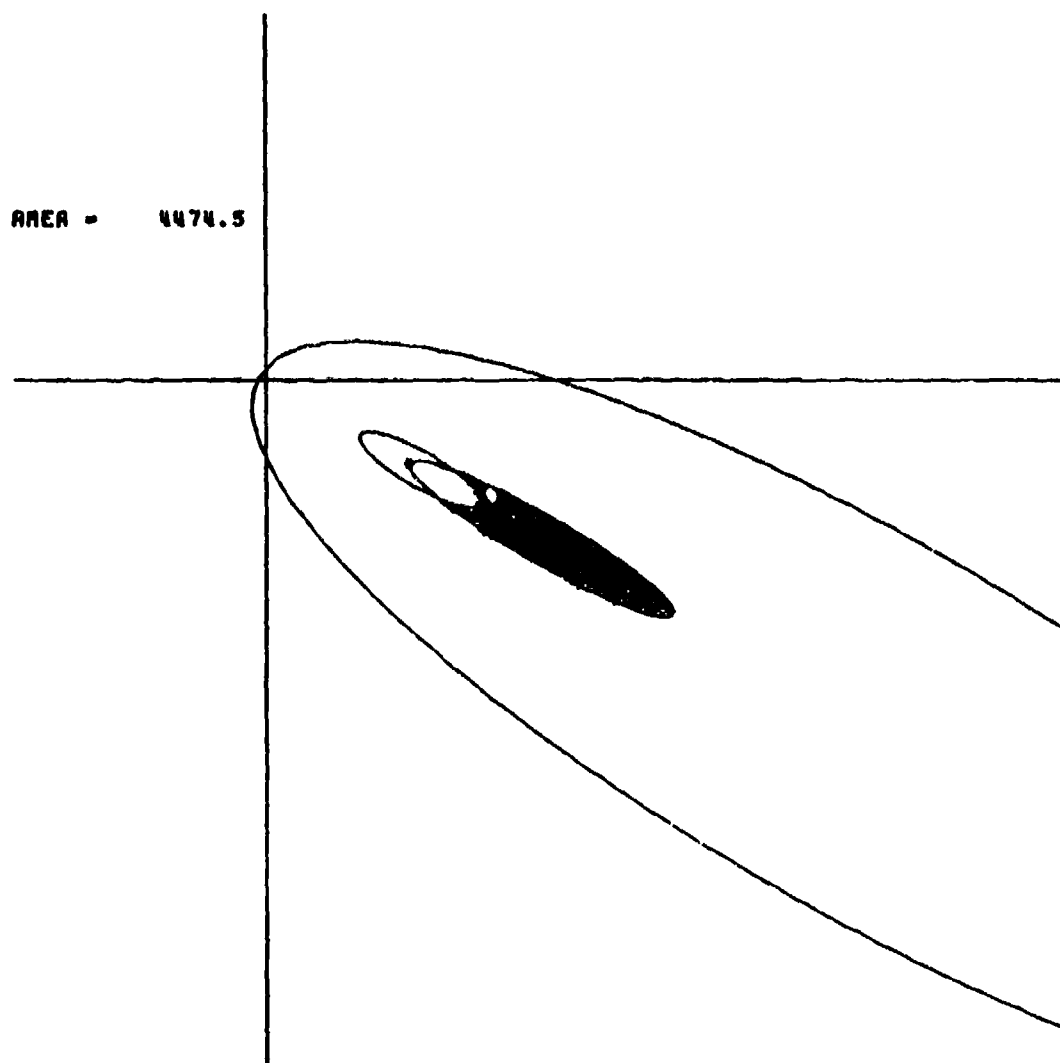


Figure 30. A_{gd} for SCAN = TRACK = 120° ($\phi_s = 0^\circ$)

AREA = 4854.7

Figure 31. A_{gd} for SCAN = TRACK = 150° ($\phi_s = 0^\circ$)

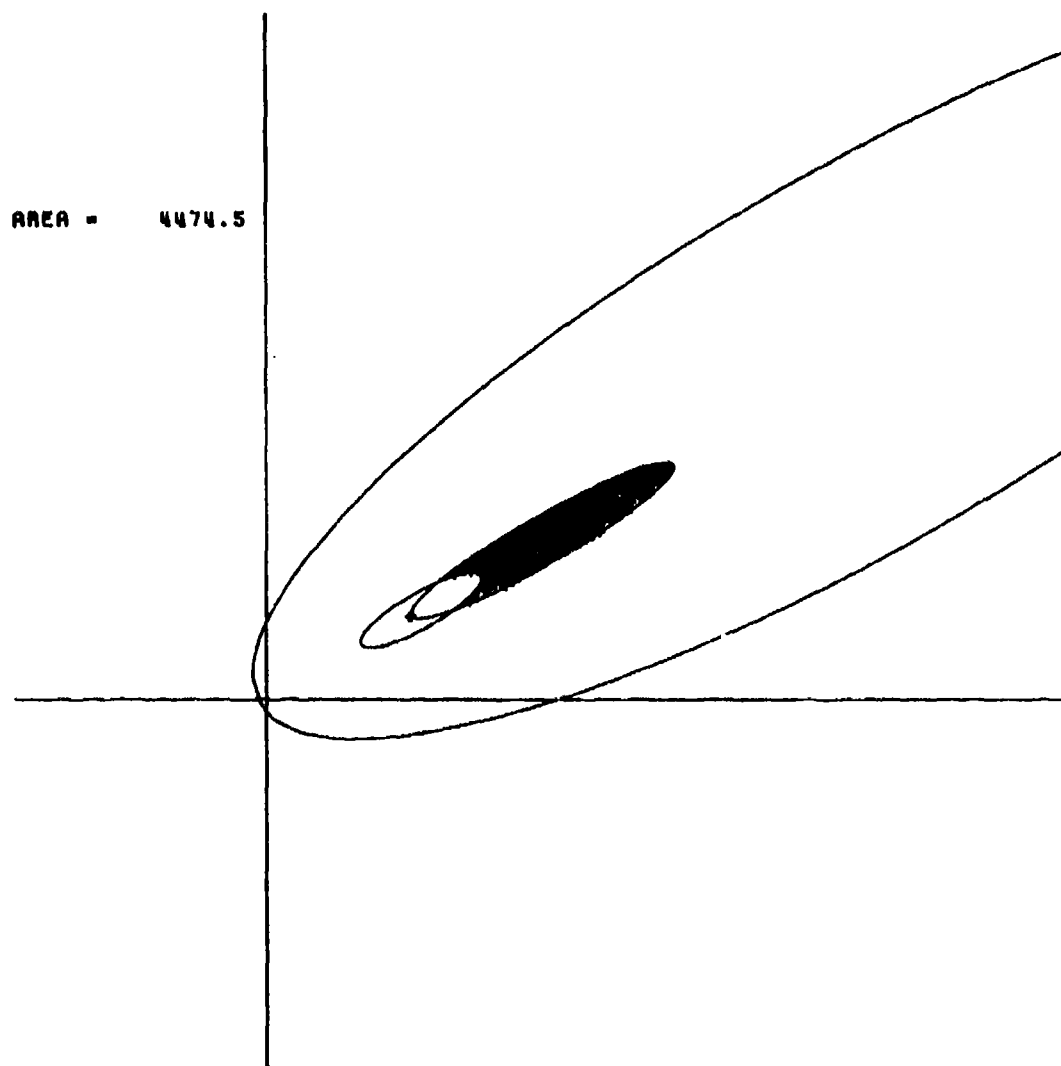


Figure 32. A_{gd} for SCAN = TRACK = 60° ($\phi_s = 0^\circ$)

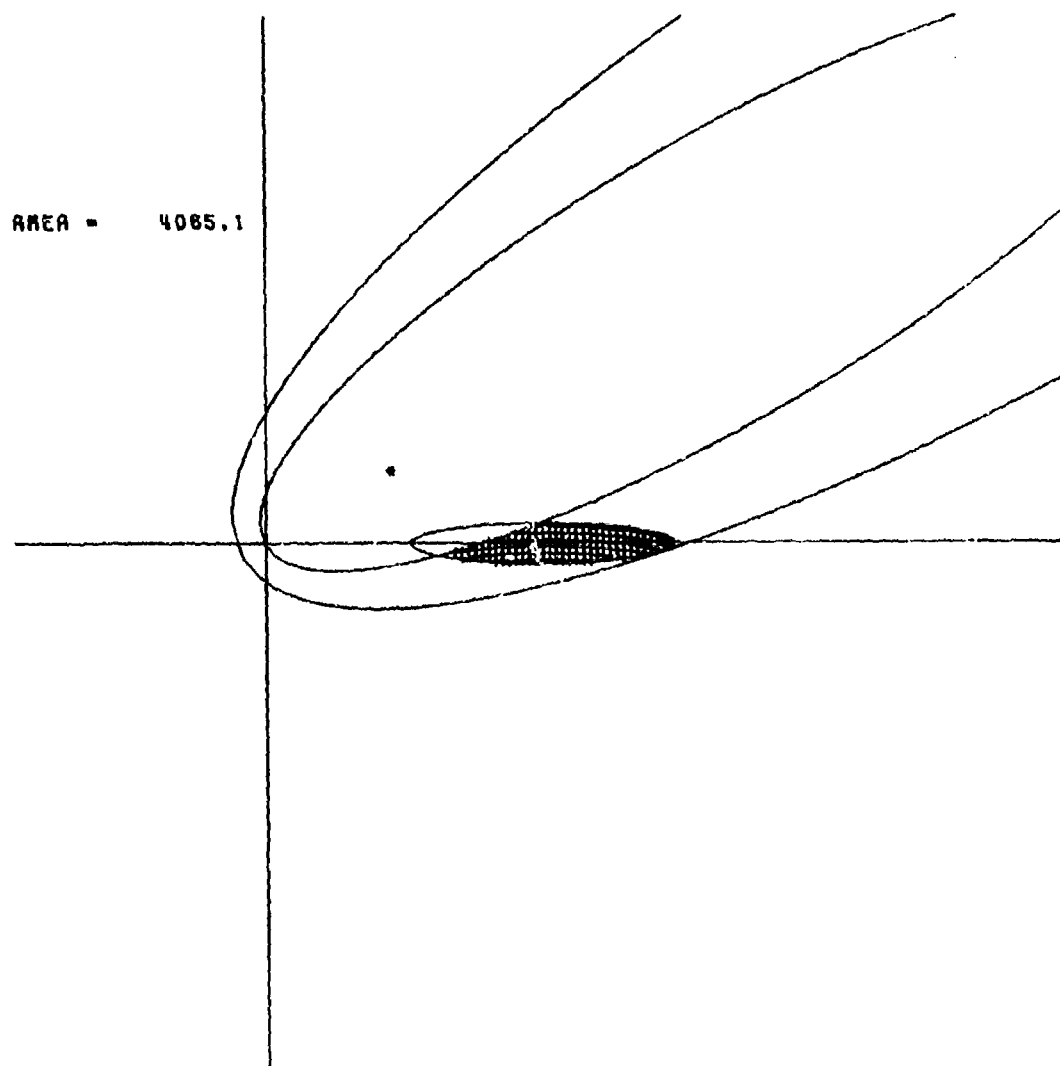


Figure 33. A_{gd} for SCAN = 90° , TRACK = 60° ($\phi_s = 30^\circ$)

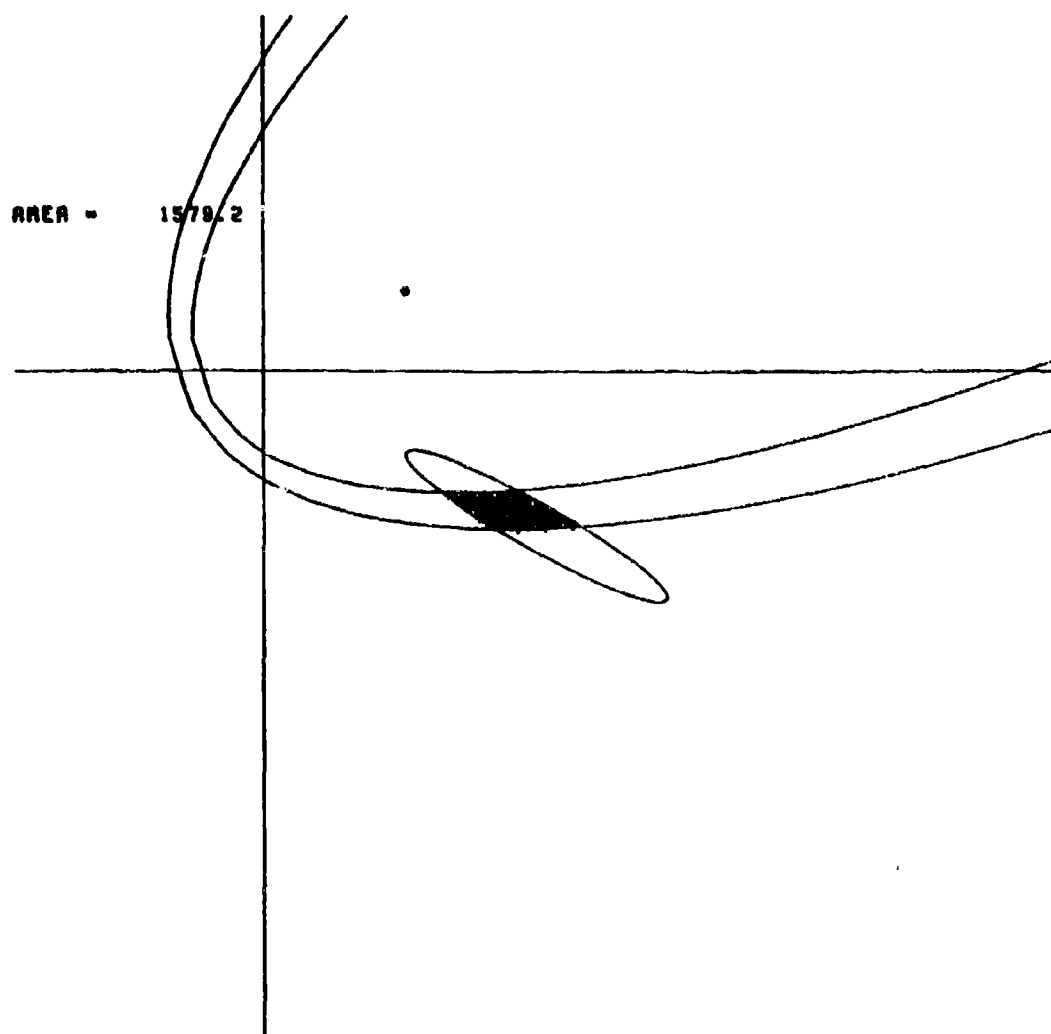


Figure 34. A_{gd} for SCAN = 120° , TRACK = 60° ($\phi_s = 60^\circ$)

RRER = 467.9

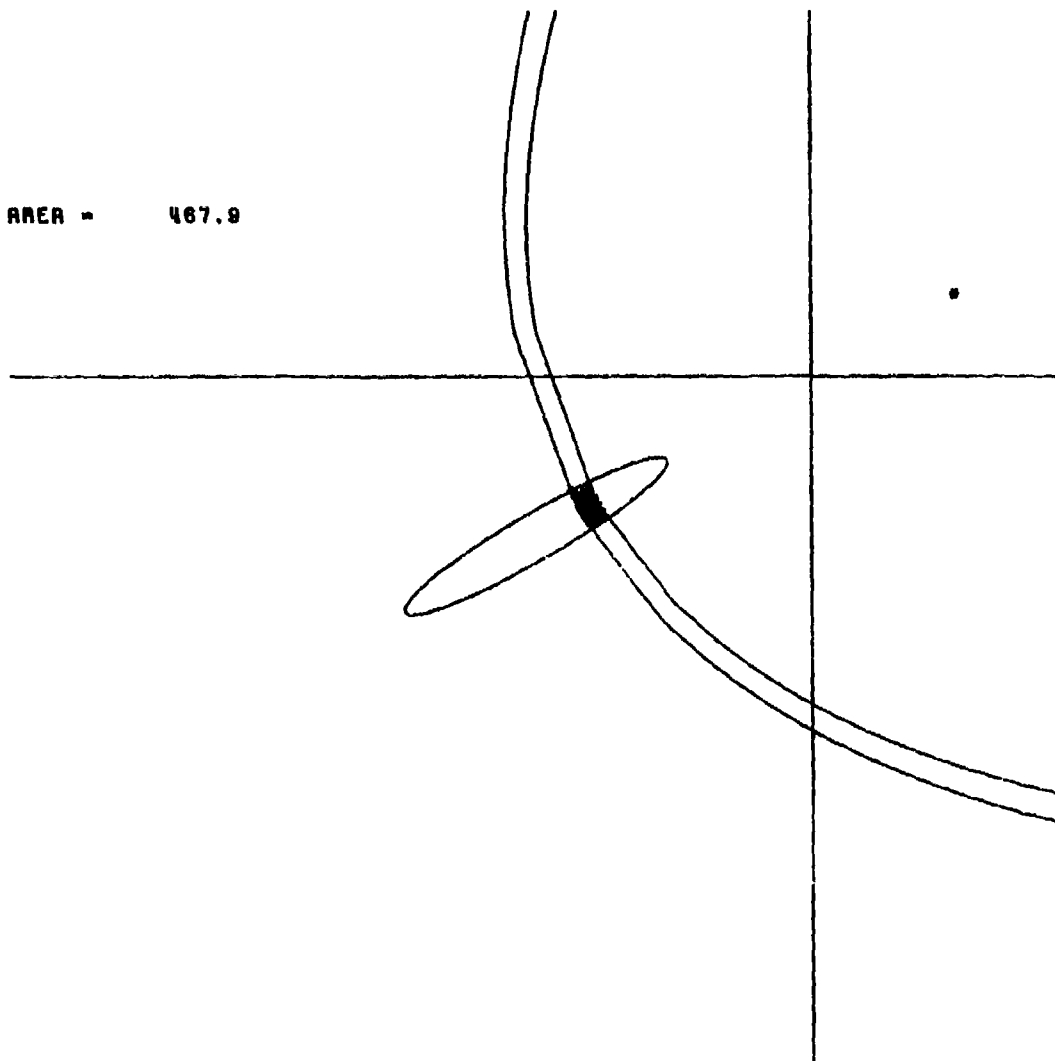


Figure 35. A_{gd} for SCAN = 60° (Back),
TRACK = 60° ($\phi_s = 180^\circ$)

AREA - 814.2

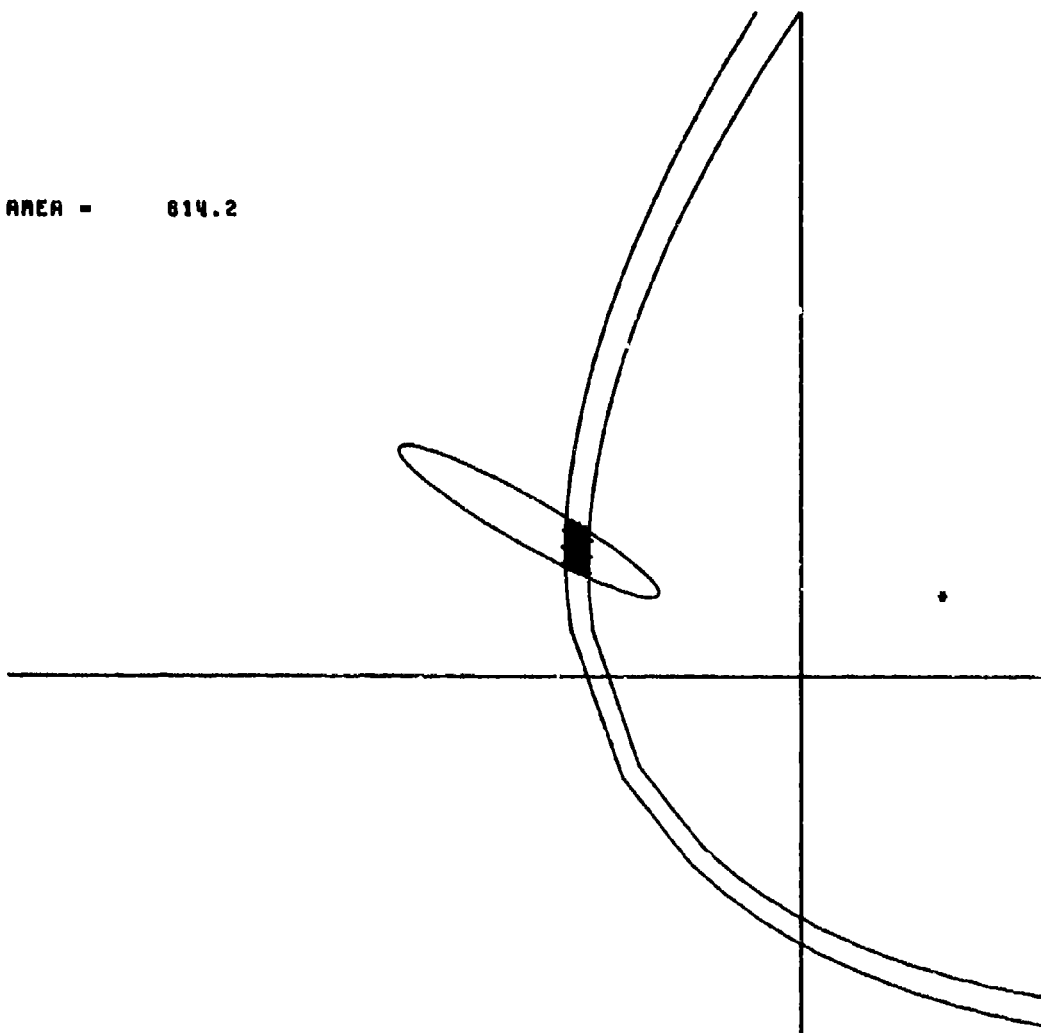


Figure 36. A_{gd} for SCAN = 120° (Back),
TRACK = 60° ($\phi_s = 120^\circ$)

5.6 DATA PROCESSING: $\bar{\sigma}_0$ VS AZIMUTH ϕ_s

Digitization and processing of the measured data are accomplished in three phases. The first phase is the conversion of analog signals to digital format, in which received power is averaged over a fixed number of pulses. These power digitizations are then converted into dBm output versus SCAN and TRACK angles on the basis of fixed power and angle calibrations for the 3 and 23 cm wavelengths.

Simultaneously, or perhaps somewhat in advance of the first phase, a second phase is carried out to compute values of the dimensionless product KI as a function of the SCAN and TRACK angles for both the 3 and 23 cm wavelengths. These results are thus available for hand calculations of σ_0 as soon as the first measured data are obtained. They serve both to check the data quality from initial passes and as a standard against which to compare later (high-speed) digital processing of the data.

The third phase is the preparation of an interface program to connect the first and second phases. Thus, the resulting program permits automatic processing, proceeding directly from recordings of raw data to the average value of terrain radar cross section per unit area, $\bar{\sigma}_0$, as a function of azimuth angle ϕ_s for fixed scattering angle θ_s and nominally fixed incidence angle θ_i . Details of these computer programs are given in Appendix D.

As a final modification of the data, a transmitter illumination correction is computed from flight information recorded during a pass. Since this correction is equivalent to a change in the transmitter antenna gain, it can be easily incorporated at the very end of the data processing procedure as a simple modification of the constant K.

In the following section, the $\bar{\sigma}_0$ results are given for

the various passes of the flights carried out during the program.

5.7 RESULTS: PLOTS OF σ_0 VS ϕ_s OVER A SET OF PARAMETER VALUES

Data are presented in this section for three flights, referred to by their dates as Flights 7/2/76, 7/9/76, and 7/17/76. Each flight consisted of a series of passes, each of which yields a particular parametric situation for elevation angles and distances. A pass is identified by its number in a given flight. Tables 7, 8, and 9 provide complete lists of parameter values for the respective flight dates listed above. For each flight, data are available at two frequencies; these data are referred to by their wavelength values as 23 and 3 cm data. Descriptions of terrain conditions appear in Section 5.8.

The first and second flights (7/2/76 and 7/9/76) were essentially of a check-out and shakedown nature; so, although the resulting data are of interest, discussion of these flights is deferred to the end of this section. The third flight (7/17/76) provides perhaps the most interesting data, since six of the passes can be paired on the basis of the same nominal θ_i and θ_s to yield both forward and backscattering conditions. The pairs are Passes 3 and 9, Passes 4 and 7, and Passes 5 and 6, where the first-mentioned of each pair is the forward scattering configuration. Therefore, the processing of data (Section 5.6) has been arranged so that data from the pairs can be combined, giving in general a portrayal of $\bar{\sigma}_0$ for ϕ_s running all the way from 0° to 180° . Due to physical limitations on SCAN angle, gaps may, in some cases, occur in the $\bar{\sigma}_0$ values near $\phi_s = 90^\circ$; in other cases, overlapping points may arise from the forward and backscattering passes.

5.7.1 FLIGHT 7/17/76

Figures 37 and 38 show $\bar{\sigma}_o$ vs ϕ_s as derived from the data of Passes 4 and 7 of Flight 7/17/76 for the 23 cm and 3 cm wavelengths, respectively. The $\bar{\sigma}_o$ results are some 5 to 10 dB higher for the 3 cm wavelength than for the 23 cm wavelength across the entire domain of ϕ_s . The aspect conditions here are 80° for θ_s and nominally 75° for θ_i .

Figures 39 and 40 show $\bar{\sigma}_o$ vs ϕ_s as derived from the data of Passes 5 and 6 of Flight 7/17/76 for the respective wavelengths of 23 and 3 cm. Once again, the 3 cm results are some 5 to 10 dB higher than the 23 cm results across all ϕ_s values. The aspect conditions here are 80° for θ_s and nominally 70° for θ_i .

Figures 37 and 38 illustrate the case of data overlap, in the vicinity of $\phi_s = 90^\circ$, resulting from the forward and backscattering passes. Figures 39 and 40 illustrate the case of a gap in the data in the neighborhood of $\phi_s = 90^\circ$.

Figures 41 and 42 show $\bar{\sigma}_o$ vs ϕ_s as derived from the data of Passes 3 and 9 of Flight 7/17/76 for the respective wavelengths of 23 and 3 cm. Here, the results are somewhat more difficult to compare. For the small values of ϕ_s , the $\bar{\sigma}_o$ values for 23 and 3 cm differ little; but, as ϕ_s increases to its mid-range, the 23 cm $\bar{\sigma}_o$ values fall rapidly while the 3 cm values change very little, resulting in the latter becoming some 10 to 20 dB greater than the former. Then, as ϕ_s approaches 180° , the 23 cm and 3 cm $\bar{\sigma}_o$ values again approach each other, the latter being only 2 to 4 dB greater than the former. The aspect conditions for Passes 3 and 9 were 80° for θ_s and nominally 80° for θ_i . For these conditions, the specular point is within or very near to being within the illuminated area A_{gd} . As a result, $\bar{\sigma}_o$ is no doubt much higher near $\phi_s = 0$ than it was for Passes 4

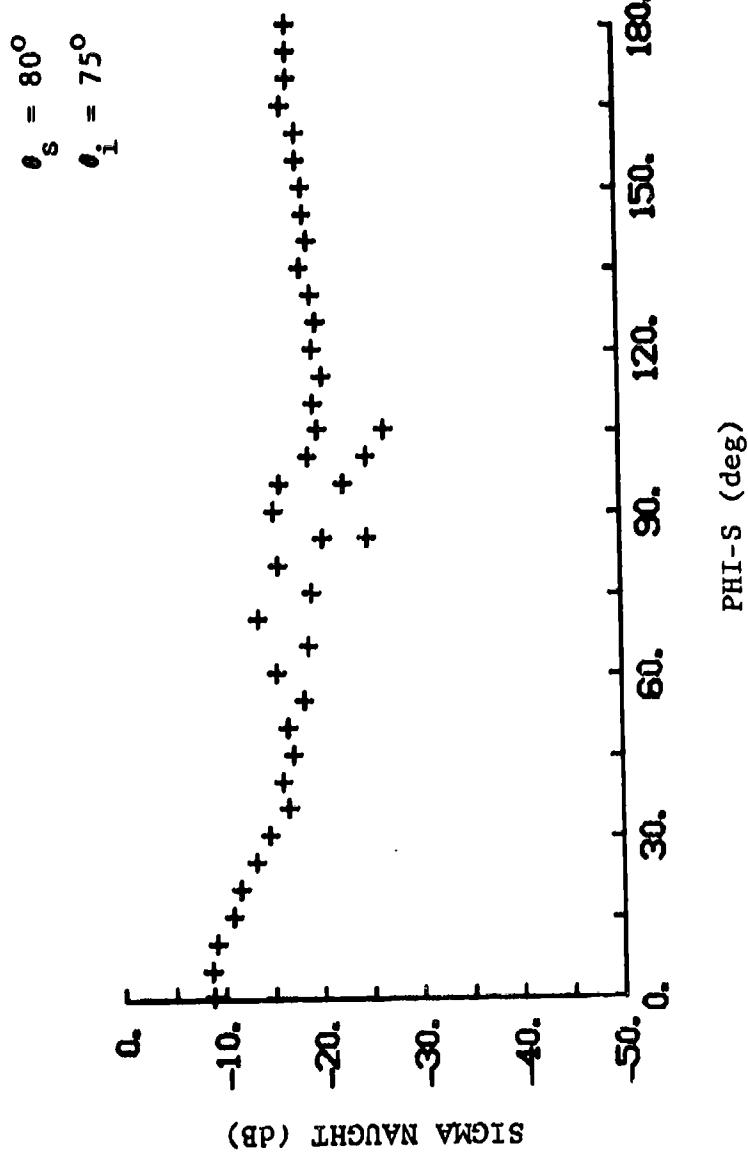


Figure 37. $\bar{\sigma}_o$ vs. ϕ_s for Passes 4 and 7, Flight 7/17/76, at 23 cm

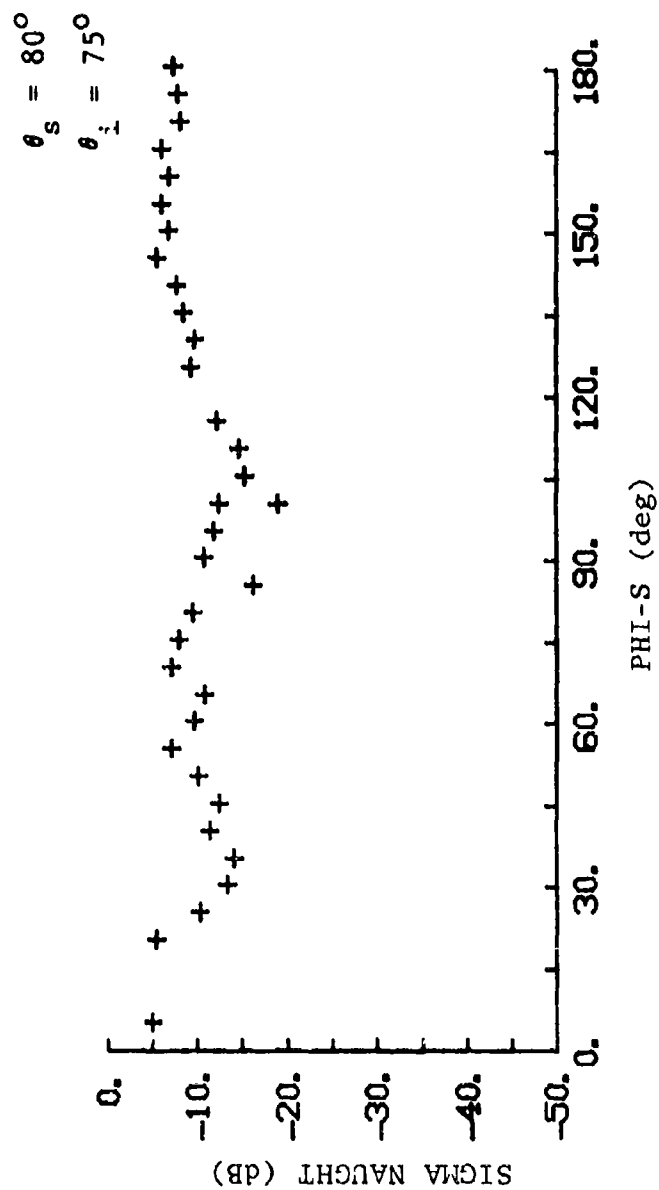


Figure 38. $\bar{\sigma}_o$ vs. ϕ_s for Passes 4 and 7, Flight 7/17/76, at 3 cm

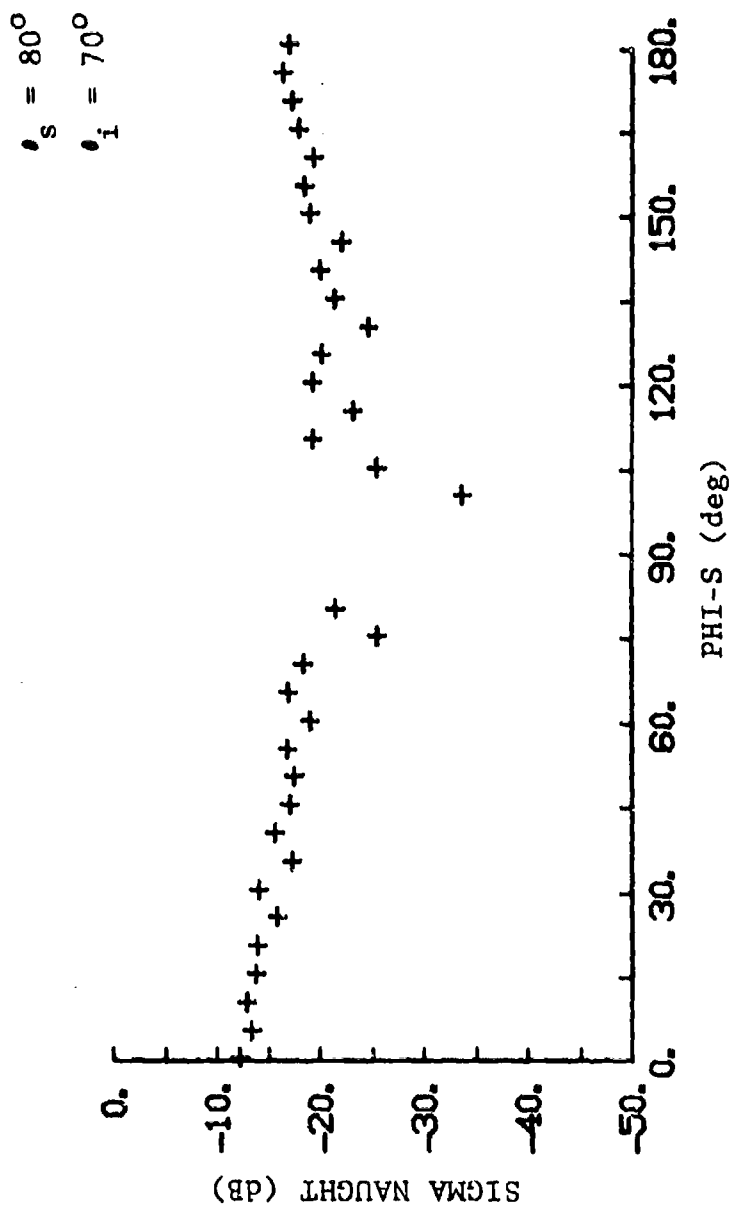


Figure 39. $\bar{\sigma}_0$ vs. ϕ_s for Passes 5 and 6, Flight 7/17/76, at 23 cm

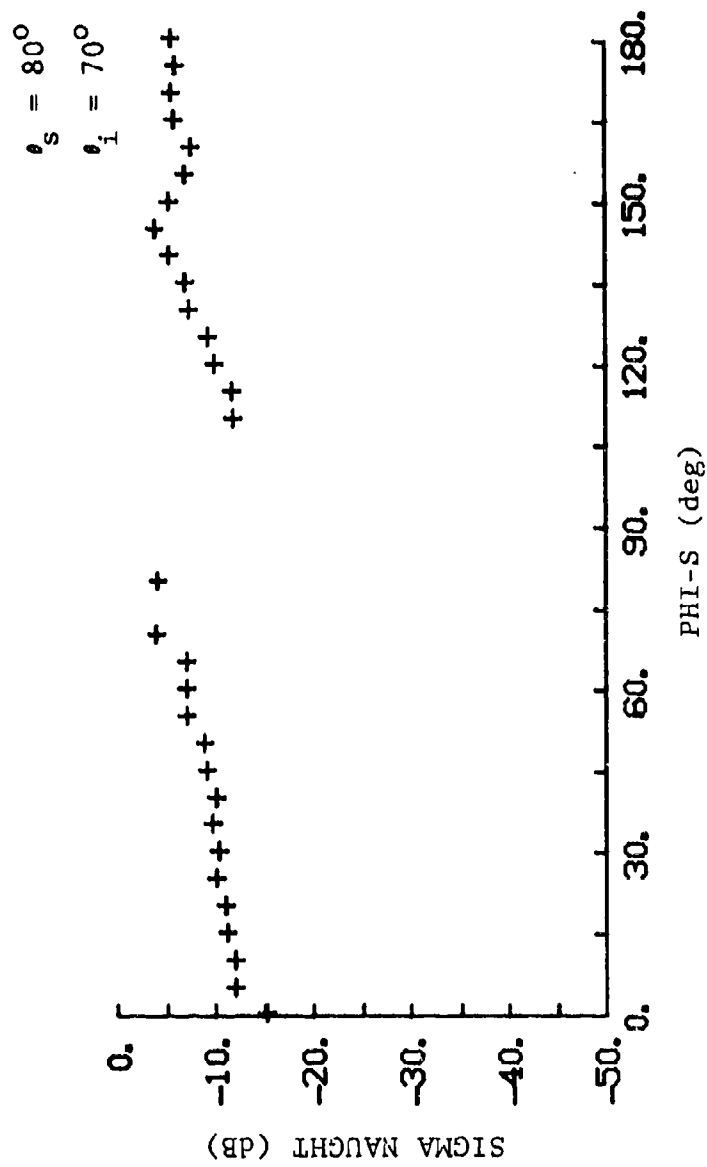


Figure 40. $\bar{\sigma}_0$ vs. ϕ_s for Passes 5 and 6, Flight 7/17/76, at 3 cm

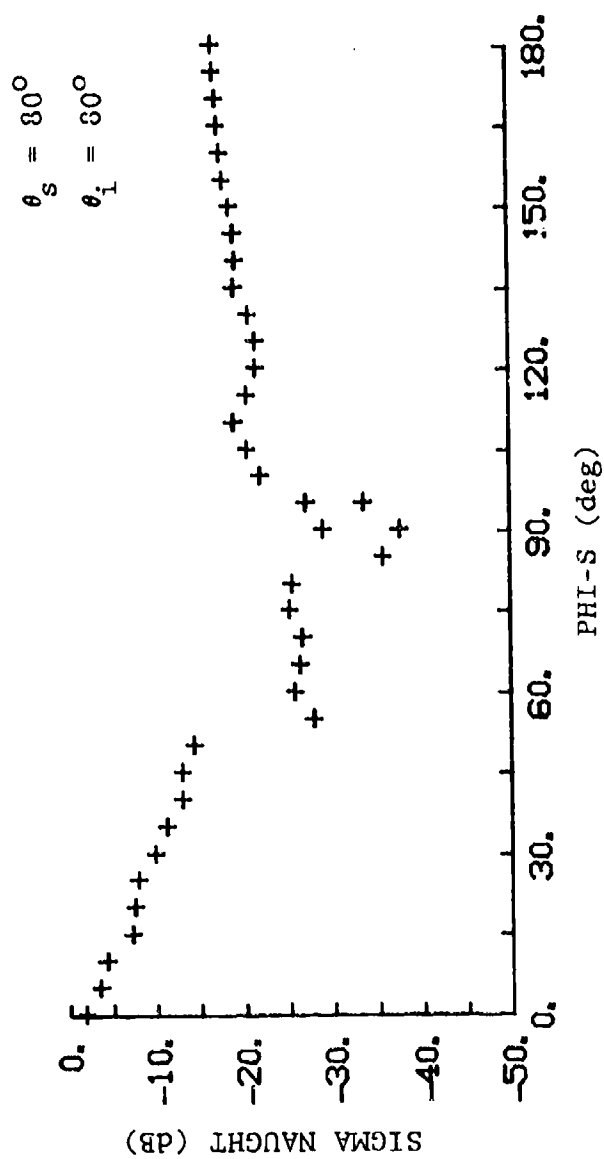


Figure 41. $\bar{\sigma}_0$ vs. ϕ_s for Passes 3 and 9, Flight 7/17/76, at 23 cm

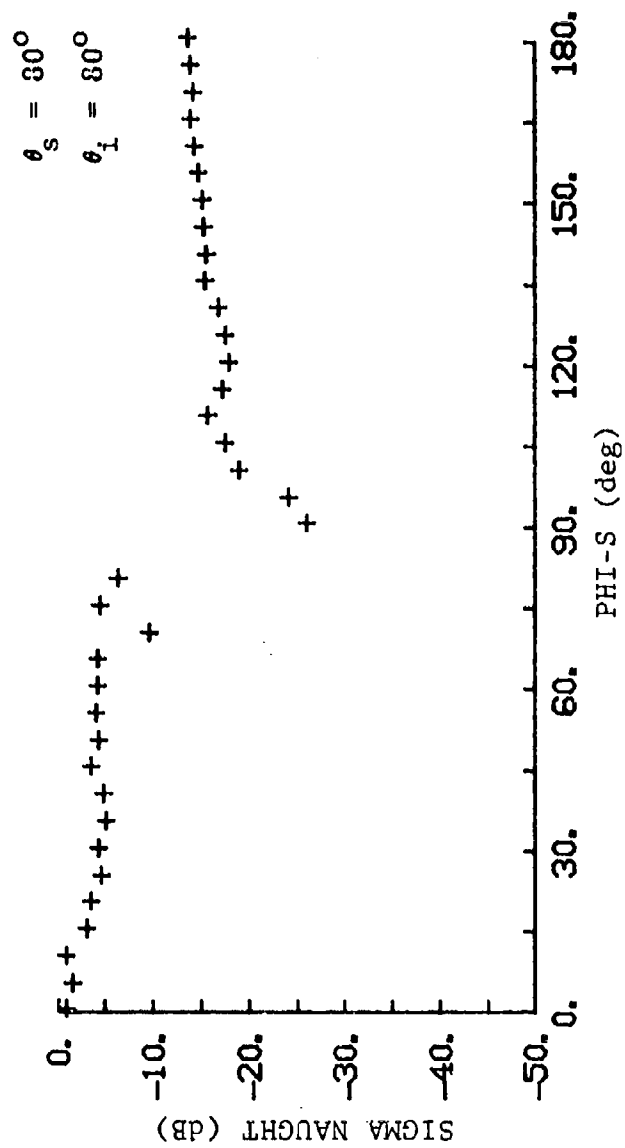


Figure 42. $\bar{\sigma}_o$ vs. ϕ_s for Passes 3 and 9, Flight 7/17/76, at 3 cm

and 7 and Passes 5 and 6 where the specular point is gated out by limiting range ellipses*. Thus, for the 23 cm data, it can be seen that a much more rapid fall-off of $\bar{\sigma}_0$ occurs as ϕ_s increases from 0° than in the data of Figures 37 or 39. However, this particular phenomenon is not present for the 3 cm $\bar{\sigma}_0$ results, since the degree of surface roughness at the 3 cm wavelength apparently mitigates the effect of the specular point in the illuminated area A_{gd} .

As is noted above, the three pairs of passes (4,7), (5,6), and (3,9) provide data at three nominally different values of θ_i , for fixed θ_s . In spite of this small number of incidence angles, it is tempting to fix the azimuth ϕ_s at various values and look at $\bar{\sigma}_0$ vs θ_i . Although it is dangerous to attempt firm conclusions concerning the behavior of $\bar{\sigma}_0$ as a function of incidence angle for such a small number of points, certain observations are in order.

Figure 43 shows six plots of $\bar{\sigma}_0$ vs θ_i , where θ_i takes only the values 70° , 75° , and 80° . The scattering angle is fixed at $\theta_s = 80^\circ$ for four of the plots and at $\theta_s = 70^\circ$ for the remaining two. The azimuth values are chosen to be $\phi_s = 0^\circ$, 45° , 90° , 135° , and 180° , the latter two being the only applicable ones for $\theta_s = 70^\circ$.

In Figure 43a, the very interesting behavior of the $\phi_s = 0^\circ$ data from Passes 3, 4, and 5 immediately attracts the attention. These data certainly increase steadily as θ_i approaches equality with θ_s , in keeping with the fact that the specular point approaches the receiver antenna footprint center as these two angles approach equality. The $\phi_s = 180^\circ$ data at $\theta_s = 80^\circ$ in Figure 43b are not too different in behavior and magnitude from those at $\theta_s = 70^\circ$ in

*These ellipses are discussed in Section 5.4.

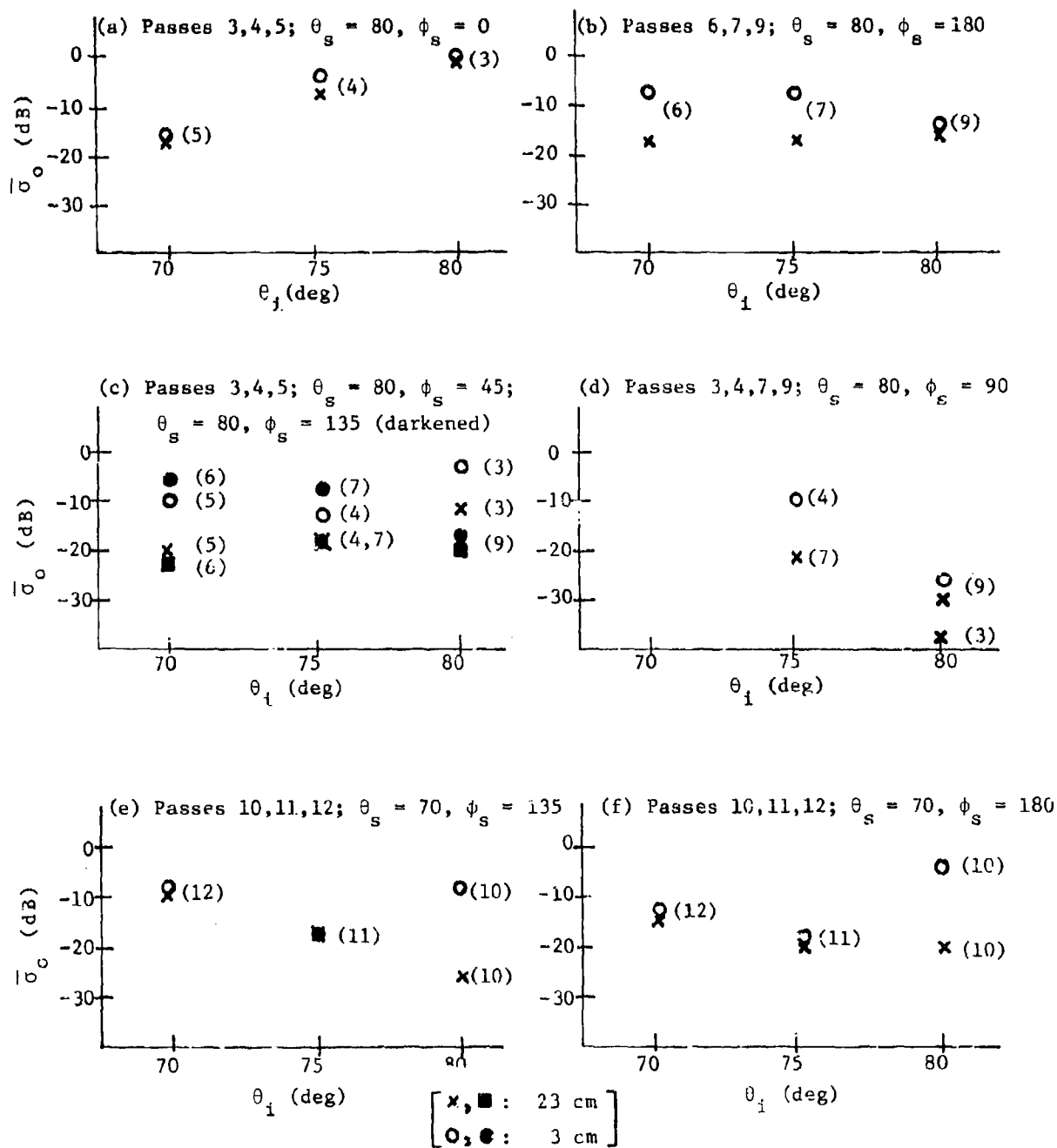


Figure 43. $\bar{\sigma}_o$ vs. θ_i for Flight 7/17/76

Figure 43f, aside from one rather high value at the 3 cm wavelength from Pass 10. Figure 43c shows a comparison between data for $\phi_s = 45^\circ$ and data for $\phi_s = 135^\circ$. The two sets are not markedly different. Finally, it should be noted that the 3 cm data in all cases range from 0 to 20 dB above the corresponding 23 cm data.

In Section 5.5, it was concluded that the log-normal distribution should be considered as a leading candidate to describe the behavior of σ_o . Realizing that a statistically rigorous determination of the distribution of σ_o cannot be made from the small number of samples available at any fixed set of parameter values, it is still tempting to compare the scatter of σ_o values with a typical standard deviation of a log-normal distribution. This comparison is made in Figure 44, using $\bar{\sigma}_o$ as the mean and $s = 5$ dB as the log-normal standard deviation. (The comparison is not exactly appropriate, since the parameter ϕ_s is permitted to vary rather than to be held fixed.) The figure shows that approximately 66% of the σ_o values lie within one standard deviation of $\bar{\sigma}_o$.

In anticipation of the next subsection, a comparison can be made between $\bar{\sigma}_o$ for Pass 7 of Flight 7/9/76 and $\bar{\sigma}_o$ for Pass 3 of Flight 7/17/76 at the 3 cm wavelength. The incidence and scattering angles for these two passes are quite similar; $\theta_s = 85^\circ$ and $\theta_i = 83^\circ$ for the former while $\theta_s = 80^\circ$ and $\theta_i = 80^\circ$ for the latter. However, the terrain conditions examined by the two passes are quite different. For pass 7, the terrain consisted of partly concrete apron and partly short grass. For Pass 3, the terrain consisted of tall weeds and scrub trees. In other words, the latter was much the rougher (at the 3 cm wavelength) of the two terrain regions. Figure 45 shows the comparison between $\bar{\sigma}_o$ values for the two passes. Clearly, the $\bar{\sigma}_o$ values for the smooth terrain (Pass 7) are some 10 dB or more lower than

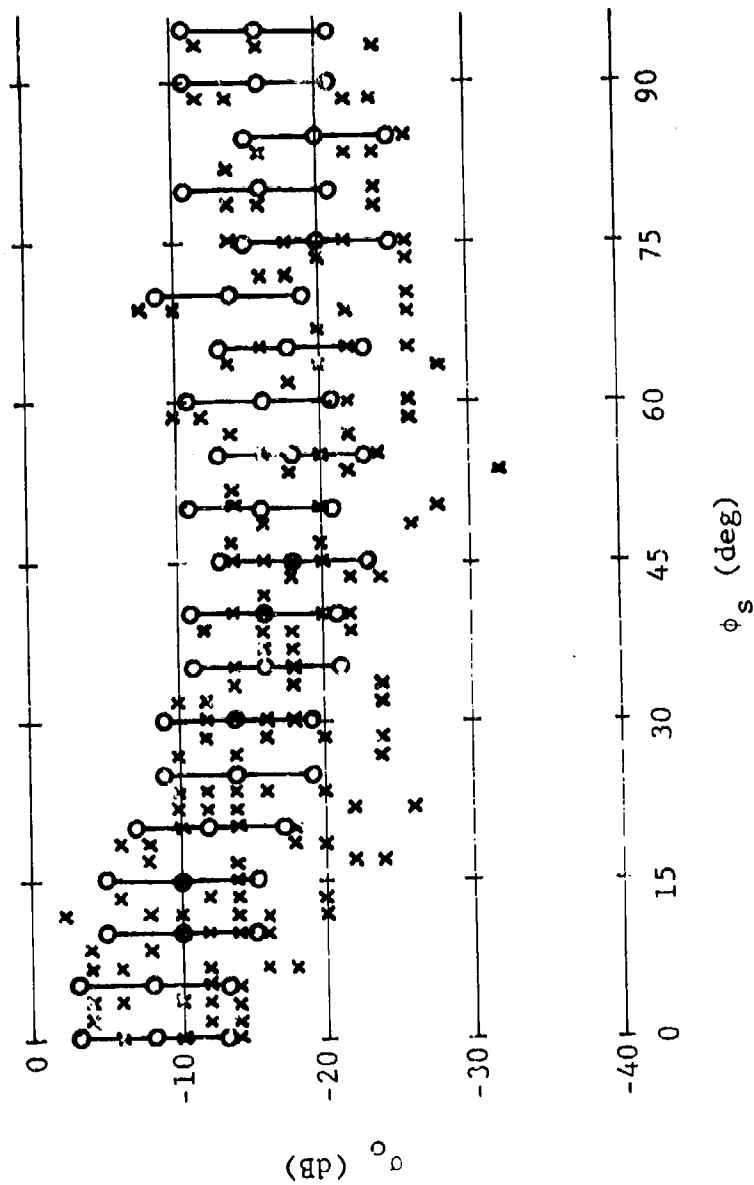


Figure 44. Comparison of σ_0 Scatter with One Standard Deviation about σ_0 Using Log-Normal Distribution of σ_0

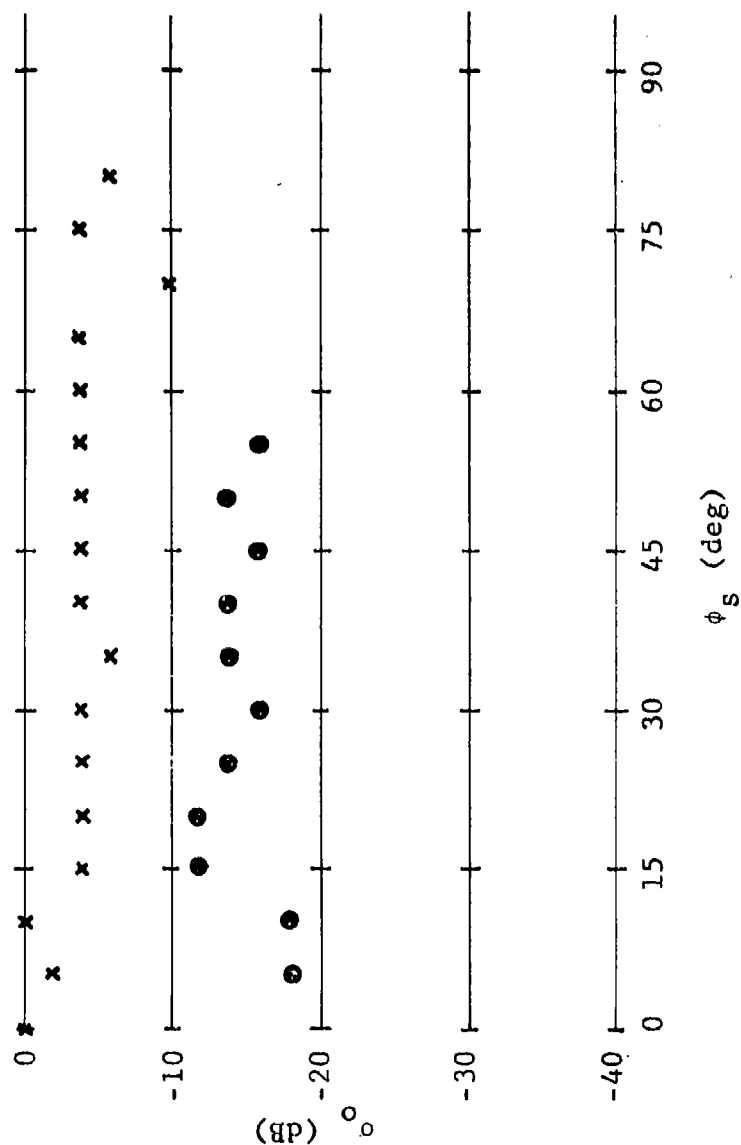


Figure 45. Comparison, at 3 cm, of σ_0 from Pass 3, Flight 7/17/76, with σ_0 from Pass 7, Flight 7/9/76 (Latter Data Circled)

the $\bar{\sigma}_0$ values for the rough terrain, over the entire range of ϕ_s for which the data are comparable ($0 \leq \phi_s \leq 55^\circ$).

A second comparison of data for these two flights is possible for the 23 cm wavelength. Here, however data are taken from the last half of each of the passes*. Figure 46 shows the comparison. Once again, it is seen that the Pass 7 data fall 10 dB or more below the Pass 3 data. An exception to this situation occurs in the vicinity of $\phi_s = 60^\circ$ where the Pass 7 data increase in magnitude. It is possible that this increase in magnitude of $\bar{\sigma}_0$ can be ascribed to an aircraft which taxied into the illuminated area during the pass. Its presence for 23 cm and not for 3 cm may result from the dominant scattering return from the aircraft being of the traveling wave type.

Comparisons can also be made between some of the subject data of this program and data recorded some years ago by Ohio State University researchers. Conditions are by no means the same for the two sets of data, yet it may be appropriate to compare those terrain conditions for which the ratio of vegetation size to wavelength is similar. For example, the Environmental Research Institute of Michigan's 23 cm data from Passes 3 and 12 of Flight 7/17/76 were recorded for terrain covered with 4 ft weeds and brush. On the other hand, some of the OSU data [13] were recorded for

-
13. R.L. Cosgriff, W.H. Peake, and R.C. Taylor, Terrain Scattering Properties for Sensor System Design (Terrain Handbook II), Engineering Experiment Station Bulletin No. 181, Ohio State University, Columbus, May 1960.

*Section 5.8 explains the reasons for giving special consideration to the first half and the last half of the data recorded during a pass, in addition to an analysis of all of the data recorded during a pass. This section also includes a ground truth characterization.

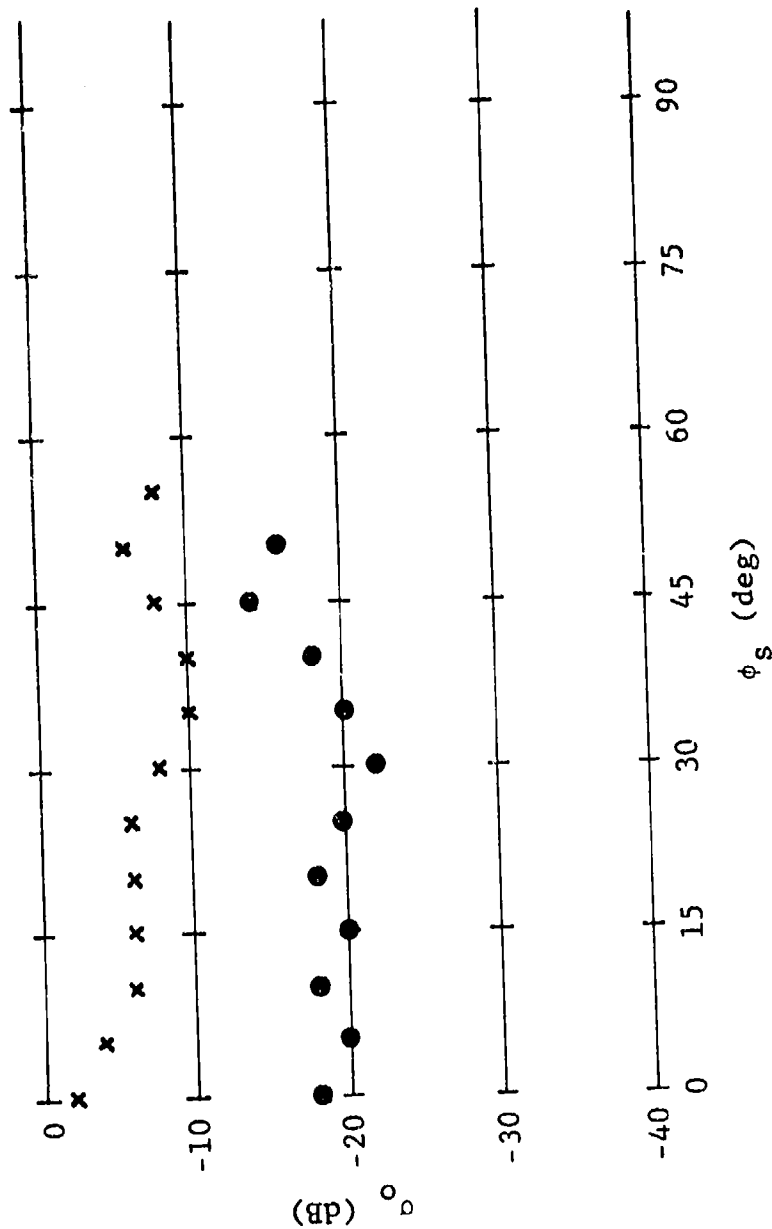


Figure 46. Comparison, at 23 cm, of σ_O from Pass 3, Flight 7/17/76, with σ_O from Pass 7, Flight 7/9/76 (Latter Data Circled)

3 inch green soybeans and 4 inch oats in head (July) at a 3 cm wavelength. Table 19 shows a comparison of these data for $\theta_i = \theta_s = 70^\circ$ (Pass 12) and 80° (Pass 3) as well as for $\phi_s = 180^\circ$. Note that the σ_o values are remarkably close.

A second comparison is possible for a forward scattering situation. In Figure 47, the incidence and scattering angles are equal and the same (80°) for both sets of data. The LRIM data in this figure are taken from Passes 3 and 9 of Flight 7/17/76; they cover 4 ft weeds and brush at the 23 cm wavelength. The OSU data shown [14] are 4 inch soybean foliage at a 3 cm wavelength. Both data sets were collected at horizontal-horizontal polarization. Although the data themselves differ markedly at some aspects, the trends for the two data sets are remarkably similar.

5.7.2 FLIGHT 7/9/76

Figures 48, 49, 50, and 51 show $\bar{\sigma}_o$ vs ϕ_s as derived from Passes 2, 5, 6, and 7 of the 7/9/76 flight. For all of these passes, the scattering angle is fixed at $\theta_s = 85^\circ$ and the incidence angle θ_i has the nominal value of 80° . Since the region of terrain examined is essentially the same for each pass, the data can be grouped to provide a larger number of samples for each of the ϕ_s values of interest. Thus, all data from each of Passes 2, 5, and 7 are grouped to provide $\bar{\sigma}_o$ vs ϕ_s as shown in Figure 48 for 23 cm, and in Figure 49 for 3 cm wavelength. The last half of data from each of Passes 2, 5, 6, and 7 are grouped to yield $\bar{\sigma}_o$ vs ϕ_s as shown in Figure 50 for 23 cm wavelength, and in Figure 51 for 3 cm wavelength.

-
14. S.T. Cost, Measurements of the Bistatic Echo Area of Terrain at X-Band, Report No. 1822-2, Ohio State University Research Foundation, Columbus, May 1965.

TABLE 19. COMPARISON OF ERIM AND OSU
BACKSCATTERING ($\phi_s = 180^\circ$) σ_o DATA

$\theta_i = \theta_s$	Description	Passes	σ_o (dB)
70	ERIM 23 cm data: 4 ft weeds & brush, 7/17/76	12	-18
70	OSU 3 cm data: 3 in. green soybeans		-22
70	OSU 3 cm data: 4 in. oats in head (July)		-20
80	ERIM 23 cm data: 4 ft weeds & brush, 7/17/76	3	-20
80	OSU 3 cm data: 3 in. green soybeans		-26
80	OSU 3 cm data: 4 in. oats in head (July)		-21

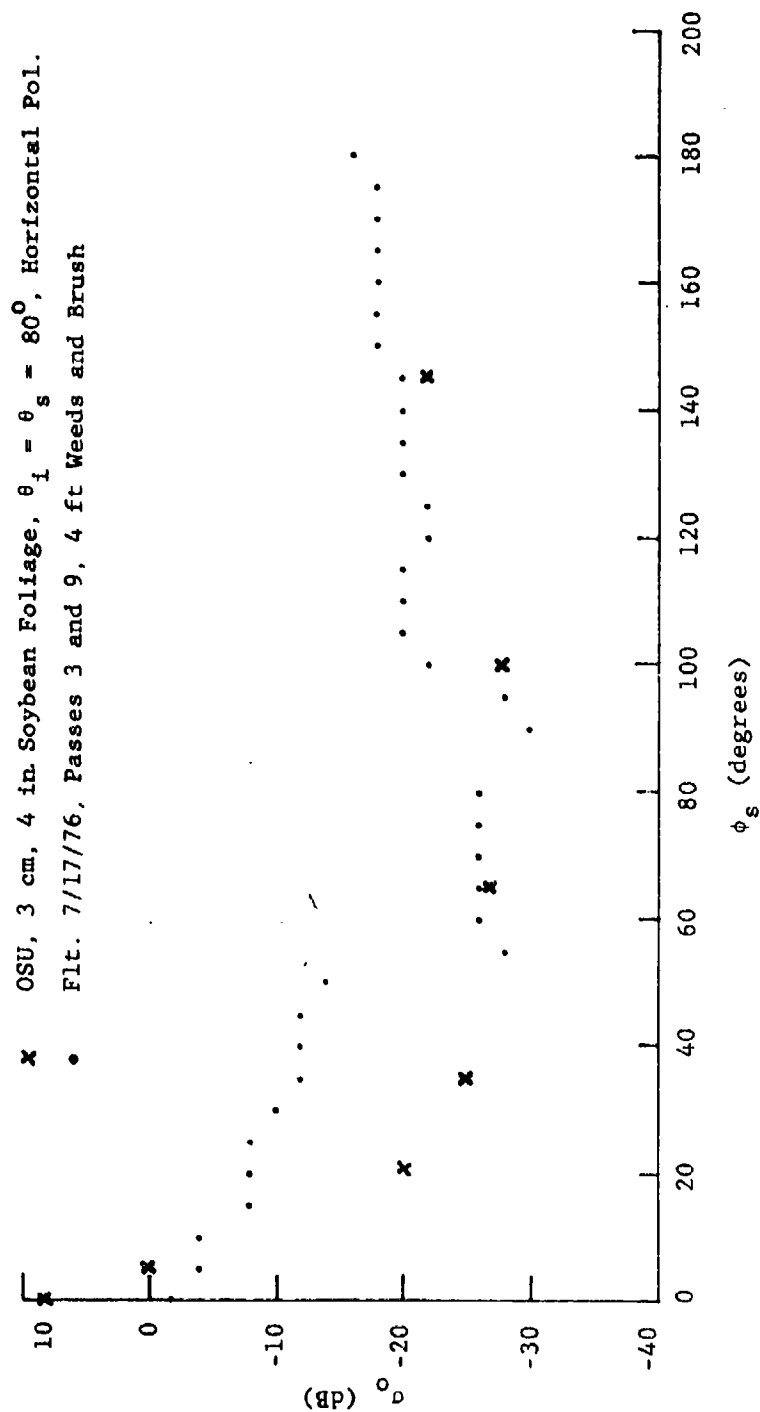


Figure 47. Comparison of ERIM and OSU Data

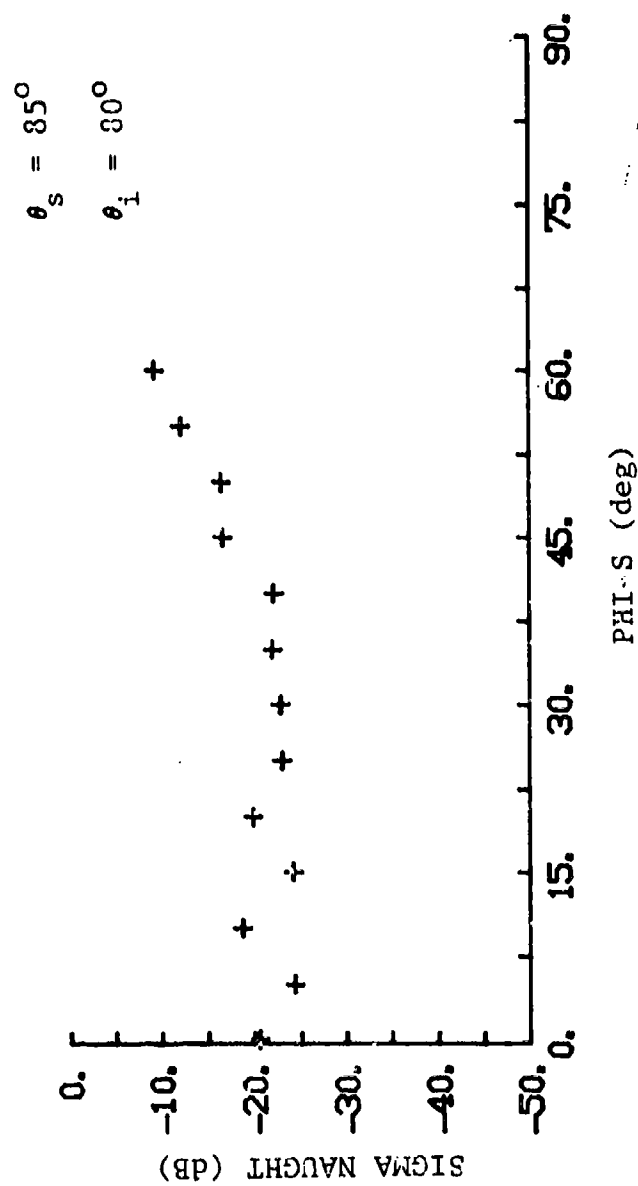


Figure 48. $\bar{\sigma}_0$ vs. ϕ_s for Passes 2, 5, and 7, Flight 7/9/76, at 23 cm (Averages Over All Passes)

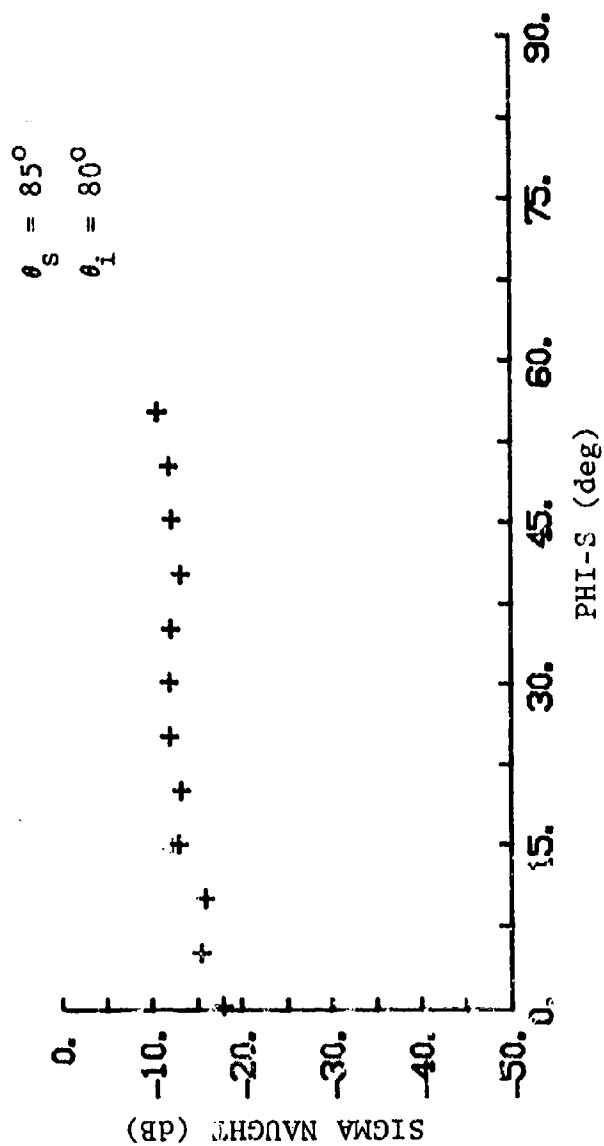


Figure 49. $\bar{\sigma}_o$ vs. ϕ_s for Passes 2, 5, and 7, Flight 7/9/76, at 3 cm (Averages Over All Passes)

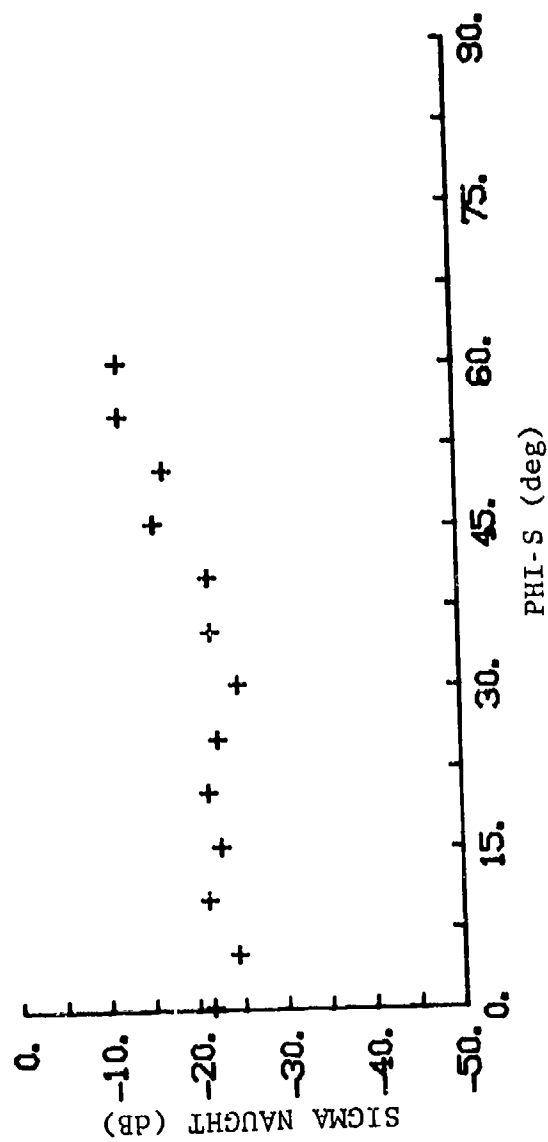


Figure 50. σ_o vs. ϕ_s for Passes 2, 5, 6, and 7, Flight 7/9/76, at 23 cm (Averages Over All Passes)

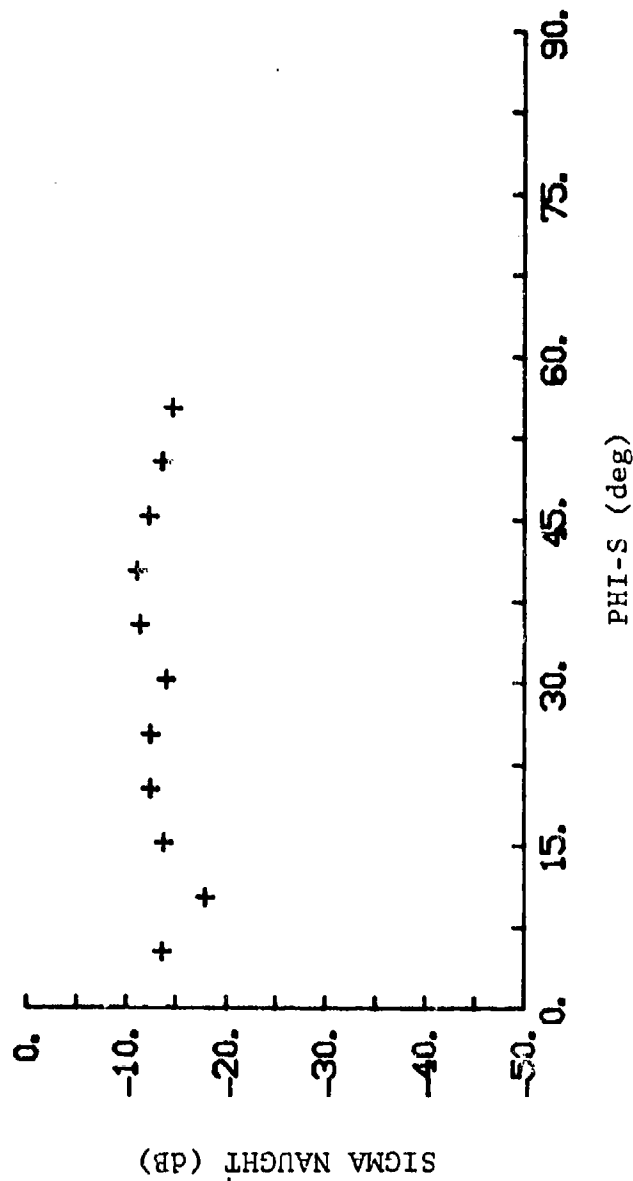


Figure 51. $\bar{\sigma}_o$ vs. ϕ_s for Passes 2, 5, 6, and 7, Flight 7/9/76
at 3 cm (Averages Over All Passes)

To give an idea of the spread of $\bar{\sigma}_0$ values for the passes discussed above, these data have been averaged for each pass and the resulting $\bar{\sigma}_0$ are all plotted on the same graph. Thus, the $\bar{\sigma}_0$ vs ϕ_s values for each of Passes 2, 5, and 7 are plotted in Figure 52 for 23 cm, and in Figure 53 for 3 cm. For each pass, all data were used in finding the averages. The $\bar{\sigma}_0$ vs ϕ_s values for each of Passes 2, 5, 6, and 7 are plotted in Figure 54 for 23 cm and in Figure 55 for 3 cm. Here, only the data from the last half of each pass were used in computing the averages.

5.7.3 FLIGHT 7/2/76

Although the measurements flight of 2 July 1976 was intended primarily for instrumentation verification and procedure evaluation, several passes provided usable data. Only limited data samples are available due to difficulty with the receiving antenna scanning system.

Due to the extensive data obtained from the two succeeding data-gathering flights, the analysis of the 2 July data was given low priority and only preliminary results are available. Examples of preliminary results are given in Figure 56 for 23 cm. As in the case of the 9 July data, the receiving antenna was at a fixed θ_s value of 85° . θ_i values of 66° and 57° were realized during the 2 July flights. The σ_0 values obtained are about 10 dB lower than those obtained for the more nearly grazing angles of Flight 7/9/76. Also, due to the difficulty with the receiving antenna scanning system, data are available from azimuth angles of only 0 to 40 degrees.

The results obtained appear to be consistent, because the scattering patterns would be expected to fall fairly rapidly for the smooth scattering surfaces of Site 1 as the difference between θ_s and θ_i increases.

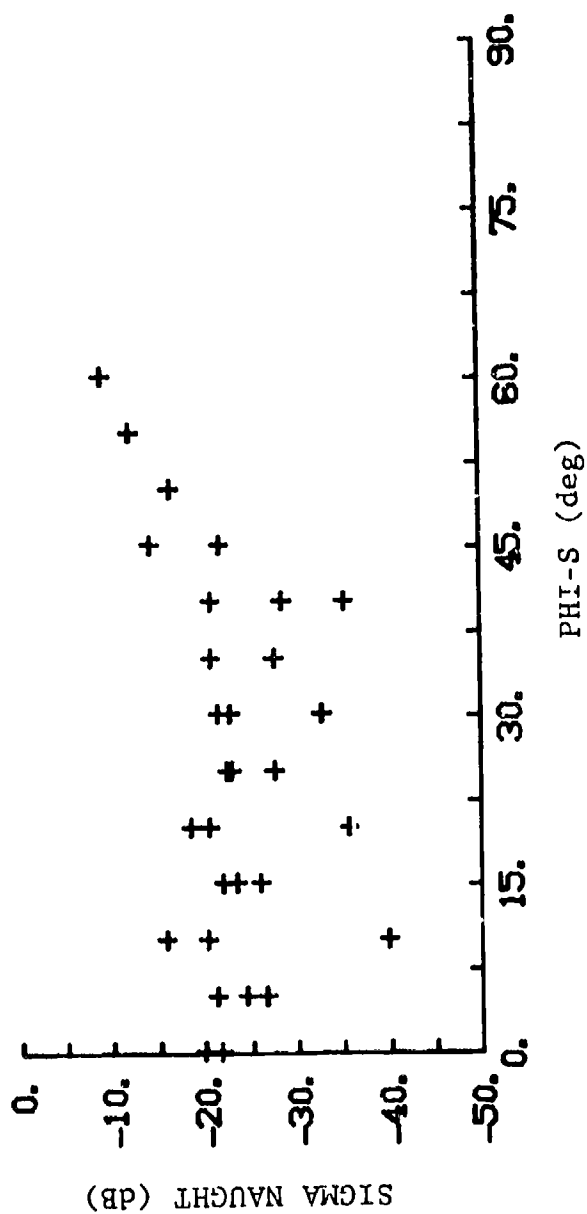


Figure 52. $\bar{\sigma}_0$ vs. ϕ_s for Passes 2, 5, and 7, Flight 7/9/76,
at 23 cm (Separate Averages for Each Pass)

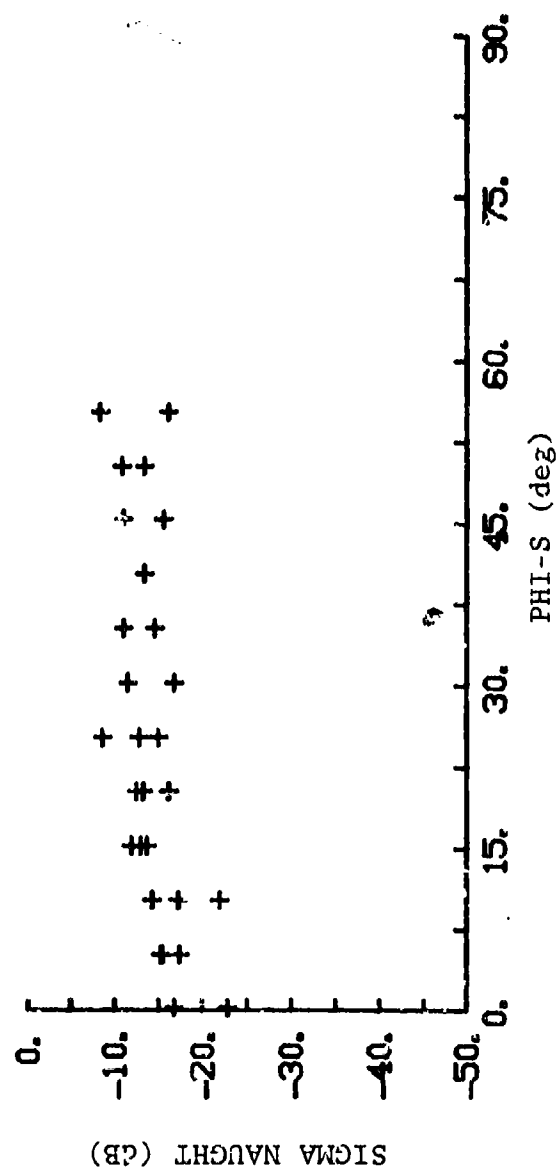


Figure 53. $\bar{\sigma}_0$ vs. ϕ_s for Passes 2, 5, and 7, Flight 7/9/76, at 3 cm (Separate Averages for Each Pass)

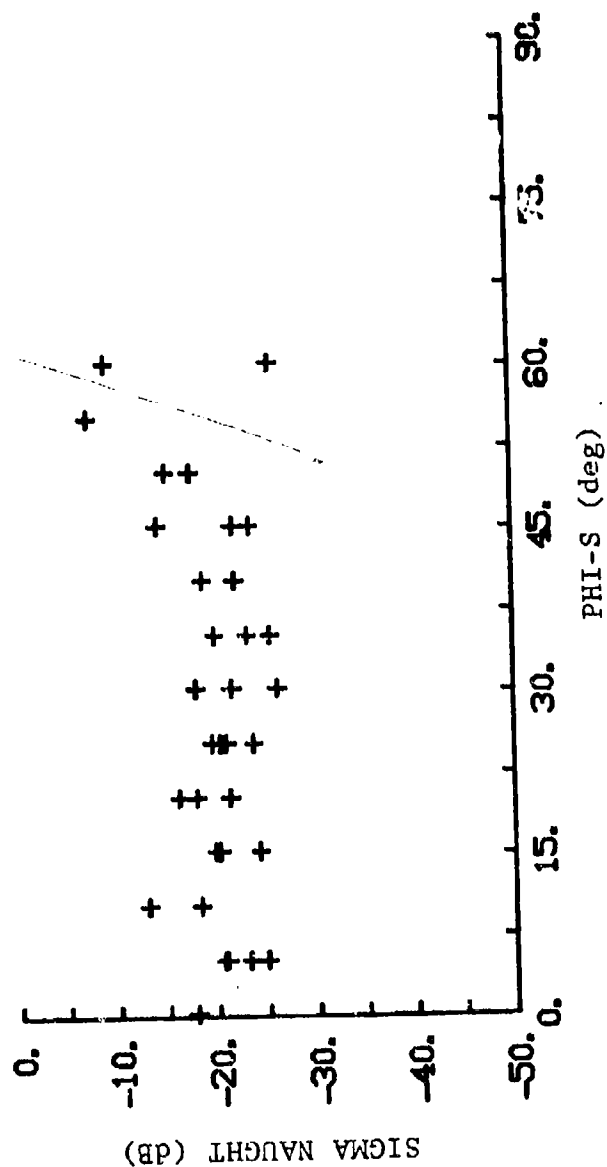


Figure 54. $\bar{\sigma}_0$ vs. ϕ_s for Passes 2, 5, 6, and 7, Flight 7/9/76, at 23 cm (Separate Averages for Each Pass)

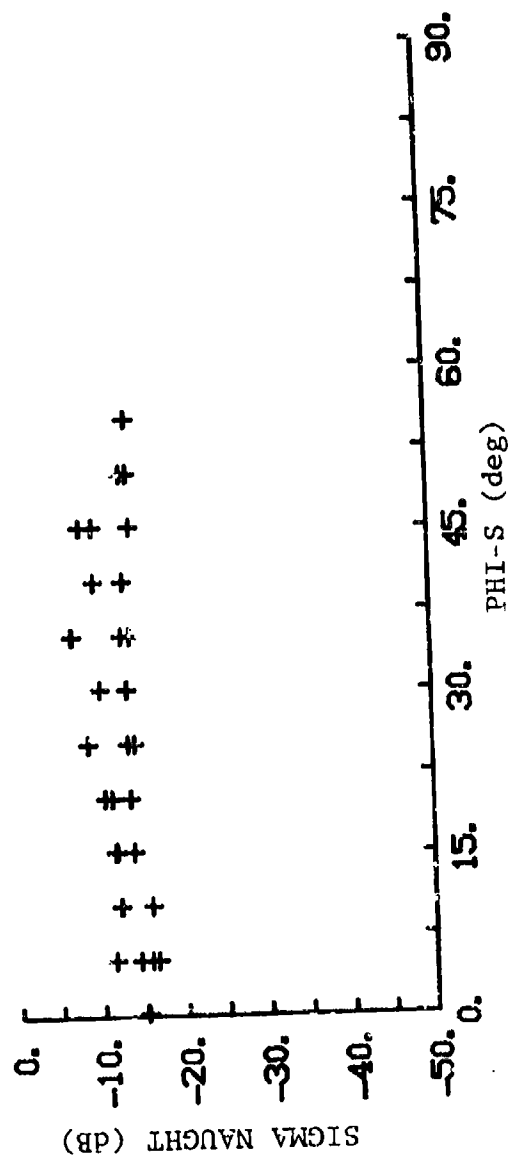


Figure 55. $\bar{\sigma}_0$ vs. ϕ_s for Passes 2, 5, 6, and 7, Flight 7/9/76, at 3 cm (Separate Averages for Each Pass)

PRELIMINARY RESULTS

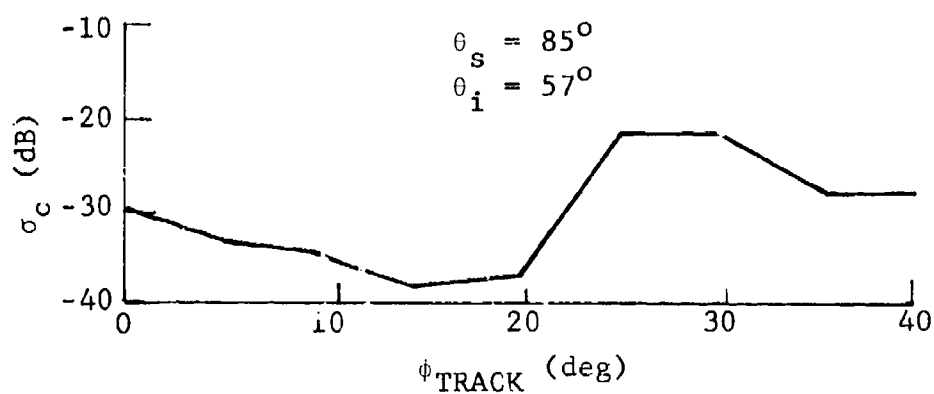
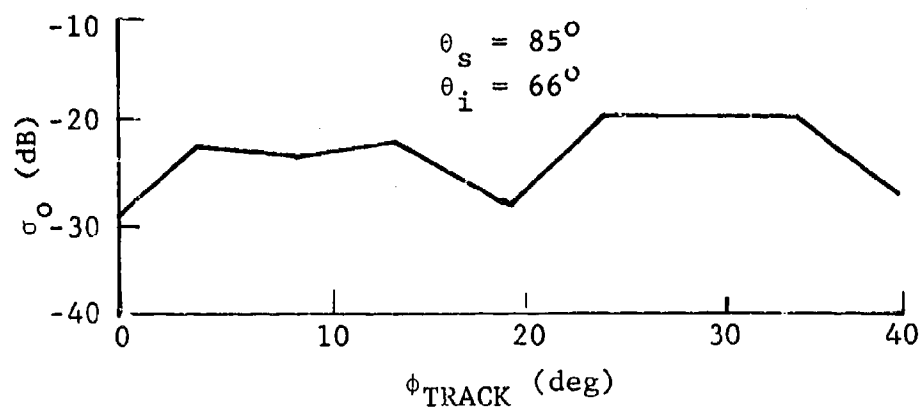


Figure 56. σ_o vs. ϕ_{TRACK} for Site 1, Flight 7/2/76, and $\lambda = 23$ cm

5.8 SUMMARY OF EXPERIMENTAL CONDITIONS AND RESULTS

The values of bistatic σ_0 obtained in this experiment are in general agreement with previous measurements, although the existing data base is very limited (Section 5.7.1). Since only a small subset of the total matrix of bistatic angles is covered in the present program, additional measurements will be necessary to obtain a complete measure of bistatic scattering characteristics. Two terrain types were measured: (1) smooth grassy terrain including cement ramp areas and (2) tall weeds with scrub trees. A summary of the terrain types and conditions existing during the measurements is given in Table 20. See also Figures 57 through 61. A summary of all digitized bistatic data is given in Table 21.

5.8.1 SYSTEM OPERATION

Instrumentation problems were encountered during the first test and data gathering flight on 2 July 1976. These problems resulted from wind loading on the receiving antenna servo drive system. As a result, the data were obtained with the receiving antenna at a fixed azimuth angle of 88° (viewing toward 268°). The servo motor was replaced and, on the two subsequent data-gathering operations (7/9/76 and 7/17/76), the antenna system functioned satisfactorily. Some delays in operation were experienced due to high wind conditions, however.

For the first and second data-gathering operations, the receiving antennas were mounted on the ERIM hangar building at a height of 45 ft above ground. During the third and final data-gathering flight, the antennas were mounted on a crane and raised to a height of 100 ft (Figure 2).

TABLE 20. DESCRIPTION OF TEST AREAS

<u>Date</u>	<u>Test Site</u>	<u>Terrain</u>	<u>Weather</u>	<u>Wind (kts)</u>	<u>Photographs</u>
7/2/76	1	Fla. grass, ramp, roughness scale: rms < 4 in.	Dry, before and during measure- ments	15-20	Figures 57, 58 and 59
7/9/76	1	Flat grass, ramp, roughness scale: rms < 4 in.	Dry	light to 10	Figures 57, 58 and 59
7/17/76	2	Tall weeds, 3 ft. to 4 ft; scrub trees 6 ft to 8 ft; ground be- neath, roughness scale: rms < 0.5 ft. p-p 1 ft.	Dry weeds (very dry for top 1/3 of height	light to 10	Figures 60 and 61



Figure 57. View from Receiving Antenna at Site 1



Figure 58. View of Grassy Area at Site 1



Figure 59. Close-Up View of Grass at Site 1



Figure 60. View from Base of 100 ft Tower at Site 2



Figure 61. Close-Up View of Weeds at Site 2

TABLE 21. SUMMARY OF DIGITIZED BISTATIC DATA

<u>Flight</u>	<u>Pass</u>	<u>CCT-File</u>	<u>Track Angle (TRACK)</u>		<u>Site No.</u>
			<u>Start (deg)</u>	<u>End (deg)</u>	
7/2/76	4	19 - 2	73	111	1
	5	19 - 3	68	100	
	6	19 - 4	61	96	
	8	19 - 5	74	107	
	10	19 - 7	77	115	
7/9/76	2	18 - 2	51	112	1
	5	18 - 3	78	94	
	6	18 - 4	47	130	
	7	18 - 5	48	132	
7/17/76	3	16 - 2	47	174	2
	4	11 - 2	49	111	
	5	11 - 3	71	140	
	6	11 - 4	49	145	
	7	11 - 5	48	141	
	9	16 - 3	41	150	
	10	16 - 4	48	150	
	11	16 - 5	50	151	
	12	17 - 2	50	149	

5.8.2 SYSTEM MEASUREMENTS

All angle measurements are oriented with respect to magnetic directions; for example, values of SCAN and TRACK are defined as 90° when the direction of look is toward magnetic West (Figure 1). During Passes 6 through 12 on 7/17/76, the direction of receiving-antenna look was rotated by 180° to obtain bistatic backscatter components; for these passes, SCAN = 90° corresponds to viewing toward magnetic East. The reference of TRACK remained the same during the entire experiment.

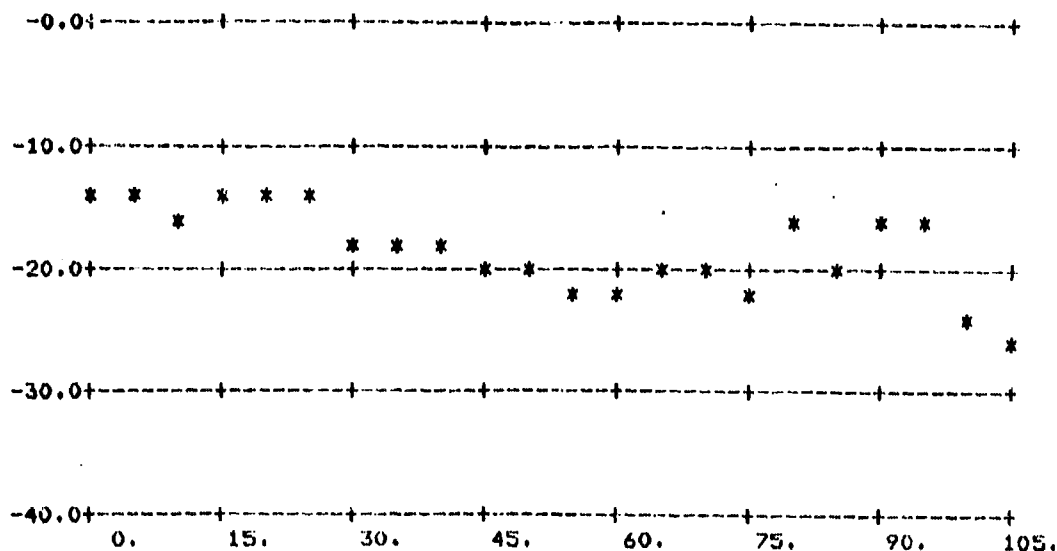
Transmitter illumination corrections are calculated using (1) ϕ_{TRACK} information, (2) aerial photographs to determine the actual ground track for each pass (maps of these ground tracks are shown in Figures 16, 17, and 18), (3) transmitter antenna scan angle records (outputs of the airborne recorder), (4) voice reference marks, and (5) timing marks. These corrections are made, when necessary, as a function of ϕ_{TRACK} angle; however, for the time interval corresponding to a single scan of the receiving antenna, the illumination correction is assumed not to change. Since the ERIM data analysis program computes the effective scattering area on the basis of the 10 dB receiver-response contour, the angular extent of this area (as viewed from the transmitter) is less than 3° ; therefore, the variation in illumination is small for most geometries. However, some situations exist where the scattering ground patch is near the first "null" (which is down approximately 11 dB) of the transmitter antenna; in these situations, there could be several dB variation within three degrees. Since the estimated transmitting antenna pointing accuracy is approximately 1° , no additional corrections were made for these situations. One of the recommendations discussed in Section

7 is a system modification to correct this problem and to reduce (by 3 dB) the error now produced by variations in illumination level. This modification would entail ground measurements of incident power.

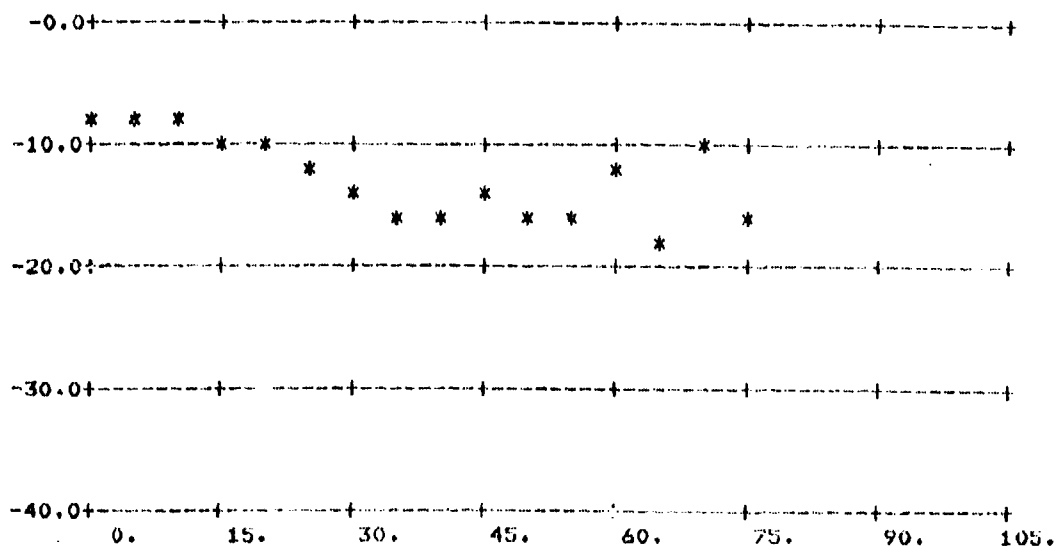
Studies of the chart records reveal that the incident power is low during the first half of each pass and increases during the last half. This could be due to antenna beam distortions caused by the aircraft wing during the forward looking angles of the spotlighting. Data are presented in Figure 62 for the first half and the last half of a pass to illustrate this situation. Questions regarding the possible distortion of the transmitting antenna pattern by the wing would be resolved by the ground power measurements referred to above.

Calculations of the specular reflection delay relative to the direct signal path were made for each geometry. Examples of these are given in Figure 9. The receiver gating is accomplished by using reference pulses on the local oscillator signal. These pulses consist of 50 nsec L.O.-off periods at the basic clock rate or PRF of the transmitter (4 kHz). The receiver is gated on $\delta \approx 50$ nsec after the direct pulse. The value of δ is adjusted so as to insure that the specular signal does not enter the receiver during the period when the receiver is gated on. As described in Appendix B, the sample-and-hold detector is delayed by approximately one-half of the received bistatic pulse length. As a result of the receiver gating delay, the specular return peak does not appear in most of the data shown in Section 5.7.

Estimates of the signal-to-noise ratio realized during the data gathering are given in Figure 63. There is some



(a) First Half ($\phi_{\text{TRACK}} < 90^\circ$)



(b) Last Half ($\phi_{\text{TRACK}} \geq 90^\circ$)

Figure 62. σ_O vs. ϕ_s for 7/17/76, Pass 4,
and 23-cm Wavelength

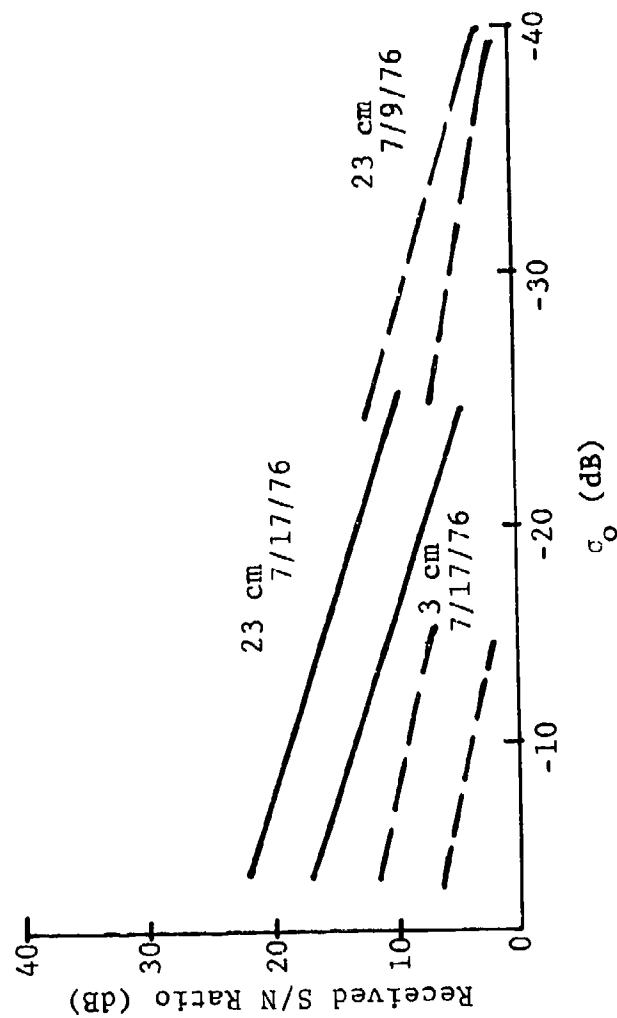


Figure 63. Estimates of Signal-to-Noise Ratio

spread in these values due to variations in the footprint area A_{gd} for various geometries. As discussed in Section 5.7, a minimum signal threshold is used in the data processing to reject samples having $S/N < 3$ dB.

5.8.3 MONOSTATIC MEASUREMENTS

Monostatic cross section density values were calculated using the SAR imagery obtained during Pass 9 on 7/2/76; the imagery is shown in Figure 64; both sites 1 and 2 are included. Calibration reflectors may be seen to the south (left) on the radar imagery. Optical signal-intensity measurements were made using the ERIM precision optical processor (POP). These measurements were made for the clutter of test area 2 and for the calibration reflector; then, their ratio was calculated. Using the cross section value of the reflector (corrected for the angle of viewing) as a standard, a backscatter reflection coefficient value of $\sigma_o = -13$ dB was obtained at $\lambda = 23$ cm. This value compares with a 23 cm value of $\sigma_o \approx -17$ dB at $\phi_s = 180^\circ$ (that is, the backscatter case) obtained from Passes 6 and 7 of the 7/17/76 flight. Not only were the transmitted and received signal paths in the same vertical plane for these passes, but they were located almost along the same straight line (between the scattering patch and the receiving antenna). For Pass 6, these paths were 10° from colinearity; for Pass 7, the difference was 5° .

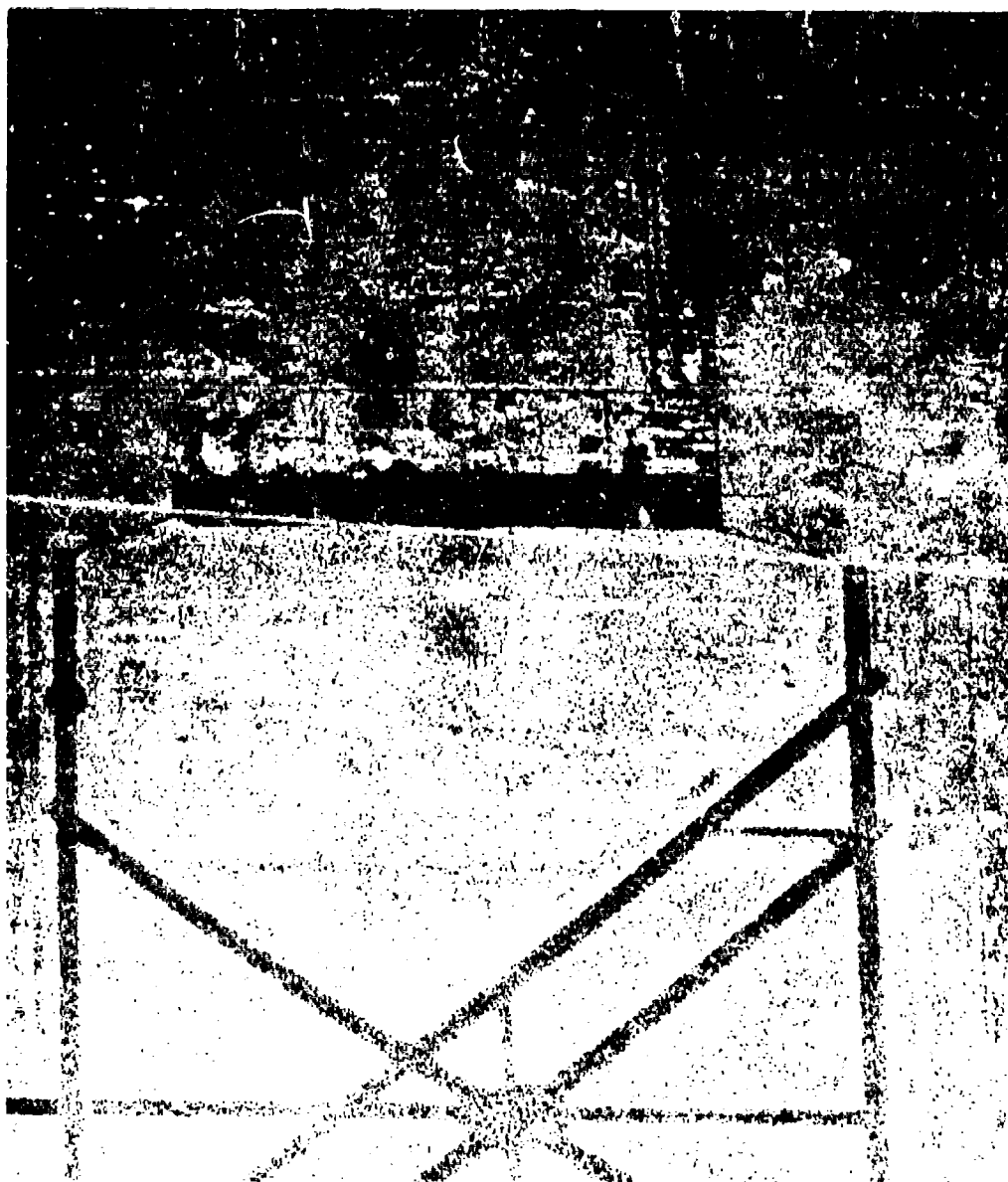


Figure 64. Imagery from Pass 9, Flight 7/2/76

6 ERROR ANALYSIS

A summary of experimental parameters used in the determination of the values of σ_o is given in Table 22; applications and accuracies are also discussed in the table. uncertainties in the absolute values of these parameters contribute to the total error in the final values of σ_o obtained. Error sources for the bistatic measurements system can be classified into three basic groups:

1. instrumentation,
2. receiving antenna response, and
3. sampling.

There is uncertainty (a) in the measured values of the transfer functions of the receivers and recorders, (b) in the basic geometric parameters of the measurements, and (c) in the illumination or incident power level. These values, when used in the bistatic propagation equation to solve for σ_o , combine to give a total instrumentation error. Contributions to the received signal power due to sidelobe response of the receiving antenna cannot be completely accounted for and thus constitute a second error source. Finally, there is an error due to the finite number of samples available from the measurement to define σ_o . This latter error will not be discussed in detail here since it has already been covered in Section 5.5.

6.1 INSTRUMENTATION ERRORS

The bistatic radar equation for σ_o can be written as follows by combining Eqs. (29), (53), and (54):

TABLE 22. RECORDED PARAMETERS WITH APPLICATIONS AND ACCURACIES

Recorded Parameter	Application in Data Analysis	Accuracy in Measurement
Aircraft velocity and drift angle	Used to calculate correction for transmitter antenna pointing and correction for transmitter antenna gain.	25%
Aircraft antenna pointing angle	Used to calculate effective transmitter antenna gain as a function of position (time) for each pass.	5° 1/2 beamwidth
Receiving antenna depression angle	Provides θ_s and r_s values.	1°
Pulse repetition rate	Provides timing for each sample.	
Calibrations for: Received power at 3 cm Received power at 23 cm Track angle TRACK Antenna angle SCAN Delay time ΔR	Basic values of P_r .	±1 dB

TABLE 22. RECORDED PARAMETERS WITH APPLICATIONS AND ACCURACIES (Continued)

Recorded Parameter	Application in Data Analysis	Accuracy in Measurement
<p>Site Description Data:</p> <p>Surface roughness</p> <p>Moisture (recent rain)</p> <p>Wind, Temperature</p> <p>Photography</p>	<p>Basic classification of scattering area used for modeling; comparison with other data.</p>	
<p>Radar Imagery:</p> <p>3 cm</p> <p>Like polarization</p> <p>Cross polarization</p> <p>23 cm</p> <p>Like polarization</p> <p>Cross polarization</p>	<p>Classification of scattering area.</p>	<p>±5 dB</p>
<p>Received bistatic power at 23 cm</p> <p>Received bistatic power at 23 cm, orthogonal polarization</p> <p>Received bistatic power at 3 cm</p> <p>Received bistatic power at 3 cm, orthogonal polarization</p>	<p>Basic measure of received power, P_r</p>	<p>±1 dB</p>

TABLE 22. RECORDED PARAMETERS WITH APPLICATIONS AND ACCURACIES (Concluded)

Recorded Parameter	Application in Data Analysis	Accuracy in Measurement
Received local oscillator power from aircraft, P_{LO}	Provides coherent local oscillator power for the four receiver channels. Continuous record of received local oscillator power recorded and used for receiver gain correction.	± 1 dB level
Track angle, receiver site to aircraft (TRACK)	Provides continuous record of incident power direction. Used to determine ϕ_{TRACK} .	$\pm 1^\circ$
Receiver look angle (SCAN)	Provides continuous record of receiver antenna viewing direction. Used to determine ϕ_{TRACK} for each sample area A_{gd}	$\pm 1^\circ$
Delay time between reception of direct signal from aircraft and sampling of bistatic signal (AR)	Used to determine area A_{gd} from which bistatic energy is scattered. Provides indication if specular signal has been received.	± 10 nsec
Transmitter power	Transmitter power level P_1	± 0.5 dB
Aircraft altitude (y_2)	Used to calculate θ_1 and r_1	± 100 ft $< 2\%$
Vertical photography	Used to verify aircraft ground track and offset distance x_2	± 300 ft $\approx 2\%$

$$\sigma_o = \frac{(4\pi)^3 P_z}{P_i \lambda^2 G_{OT} G_{OR} L \int_{A_{gd}} \frac{f_T f_R W_{\rho\phi} h[t(A)] dA}{r_i^2 r_s^2}} \quad (55)$$

An error in any of the quantities in Eq. (55) leads to an error in the value of σ_o . Figure 65 provides a simplified schematic of a bistatic measurement channel as an aid in this discussion. The instrumentation errors which occur in such a channel fall into two categories, systematic and random.

The systematic errors add a constant bias to the measurements; Table 23 lists the sources of these errors. It is estimated that neither the transmitter power nor the receiver power can be measured to better than ± 1 dB; in addition to an error of about ± 0.5 dB in the power meter, the transmitter power is monitored through a directional coupler whose coupling coefficient may be in error by approximately ± 0.5 dB. The received power is found by comparison with a calibrated source; the estimated error for measuring the power in this reference source is also ± 1.0 dB. From experience, it is estimated that the peak antenna gain can be found within ± 0.6 dB. There are losses in the transmission lines between the transmitter and the transmitting antenna, in rotary joints, in the radome, in the troposphere, and in the transmission lines between the receiving antenna and the input to the receiver. At the wavelengths used in this experiment, atmospheric attenuation will be negligible. The uncertainty in the transmission line attenuation will therefore be the dominant factor in computing the losses. Finally, the receiver gain will drift slightly from its value at calibration.

The maximum value of the systematic error is ± 4.7 dB, but it is unlikely that all the errors will add linearly;

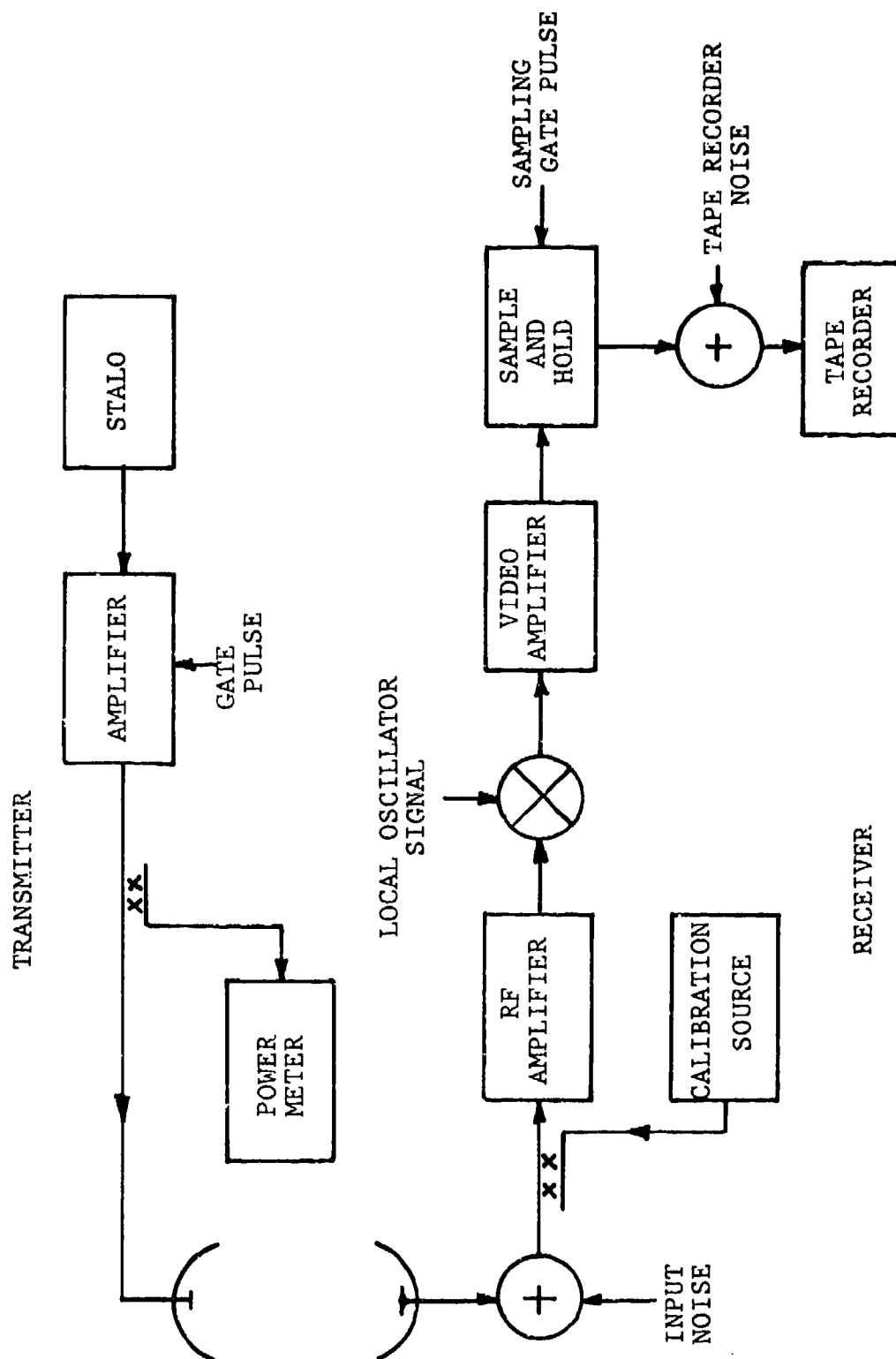


Figure 65. Simplified Block Diagram of a Bistatic Measurement Channel

TABLE 23. ESTIMATES OF SYSTEMATIC ERRORS
(Log-normal distributions assumed)

<u>Source</u>	<u>Magnitude</u> (dB)
Transmitter power error	± 1.0
Received power error	± 1.0
Transmitter antenna peak gain error	± 0.6
Receiving antenna peak gain error	± 0.6
Losses in microwave components, radome, and atmosphere	± 1.0
Maximum gain drift with temperature	<u>± 0.5</u>
Maximum = 4.7	
RMS Value = 2.0	

hence, an RMS value of 2 dB is more representative of what will occur in practice.

Table 24 lists the sources of random error. The first source is the variation in transmitting antenna gain because of pointing errors. During the spotlight operation, it was not possible to aim the antenna precisely at the receiving tower, and the transmitting antenna boresights were determined to be in error by as much as 10 degrees. Uncertainty in the transmitting antenna gain was the largest single error source.

Experience has shown that the aircraft can be flown down a tube 400 ft wide; hence the position error is ± 200 ft. At a range of 10,000 ft, this results in an error of about ± 0.2 dB in R_i . Estimated variations in the level of the terrain result in an error of ± 0.2 dB in R_g . Multipath propagation can cause fading; however, there was no evidence of multipath effects in the measurements.

The other random errors in the instrumentation are in the receiver and recorder. First, there is receiver noise. At 3 cm, the signal-to-noise ratio is estimated to be about 20 dB (after noncoherent integration) at a slant range of 20,000 ft, which results in an error of about ± 0.4 dB; the signal-to-noise ratio is higher and the error is therefore less at 23 cm. Since S/N depends on the slant range, the error resulting from receiver noise increases with slant range.

The receiver gain is a function of L.O. (local oscillator) power, as the conversion loss in the mixer depends on the level of this power. If L.O. power is above a threshold value, the conversion loss increases about 1 dB with each 1 dB decrease in L.O. power. The threshold level and variation of the conversion loss depend on the particular mixer in

TABLE 24. ESTIMATES OF RANDOM ERRORS

<u>Source</u>	<u>Magnitude</u> (dB)
Transmitting antenna pointing errors	±4.0
Position uncertainty of transmitter	±0.2
Height variation of ground	±0.2
Receiver noise (26 dB S/N after non-coherent processing)	±0.4
Receiver gain error (L.O. power variation and other factors)	±1.0
Sample and hold error (10 nsec jitter)	±1.3
Tape recorder error (noise and jitter)	±0.3
Maximum = 7.4	
RMS Value = 3.5	

the system; actual measurements were made on the receiver and their results are discussed in Appendix B. Uncertainty in the receiver gain because of local oscillator power variation is estimated to be ± 1 dB.

The sample-and-hold circuit (S-H) is another large contributor to the random error. Jitter on the hold command causes the S-H to be triggered in such a way that (1) the data are sampled at the wrong time, (2) the voltage stored will be slightly in error, (3) the voltage stored will decay with time, and (4) there will be feedthrough during the hold mode. With a well-designed sample-and-hold circuit, the last three factors are negligible compared to the timing error. Regarding the latter, the receiver has a threshold circuit and the hold circuit is pulsed whenever a threshold level is exceeded. The timing error depends on the threshold level, the signal-to-noise ratio, and the sidelobe energy entering the receiver. (A signal-to-noise ratio of 10 to 23 dB was noted at 23 cm; see Figure 63) Measurements on S-H show that the RMS timing error is 10 nanosec, resulting in an RMS error of about 1.3 dB in the output signal.

With certain geometries and σ_0 characteristics, the specular return entering the receiving antenna sidelobes could exceed the threshold and trigger the sample-and-hold circuit too early, resulting in bad data. However, with the geometrical situation used, this effect was not observed.

Since the output signal is recorded on magnetic tape, tape recorder noise degrades performance. In an FM tape channel, the ratio of the full scale signal to the RMS noise is about 44 dB. To prevent saturation on occasional large returns, the drive level to the tape recorder will normally be about 10 dB below the maximum signal; hence,

the signal-to-noise ratio out of the tape recorder will be 34 dB and the tape recorder will thus add a random error of ± 0.3 dB.

The RMS value of all the random errors is about 3.5 dB. The estimated total error for both the systematic and random components will be the square root of the sums of the squares or about ± 6.6 dB for the instrumentation. As discussed in Section 7, this error can be reduced to about ± 3.5 dB in future measurements. (For comparison, with the ERIM rotary platform, monostatic cross sections are measured to better than 4 dB [15]; also, the estimated accuracy was ± 6 dB during the ERIM monostatic clutter measurements [16].)

6.2 RECEIVING ANTENNA PATTERN ERRORS

The power received, P_r , in each of the receiving channels contains three components, as follows:

$$P_r = P_{ml} + P_{sl} + P_{cc} \quad (56)$$

P_{ml} is obviously the desired component, while P_{sl} (sidelobe contribution) and P_{cc} (cross polarization contribution) will cause errors in the σ_o measurements.

From the bistatic radar equation, assuming a broad transmitter beam, large R_i , and a narrow receiver beam (so that the receiving antenna footprint is always within the

15. This reference will be made available to qualified military and government agencies on request from RADC (OCSA) Griffiss AFB NY 13441.
16. R.W. Larson and W. Carrara, Measurements of X-band Clutter Statistics with an Amplitude Calibrated Radar Report No. AFAL-TR-74-44, Environmental Research Institute of Michigan, Ann Arbor, June 1974.

transmitting antenna footprint and the σ_o in the former area can be considered constant),

$$P_{m\ell} \propto \frac{\sigma_{o_{m\ell}} A_{m\ell} G_{m\ell}}{R_s^2} \quad (57)$$

If the beamwidth of the receiving antenna is β_r , then

$$A_{m\ell} = \underbrace{\beta_r y_2 \sec \theta_s \tan \theta_s}_{\text{length}} \cdot \underbrace{\beta_r y_2 \sec \theta_s}_{\text{width}} \quad (58)$$

Using Eq. (58) and the fact that $R_s = y_2 \sec \theta_s$, Eq. (57) becomes

$$P_{m\ell} \propto \sigma_{o_{m\ell}} \beta_r^2 \tan \theta_s G_{m\ell} \quad (59)$$

Let $G_{s\ell}$ represent the far-out sidelobe receiving antenna gain level which is assumed to be constant. Based on an Ohio State report [17], it will be assumed for the purposes of illustration that bistatic σ_o values can be approximated by a Gaussian function on a pedestal. Thus,

$$\sigma_o = \sigma_{o_{\max}} \exp \left\{ -1.385 \left[\left(\frac{\theta_s - \alpha_o}{\alpha_{\theta_s}} \right)^2 + \left(\frac{\phi_s}{\alpha_{\phi_s}} \right)^2 \right] \right\} + \sigma_{o_p} \quad (60)$$

This equation gives the general σ_o trend for loam or smooth sand when $\sigma_{o_p} \ll \sigma_{o_{\max}}$ and should approximate the terrain of test site 1.

-
17. W.H. Peake and T.L. Oliver, The Response of Terrestrial Surfaces at Microwave Frequencies, Technical Report No. AFAL-TR-70-301, Ohio State University, Columbus, May 1971.

For P_{ml} , it was assumed that σ_o is constant and that the receiving antenna beam is narrow. Now, if a wide scattering lobe and a constant receiving antenna gain are assumed, an approximate relationship for P_{sl} can be written by following steps similar to those used to find P_{ml} :

$$P_{sl} \propto \sigma_{o_{max}} \alpha_{\theta_s} \alpha_{\phi_s} \tan \alpha_o G_{sl} \quad (61)$$

Then, combining Eqs. (59) and (61) gives

$$\frac{P_{ml}}{P_{sl}} \propto \frac{\sigma_{o_{ml}} \beta_r^2 \tan \theta_s G_{ml}}{\sigma_{o_{max}} \alpha_{\theta_s} \alpha_{\phi_s} \tan \alpha_o G_{sl}} \quad (62)$$

With loam or smooth sand, the σ_o 3 dB lobe widths α_{θ_s} and α_{ϕ_s} are on the order of 10° . Since β_r is 5° ,

$$\frac{P_{ml}}{P_{sl}} \propto \frac{\sigma_{o_{ml}} G_{ml}}{4 \sigma_{o_{max}} G_{sl}} \quad (63)$$

if the tangents are approximately equal. Since P_{ml}/P_{sl} is 6 dB, if the average receiver antenna sidelobe level is 30 dB down, P_{ml} will equal P_{sl} 24 dB down from the $\sigma_{o_{max}}$. Thus, for this type of bistatic scattering pattern, measurements are valid only in the vicinity of the σ_o mainlobe unless antenna sidelobe power is gated out; this was done in this experiment.

Figure 66 shows plots of (1) a one-dimensional σ_o model and (2) the calculated σ_o value using a rectangular receiving beam and sidelobes 30 dB down. Note that calculated σ_o levels off to 25 dB below the mainlobe power. The receiving antenna beamwidth is 5° compared with a 3 dB lobe width of 14° for σ_o . The significant beamwidth of

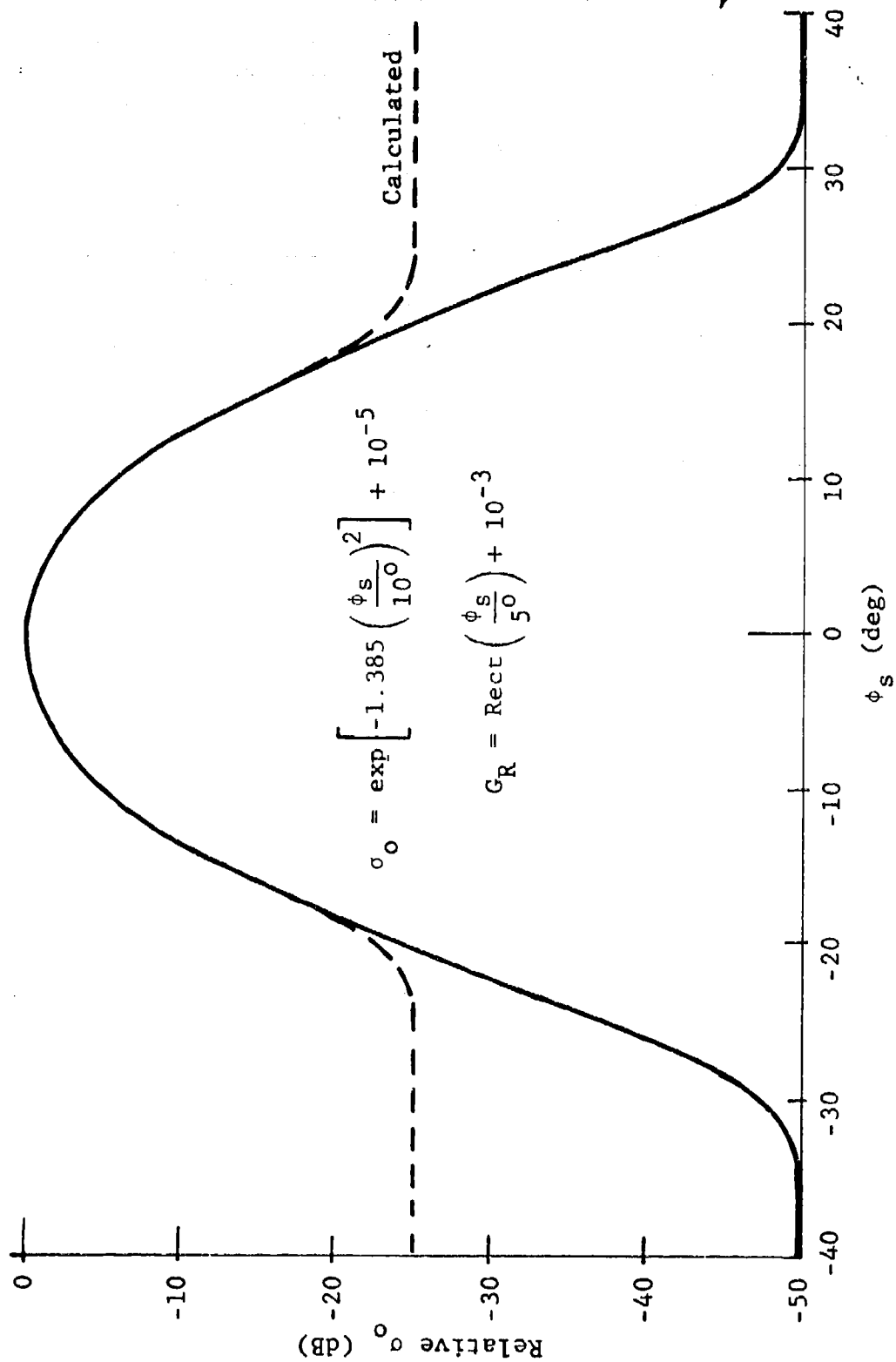


Figure 66. One-Dimensional Model of σ_o and Calculated Values

the receiving antenna causes the calculated power to be slightly above the σ_o model curve for $\phi_s = \pm 10$ or $\pm 20^\circ$ and slightly less than the model value near $\sigma_{o_{\max}}$ ($\phi_s = 0$); each of these errors is less than one dB. For rough surfaces, the σ_o mainlobe (that is, the specular reflection) is much less pronounced; as a result, there is less of a problem with the antenna sidelobe energy.

6.2.1 SIDELobe EFFECTS ON DATA

In the measurement situation for which data were obtained, the time delay between the specular return and the bistatic return is greater than the 90 nsec pulse width; here, range gating eliminated the specular return coming through near sidelobes. Figure 9 shows a plot of the difference between the time delays for the bistatic returns and the direct-path signal as a function of receiver azimuth angle from broadside for two aircraft positions, 45° ahead of broadside and broadside. The differences between the time delays of the specular return and the direct path are also shown. For this figure, the transmitter height y_2 is 7,000 ft and the distance x_2 between the transmitter and the receiver at broadside is 20,000 ft. The receiver height y_1 is 100 ft and the scattering angle θ_s is 45° . Figure 9 shows that the effectiveness of range gate discrimination varies considerably with the geometry; therefore, the additional delay δ is added when necessary.

The instrumentation system (Appendix B) utilizes a receiver gate of approximately 2 μ sec duration. This duration, in combination with the width of the transmitter pulse, results in the gating out of most of the sidelobe power. In fact, the measurement results* show less than a

* Several computer model examples were provided by GRC to demonstrate the effects of sidelobe power.

1 dB error due to sidelobe power for the geometry used. These results were obtained using the 10 dB receiving antenna response contour, which corresponds to a beamwidth of approximately 9.36° .

In order to investigate other parameter values not covered in the experiment, values of σ_0 were calculated as a function of receiving antenna beamwidth. These calculations show that increasing the beamwidth to 19° changes the σ_0 value by only 0.6 dB, even though (with the geometry of Flight 7/17/76) the resulting integration area extends to the horizon. A separate (hand) calculation was made which included 6 receiving-antenna sidelobes (corresponding to the total receiver "on" gate time); this calculation shows a change of less than 1 dB in the σ_0 value, as compared with the data analysis results based on the 10 dB contour geometry.

Based on these two calculations and the measurement results, the σ_0 error from sidelobe contributions is estimated to be less than 1 dB.

6.2.2 POLARIZATION ISOLATION

Appendix B discusses P_{cc} , the power cross-coupled into a receiving channel because the cross-polarization isolation in the transmitting or receiving antenna is not infinite. For example, if the transmitting antenna is vertically polarized, some power with horizontal polarization will be transmitted because of antenna properties or aircraft pitch. The cross-coupled power is normally significant only in the cross-polarized receiving channel, because the cross-coupled power is insignificant compared with the parallel-polarized power in the parallel channel. For example, if the cross-polarization isolation were 25 dB,

P_{ml} and P_{cc} would be equal if σ_{OVV} is 25 dB above σ_{OVH} . In fact, the measured isolations for the 3 and 23 cm wavelength transmitting and receiving antennas range from 20 to 31 dB.

6.3 ERROR ANALYSIS CONCLUSIONS

6.3.1 INSTRUMENTATION ERRORS

Instrumentation errors can be classed as systematic or random. The systematic error is estimated to have a maximum value of 4.7 dB and an RMS value of 2.0 dB; the random error has an estimated RMS value of 3.5 dB. These errors are believed to be realistic since they are based on instrumentation tests and the results of the data-gathering experiments. Transmitter antenna pointing is the largest single source of error. The total error is estimated to be ≈ 6 dB.

The problem of energy entering the receiver sidelobes must be considered for the measurement geometries in the program. Range gating has insured that the specular return was not received through the antenna mainlobe. The average sidelobe response of 24 dB down provides adequate spatial filtering in the specular plane. A limiting factor in the measurement of cross-polarized σ_0 is the cross-polarization isolation of the transmitting and receiving antennas; this isolation ranged between 20 and 31 dB for the 3 and 23 cm wavelength transmitting and receiving antennas.

Errors due to sampling effects are introduced at different points in the data gathering and analysis process. The finite sampling window of the sample-and-hold detector results in a location ambiguity of 10 nsec or 10 ft of processed error. However, this produces negligible error in the σ_0 calculation. The basic timing error in the S-H results in a 1.3 dB error in the output signal. Tape recorder noise will add 0.3 dB to the total error.

6.3.2 SAMPLING ERROR

Error bounds (or confidence) in the estimate of the mean value of σ_0 are a function of the number of independent samples, as discussed in Section 5.5. The average number of independent samples of each 23 cm data point is about 10, giving a 5 dB spread in the 95% confidence interval for the mean value (Figure 28). Similarly, the average number of independent samples for 3 cm data points is 35, giving a 3.5 dB spread in the 95% confidence interval for the mean value.

7 CONCLUSIONS AND RECOMMENDATIONS

The following conclusions and recommendations can be made based on results reported in the preceding sections. A more detailed discussion of conclusions about the data obtained is given in Section 5.7.

7.1 CONCLUSIONS

During the course of this program, a system was developed for the determination of bistatic scattering coefficients of terrain. The system consists of two integral parts. The first part is a coherent data-gathering system; this includes transmitters and receivers which provide simultaneous measurements at 23 cm and 3 cm wavelengths with a dual-polarization capability (that is, parallel and crossed polarizations) at each wavelength. The second part is a data processing system; its principal element is a data reduction and analysis computer program for the conversion of raw recorded power and aspect data into bistatic scattering coefficients.

The bistatic instrumentation has been used in this program to gather data for large incidence and scattering angles. However, it is capable of obtaining data at any combination of incidence and scattering angles for a complete range of bistatic azimuth angle from 0° to 180° . The measurement technique was specially designed to ensure an adequate number of samples for the determination of $\bar{\sigma}_0$, under the assumption that σ_0 is log-normally distributed for a fixed set of aspect, wavelength, and polarization conditions. The efficacy of the log-normal assumption was reinforced by observing that, for most passes, the scatter of σ_0 values was such that some 66% were within 5 dB of $\bar{\sigma}_0$.

Limitations on the range of σ_0 values that can be measured are due to the measurements geometry required and the available power. Values of σ_0 as low as -20 dB at 3 cm and -40 dB at 23 cm can be measured.

The σ_0 results obtained from the data processing program are in general agreement with the small amount of data available from other measurement programs. In addition, these σ_0 results agree well with an independent analysis of the same data carried out by General Research Corporation. It was also found that $\bar{\sigma}_0$ values matched quite well at the common aspect points (near $\phi_s = 90^\circ$) for forward and backscattering passes, which were generally separated in time by an hour or more. Such matching of $\bar{\sigma}_0$ data points confirms the validity of the data-gathering and processing methods.

Values of σ_0 were obtained for two terrain types which have roughness scales differing by approximately an order of magnitude. The results show that σ_0 values from the two sites differ by about 10 dB, with the lower σ_0 values corresponding to the smoother site. Also, a comparison of σ_0 as a function of wavelength was made, with the general conclusion that 3 cm σ_0 values are approximately 10 dB larger than 23 cm σ_0 values for each test site.

This experiment is the first to obtain bistatic scattering data from air-ground geometry using coherent instrumentation. The instrumentation operated very well during the data gathering program; clearly, its great flexibility would permit its use (1) for two-aircraft, coherent measurements of either scattering coefficients or clutter statistics or (2) for coherent bistatic system demonstration.

7.2 RECOMMENDATIONS

The requirement for quantitative measures of bistatic scattering coefficients and for bistatic clutter statistics still exists, although results from the work reported here have contributed to the start of a data base for bistatic scattering. In order to broaden the available data base so that the distribution of σ_0 can be determined for a fixed set of aspect, wavelength, and polarization parameters, it is recommended that additional bistatic measurements be made using the instrumentation and analysis techniques developed during this program. To implement this general objective, the following specific recommendations are made:

1. Additional analysis should be performed on the empirical data obtained from the present program. This should include (a) analysis to obtain σ_0 values from the cross-polarization data available and (b) utilization of the ΔT channel records to verify the scattering area values used in the completed analysis.
2. Several system modifications are recommended. One of these would be the installation of a two-channel receiving/recording system to receive and record a measure of incident power. Such an absolute measure would be used directly in the computation of σ_0 , eliminating the necessity to determine transmitter antenna pointing direction during each spotlight pass. This modification would improve the accuracy of the absolute values of σ_0 by approximately 3 dB (Section 5.8.2). Also, if measurements of lower σ_0 values at 3 cm are desired, transmitter power can be increased for this wavelength. Finally,

several additional modifications to simplify the overall operation of the data-gathering instrumentation and the data-processing system would be appropriate.

3. Additional data-gathering flights should then be conducted in order to cover a larger range of bistatic angles and a variety of terrain types.
4. The existing instrumentation should be incorporated into a two-aircraft, bistatic, four-channel, coherent, measurements system so as to provide data from which further estimates of clutter statistics can be obtained. Because of the increased flexibility of the two-aircraft system, such data can be obtained for a wider variety of terrain types. Also, such a system can be used as a demonstration of the operational bistatic system.

REFERENCES

1. W.H. Peake and T.L. Oliver, The Response of Terrestrial Surfaces at Microwave Frequencies, Report No. AFAL-TR-70-301, Electrosience Laboratory, Ohio State University, Columbus, May 1971.
2. F.E. Nathanson, Radar Design Principles, McGraw-Hill Book Co., New York, 1969, Ch. 2.
3. M.I. Skolnik, Ed., Radar Handbook, McGraw-Hill Book Co., New York, 1970, Chap. 25, p. 15.
4. M.W. Long, Radar Reflectivity of Land and Sea, Lexington Books, D.C. Heath and Co., Lexington, Mass., 1975, Figure 5-9.
5. Op. cit. (Ref. 4), Chap. 5.
6. Microwave Journal Technical and Buyer's Guide, February 1, 1968, p. 132.
7. Op. cit. (Ref. 6), p. 133.
8. D.E. Barrick, Normalization of Bistatic Radar Return, Report No. 1388-13, Ohio State University Research Foundation, Columbus, January 1964.
9. Op. cit. (Ref. 1).
10. S. Silver, Microwave Antenna Theory and Design, MIT Radiation Lab. Series, No. 12, Boston Technical Lithographers, Inc., Lexington, Mass., 1963.
11. E. Jahnke and F. Emde, Tables of Functions with Formulae and Curves, Dover Publications, New York, 1945.
12. Op. cit. (Ref. 4), p. 156.
13. R.L. Cosgriff, W.H. Peake, and R.C. Taylor, Terrain Scattering Properties for Sensor System Design (Terrain Handbook II), Engineering Experiment Station Bulletin No. 181, Ohio State University, Columbus, May 1960.
14. S.T. Cost, Measurements of the Bistatic Echo Area of Terrain at X-Band, Report No. 1822-2, Ohio State University Research Foundation, Columbus, May 1965.
15. This reference will be made available to qualified military and government agencies on request from RADC (OCSA) Griffiss AFB NY 13441.

REFERENCES
(Continued)

16. R.W. Larson and W. Carrara, Measurements of X-Band Clutter Statistics with an Amplitude Calibrated Radar, Report No. AFAL-TR-74-44, Environmental Research Institute of Michigan, Ann Arbor, June 1974.
17. Op. cit. (Ref. 1).
- A-1. R. Beckmann and A. Spizzichino, The Scattering of Electromagnetic Waves from Rough Surfaces, MacMillan Company, New York, 1963, p. 410.

SYMBOLS

English:

a	dish radius
A	area variable
a'	semi-major axis of receiving antenna footprint ellipse
A/C	aircraft
A_{gd}	scattering area
a_{ij} } a_{kl} } a_{ml}	points in area A_{gd}
	area of receiving antenna mainlobe footprint
A_R	receiving antenna aperture
B	bandwidth
b'	semi-minor axis of receiving antenna footprint ellipse
bpi	bits per inch
c	speed of light
ctr x	x-coordinate of center of receiving antenna footprint ellipse
ctr y	y-coordinate of center of receiving antenna footprint ellipse
D	dish diameter = $2a$
d	direct distance from transmitter to receiver = $\sqrt{x_2^2 + z_2^2 + (y_2 - y_1)^2}$
dA	scattering surface element
DME	distance measurement equipment
dP_r	incremental power at receiver antenna
dS_s	power density of the scattered wave at a distance r_s from the scattering surface element dA
$E_f(X) \leq 1$	elliptical footprint area where $X = T(\text{ransmitter})$ or $R(\text{eceiver})$

$$E_r = 1$$

range ellipse (intersection of ellipsoid $|P - P_1| + |P - P_2| = 2q$ with a flat earth, where P is a variable point

$$\left. \begin{array}{l} E_{r1} \\ E_{r2} \end{array} \right\}$$

successive range ellipses defined by the receiver sampling time and the transmitter pulse length

f

radar frequency

F

focal length of antenna

f_d

Doppler frequency (absolute)

f_{do}

reference Doppler signal

f_{dr}

relative Doppler frequency

f_T

transmitter antenna power gain pattern = 1

f_R

receiver antenna power gain pattern = $\Lambda_2^2(u)$

$f_{1/2}$

width of frequency spectrum between 0 and 1/2-power point

G

receiving antenna gain

G_{ml}

antenna gain for mainlobe

G_0

antenna peak gain

G_{OR}

receiving antenna peak gain

G_R

receiving antenna (average) gain

G_{RH}^*

peak gain at horizontal polarization for vertically polarized receiving antenna

G_{Rsl}

gain of receiving antenna in sidelobe region

G_{RV}

vertically polarized receiving antenna peak gain

G_{sl}

antenna gain for far-out sidelobes

G_T

transmitting antenna (average) gain

G_{TH}^*

peak gain at horizontal polarization for vertically polarized transmitting antenna

G_{TV}	vertically polarized transmitting antenna peak gain
HH	horizontal-horizontal polarization
$h[t(A)]$	response function for receiving antenna
HV	horizontal-vertical (crossed) polarization
I	$\int_{A_{gd}} \frac{f_T f_R W_{\rho\phi} h[t(A)]}{r_i^2 r_s^2} dA$
i	integer
j	integer
$J_2(u)$	second-order Bessel function of argument u
k	integer
K	$\frac{\lambda^2 G_{OT} G_{OR} L}{(4\pi)^3}$
k_B	Boltzmann's constant
K_O	kernal which includes the range and power pattern factors as well as the constants P_i and K
ℓ	integer
L	total system losses
L_{ap}	aperture length
L.O.	local oscillator
MTS	Michigan Terminal System
N	number of samples obtained in a 5° azimuth interval (that is, per receiver beam position)
n	number of ground patches for which data are collected
\tilde{N}	number of samples which are coherently integrated
p	ground distance corresponding to a received pulse length
P	integration point
P_{av}	average transmitted power

P_{cc}	power cross coupled into receiver of wrong polarization
P_d	direct power (enters through sidelobes)
P_i	transmitted power
P_i'	power incident in scattering area A_{gd}
P_{ml}	power received via the mainlobe
POP	precision optical processor
P_r	received power = $P_i \sigma_o KI$
P_r'	power incident on receiving antenna aperture
PRF	pulse repetition frequency
P_{rV}	vertical-channel received power
P_s	specular point
P_{sl}	power received via the sidelobes
$\bar{P}_1 = (0, y_1, 0)$	receiver location vector
$P_1(x_1, y_1, z_1) \leftrightarrow R(0, y_1, 0)$	receiver R location in (x_o, y_o, z_o) coordinate system
$\bar{P}_2 = (x_2, y_2, z_2)$	transmitter location vector
$P_2(x_2, y_2, z_2) \leftrightarrow T(x_2, y_2, z_2)$	Transmitter T location in (x_o, y_o, z_o) coordinate system $r_2 = \sqrt{x_2^2 + y_2^2 + z_2^2}$
q_s	complement of the squint angle (that is, the angle between the plane of incidence and the vertical plane containing \bar{V})
r	variable radius to point in antenna aperture ($0 \leq r \leq a$)
$R = R_i + R_s$	total bistatic signal path from transmitter via scattering area to receiver
r_A	radius of circular scattering area
r_i	distance from transmitter to integration point

R_i	distance from transmitter to origin of x, y, z system (center of receiving antenna footprint)
RMS	root-mean-square
r_s	distance from receiver to integration point
R_s	distance from receiver to origin of x, y, z system (center of receiving antenna footprint)
$R(0, y, 0)$	receiver location in x_o, y_o, z_o coordinate system
$r_2 = \sqrt{x_2^2 + y_2^2 + z_2^2}$	distance between x_o, y_o, z_o origin (receiver foot) and transmitter
s	standard deviation
\hat{s}	variable unit vector which traces out a cone
SAR	synthetic aperture radar
$SCAN = 90^\circ - \phi_{SCAN}$	navigational angle measured from the negative z_o -axis to the line which runs from the receiver foot to center of the receiving antenna footprint
S-H	sample and hold
S_i	power density incident upon scattering surface element dA
S_n	average of single-pulse received power values over a 5° azimuthal interval
S/N	signal-to-noise ratio
STALO	stable local oscillator
t	time
T	time between independent samples for Gaussian clutter spectrum
T_i	sampling time interval
T_N	noise temperature of the receiver
T_p	time on a patch
$TRACK = 90^\circ - \phi_{TRACK}$	navigational angle measured from the negative z_o -axis to the line which runs from the receiver foot to the transmitter foot

$u = \frac{\pi D}{\lambda} \sin \psi_s$	argument of Bessel function $J_2(u)$
\vec{v}	vector
\hat{v}	unit vector
V	aircraft velocity
\vec{V}	aircraft velocity vector
\vec{v}_c	fixed vector to some arbitrary point on beam axis
v_d	Doppler velocity
VH	vertical-horizontal polarization
VV	vertical-vertical polarization
\hat{w}	unit vector defining axis of cone
$W_{\rho\phi}$	weight function describing the variation of σ_0 over the area A_{gd}
x_i^2	single-pulse measure of received power
x_{00}	x_0 -coordinate of either of two points in the ground ($y_0 = 0$) plane which are the intersections of the receiver footprint ellipse with a slant plane containing the receiver antenna field pattern cone axis and which is normal to the vertical plane containing the same axis
(x_0, y_0, z_0)	range-curve coordinate system with origin at receiver foot, etc.
$(x_1, y_1, z_1) = R(0, y_1, 0)$	coordinates of receiver in (x_0, y_0, z_0) system
x_2	ground distance between receiver foot and projection of flight path on ground along normal to flight path (also, x-coordinate of transmitter) in x_0, y_0, z_0 coordinate system
$(x_2, y_2, z_2) = T(x_2, y_2, z_2)$	coordinates of transmitter in (x_0, y_0, z_0) system
y_1	height of receiver (y-coordinate of receiver in x_0, y_0, z_0 coordinate system)

y_2	transmitter altitude (y-coordinate of transmitter in x_0, y_0, z_0 coordinate system)
z_{00}	z-coordinate of either of two points in the ground ($y_0 = 0$) plane which are the intersections of the receiver footprint ellipse with a slant plane containing the receiver antenna field pattern cone axis and which is normal to the vertical plane containing the same axis
<u>Greek:</u>	
α	angle between receiver-to-patch direction and receiver-to-transmitter direction
α_c	half angle of cone
α_o	specular angle = $\theta_i = \theta_s$ for specular reflection
α_{θ_s}	lobe width for σ_o in the plane of angle θ_s
α_{ϕ_s}	lobe width for σ_o in a plane perpendicular to the plane of angle θ_s and passing through R_s
β	antenna beamwidth
β_r	receiving antenna beamwidth
β_t	transmitting antenna beamwidth
δ	additional time delay provided to insure separation of direct and bistatic signals
Δf_d	Doppler shift
$\Delta_R = R - d$	difference between scattered path length and direct path length
ΔT	time at receiver from end of direct path pulse to time at which received bistatic pulse is sampled
$\Delta\theta = \text{sampling angle}$	half of angle subtended at transmitter or at receiver by scattering areas
$\Delta\theta_i$	transmitter sampling angle

$\Delta\theta_s$	receiver sampling angle (that is, the scattering angular interval subtended by the ground patch)
η	angle defining some fixed power contour, or value of ψ_s , measured from beam axis
θ	angle measured from the normal to the scattering area
θ_d	angle between aircraft velocity vector and direction of incidence
θ_i	incidence angle (at patch) of radiation from transmitter
θ_{limit}	maximum value for $\theta_i = \theta_s$
θ_s	scattering angle (at patch) of radiation to receiver
λ	radar wavelength
$\Lambda_2(u) = \frac{8J_2(u)}{u^2}$	where $J_2(u)$ is 2nd-order Bessel function of argument u
μ	mean value
ρ	one of polar coordinates of point in x-y plane of x, y, z coordinate system
σ	radar cross section
σ_o	RCS per unit area = radar cross-section density
$\bar{\sigma}_o$	mean of n samples
$\sigma_{o_{ml}}$	radar cross-section density for receiver mainlobe footprint
σ_{op}	cross-section density in pedestal region
τ	transmitter pulse length
ϕ	one of polar coordinates of point in x-y plane of x, y, z coordinate system
$\phi_{i1} \}$ $\phi_{i2} \}$	angles from the ground track to the two edges of the footprint
ϕ_s	supplement of angle formed by receiver foot, surface increment reference point, and transmitter foot (in x, y, z system)

$\phi_{\text{SCAN}} = 90^\circ - \text{SCAN}$ angle between x_0 -axis and x' -axis (that is, pointing direction of transmitter antenna)
 $\phi_{\text{TRACK}} = 90^\circ - \text{TRACK}$ angle between x_0 -axis and line from receiver foot to transmitter foot
 ϕ_{TRANS} transmitter antenna pointing angle
 ψ bistatic angle between transmitter-to-ground signal path and ground-to-receiver signal path
 ψ_i (variable) angle measured from beam axis of transmitter antenna
 ψ_s (variable) angle measured from beam axis of receiver antenna

SYMBOLS: ADDENDUM

E

Polarization-angle error between transmitting
and receiving antenna axes

APPENDIX A THEORETICAL ANALYSIS AND DESIGN CONSIDERATIONS

This appendix gives a comparative discussion of some of the parameters which govern bistatic clutter measurements and from which system requirements can be established. Analyses of the measurement system indicate that a bandwidth of about 30 MHz is required to separate the direct-path signal from the bistatic signal. A narrow circular receiving antenna beam is necessary to limit the measurement region, and the scattering geometry can be determined from the orientation of the receiving antenna beam. The incident geometry can easily be determined by measuring the signal delay (ΔR) and the absolute Doppler shift. However, neither of these methods is used in this program, although the signal delay, ΔR , is measured and recorded. Incidence geometry is afforded by using the spotlight radar transmitter.

A.1 REQUIREMENTS AND BISTATIC RELATIONSHIPS

The system is required to measure the radar bistatic cross section for an idealized patch of the ground surface, A_{gd} , bounded by a circle of diameter $2r_A$, such that:

1. The area A_{gd} is small enough to subtend an angle less than $2\Delta\theta$ at either the transmitter or the receiver positions. In other words, a cone with an apex at either the receiver or the transmitter and whose intersection with the surface encloses A_{gd} should have a half angle less than $\Delta\theta$.
2. The area A_{gd} is large enough to represent an adequate spatial averaging of the terrain.
3. The ranges of angles θ_i , θ_s , and ϕ_s for which

items (1) and (2) above are satisfied must be as large as possible ($0 \leq \theta_i \leq \pi/2$, $0 \leq \theta_s \leq \pi/2$ and $0 \leq \phi_s \leq \pi$).

A.1.1 SAMPLING ANGLE $\Delta\theta$

The sampling angle $\Delta\theta$ which defines the half angle of the cone enclosing the measured area is related to the scattering geometry as follows:

$$\Delta\theta_i \approx \frac{r_A}{R_i} \cos \theta_i = \frac{r_A}{y_2} \cos^2 \theta_i \quad (A-1)$$

$$\Delta\theta_s \approx \frac{r_A}{R_s} \cos \theta_s = \frac{r_A}{y_1} \cos^2 \theta_s \quad (A-2)$$

where $\Delta\theta_i$ and $\Delta\theta_s$ are the angles corresponding to the transmitter and receiver, respectively. It is evident that for $\theta_i = \theta_s$, $\Delta\theta_s > \Delta\theta_i$ since $y_1 < y_2$.

A.1.2 LOWER LIMIT ON BANDWIDTH

A lower limit on the bandwidth can be based on the time separation between the direct transmitter - receiver path and the transmitter - surface - receiver path. To explain this, an approximate expression is derived for ΔR , the difference between the transmitter-surface-receiver path ($R = R_i + R_s$) and the direct path d .

From Figure A-1, the law of cosines yields

$$\begin{aligned} d^2 &= R_i^2 + R_s^2 - 2R_i R_s \cos \psi \\ &= R_i^2 + R_s^2 + 2R_i R_s - 2R_i R_s (1 + \cos \psi), \end{aligned} \quad (A-3)$$

where ψ is the angle between the incident and reflected directions. Then, since $R = R_i + R_s$,

$$R^2 - d^2 = 2R_i R_s (1 + \cos \psi) \quad (\text{A-4})$$

$$\Delta R(2R - \Delta R) = 2R_i R_s (1 + \cos \psi) \quad (\text{A-5})$$

or

$$(\Delta R)^2 - 2R(\Delta R) + 2R_i R_s (1 + \cos \psi) = 0 \quad (\text{A-6})$$

whence

$$\Delta R = R - R \sqrt{1 - \frac{2R_i R_s}{R} (1 + \cos \psi)} \quad (\text{A-7})$$

$$\frac{R_i R_s}{R} = \frac{R_i R_s}{R_i + R_s} \approx R_s \quad (\text{A-8})$$

The last equation is true for most cases of interest where $y_2 \gg y_1$ since

$$R_s = \frac{y_1}{\cos \theta_s} \quad \text{and} \quad R_i = \frac{y_2}{\cos \theta_i} \quad (\text{A-9})$$

whence

$$\frac{R_i}{R_s} = \frac{y_2}{y_1} \frac{\cos \theta_s}{\cos \theta_i} \quad (\text{A-10})$$

Even for the severe case of $\theta_s = 80^\circ$ and $\theta_i = 10^\circ$, it turns out, using $y_2 = 3000$ ft and $y_1 = 100$ ft, that

$$\frac{R_i}{R_s} = \frac{3000}{100} \times \frac{\cos 80}{\cos 10} = 5.3 \quad (\text{A-11})$$

Also,

Using the above approximation (A-7) reduces to

$$\Delta R \approx R - R \sqrt{1 - \frac{2R_s}{R} (1 + \cos \psi)} \quad (\text{A-12})$$

Since

$$R_s \ll R ,$$

ΔR can be approximated by

$$\Delta R \approx R_s (1 + \cos \psi) , \quad (\text{A-13})$$

where the bistatic angle ψ can be given in terms of θ_i , θ_s , and ϕ_s as

$$\cos \psi = \cos \theta_i \cos \theta_s - \sin \theta_i \sin \theta_s \cos \phi_s . \quad (\text{A-14})$$

Since $\cos \psi$ assumes its smallest value when $\phi_s = 0$, the expression for ΔR reduces to

$$\Delta R_{\min} \approx R_s [1 + \cos (\theta_i + \theta_s)] . \quad (\text{A-15})$$

Discrimination between the signal reflected from the surface and the direct path signal, based upon the time separation between the two signals at the receiver, imposes a lower limit on the receiver bandwidth for a maximum value of $\theta_i + \theta_s$.

It is natural to assume equal maximum values for θ_i and θ_s , say θ_{limit} ; hence,

$$\Delta R_{\min} \approx y_1 \frac{1 + \cos 2\theta_{\text{limit}}}{\cos \theta_{\text{limit}}} = 2y_1 \cos \theta_{\text{limit}} . \quad (\text{A-16})$$

Substituting $\Delta R = c/B$ where B is the system bandwidth and

c the velocity of propagation, the bandwidth is found to be

$$B = c / (2y_1 \cos \theta_{\text{limit}}) . \quad (\text{A-17})$$

Table A-1 depicts some values for θ_{limit} and the required bandwidth for $y_1 = 100$ ft.

A.1.3 CURSOR SYSTEM

The cursor system refers to the method used to define the region for which the bistatic cross section is measured. In addition to the requirements mentioned above on the definition of the region, it is necessary to be able to calculate, with reasonable precision, the area of the region. It is also necessary to provide sufficient isolation against reflections from neighboring regions, especially those that have a high bistatic cross section.

The options available in a coherent radar system include antenna beam selectivity, range resolution, and Doppler filtering or synthetic aperture processing. In addition, interferometer techniques can be combined with the radar system to improve angular resolution. The following discussion provides an estimate for the resolution available from these options to help design a working system.

In calculating the resolution capability of these techniques, use is made of the parameter $\Delta\theta$ corresponding to the half-angle of the cone (inside which the data are collected) around a given scattering direction rather than of the surface distance resolution, since the former is the more relevant for present purposes than the latter.

1. Antenna Pattern Selectivity

Antenna pattern selectivity is particularly suitable for bistatic measurement, since the angular interval $2 \Delta\theta$

TABLE A-1. BANDWIDTH VS. θ_{LIMIT}

θ_{limit} (deg)	B (MHz)
10	5.00
20	5.24
30	5.68
40	6.42
50	7.66
60	9.84
70	14.39
80	28.34
85	56.47

is independent of the scattering angle θ_s and is determined by the antenna beamwidth. Also, the received power is independent of the receiving antenna gain and the scattering area to receiver range R , as long as the area of the scattering region is determined solely by the receiving antenna beam.

The radar range equation can be expressed in terms of the effective receiving aperture A_R and the area A_{gd} on the ground determined by the receiving antenna as

$$P_r = \frac{P_i G_T}{4\pi R_i^2} \frac{A_{gd} \sigma_o}{4\pi R_s^2} A_R . \quad (A-18)$$

Then, making use of the facts that, for an aperture of length L_{ap} ,

$$A_R = \frac{G_R \lambda^2}{4\pi} \approx L_{ap}^2 \quad (A-19)$$

and

$$A_{gd} = R_s^2 \left(\frac{\lambda}{L_{ap}} \right)^2 ,$$

The radar range equation becomes

$$P_r = \frac{P_i G_T \lambda^2}{(4\pi)^2 R_i^2} \sigma_o . \quad (A-20)$$

The antenna beamwidth β is given approximately by

$$\beta \approx \frac{\lambda}{L_{ap}} . \quad (A-21)$$

To realize $\Delta\theta < 2.5^\circ$,

$$L_{ap} = \frac{\lambda \times 180}{2 \times 2.5 \times \pi} = 11.46\lambda .$$

For $\lambda = 23$ cm,

$$L_{ap} = 264 \text{ cm} = 8.67 \text{ ft.}$$

For $\lambda = 3$ cm,

$$L_{ap} = 34.4 \text{ cm} = 1.13 \text{ ft.}$$

2. Range Resolution

In reference to Figure A-1,

$$R_i = \frac{y_2}{\cos \theta_i} , \quad (A-22)$$

$$R_s = \frac{y_1}{\cos \theta_s} , \quad (A-23)$$

$$R = R_i + R_s = \frac{y_2}{\cos \theta_i} + \frac{y_1}{\cos \theta_s} , \text{ and} \quad (A-24)$$

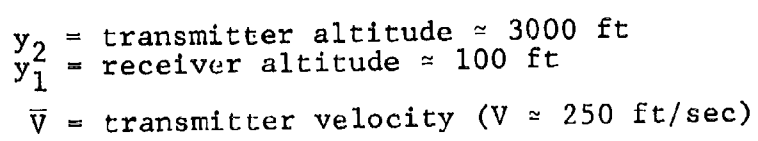
$$\frac{\partial R}{\partial \theta_s} = y_1 \frac{\sin \theta_s}{\cos^2 \theta_s} . \quad (A-25)$$

Therefore,

$$\Delta \theta = \frac{\Delta R \cos^2 \theta_s}{y_1 \sin \theta_s} \quad (A-26)$$

R is related to the effective receiver bandwidth by

$$\Delta R = \frac{c}{B} \quad (A-27)$$



A-9

Based on this relationship, the bandwidth required to resolve an angular interval $\Delta\theta$ is given by

$$B = \frac{c}{y_1 \Delta\theta} \frac{\cos^2 \theta_s}{\sin \theta_s} . \quad (A-28)$$

For an angular interval of 5° and $y_1 = 100$ ft, the required system bandwidth vs θ_s is tabulated in Table A-2. It is important to notice that range resolution capability can be used near grazing for angular resolution, where (1) the angular error $\Delta\theta$ gets to very small values which are hard to realize by antenna pattern selectivity and (2) the scattering measurements need that type of accuracy.

For measurements of σ_0 for $\theta_s \leq 60^\circ$ range gating cannot be consistently used, values of angular resolution as a function of θ_s for 30 MHz pulse bandwidth are given in Table A-3. Range gating can be used to separate the signal received via the direct path from the signal received via the bistatic scattered path. Also, range gating can be utilized to filter sidelobe contributions to the total received signal.

3. Simple Doppler Filtering

Considering the nominal values for the aircraft velocity (250 ft/sec) and the receiving tower height ($y_1 = 100$ ft), a nominal Doppler resolution (5 Hz) can be related to the angular measurement interval around θ_i and θ_s . The Doppler velocity v_d is given by

$$v_d = V \cos \theta_d . \quad (A-29)$$

Doppler frequency can be expressed as

$$f_d = \frac{V}{\lambda} \cos \theta_d . \quad (A-30)$$

Then,

TABLE A-2. BANDWIDTH REQUIRED FOR
 $\Delta\theta = 5^\circ$, $y_1 = 100$ FT

θ_s (deg)	B (MHz)
15	406.6
20	291.2
25	219.2
30	169.2
35	131.9
40	103.0
45	79.8
50	60.8
55	45.3
60	32.6
65	22.2
70	14.0
75	7.8
80	3.5

TABLE A-3. $\Delta\theta$ VS. θ_s FOR BANDWIDTH OF
30 MHz AND $y_1 \approx 100$ FT

θ_s (deg)	$\Delta\theta$ (deg)
15	67.67
20	48.53
25	36.54
30	28.20
35	22.00
40	17.16
45	13.29
50	10.14
55	7.55
60	5.43
65	3.70
70	2.34
75	1.30
80	0.57

$$\Delta f_d = \frac{v}{\lambda} \Delta \theta_d \sin \theta_d \quad (A-31)$$

or

$$\Delta \theta_d = \frac{\lambda}{v \sin \theta_d} \Delta f_d \quad (A-32)$$

The angle θ_d is related to the incidence geometry as follows:

$$\cos \theta_d = \sin \theta_i \cos q_s \quad (A-33)$$

Then,

$$\sin \theta_d \frac{\partial \theta_d}{\partial q_s} = \sin \theta_i \sin q_s \quad (A-34)$$

and so

$$\Delta q_s = \frac{\sin \theta_d}{\sin \theta_i \sin q_s} \Delta \theta_d \quad (A-35)$$

or

$$\Delta q_s = \frac{\lambda}{v} \frac{1}{\sin \theta_i \sin q_s} \Delta f_d \quad (A-36)$$

Table A-4 gives the value of Δf_d in Hz for different values of Δq_s in degrees for $\theta_i = 30^\circ$ and $q_s = 80^\circ$. The Doppler frequency used in the above calculation refers to the absolute Doppler frequency. Measurement of this absolute Doppler requires a non-modulated reference from the transmitter to the receiver. The absolute Doppler shift can be evaluated by studying the time history of the reference Doppler signal f_{do} . It is also of interest to study the relation between the relative Doppler

TABLE A-4. CHANGE IN DOPPLER VS. CHANGE
IN SQUINT ANGLE COMPLEMENT

Δq_s (deg)	Δf_d (Hz)
0.5	1.3
1.5	3.9
2.0	5.2
2.5	6.5
3.0	7.9
3.5	9.2
4.0	10.5
4.5	11.8
5.0	13.1
5.5	14.4
6.0	15.7

$$f_{dr} = f_d - f_{do} \quad (A-37)$$

and the angle ϕ_s . This Doppler, f_{dr} , is proportional to the rate of change of the path length difference ΔR (see Eqs. A-13 and A-14)

$$\begin{aligned} f_{dr} &= \frac{1}{\lambda} \frac{d\Delta R}{dt} \\ &\approx \frac{R_s}{\lambda} \frac{d \cos \psi}{dt} \\ &= - \frac{y_1}{\lambda} \sin \theta_i \tan \theta_s \frac{d \cos \phi_s}{dt} \\ &= \frac{y_1}{\lambda} \sin \theta_i \tan \theta_s \sin \phi_s \frac{d\phi_s}{dt} \end{aligned} \quad (A-38)$$

$d\phi_s/dt$ can be easily calculated by considering the planar projection of the scattering geometry in Figure A-2. This consideration leads to

$$\frac{d\phi_s}{dt} = \frac{V \sin(q_s - \phi_s)}{y_1 \tan \theta_s}, \quad (A-39)$$

whence the relative Doppler becomes

$$f_{dr} = \frac{V}{\lambda} \sin \theta_i \sin \phi_s \sin(q_s - \phi_s) \quad (A-40)$$

since $q_s \approx \pi/2$.

Thus,

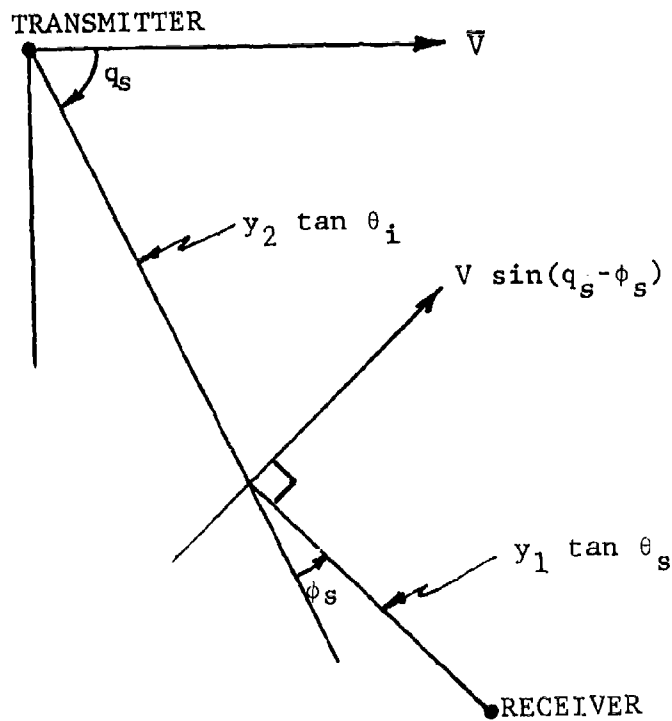


Figure A-2. Scattering Geometry for Relative Doppler

$$f_{dr} = \frac{V}{2\lambda} \sin \theta_i \sin 2\phi_s \quad (A-41)$$

and so

$$\frac{f_{dr}}{\partial \phi_s} = \frac{V}{\lambda} \sin \theta_i \cos 2\phi_s \quad (A-42)$$

From the latter, the increment of ϕ_s can be written as

$$\Delta \phi_s = \frac{\lambda}{V} \frac{\Delta f_{dr}}{\sin \theta_i \cos 2\phi_s} \text{ radians} \quad (A-43)$$

For the values

$$\lambda = 23 \text{ cm} ,$$

$$V = 250 \text{ ft/sec} ,$$

$$\theta_i = 30^\circ , \text{ and}$$

$$\Delta \phi_s = 0.3459 \frac{\Delta f_{dr}}{\cos 2\phi_s} \text{ degrees} \quad (A-44)$$

Table A-5 gives the required values of Δf_d for $\Delta \phi_s = 2^\circ$ for different values of ϕ_s . In all of the above Doppler measurements, the time of measurement must be greater than the inverse of the Doppler spread Δf_d . This severely restricts the possibility of measuring the relative Doppler f_{dr} . This is because, even if the Doppler frequency can be measured to within a fraction of a cycle, the maximum number of points/path is limited to a small number. For example, using the nominal value for the aircraft velocity as 250 ft/sec, a

TABLE A-5. CHANGE IN DOPPLER VS. ϕ_s

ϕ_s (deg)	Δf_d (Hz)
5	5.695
10	5.434
15	5.008
20	4.430
25	3.7.7
30	2.891
35	1.978
40	1.004
45	0.000

23 cm wavelength antenna beamwidth 10° to 12° , and a nominal value of $R_1 = 4$ to 5 miles, the transmitter beam illuminates the useful measurement area for about 20 seconds. If 2° accuracy is required in the estimate of ϕ_s , the measurement time is about 3 seconds, which means only 6 measurements per path. An even more severe limitation would arise if an attempt were made to use simple Doppler filtering to limit the bistatic measurement area.

A.1.4 CONCLUSION

The above analysis concludes that, within available capabilities of a bandwidth ≤ 50 MHz and simple Doppler filtering (no synthetic aperture processing) with a passband width of about 5 Hz:

1. Range gating and Doppler filtering cannot both be used to limit the measurement area (cursor system) except, possibly, for scattering angles near grazing.
2. Antenna beamwidth is particularly suitable and easier to use for determining the measurement area.
3. Range delay and absolute Doppler frequency measurements (simple Doppler filtering) can be used to determine the direction of incidence (θ_1 and ϕ_s). The reference for the absolute Doppler measurement can be obtained by study of the signal history of the direct path.
4. The range of scattering geometry is limited to the region described below:
 θ_1 : 30° to 80° (From aircraft altitude and maximum range considerations)

θ_s : 15° to 80° (The lower limit is set by the mechanical limit for scanning a 10 ft dish in the vertical plane.)

ϕ_s : 0° to 90° (In the forward scattering region.)

A.2 BISTATIC MEASUREMENT GEOMETRIES

This section describes problems and geometries associated with bistatic radar cross-section measurements. In the overall program, ERIM measured the bistatic terrain cross section as a function of the angles θ_i , θ_s , and ϕ_s shown in Figure A-1. Data in the neighborhood of $\phi_s = 0$ are of particular interest, although data in other regions are also important. Major problem areas are: (1) resolution, (2) selectivity, (3) signal-to-noise (S/N) ratio, (4) calibration, (5) data processing, (6) data statistics, and (7) data analysis. This section discusses the first three factors, and the last from the viewpoint of sidelobe contribution to received power.

Consider resolution. For meaningful data, the angles $\Delta\theta_i$, $\Delta\theta_s$, and $\Delta\phi_s$ which the scattering patch subtends at the transmitter or receiver must be small compared with θ_i , θ_s , and ϕ_s . The three methods of resolving the patch are antenna selectivity, ranging, and Doppler processing.

Good selectivity is important, because the power measured from a scattering patch must not be contaminated by the direct signal from the antenna, or by the power entering the sidelobes of the receiving antenna.

An adequate S/N ratio, which depends on the radar parameters, the geometry, and the type of processing, is necessary for accurate measurements.

A.2.1 SIDE-LOOKING SYSTEMS

Figure A-3 is a sketch of the side-looking geometry. The transmitting antenna has a narrow beam (12° at $\lambda = 23$ cm) orthogonal to the aircraft flight path. As the aircraft passes the receiving tower, the receiving system picks up the scattered signal. Since the tower height is much less than the aircraft altitude, the measured terrain is near the tower.

Consider ranging for resolving the terrain patches. The constant time delay contours lie far apart on the ground. Figure A-4 shows typical contours for an aircraft height of 3500 ft and a minimum ground separation of 4000 ft. The signal reaching the receiving antenna first follows the free-space path; this path length is 5249.8 ft. The first scattered return, which comes via the specular reflection point, has a path length of 5381.5 ft. Since the path difference is about 130 ft, the range resolution must be better than 130 ft to gate out the direct signal coming through the receiving antenna sidelobes. Power calculations show that the direct signal power will be much greater than the scattered power; therefore, range gating will be essential.

Figure A-4 has contours for path differences of 30, 60, 325, and 625 ft compared with the minimum path length via the specular reflection point. Since the contours are far apart, fine range resolution is necessary for isolation. A 30 MHz bandwidth yields a range resolution of 10 m, but $\Delta\theta_s$, the scattering angle subtended by the ground patch, is too large for measurement purposes, particularly near the tower. Ranging, however, is still needed for the rejection of the direct signal and sidelobe energy. Antenna selectivity remains the only method of securing resolution in the direction toward the flight path. For a narrow elevation beam, the

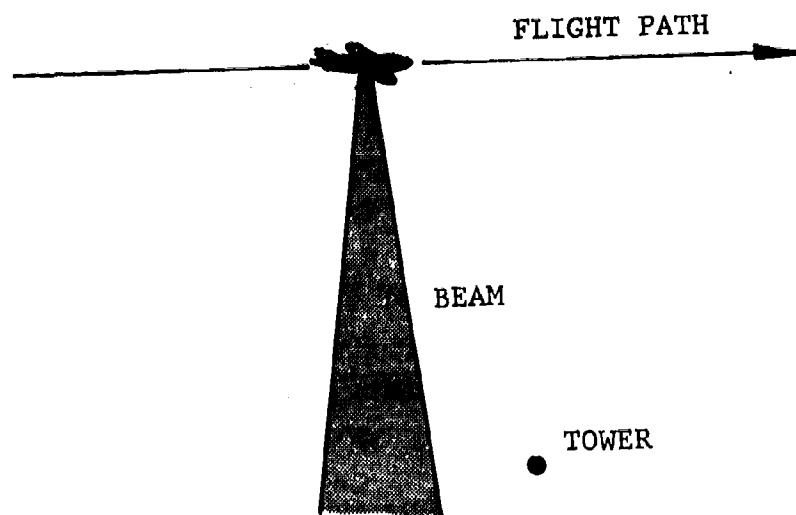


Figure A-3. Side-Looking Geometry

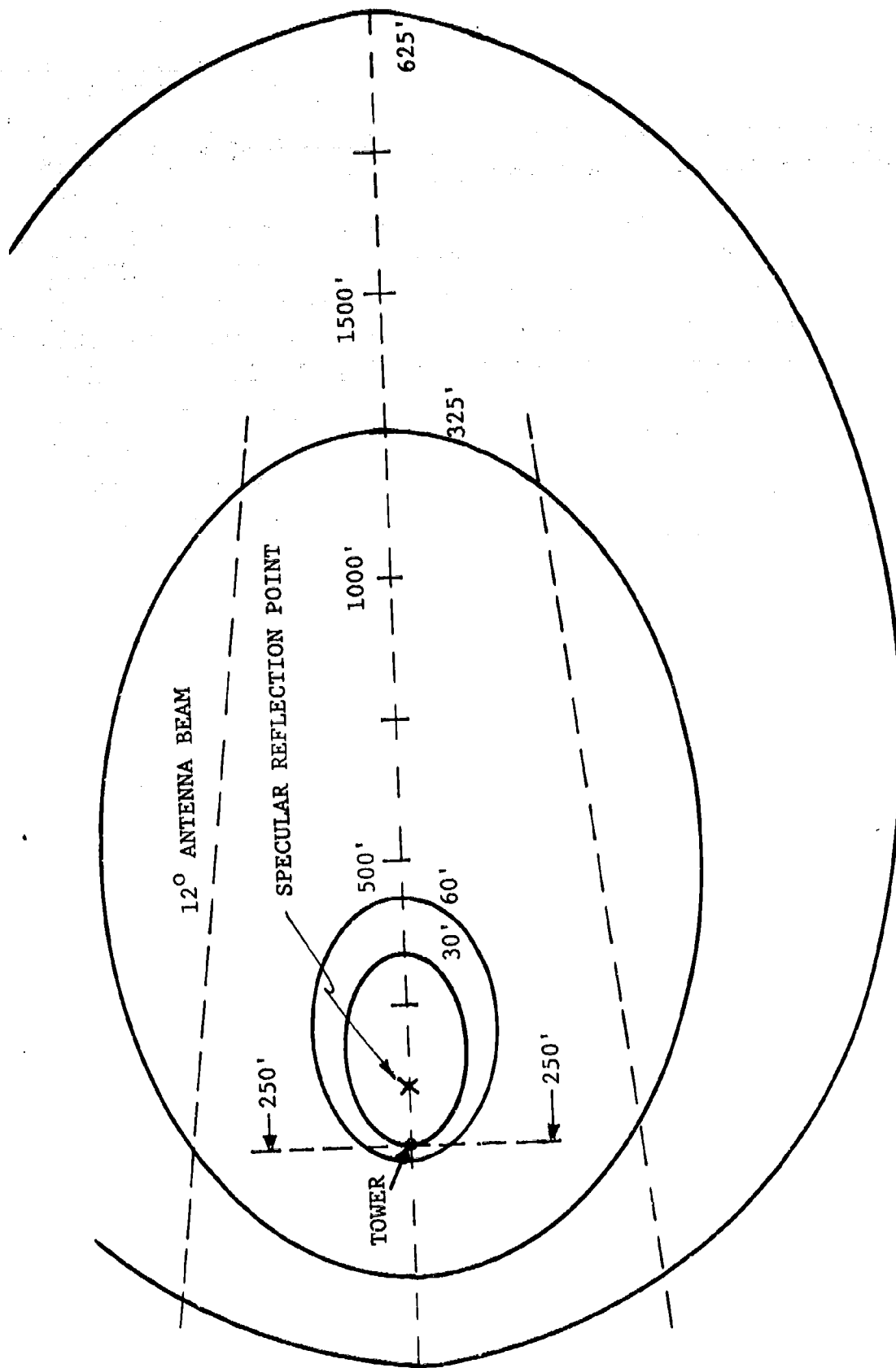


Figure A-4. Constant Range Ellipses
 (Tower Height = 100 ft, Aircraft
 Height = 3500 ft, and Minimum Ground
 Range = 4000 ft)

receiving antenna must have a large vertical aperture with weighting for sidelobe reduction.

Parallel to the flight path, a wide aperture with the corresponding narrow beam will furnish the necessary angular selectivity or, alternatively, Doppler processing will yield resolution which is independent of the slant range from the receiving antenna. With a monostatic synthetic array radar and a broadside antenna, the theoretical resolution is half the antenna aperture or $D/2$. For the geometry of Figure A-3, the best possible resolution with a stationary antenna and Doppler processing is D . In the bistatic case, the phase shift is half that in the monostatic case, doubling the resolution.

With synthetic aperture processing, the target must remain within a range resolution cell in spite of range curvature. For Figure A-4, the slant range to a patch will vary $5 \frac{1}{4}$ ft during a pass with a 12° transmitter beam. At a 20,000 ft range, the slant-range change increases by $36 \frac{1}{2}$ ft; hence, the range resolution must then be greater than $36 \frac{1}{2}$ ft. A 30 MHz bandwidth with 30 ft resolution is not possible at this range. Range curvature thus dictates a compromise between range and azimuth resolution.

An alternate receiving system has an antenna beam narrow in elevation but broad in azimuth as in Figure A-5. Synthetic aperture processing supplies good azimuth resolution for patch separation, but the maximum allowable value of $\Delta\phi_s$ limits the azimuth resolution. If $\Delta\theta_s < 3.5^\circ$, only half of the 12° transmitter beamwidth can be processed, and the azimuth resolution is twice the transmitting antenna aperture or 13.4 ft. When $\theta_s = 45^\circ$, a 13.4 ft width subtends an angle of 5.5° from the 100 ft receiving tower. Here again, there is a trade-off. Fine azimuth resolution requires too large a

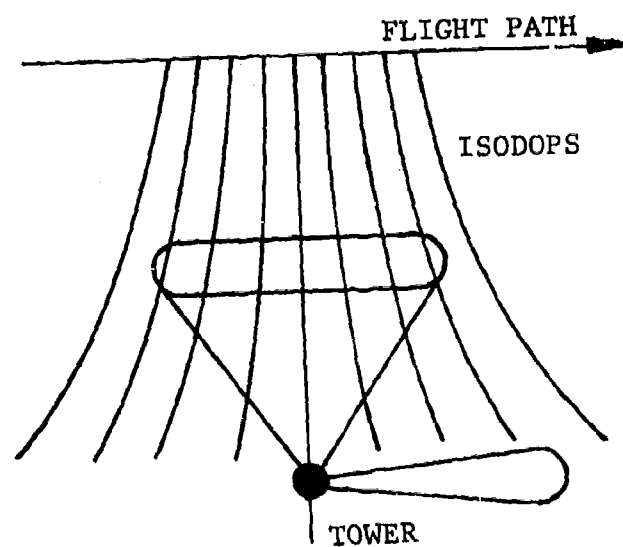


Figure A-5. Receiving System with Narrow Fixed Beams

value of $\Delta\phi_s$ from the transmitter; on the other hand, with poorer resolution, the patch subtends too large a $\Delta\phi_s$ value at the receiver.

The angle θ_s determines the number of data points per pass; there are more points when the antenna has a low depression angle. When $\theta_s = 45^\circ$, there are about 15 data samples per pass; when $\theta_s = 80^\circ$, the number of data samples increases to 85.

For $45^\circ < \phi_s < 135^\circ$, a similar system can be used, except that the receiving antenna beam becomes narrow in azimuth and broad in elevation (Figure A-5). Synthetic aperture processing can supply fine resolution in the direction normal to the isodops.

The fixed-beam system has the advantage of mechanical simplicity, because the antenna does not scan. Its disadvantages are a more complex receiver and processing compared with a scanning system.

If trading simplicity in the receiver for poorer resolution is acceptable, an unfocused synthetic array can be used. With an unfocused array, the resolution is approximately:

$$\sqrt{\frac{\lambda R_i}{2}}$$

for the geometry of Figure A-3. At a slant range of 5000 ft and a wavelength of 23 cm, the unfocused resolution will be 43 ft. Better resolution is necessary near the tower to keep $\Delta\phi_s$ small enough.

Another method of acquiring data is to scan the area near the receiving tower with a large dish as the aircraft flies past and illuminates the area (Figure A-6). A 3° receiving beam requires a 5 m dish at a 23 cm wavelength. The

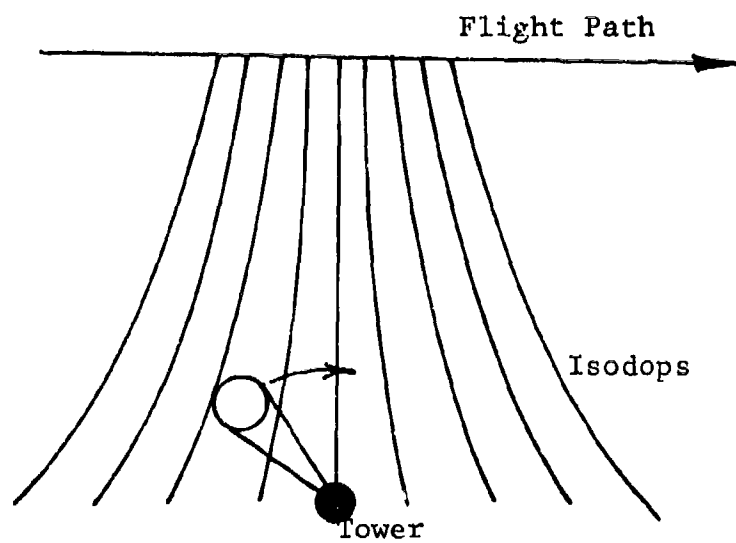


Figure A-6. Receiving System with Narrow Scanning Beam

12° transmitter beam is 650 ft wide at the 5300 ft slant range of Figure A-4. At a velocity of 250 fps (170 mph) the beam passes over the receiving tower in 2.6 seconds, requiring a rapid scan. With a 3° beamwidth, there are 60 data points for a 180° scan. There is no synthetic aperture processing with this system, and the receiver can be either coherent or noncoherent. With a coherent receiver, the S/N ratio is greater because coherent pulse integration is more efficient than noncoherent.

The scanning receiving system has the advantage of simplicity. The disadvantage is mechanical; it is difficult to turn a large antenna rapidly enough to scan the illuminated area. Increasing the slant range to 5 miles increases the illumination time to 13 seconds and lowers the required scanning speed. With a dual-polarized feed, data can be collected with parallel and crossed polarizations simultaneously, reducing the number of passes required.

A.2.2 SPOTLIGHT SYSTEM

After evaluating the various measurement techniques considered (and reviewed in this appendix), the spotlight bistatic measurement technique was selected for the operational system. This technique is illustrated in Figure 8.

The results of the analyses discussed in this appendix show that the use of a receiving antenna aperture to define the scattering area A_{gd} provides the most accurate measure of A_{gd} ; this approach is utilized as part of the spotlight bistatic technique. Also, the data reduction process for the spotlight technique was determined to be more easily programmed and to have greater accuracy, when compared with the other techniques considered. In summary, the spotlight technique satisfies the following major requirements:

1. Basic sampling theory requires as many independent samples of σ_0 as possible for each set of bistatic angles, with four being the minimum acceptable number. The spotlight geometry, along with the scanning receiving antenna, provides a maximum number of data samples for each data-collection pass. Adequate sampling is a particular problem at 23 cm, as discussed in Section 5.5, and this problem is resolved by the use of the spotlight technique.
2. The spotlight system provides data over the complete azimuthal range of angles for any realizable incidence and scattering angles.
3. With the information obtained from the automatic tracking system (that is, the illumination angle from the aircraft to A_{gd}) and the angular information from the receiving antenna scan, the bistatic azimuth angle is easily determined.

Operational parameters are adjusted so that the receiving antenna scans through the specified range of ϕ_{SCAN} during a period in which the illumination angle, ϕ_{TRACK} , changes by 5° or less. The separation between the receiver and the transmitter is made large to insure that the area illuminated by the 12° transmitting antenna beam is larger (by at least a factor of 3) than the sector scanned by the receiving antenna. Based on these considerations, the required receiving antenna scan time (one-way scan) was determined to be 8 seconds.

The geometry and power available allowed the measurement of a minimum σ_0 value of -40 dB at 23 cm and -20 dB at 3 cm.

A.2.3 SIDELobe CONTRIBUTION TO RECEIVED POWER

For those situations where the specular point may be present in the sidelobe region of the receiver antenna footprint, one must be concerned that its effect may outweigh the mainbeam return. This section addresses this problem and concludes that the presence of the specular point in a receiver antenna sidelobe should not give undue weight to that portion of the return.

Reference A-1 provides the observation (from Grant and Yaplee measured data, 1957) that, at $\lambda = 3$ cm, grass-covered terrain may behave like an isotropic radiator with

$$\sigma(\theta) = \sigma_0(0) \cos^2 \theta, \quad (\text{A-45})$$

where $\sigma_0(0)$ is the normal incidence monostatic return which may vary between -30 dB and -15 dB. Thus (Figure A-7), there is about a 15 dB variation in $\sigma_0(\theta)$ over a 30° angle off normal.

Not all measured data agree with the above. Some observations show $\sigma_0(\theta)$ dropping off more rapidly from the normal-incidence value than the above equation indicates. Nevertheless, Eq. (A-45) affords a starting point for further discussion.

One approach is to apply the above equation to the bistatic case by stretching the Bistatic Theorem. This theorem says that, if scattering surface curvature is large enough, smooth enough, and perfectly conducting (the latter two conditions are surely not fulfilled), the bistatic return is

A-1. R. Beckmann and A. Spizzichino, The scattering of Electromagnetic Waves from Rough Surfaces, MacMillan Co., New York, 1963, p. 410.

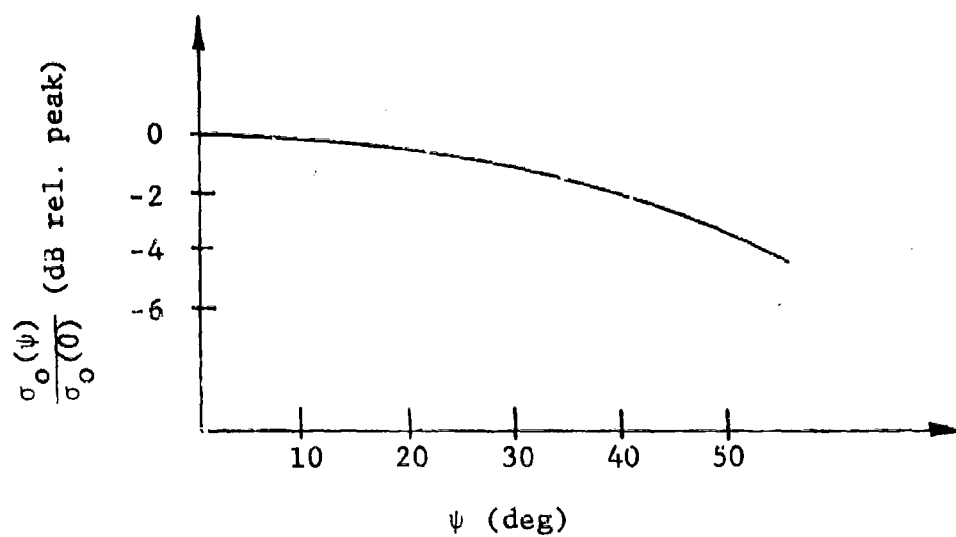


Figure A-7. Theoretical Estimate of $\sigma_O(\psi)/\sigma_O(0)$
for Short Grass at $\lambda = 3$ cm

equivalent to the monostatic return at the bisector of the bistatic angle. Assuming the applicability of this theorem to terrain scattering, one can conclude, with the help of the above equation, that specular and non-specular returns should not differ much, at least out to equivalent monostatic angles of 30° off-normal. Thus, if the specular point should fall in a receiver sidelobe, it would not unduly overweigh the contribution from that sidelobe. So one may account for sidelobe energy simply on the basis of proportional area subtended by a certain sidelobe angular width (fixed by some pre-assigned level of interest).

This last approach is used to estimate the amount by which sidelobe return falls below mainlobe return, using -30 dB/ML* contours as the level of interest. In this event, only the first sidelobe is of importance since the second sidelobe peak is -33.6 dB/ML. For a range of values of θ_s , one finds the levels by which mainlobe return exceeds (in dB) sidelobe return; see Table A-6.

A.3 TWO AIRCRAFT MEASUREMENT SYSTEM

Using two aircraft, one with an illuminating source and a second with the receiving system, bistatic images can be formed from recorded received signals in a manner similar to SAR system techniques. This provides bistatic scattering data for a very wide area, bistatic clutter statistics can then be obtained for a very wide range of terrain types and scenes.

*dB relative to the mainlobe.

TABLE A-6. RATIOS OF MAINLOBE TO
SIDELOBE RETURN

θ_s (deg)	ML/SL (dB)
15	22.8
30	22.7
45	22.5
60	21.9
75	17.7

APPENDIX B INSTRUMENTATION

A brief discussion of the instrumentation for the bistatic measurements program is presented in Section 3. The purpose of this appendix is to provide additional details regarding certain aspects of the experimental system. In particular, further information is given on bistatic antennas (Section B.1), bistatic receivers (B.2), and data recorders (B.3).

B.1 BISTATIC ANTENNAS

B.1.1 PRIMARY FEED DESIGNS FOR RECEIVING ANTENNAS

The 3 cm wavelength feed consists of a 2.5 x 2.5 cm square section of waveguide fitted with mode suppressors and impedance devices. The radiating aperture is flared slightly to provide the necessary illumination for the 46 cm diameter reflector. Vertical and horizontal polarizations are obtained by appropriately exciting the square waveguide from its rear and side walls.

The 23 cm wavelength feed consists of four dipoles arrayed in a $0.6 \times 0.6\lambda$ square configuration. One parallel set of dipoles provides reception at horizontal polarization and the other (orthogonal) pair provides vertical polarization. The four dipoles are mounted nominally $\lambda/4$ in front of a 30.5 cm diameter ground plane to achieve the desired illumination taper for the 3.1 m diameter parabolic reflector.

Note that each reflector has a focal length-to-diameter ratio F/D of 0.45.

B.1.2 RECEIVING ANTENNA SYSTEM TEST RESULTS

The VSWR, antenna gain, polarization isolation, half-power beamwidth, and first sidelobe level were measured for both the 3 cm and the 23 cm wavelength antenna systems. Typically, the VSWRs of both feeds are less than 1.5:1 relative to 50 ohms and both antenna gains are 30 dB above isotropic.

Pattern data were collected for five orientations of the antennas. With the observer stationed behind the transmitting antennas and looking toward the receiving antennas (while the two antenna systems are pointed toward each other), both antennas were initially positioned (Orientation No. 1) so that the transmitting horn and one set of receiver dipole elements were vertically polarized. For Orientations Nos. 2 and 3, the transmitting and receiving antennas were simultaneously rotated (+) 30 and 60° clockwise (as viewed from the transmitter) about their axes. For Orientations Nos. 4 and 5, the antennas were similarly rotated counter-clockwise (-) 30 and 60°. The data are summarized in Tables B-1 and B-2 for the 3 cm and 23 cm wavelength antennas, respectively.

The complete receiving antenna system is mounted on a pedestal to permit azimuth scanning. Since an APS-23 radar antenna pedestal was available at ERIM, it was used during the experiment. Unfortunately, the torque capacity of the pedestal was limited. One servo drive motor was destroyed by wind loading; the wind velocity was approximately 15 kts. All subsequent operation was therefore limited to conditions when winds were less than 10 kts.

B.1.3 CROSS-POLARIZATION ISOLATION

During the bistatic measurement program, both parallel and cross-polarized σ_0 values were measured. The cross-

polarization isolation of both the transmitting and receiving antennas places a lower limit on the cross-polarized σ_o values that can be measured; this appendix discusses that limit.

The bistatic radar equation gives the relationship between the received and transmitted power. Thus,

$$P_r = \frac{P_i G_T G_R L \lambda^2 \sigma_o A_{gd}}{(4\pi)^3 R_i^2 R_s^2} \quad (B-1)$$

In order to investigate cross-polarized σ_o , it is necessary to account for additional components. For simplicity, assume for the purposes of this analysis that the transmitting antenna is radiating vertical polarization and it is desired to measure σ_{oVV} and σ_{oVH} . Assume also that there are two receiving antennas, one with vertical and the other with horizontal polarization.

Ideally, the aircraft would transmit only vertical polarization, but in practice there is also a horizontal component. Let G_{TV} and G_{TH}^* be the transmitting antenna gains with vertical and horizontal polarization, respectively; an asterisk is used to designate the spurious gain component.

The power received by the vertical receiving channel, P_{rV} , will then be

$$\begin{aligned} P_{rV} = & \overset{(1)}{G_{RV} G_{TV} \sigma_{oVV}} + \overset{(2)}{G_{RV} G_{TH}^* \sigma_{oHV}} \\ & \overset{(3)}{+ G_{RH}^* G_{TV} \sigma_{oVH}} + \overset{(4)}{G_{RH}^* G_{TH} \sigma_{oHH}} \end{aligned} \quad (B-2)$$

Term (1) on the right side of Eq. (B-2) is the desired power component. Term (2) represents power coupled into the

vertical receiving channel through the cross-polarization scattering coefficient σ_{OHV} ; this power was transmitted to the ground with horizontal polarization and gain G_{TH}^* . The third term represents power coupled into the channel through the cross-polarization scattering coefficient σ_{OVH} and received with antenna gain G_{RH}^* . Finally, term (4) represents power coupled through both spurious antenna gain components (G_{TH}^* and G_{RH}^*) and the parallel-polarization scattering coefficient σ_{OHH} .

By reciprocity,

$$\sigma_{OVH} = \sigma_{OHV} \quad (B-3)$$

Normally, σ_{OVH} is 8 or more dB below σ_{OVV} or σ_{OHH} . The cross-polarization isolations for the transmitting and receiving antennas are all better than 20 dB*, that is, G_{TH}^* and G_{RH}^* are each at least 20 dB below G_{TV} and G_{RV} , respectively. Then, terms (2) and (3) are each at least 28 dB below (1), and term (4) is at least 40 dB below (1). With smooth materials such as sand, $\sigma_{OVH} \gg \sigma_{OVV}$ at some angles and an appreciable error in the measurement can result, because (2) and (3) will then be large compared with (1).

For the cross- or horizontally-polarized receiving channel, the received power P_{RH} can be written

* Cross-polarization isolations for the transmitting antennas are > 25 dB (3 cm wavelength) and > 20 dB (23 cm wavelength). Similarly (see Tables B-1 and B-2), the respective isolations for the receiving antennas are > 27 dB and > 31 dB.

TABLE B-1. 3 cm WAVELENGTH RECEIVING ANTENNA DATA

Frequency = 9.45 GHz
 Gain = 30.5 dB/isotropic
 Cross-Polarization Isolation = 27 dB

<u>Polarization</u>	<u>Sidelobe (dB)</u>	<u>3 dB Beamwidth (deg)</u>
H	-24	5.8
V	-22	5.8
+30	-24	5.7
+60	-23	5.8
-30	-24	5.7
-60	-25	5.8

TABLE B-2. 23 cm WAVELENGTH RECEIVING ANTENNA DATA

Frequency = 1.315 GHz
 Gain = 30.2 dB/isotropic
 Cross-Polarization Isolation = 31 dB

<u>Polarization</u>	<u>Sidelobe (dB)</u>	<u>3 dB Beamwidth (deg)</u>
H	-24	5.8
V	-24	6.0
+30	-25	5.9
+60	-25	6.8
-30	-25	5.9
-60	-27	6.0

$$\begin{aligned}
 P_{RH} &\approx G_{RH} G_{TV} \sigma_{OVH} + G_{RH} G_{TH}^* \sigma_{OHH} \\
 &+ G_{RV}^* G_{TV} \sigma_{OVV} + G_{RV}^* G_{TH} \sigma_{OHV} .
 \end{aligned}
 \tag{B-4}$$

Terms (1) and (4) in Eq. (B-4) represent the desired scattered power; term (1) is 40 dB or more above (4) because G_{RV}^* and G_{TH}^* are each 20 dB or more below G_{RH} and G_{TV} , respectively. For an accurate measurement of σ_{OVH} , it is required that

$$\begin{aligned}
 G_{RH} G_{TV} \sigma_{OVH} &>> G_{RH} G_{TH}^* \sigma_{OHH} \text{ and} \\
 G_{RH} G_{TV} \sigma_{OVH} &>> G_{RV}^* G_{TV} \sigma_{OVV} ,
 \end{aligned}
 \tag{B-5}$$

or, rewriting,

$$\frac{G_{TV}}{G_{TH}^*} >> \frac{\sigma_{OHH}}{\sigma_{OVH}}
 \tag{B-6}$$

and

$$\frac{G_{RH}}{G_{RV}^*} >> \frac{\sigma_{OVV}}{\sigma_{OVH}} .
 \tag{B-7}$$

Equations (B-6) and (B-7) state that the cross-polarization isolations of the transmitting and receiving antennas must be much greater than the ratio of the parallel to the cross-polarization σ_o components.

Errors in the geometrical alignment between the transmitting and receiving antennas can increase the spurious responses. Table B-3 lists the ratios of cross-polarized to parallel-polarized components at the receiver resulting from

TABLE B-3. SPURIOUS CROSS-POLARIZED COMPONENT CAUSED BY AN ERROR BETWEEN TRANSMITTING AND RECEIVING ANTENNA AXES

<u>Angular Error</u> (deg)	<u>Cross-Polarized Component</u> (dB)
1	-35
2	-29
3	-26
4	-23
5	-21
6	-20

$$\frac{\text{Cross-Polarized Component}}{\text{Parallel-Polarized Component}} = \frac{\sin^2 \epsilon}{\cos^2 \epsilon}$$

ϵ = alignment error between antenna axes

various angular orientation errors between the transmitting and receiving antennas. Note that an error of 6° reduces the isolation to 20 dB.

Based on the above analysis, it is clear that, in any bistatic data gathering program, the receiving and transmitting antenna orientations must be kept parallel in order to minimize spurious components in the received signals. Also, σ_{OVH} values which are too far below σ_{OHH} or σ_{OVV} must be discarded, because such readings will be contaminated by feedthrough of σ_{OHH} or σ_{OVV} .

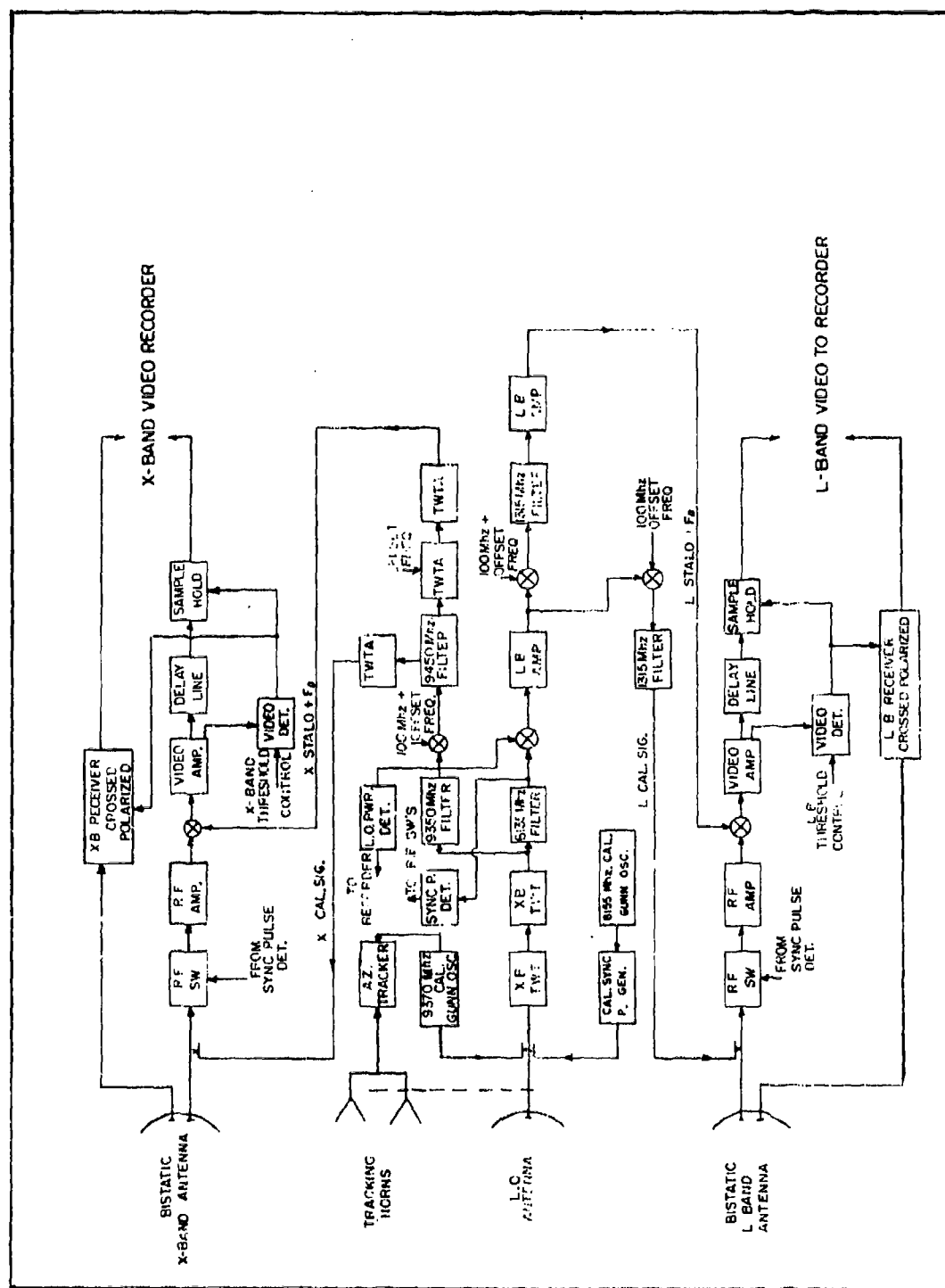
B.2 BISTATIC RECEIVERS

This section discusses the operation of the bistatic receivers; see Figures B-1 through B-5.

B.2.1 REQUIRED FUNCTIONS

An automatic means of gathering data on a pulse-to-pulse basis is needed to measure the bistatic σ_o during the flight tests. The method selected is to use the received video itself to trigger the sample-and-hold circuit, which then measures the amplitude of the video signal via a delay line. In order to implement such a technique, the following functions are required:

First, a device is needed to switch the bistatic receivers off until the direct-path transmitted pulse has passed the receiving antenna platform. This is done by installing RF switches at the inputs of the 3 cm and 23 cm wavelength parallel receivers (see Figure B-1); these switches insure that only the bistatic signal returns from the ground are allowed to enter the inputs of the receivers. To accomplish this, a synchronizing pulse originating aboard the C-46 is received and detected at the ground site; it is



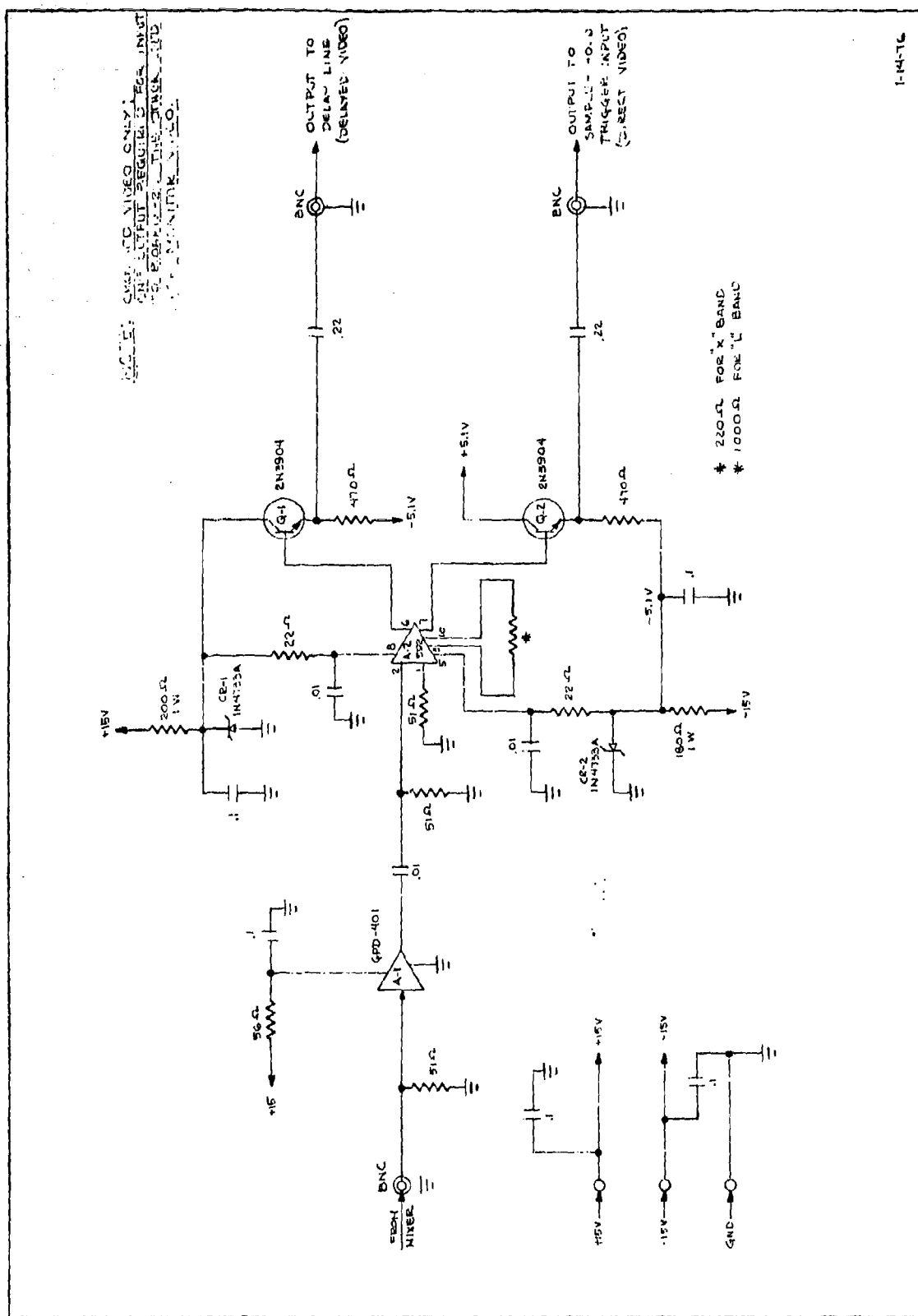


Figure B-2. Video Amplifier Circuit Diagram

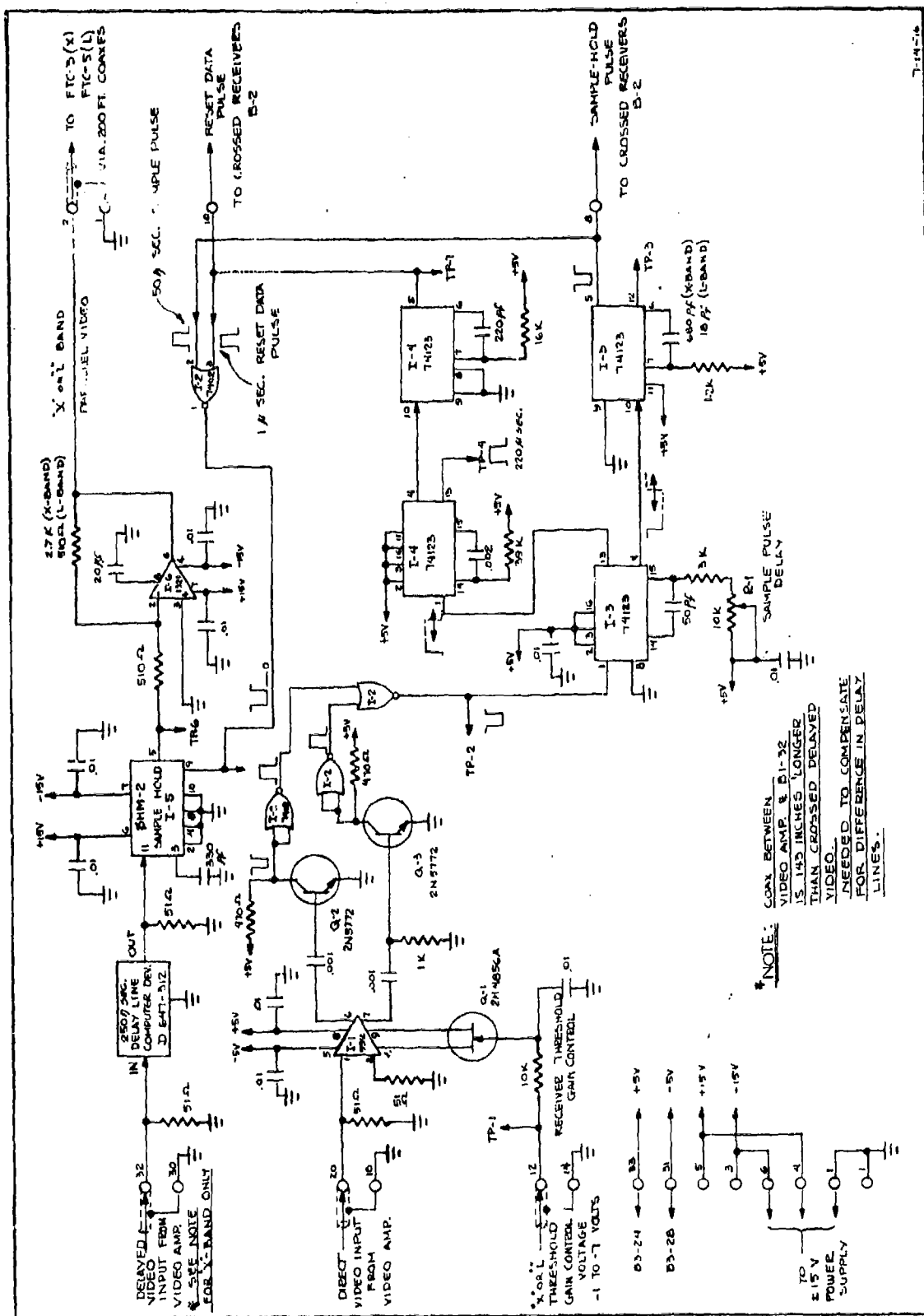


Figure B-3. Parallel Receiver Circuit Diagram

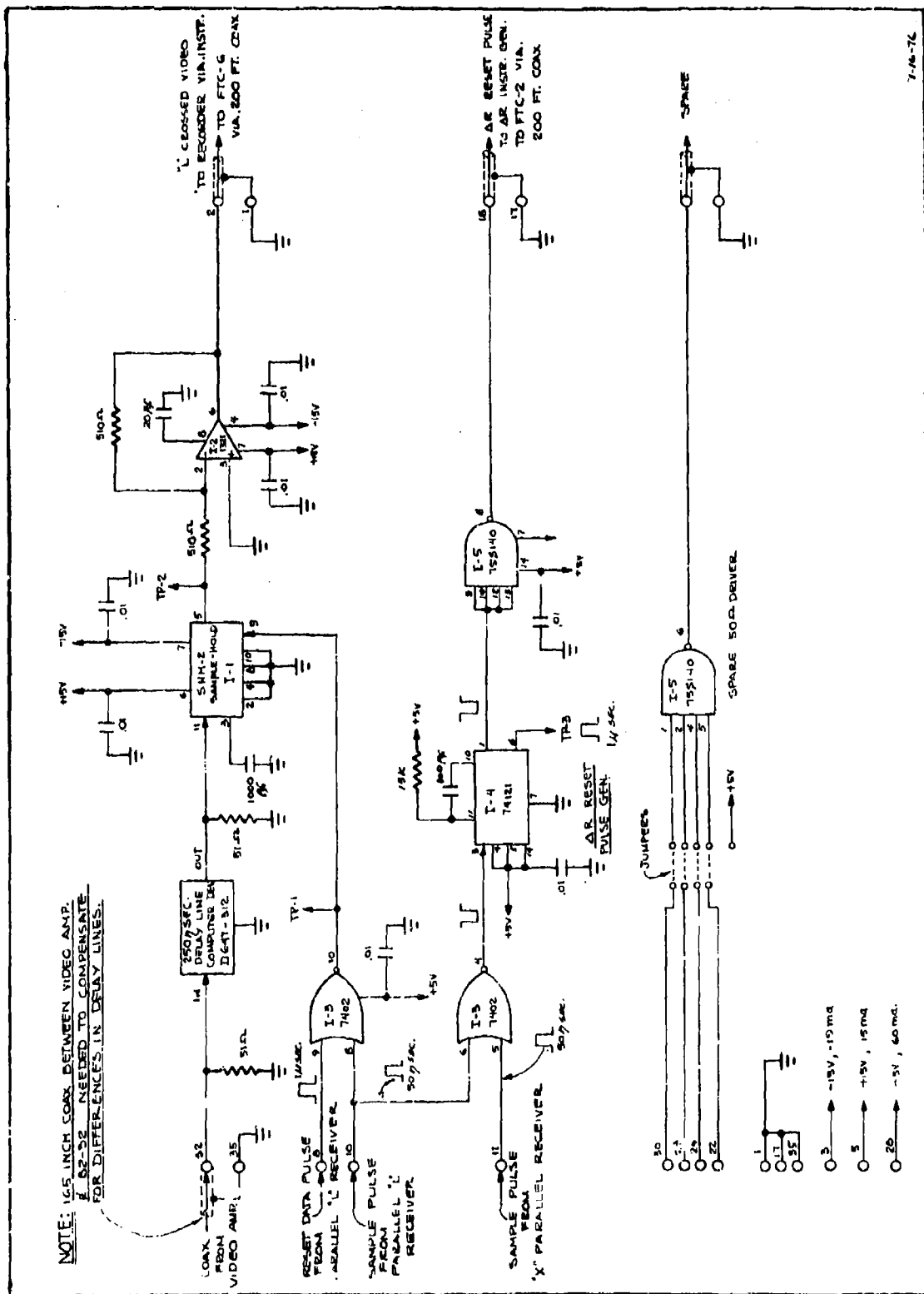


Figure B-5. Crossed Receiver Circuit Diagram for $\lambda = 23$ cm

then conditioned with appropriate delays and used to trigger the RF switches. The RF switch "on" time did not exceed 3 μ sec during the flight tests; a minimum "on" time of 1.6 μ sec was used on the last flight. The "off" time provided attenuation greater than 60 dB at the input of each receiver.

Second, the received video pulse needs to be delayed in order that the sample-hold gate can measure its peak amplitude. A 250 nsec delay line with rise and fall times of less than 20 nsec is used to perform the delayed video pulse function (see Figures B-1, B-3, B-4, and B-5).

Third, a threshold gain adjustment is needed to control the 3 cm and 23 cm wavelength receivers in order to keep the receivers from triggering on noise or signals received via the sidelobes of the antenna. This function is implemented by controlling the gain of a video amplifier used to trigger the sample-hold circuits. The threshold setting is adjusted using a known calibrate input RF signal controlled from the van.

B.2.2 SEQUENCE OF EVENTS

The following sequence of events occurs in order to obtain the desired data on a pulse-to-pulse basis:

1. The RF switches in the two parallel-polarization receivers are triggered "on" (minimum attenuation) for a predetermined time interval of 1.5 to 3.0 μ sec.
2. If an RF signal is present during this "on" time, it is amplified and detected at the video mixer, resulting in a coherent bipolar video pulse of at least 50 nsec width in each receiver.
3. Each received pulse is further amplified by a video amplifier (Figure B-2) whose output is

coupled both to a delayed video path and to a direct video path. The delayed path is the data acquisition channel and utilizes a 250 nsec delay line. In the direct channel, the video pulse is further amplified, making it possible for this pulse to trigger a delay gate. Since the video pulse can be either positive- or negative-going, appropriate interface logic is required in order to trigger on either polarity. The leading edge of the video pulse triggers the delay gate, which, in turn, triggers a 100 nsec sample-hold gate.

4. The delay gate control is adjusted so that the 100 nsec sample-hold gate intercepts the delayed video pulse at such a time as to cause a peak voltage response at the output of the sample-hold circuit. Each sample-hold gate is also coupled to the corresponding crossed-polarization receiver sample-hold circuit to perform the same function. In this manner, the peak amplitude of each 50 nsec video pulse is held for data processing.
5. The output of the sample-hold delay circuit also triggers a data-reset delay circuit. This delay is 220 μ sec; at the end of this time interval, a 1 μ sec data-reset pulse occurs. The 1 μ sec pulse resets each sample-hold circuit to zero volts. Thus, the output of each sample-hold circuit displays a rectangular waveform of 220 μ sec with a reset time of about 30 μ sec. This 30 μ sec reset time between PRF pulses was selected because the FR-1300 tape recorder has rise and fall times of about 20 μ sec; thus, the tape recorder is allowed to recover before the next PRF data pulse occurs.

The sample-and-hold data pulse (receiver output) is amplified and directed down a 200 ft coax where it is coupled to the instrumentation boards. The instrumentation boards condition the receiver outputs for the FR-1300 tape recorder and the analog strip-chart recorder. An analog readout of the data is implemented by injecting the digital data (sample-hold output) into a true RMS-to-dc converter. The converter output is further conditioned through a logarithmic amplifier before being coupled to the strip-chart recorder for monitoring purposes.

B.2.3 SAMPLE-HOLD OUTPUT RESPONSE

In order to properly adjust the bistatic receivers, a test was conducted to determine their output response. In this test, a pulse generator was used to simulate the received RF pulse at the input to the video amplifier; a 40 nsec pulse width occurring at a 4 kHz PRF rate served as the video input signal. The input amplitude was maintained constant while incremental adjustments of the sample-hold time delay circuit were made. Figure B-6 shows the measured output response; this curve represents the shape of the sampled test pulse.

The input pulse from the pulse generator had a rise and fall time of less than 5 nsec. Note, however, that the rise and fall time is about 25 and 20 nsec, respectively, for the output plotted in Figure B-7. This occurs because the rise and fall times of the delay lines are a nominal 20 nsec. The dotted lines shown in the figure are drawn because the output response at delays of -50 and +40 nsec from the peak value exhibits a voltage polarity reversal. This polarity reversal is caused by the overshoot characteristics of the video amplifier.

The normal operating setting of the sample-hold delay

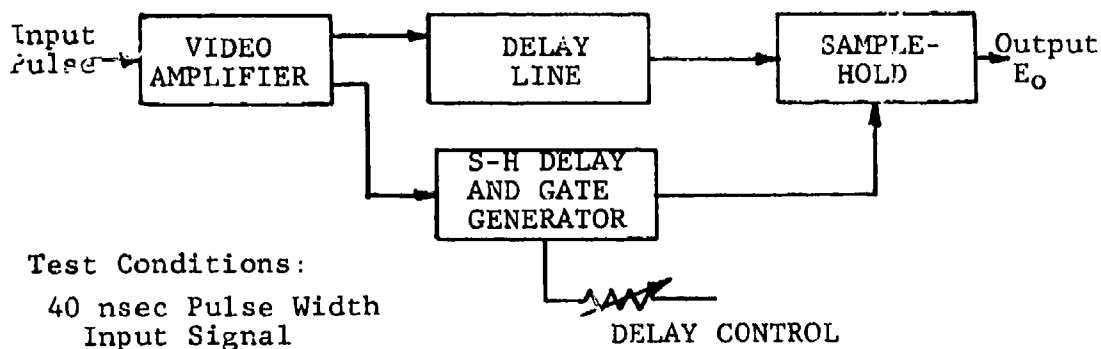
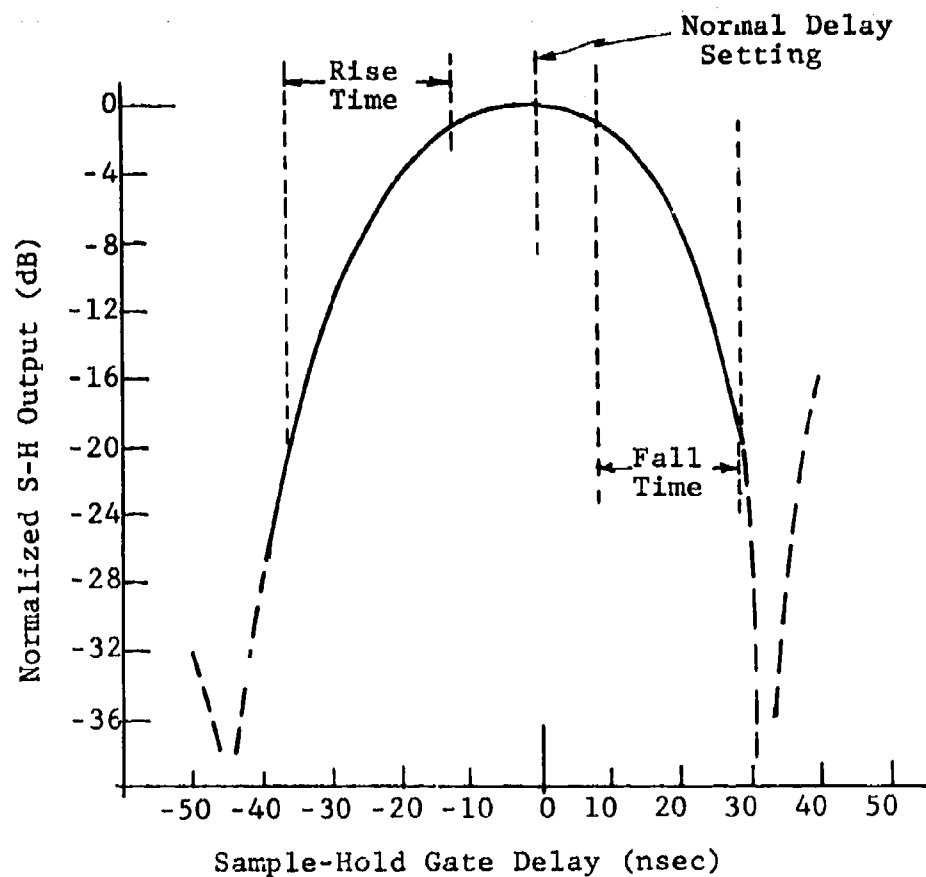


Figure B-6. Sample-Hold Output Response vs. Sample-Hold Gate Delay

is to center the sample-hold gate at the peak of the pulse response. This is done by using the system's 50 nsec RF calibration pulse as the input while observing the output with a digital RMS voltmeter.

B.2.4 LOCAL OSCILLATOR

A 46 cm diameter, parabolic, 3 cm wavelength antenna is used to receive the two STALO frequencies transmitted from the aircraft. This antenna is mounted on the tracker pedestal and is boresighted with respect to the two azimuth tracking horns. The 9350 and 8135 MHz STALO frequencies transmitted from the aircraft make the bistatic dual-band receivers coherent with respect to the transmit pulses. These two frequencies are amplified and mixed to produce the L.O. frequencies for the 3 and 23 cm wavelength receivers.

Figure B-7 shows plots of the output L.O. powers versus the input RF powers; two Gunn oscillators were used to simulate the received 3 cm STALO frequencies for this test. The oscillators' outputs were coupled to the input of the first TWT via a directional coupler (see Figure B-1). The 9350 MHz frequency is amplified, up-converted to 9450 MHz, and amplified again, resulting in the output power level shown in Figure B-7. Similarly, the 23 cm L.O. signal is the difference frequency (1215 MHz) which results from mixing the 9350 and 8135 MHz signals. In the figure, both bands show a wide range of operating input power levels corresponding to approximately constant output L.O. power levels. Based on Figure B-7, the operating range is defined to include all input power levels which exceed -70 dBm and which are less than -45 dBm.

Instrumentation is provided in the system with which to record the received STALO input power levels. These levels are monitored by the analog strip chart recorder.

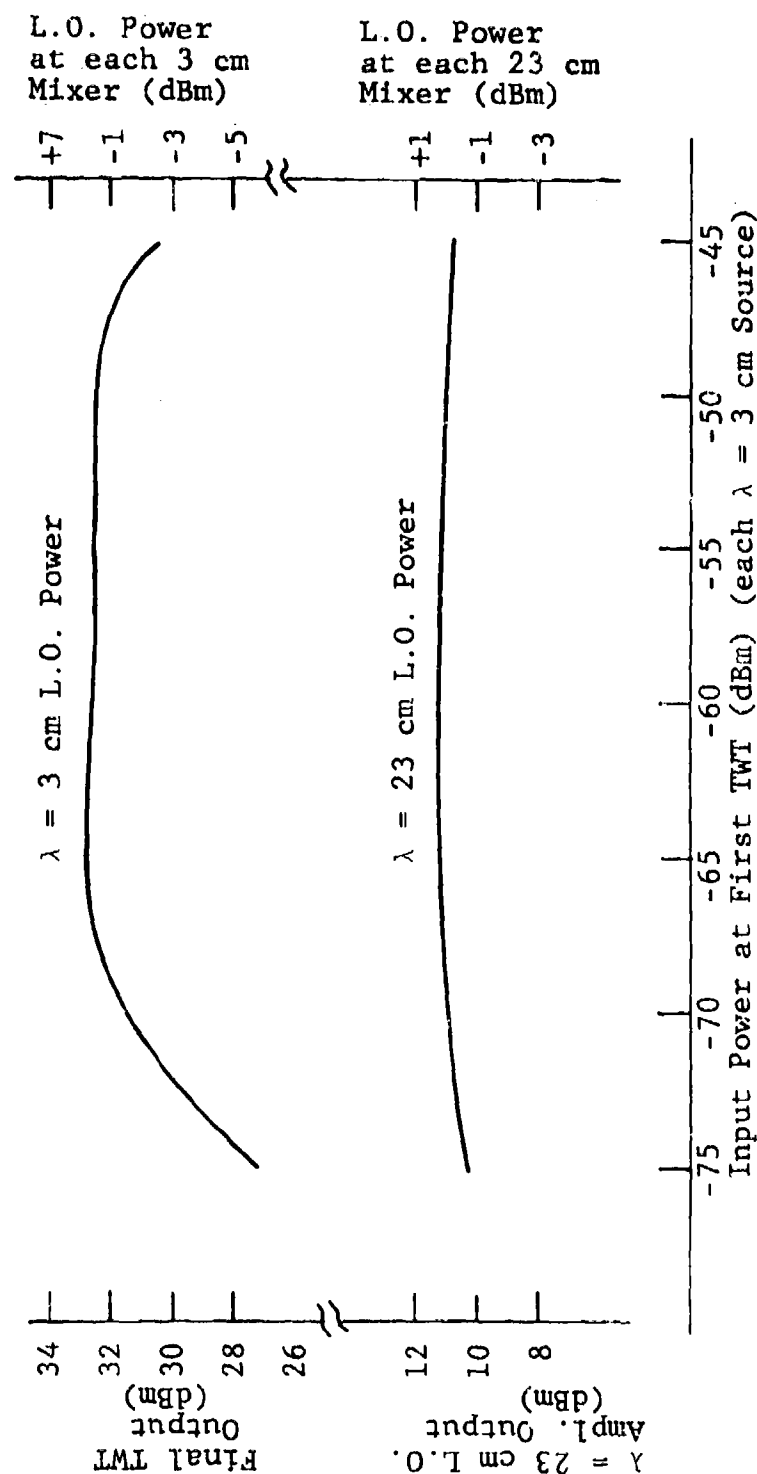


Figure B-7. Received STALO Powers vs. 3 and 23 cm L.O. Power

It can be determined from the chart recording if the received STALO powers exceed the minimum -70 dBm level needed to maintain the proper L.O. power levels.

Figure B-8 shows the conversion losses of the 3 and 23 cm mixers versus L.O. power used in the bistatic receivers. Note that neither loss varies any more than 0.5 dB over the operating range indicated by the dotted lines in the figure.

B.2.5 BISTATIC CIRCUIT BOARD DESCRIPTIONS

This section describes fifteen circuit boards employed in the bistatic receiving system.

Board 1: Sync Generator and PRF Instrumentation

Board 1 (Figure B-9) conditions the received PRF synchronizing (sync) pulse from the C-46 aircraft. A 200 nsec pulse from the sync pulse threshold detector is conditioned to:

1. generate a 1 μ sec sync pulse with the proper delay to trigger the bistatic receivers on,
2. supply a system PRF trigger for an oscilloscope for alignment and monitoring purposes,
3. provide a trigger to measure and record the ΔR , and
4. stretch the PRF pulse for recording and monitoring purposes.

R-1 is used to delay the 1 μ sec sync pulse and can be adjusted properly by monitoring TP-1. TP-2 is a test point where the 60 μ sec PRF pulses which are coupled to the FR-1300 tape recorder can be monitored. Logic and driver circuits, I5 and I6, function to enable the PRF for recording and to drive LED indicators located on the control panel.

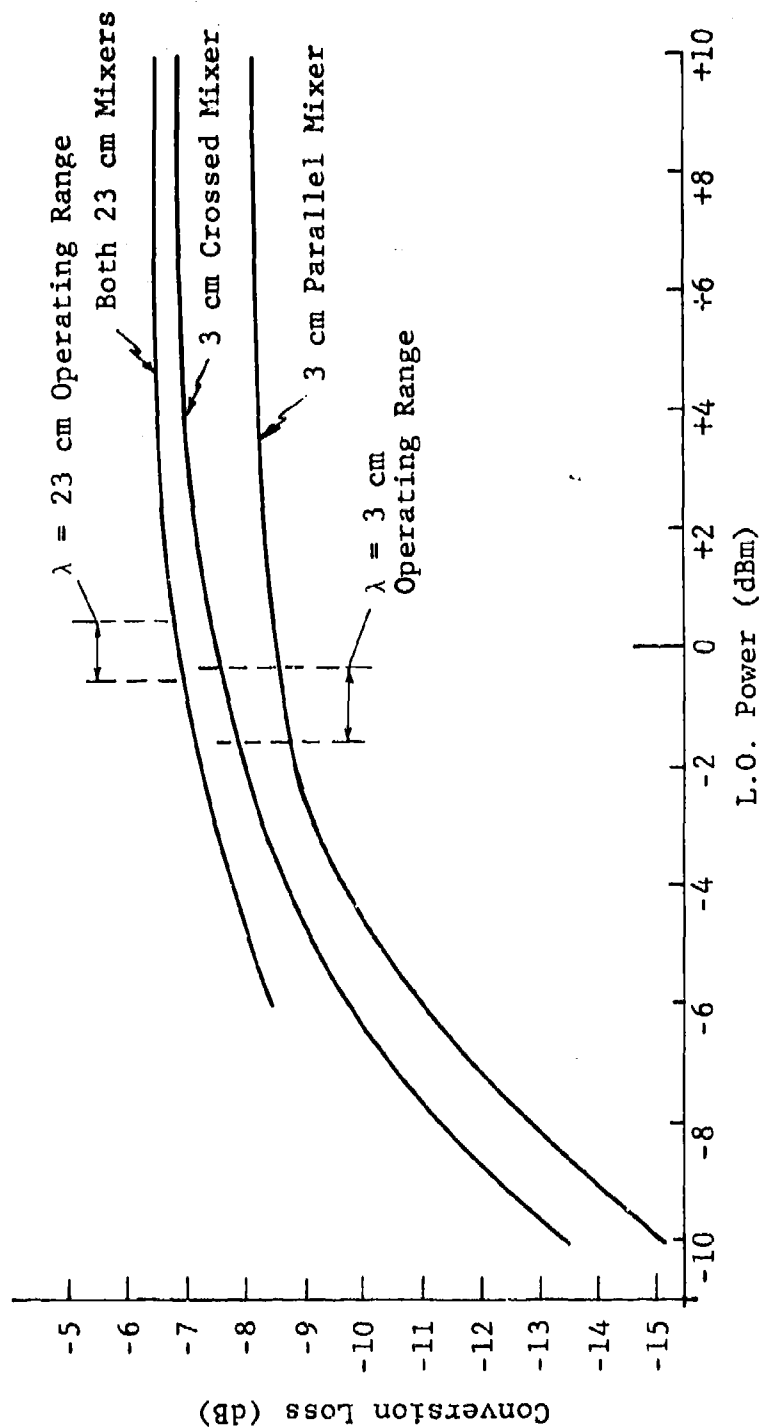


Figure B-8. Conversion Losses vs. L.O. Power

Board 2: Calibration PRF Generator

Board 2 (Figure B-10) contains an internal PRF generator to simulate the received PRF signals when the system is not operating. Its functions include:

1. a basic 8 kHz PRF trigger generator,
2. a sync pulse generator,
3. a 50 nsec pulse width generator to control the RF pulses,
4. logic to simulate the dual-band PRF alternate pulsing sequence, and
5. a ΔR range delay generator to calibrate the ΔR instrumentation.

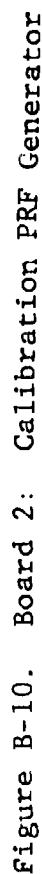
R-4 is used to adjust the calibration PRF to match the PRF of the C-46 radar.

I2 develops a 150-200 nsec pulse used to trigger the 8155 MHz PIN modulator "off" in the RF receiving section. Its function is to simulate the received sync pulse from the aircraft. The sync pulse threshold detector located in the RF section is activated by this RF attenuation pulse.

R-3 controls the 50 nsec pulse used to trigger the two RF switches in the 3 and 23 cm RF calibration paths. The RF pulses simulate the received bistatic data pulses. A range delay control circuit, I-2 and I-3, provides a means to calibrate the ΔR channel. Controls R-1 and R-2 are used to adjust the maximum and minimum range of the calibrated ΔR channel. The maximum range of the ΔR is determined by the last step of the staircase voltage driving I-3.

Logic integration circuits I5 and I6 control alternate sequencing of the dual-band PRF function. The normal position of the SW-1 control alternates the sequencing of the

1-24-76 LCN



dual-band PRF function. The normal position of SW-1 is the Toggle position. When SW-1 is in the 1:1 position, a 50 nsec pulse triggers the 3 and 23 cm RF switches at the same time.

When the system control panel switch is in the Operate position, the calibration PRF generator is inhibited. A bias voltage to attenuate the PIN modulators to their maximum (80 dB) via Q1 and Q2 also occurs in the system's operate position. This attenuation function essentially cuts off the RF signal developed from the two 3 cm Gunn oscillators used to simulate the received RF signals from the C-46 aircraft.

Board 3: ΔR Instrumentation Generator

Instrumentation for the ΔR recording is implemented on Board 3 (Figure B-11). ΔR is measured on each PRF pulse and calibrated with reference to the sync pulse. The leading edge of the detected sync pulse via Board 1 starts the timing sequence in order to measure ΔR . A ΔR integrator reset pulse is enabled at this time; this discharges the integrator (I-6). When the reset pulse has passed, the integrator (I-6) begins to charge again. A linear ramp voltage with a constant slope continues to charge until the leading edge of the ΔR reset pulse occurs. At this time, the ramp charge stops and the voltage level is held until the next sync pulse occurs. If a ΔR reset pulse does not occur (as would be the case if no bistatic signal is detected), a late- ΔR reset pulse will stop the range ramp voltage charge. I-1 and I-4 implement the late- ΔR reset pulse which is OR-ed at I-3 along with the normal ΔR pulse. The late- ΔR reset pulse limits the range measurement and keeps the integrator, I-6, from saturating. R-2 and R-3 are controls to condition the ΔR measurement for the recorder.

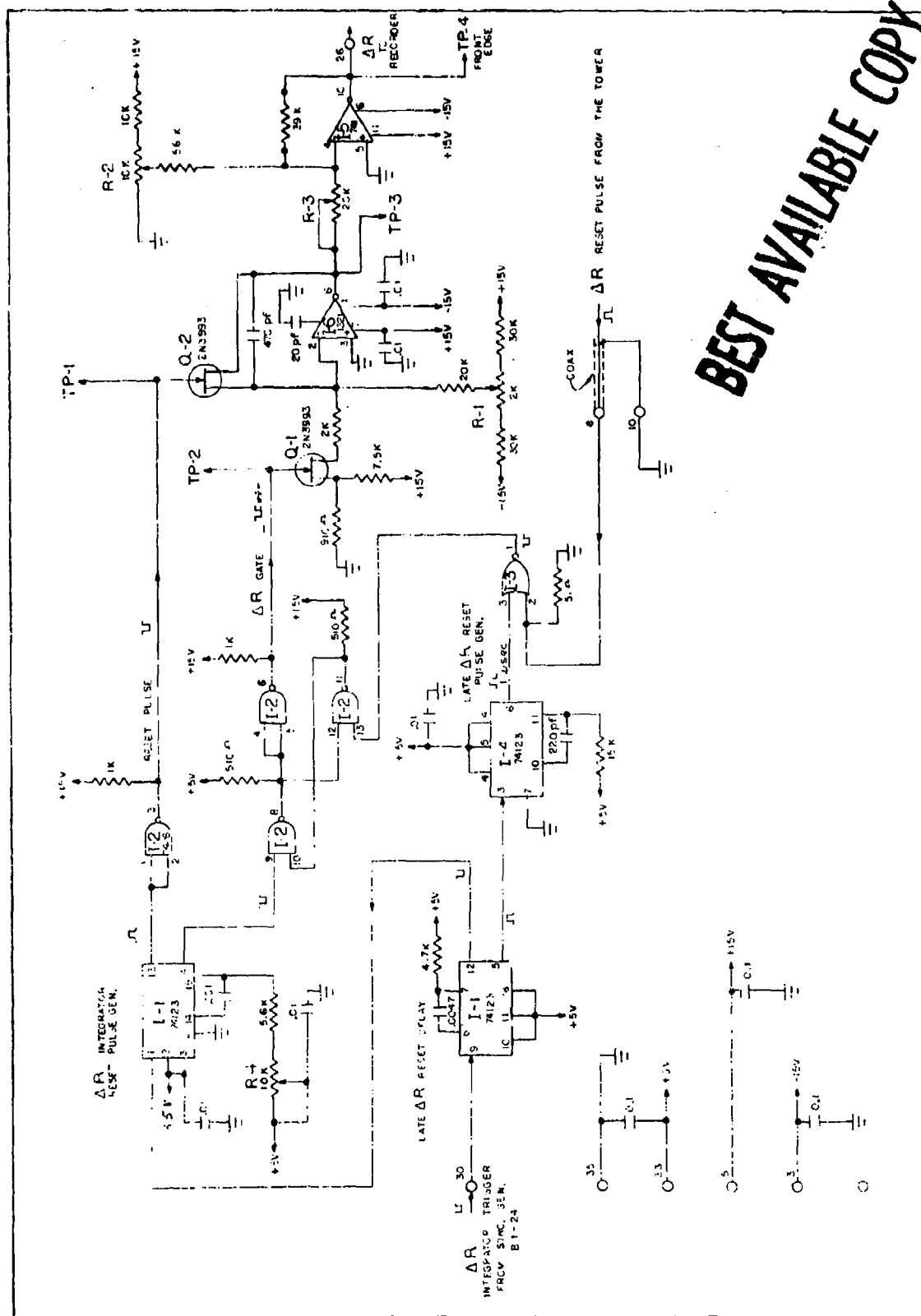


Figure B-11. Board 3: ΔR Instrumentation Generator

Boards 4 and 5: 3 and 23 cm Wavelength Video Instrumentation

Boards 4 and 5 (Figure B-12) contain the 3 and 23 cm video instrumentation, respectively. The parallel and crossed sample-hold video from the bistatic receivers are coupled to the inputs of their respective boards. The video to the tape recorder is buffered through amplifiers. R-3 and R-7 are adjusted to keep the video from saturating the tape recorder.

Each video input is coupled to another amplifier and conditioned for recording the data on the H-P analog recorder. The sample-hold bipolar video is coupled to a true RMS-to-dc converter (A-1 or A-3). The dc output of the converter is processed through a logarithmic amplifier (A-2 or A-4) before being applied to the analog recorder. The output of the log amplifier is adjusted to give a 10 dB change for each volt of input signal. The log amplifiers are capable of a 50 dB dynamic range.

Board 6: Data Logic and Angle Instrumentation

Board 6 (Figure B-13) circuits automate an alert and start-stop data capability. The scan angle and tracker angle position voltage instrumentation are also contained on this board.

The data alert and start-stop data logic are referenced to the tracker angle voltage. By comparing the initial control voltages located on the front panel with the tracker's angle volts, an alert and start-stop data logic signal is developed. The data alert and start-stop data controls are set prior to a pass and are read directly in degrees from broadside. The data alert control is usually set 5° less than the start-stop data control, rendering a 5-10 second delay before a start-data condition. A data alert logic

BEST AVAILABLE COPY

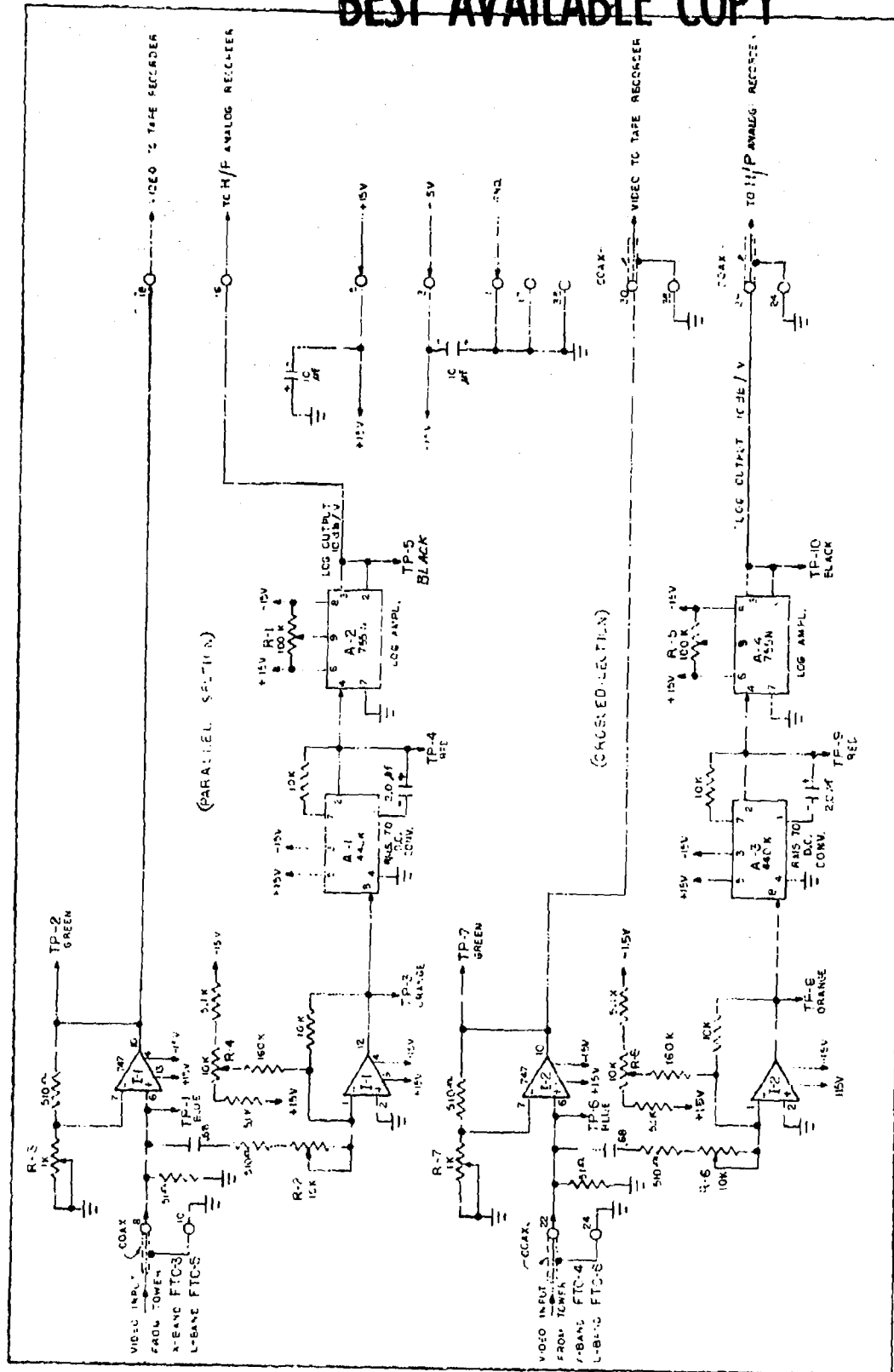
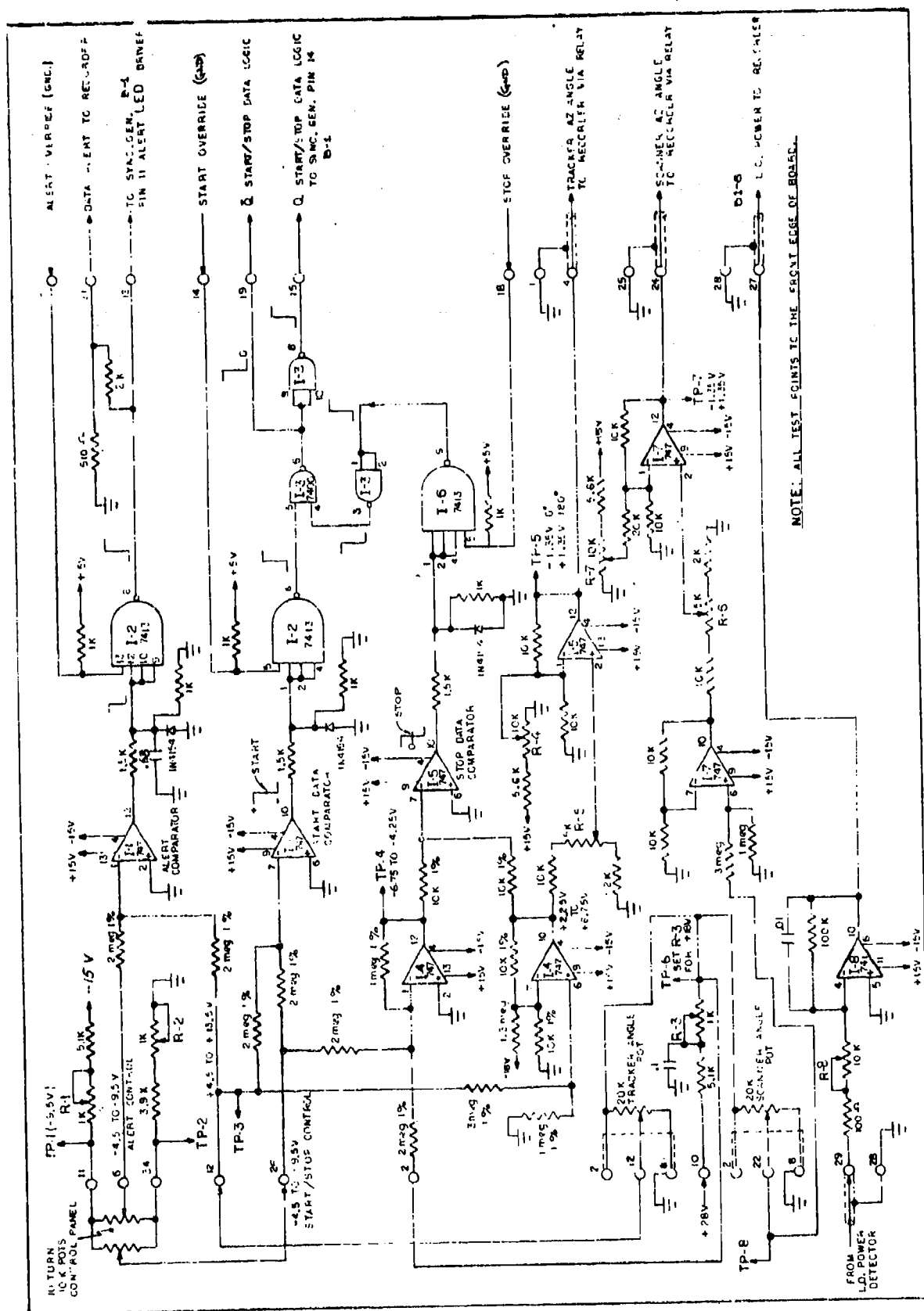


Figure B-12. Boards 4 and 5: 3 and 23 cm Wavelength Video Instrumentation



voltage occurs at this time, illuminating an LED indicator on the control panel. When the tracker angle coincides with the preset start-stop data control, a logic signal occurs, enabling the PRF pulses to be recorded on the tape recorder. An LED indicator also illuminates at this time.

The start-stop logic circuit on Board 6 is designed to enable and inhibit the PRF pulses to the recorder in equal angle segments with reference to either side of broadside. For example:

The start-stop data control is set initially for 50° . When the tracker angle reaches 50° , the enable logic signal will be on for $\pm 40^{\circ}$ either side of broadside. When the tracker angle reaches 130° , a stop logic signal occurs, inhibiting the PRF pulses to the recorder.

Angle alignment controls for both the tracker and scanner antenna position read out are included on Board 6. Tracker and scanner antenna angle position scaling controls and associated amplifiers for recording purposes are also contained on this board.

Board 7: Dual-Band Offset Frequency Generators

Offset frequency generators are implemented on Board 7 (Figure B-14). Two sawtooth generators are used to offset the 100 MHz frequency of the 3 and 23 cm multipliers. The offset frequency generators establish a known frequency for processing the bipolar video. Both generators have a frequency range adjustment of 10 Hz to 2 kHz.

The 3 and 23 cm offset generators are capable of operating at different frequencies, if desired. When both offset frequencies are to be equal, the 23 cm generator is slaved to the 3 cm generator.

BEST AVAILABLE COPY

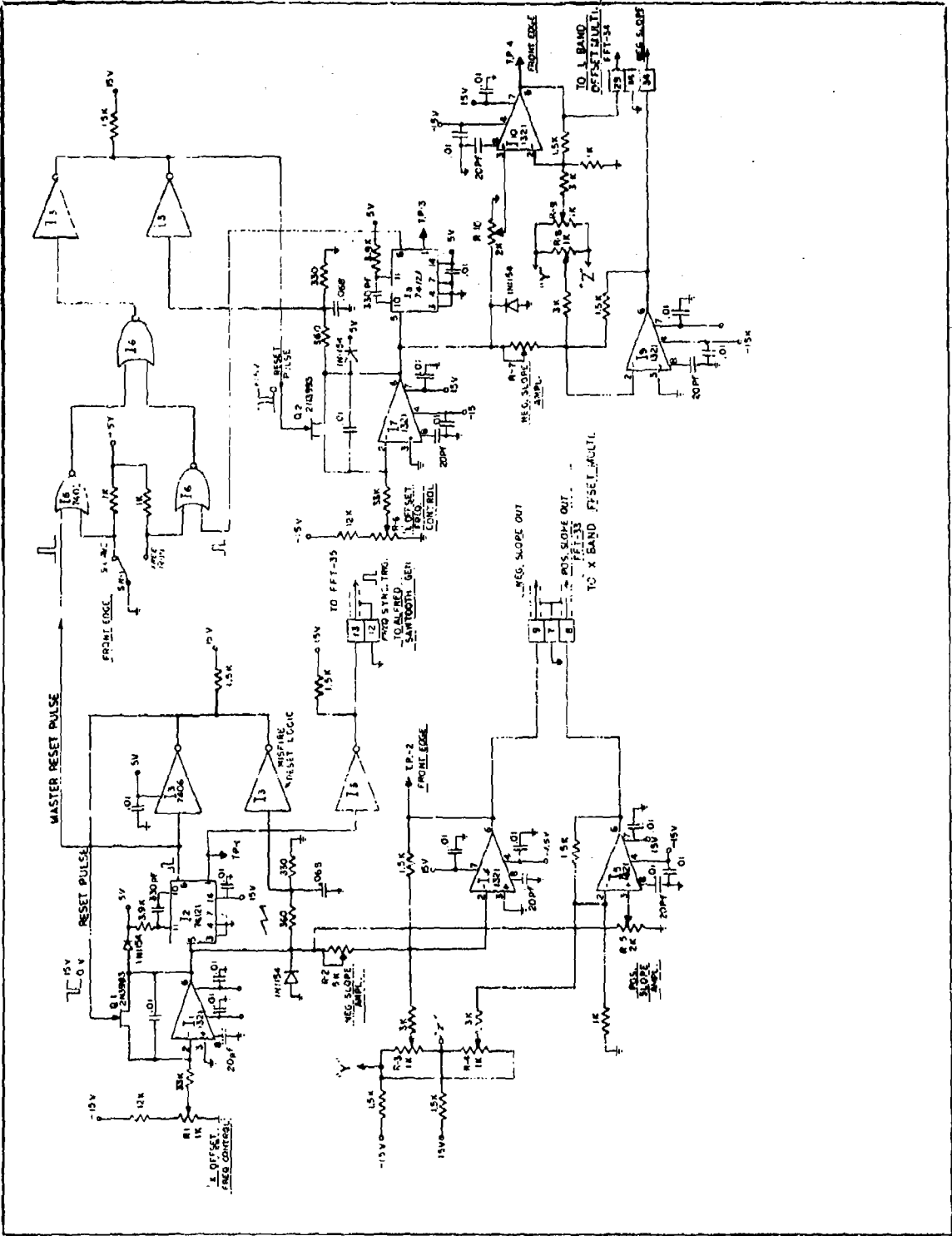


Figure B-14. Board 7: Dual-Band Offset Frequency Generator

A frequency sync pulse is also generated from the 3 cm generator. Its purpose is to keep the serrodyne sawtooth generator operating at the same frequency as the 3 cm offset frequency generator.

Positive or negative slope outputs are available from each generator. This feature allows the multiplier frequency to be shifted either above or below its normal 100 MHz output frequency.

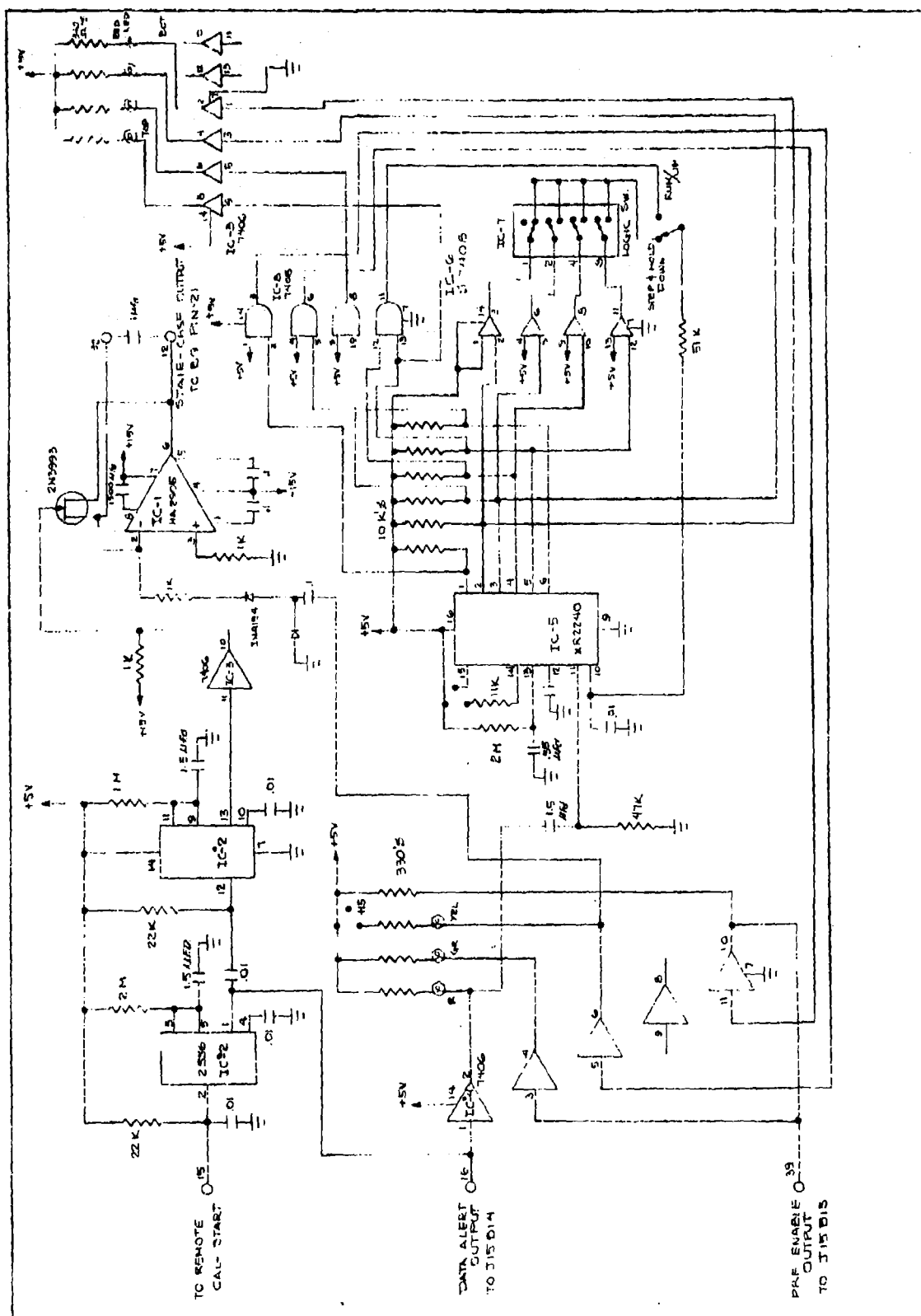
Board 8: Calibration Step Generator

Board 8 (Figure B-15) provides a means to calibrate the bistatic system. A staircase generator is constructed to sequence 13 discrete voltage steps. Each step has a time interval of about 2 seconds.

The sequence begins by manually activating the start calibrate pushbutton switch on the control panel. A data alert output occurs immediately, which lasts for about 1 second. The stepping sequence follows, resetting the generator from the 13th step to the 1st step. When the first step starts, a PRF-enable output occurs, allowing the calibrate-PRF pulses to be recorded. The PRF-enable output lasts until the 13th step begins. The 13th step (the maximum voltage step) is held until the sequence is again enabled by the start calibrate switch. LED indicators which indicate the step sequence are implemented on Board 8. All voltage steps are coupled to the step driver (Board 9) to perform the various functions described below.

Board 9: Step Driver

The staircase output from Board 8 drives six amplifiers contained on Board 9 (Figure B-16). Two of the amplifiers are presently spares while the other four amplifiers perform



the following functions:

The I1 and I2 outputs control the RF attenuation of the 3 and 23 cm linear attenuators as a function of the voltage steps. I4 controls the step voltage applied to the ΔR calibration delay circuit located on Board 2. I3 is used to put the calibration voltage steps on the tracker and scanner-angle recorder channels.

Boards 10 and 11: Antenna Demodulator-Servo Amplifier Driver

Boards 10 and 11 (Figure B-17) are used to control the position of the tracker and bistatic antennas, respectively. The antennas can be controlled manually or automatically, as determined by a selector switch mounted on the board. A synchronous error signal determined from a Theta control located on the control panel is coupled to a demodulator when manual positioning of the antenna is required. The demodulator dc output is coupled to an amplifier, which in turn is used as the azimuth drive input to the antennas' power amplifier. When automatic tracking or scanning is used, the demodulator circuit (IC-1, IC-2, and IC-3) is switched out; a dc error signal is used instead. The error signal for the tracker is coupled from the automatic angle tracking circuits. The error signal for the bistatic antenna is coupled from the output of the scan generator interface circuit (Board 12).

In addition to the azimuth drive output, antenna limit control circuits are implemented on Boards 10 and 11. The purpose of the limits is to control the antenna's angular position. A rate limit is also included by sensing the tach signal of the antenna. If the antenna rate exceeds the predetermined rate set by R-4 or R-5, the azimuth drive signal is cut off. Controls R-1 and R-2 determine the maximum angular position allowed either left or right of broadside.

This is done by comparing the azimuth angle volts with the right-left limit voltages. If the azimuth angle volts exceeds either limit, the azimuth drive signal is inhibited.

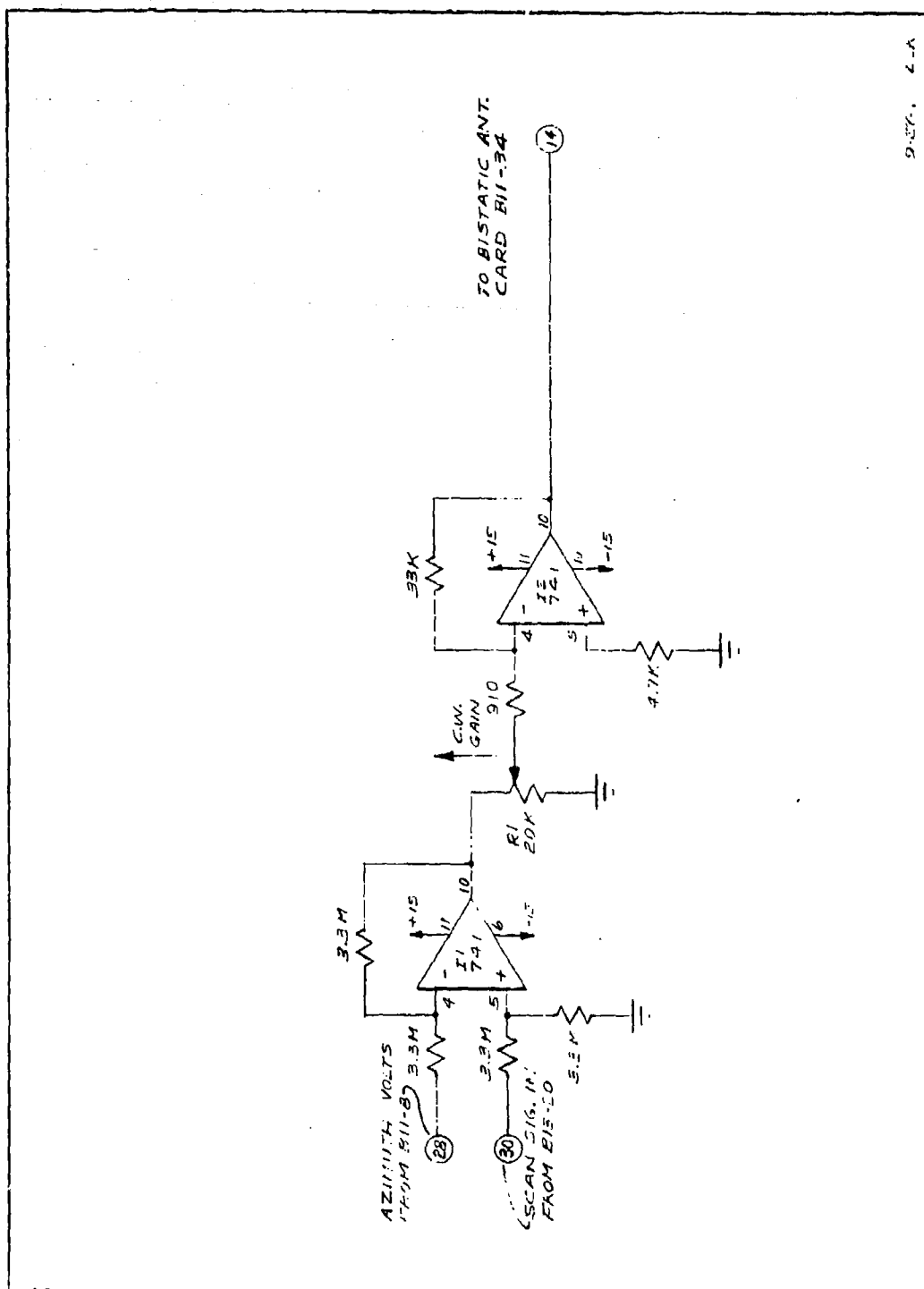
Board 12: Interface Scan Generator to Antenna Drive

Board 12 (Figure B-18) generates a scan error signal when the bistatic antenna is in its scan mode of operation. The scan voltage from the scan generator located on Board 13 determines the position of the bistatic antenna. This scan voltage is compared with the actual antenna azimuth volts, resulting in an error signal as the scan generator voltage changes. The output (error signal) is coupled to Board 11 to be used as a servo drive signal.

Boards 13 and 14: Scan Generator

Boards 13 and 14 (Figures B-19 and B-20) implement the scan generator necessary to scan the bistatic antenna. Controls are provided on the control panel with which to determine the scan rate and the left-right angle limits. The scan voltage does not occur until a start-data logic command is enabled from Board 6. When the scanner's selector switch is in the automatic position and no start-data logic command is present, the bistatic antenna is slaved to the left position limit. When the start logic command occurs, the scan integration (IC-4) begins to function, generating a ramp voltage to position the antenna to the right. When the right antenna position limit voltage equals the scan output voltage, a logic signal occurs which reverses the scan output slope.

The antenna will then begin to scan back to the left. When the left limit is reached, the antenna will move from left to right again. When the stop-data logic command occurs, the park mode is again activated, reverting the



9-576, 4-A

Figure B-18. Board 12: Interface Scan Generator to Antenna Drive

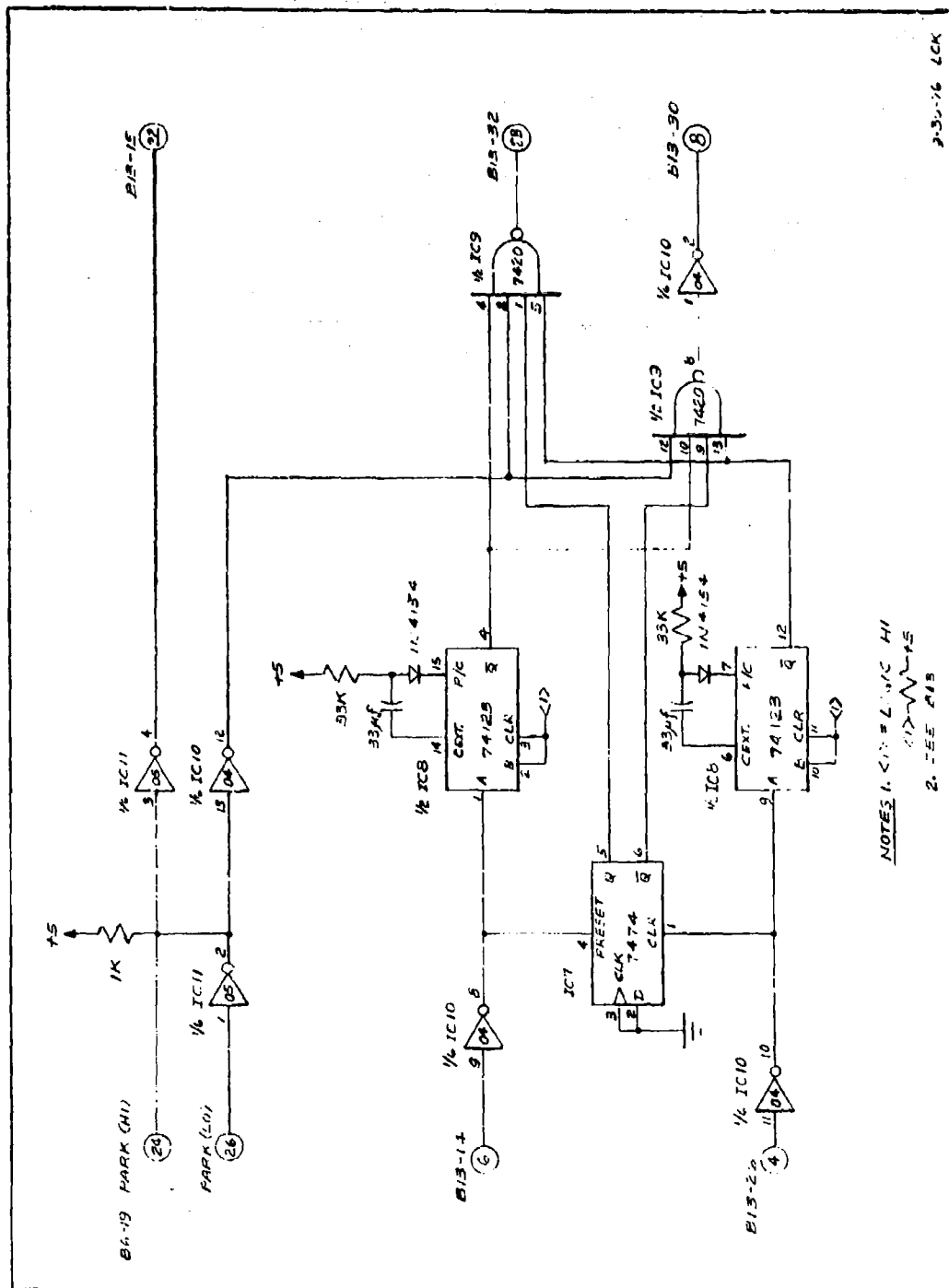


Figure B-20. Board 14: Scan Generator

antenna to the left limit, regardless of where in its scan the antenna happens to be.

Board 15: Relay Board

All the system's relays are mounted on Board 15 (Figure B-21). The relays switch the necessary functions to the correct position, depending upon the system mode-selector switch.

B.2.6 CALIBRATION

The 3 and 23 cm bistatic receivers were calibrated by automatic step-control attenuator systems. The block diagram in Figure B-22 describes each of the two (3 and 23 cm) calibration systems which are installed in the van. The RF signal input to the calibration system is CW and has been offset by 500 Hz with respect to the L.O. frequency. The 50 nsec pulse-width generator pulses the RF switch, simulating the transmitted bistatic pulse aboard the C-46 aircraft. An internal PRF generator operates at the same PRF as the transmitter in the aircraft and triggers the pulse-width generator. When pulsed off, the RF switch attenuates the input signal by 60 dB. Full peak power is realized when the RF switch is pulsed on. At the output of the calibration system, two 175-ft coaxial cables feed the calibrated RF pulses to the inputs of the parallel and crossed-polarization bistatic receivers via a power splitter and directional couplers.

The peak power is measured by applying a dc voltage to the CW terminal of the RF switch; this removes the attenuation through the switch. The resulting CW signal is fed via a directional coupler to the spectrum analyzer which displays both frequency and power. The RF programmable

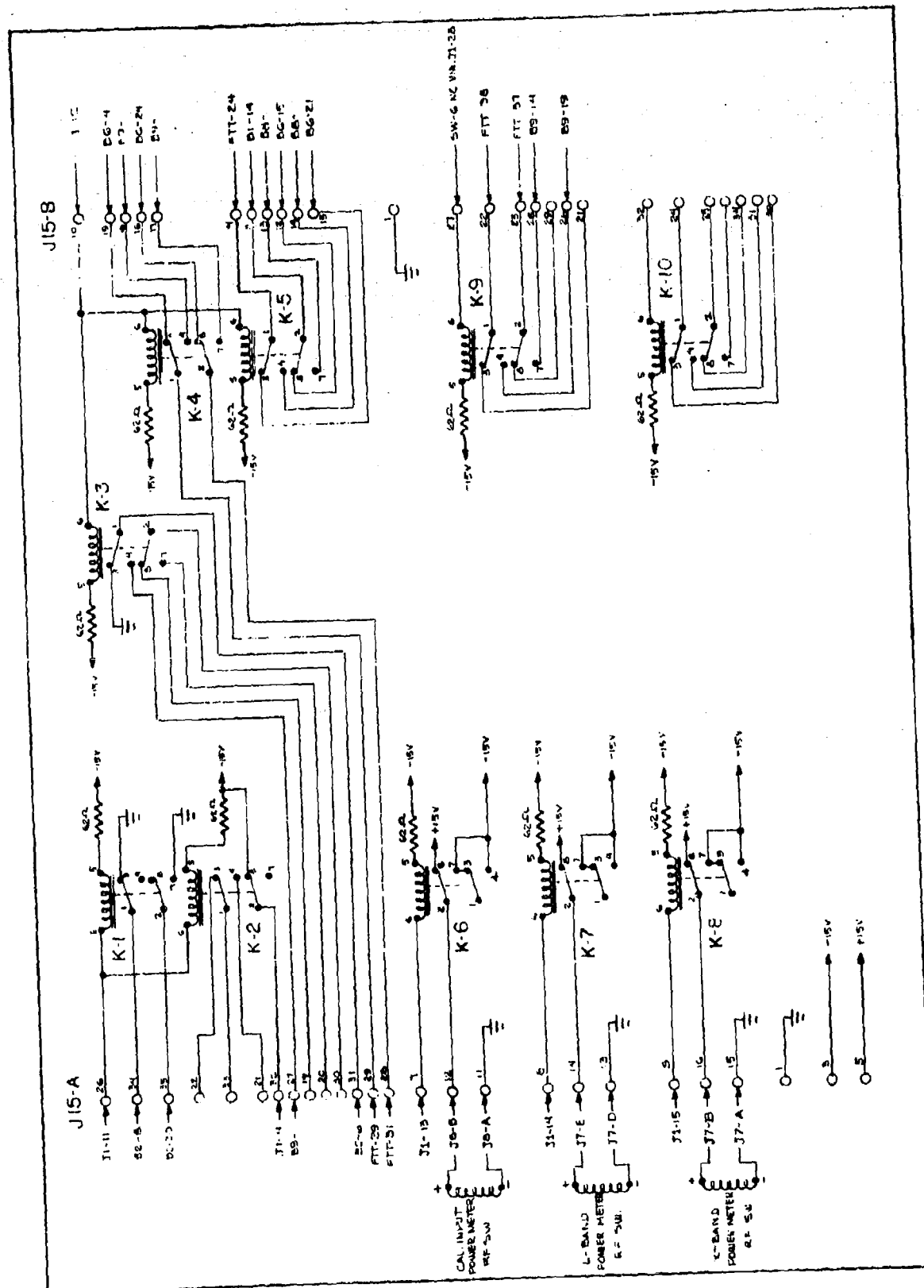


Figure B-21. Board 15: Relay Board

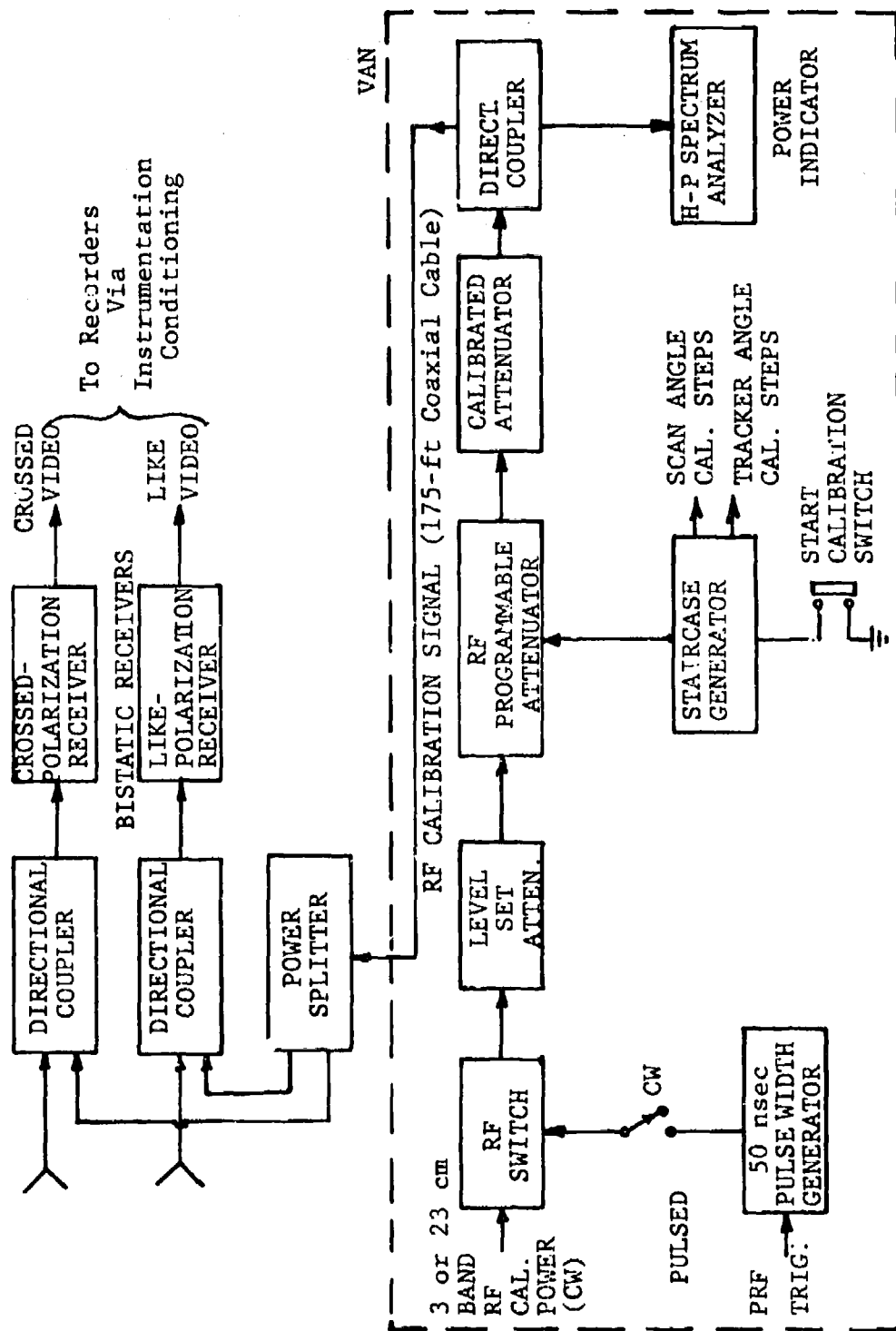


Figure B-22. Block Diagram of 3 or 23 cm Calibration System

attenuator is at its minimum attenuation level (1st step) when this measurement is made. The level set attenuator is then adjusted for the desired power setting. All RF losses between the measuring points and the input to the bistatic receivers are known. Thus, the maximum peak power of the calibration signal for any attenuation level set can be determined.

The voltage-controlled, programmable attenuator is used to automatically calibrate the bistatic receivers. The staircase generator drives the attenuator with each step lasting for about two seconds. Each voltage step corresponds to a given amount of RF attenuation. Thus, the absolute RF input power to the bistatic receivers is known for each calibration step.

The following procedure is used to calibrate the bistatic receivers.

1. The system control panel switches are placed in the calibrate position.
2. The two X-band Gunn oscillators (not shown in Figure B-22) are adjusted to a -60 dBm output power level in order to simulate a received local-oscillator-input-power signal from the aircraft.
3. The calibrate/L.O. power monitor switch is turned to its Cal. position. The RF power is measured on the spectrum analyzer by switching the pulsed/CW switch to CW.
4. The pulsed/CW switch is switched to pulsed position. The calibrated attenuator is adjusted for the desired threshold power setting. Threshold gain controls located

on the control panel for both 3 and 23 cm bistatic receivers are then adjusted by observing the bipolar sample-hold video on an oscilloscope. The threshold gains are adjusted so that the video is just beginning to be sampled and held at this given input power setting.

5. A front panel control switch is pressed to start the calibration function. The first step in the staircase corresponds to the peak power measured in step 3 above.

A total of twelve equal voltage steps drive the RF attenuators which increase the 3 cm attenuation to greater than 30 dB on the last step. The 23 cm attenuator has a range greater than 60 dB. The last step in the staircase holds at this position, keeping the calibration signal path attenuated, until the start calibrate switch is again operated.

6. The system control panel switches are placed in the operate position.

In the operate position, the internal PRF of the system is inhibited; this attenuates the calibration RF signal path by greater than 60 dB via the RF switches (one of which is shown in Figure B-22). The combined attenuation of the RF switches and programmable attenuators keep any signals from entering the bistatic receivers via the calibration RF signal path during operation.

7. The Gunn oscillators are attenuated to keep them from interfering with the operational mode, making the system ready to receive the STALO frequencies transmitted from the aircraft.

B.3 DATA RECORDING

B.3.1 BISTATIC RAW DATA TAPE FORMAT

The tapes recorded in the aircraft are 7-track, 800 bpi (NRZI), and written with odd parity (see Figure B-23). These tapes are structured so that one tape file (delineated by a tape mark) corresponds to one aircraft data pass or one complete calibration run (see Figure B-24). The files are made up of fixed length records containing 6000, 12-bit words each. These records are arranged so that each group of 6 consecutive words consists of one sample from each of the six information channels at one particular time. The channels include (1) 3 cm, parallel-polarization video, (2) 23 cm, parallel-polarization video, (3) scan angle, (4) tracker angle, (5) 3 cm cross-polarization video, and (6) 23 cm, cross-polarization video. Thus, one record consists of 1000 six-word samples, one sample being taken at every radar pulse (see Figure B-25). Sampling continues across record boundaries; however, one radar pulse is missed (not sampled) between records. The last record in any file is padded with zeroes, if there are insufficient data to fill the full 6000 words. The 12-bit words are placed on the tape with the less significant 6-bits. Each of these words is interpreted as an unsigned integer in the range 4095 to 0. These values can easily be converted to signed values by subtracting 2048 from each word, leaving values in the range 2047 to -2048. When in this form, a word of zero corresponds to no signal on the video channels.

B.3.2 DESCRIPTION OF CALIBRATION RUN

A calibration run consists of a series of 12 steps in the input power to the four video channels and in the levels of the two angle channels; the steps are decreasing in power

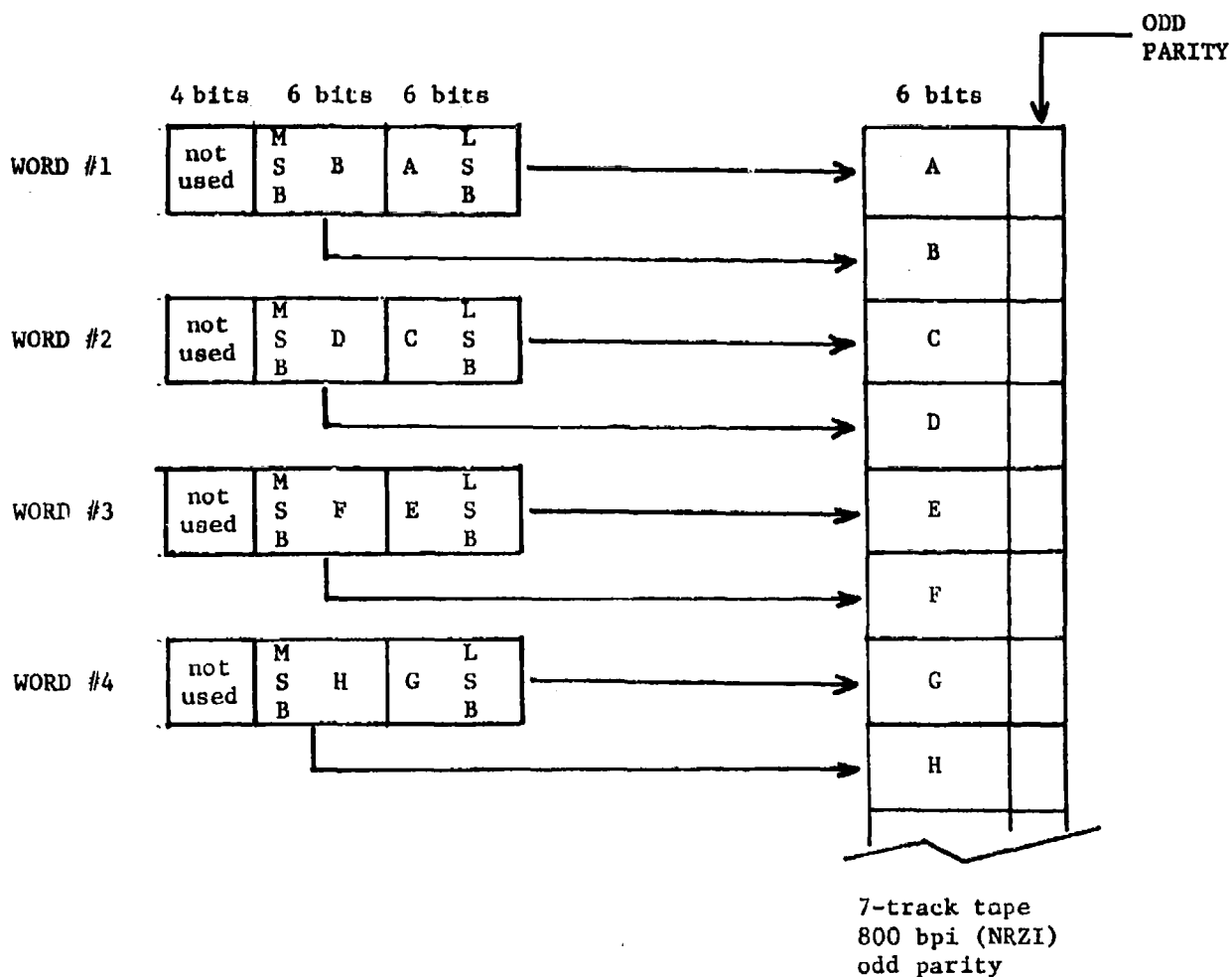


Figure B-23. Map from 16-Bit Word to 7-Track Tape

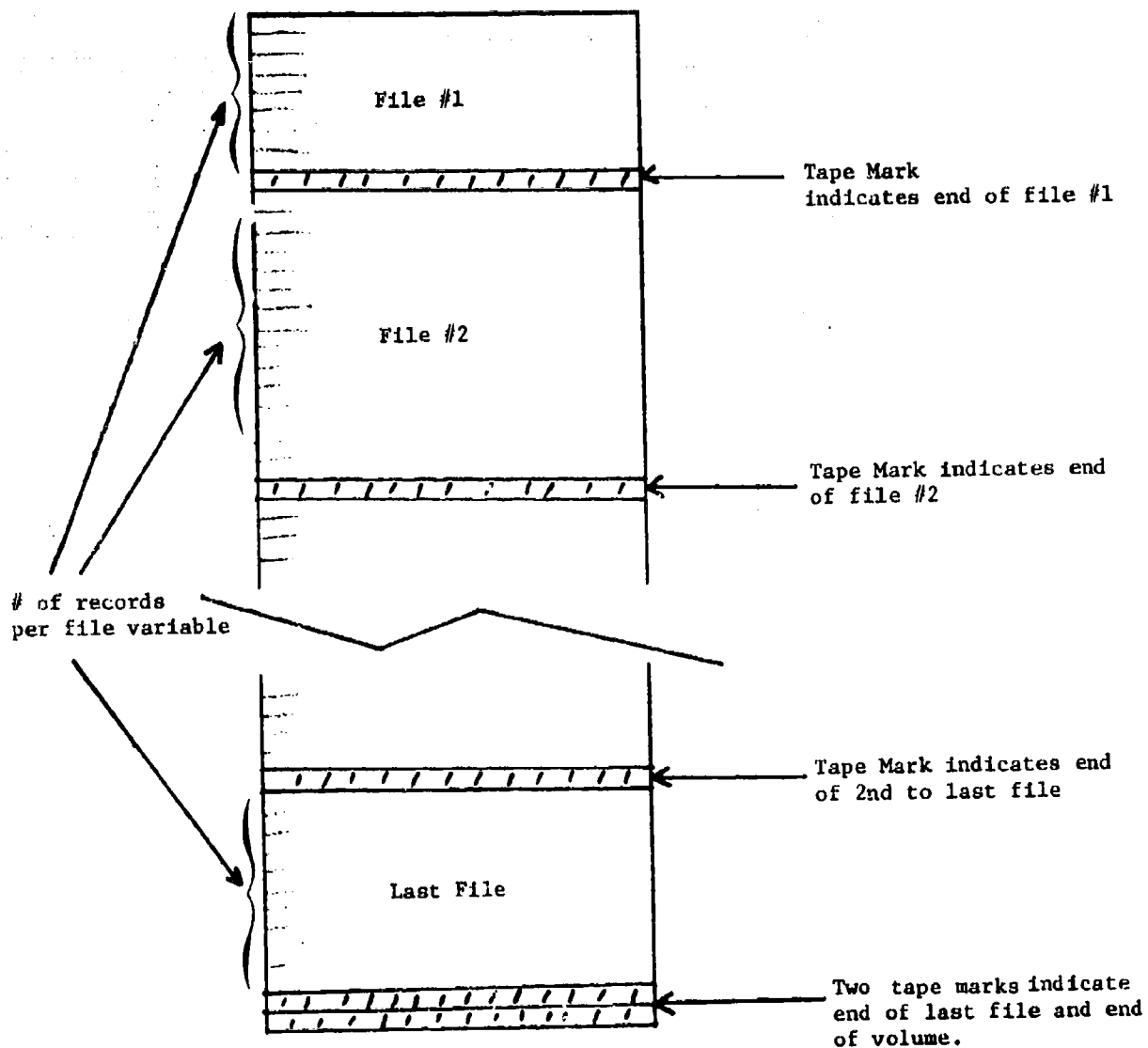


Figure B-24. Tape Format

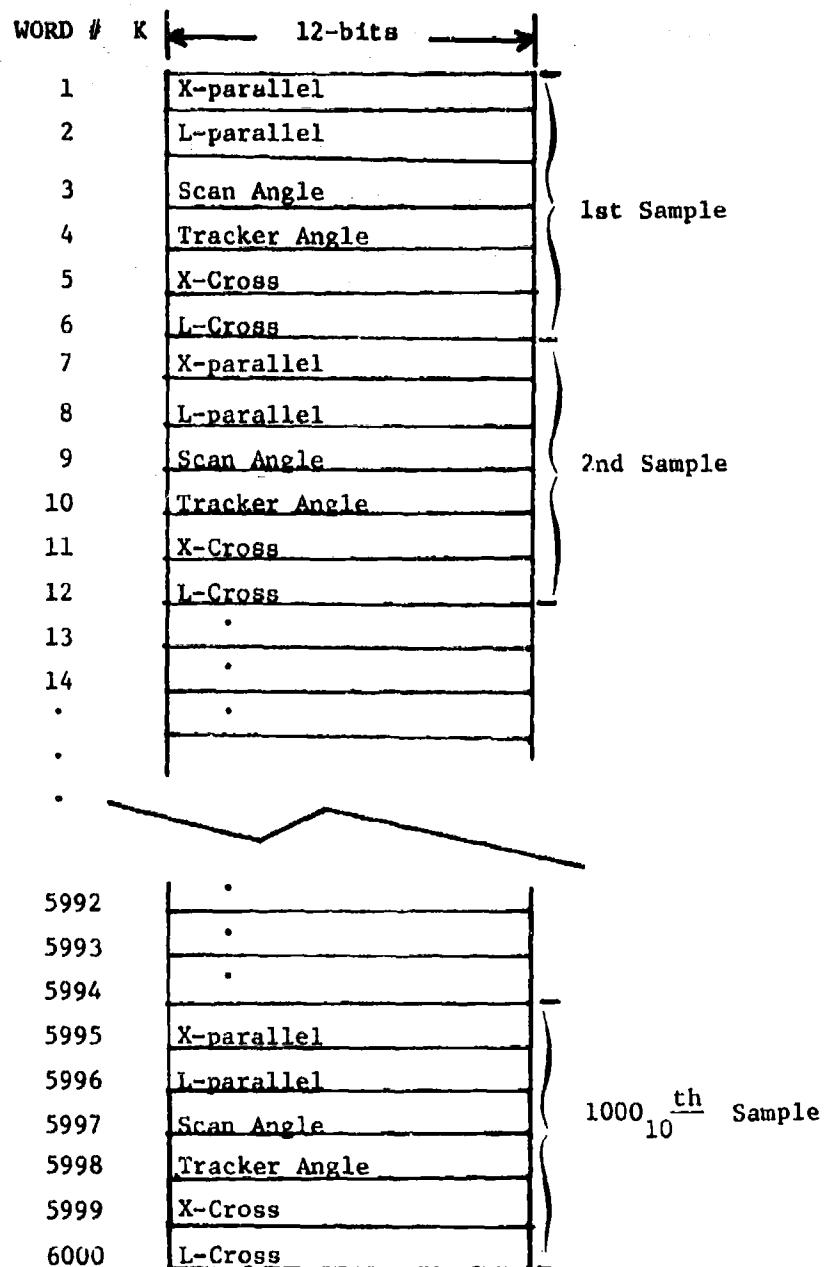


Figure B-25. Format of Tape Records

and angle level. There are approximately 9000 samples
(6 words each) or 9 records per step, making a calibration-
run file approximately 108 records long.

APPENDIX C DATA COLLECTION

A major part of the data gathering and data preparation tasks was concerned with quality control. Considerable effort was spent in the development of operational equipment, checklists, and procedures to be certain that all required quantities were recorded. This appendix presents (Section C.1) a summary of the procedures developed for incident power level correction and (Section C.2) the checklists and log form used.

C.1 INCIDENT POWER LEVEL CORRECTION

As illustrated in Figure C-1 the bistatic measurements utilized a spotlight technique in order to obtain a maximum number of data samples for each pass. In order to complete the calculation of σ_0 , transmitter antenna pointing information must be determined in order to provide correction factors for the incident power level*. The purpose of this section is to illustrate the data reduction technique used to determine that correction.

The transmitting antenna spotlights the scattering area throughout a 90° angle. This is illustrated in Figure C-1 where the scattering area is first illuminated with the transmitting antennas (both 3 cm and 23 cm) squinted forward 45° with respect to the aircraft's broadside direction. The transmitter antenna spotlights the area through 90° or until viewing at a 45° angle aft of broadside. Spotlighting is accomplished using a manual servo control with a synchro

*With reference to the recommendations section, this tedious step can be removed from future measurements by providing receivers which measure incident power directly. In this way, the accuracy will be improved by 3 dB.

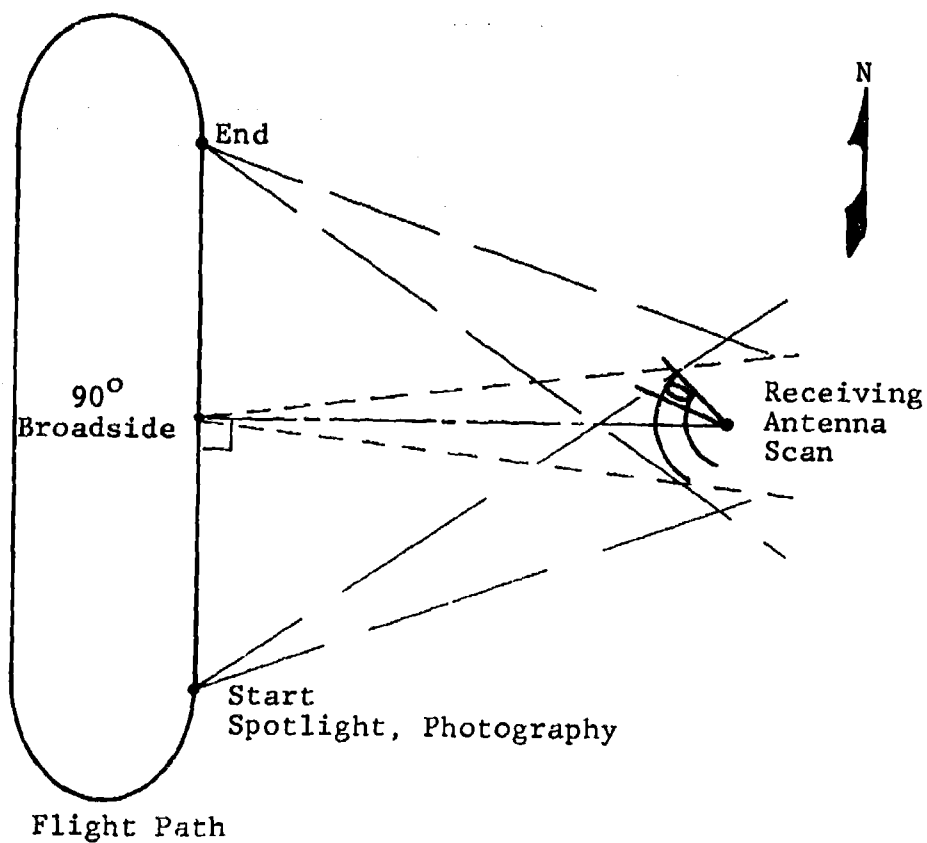


Figure C-1. Data Gathering Flight Path
for Bistatic Measurements

angular readout. Ground tracks and altitudes are selected to provide the desired incident angle θ_i . These tracks are plotted with respect to a local VOR navigation station. The offset distance x_2 is thus determined, within some error bount resulting from flight path variations. The antenna pointing angle ϕ_{TRANS} is then plotted as a function of time on an x-y chart recorder in the aircraft for the offset distance x_2 and for an expected range of aircraft ground velocities. Aircraft velocity is determined for each pass during line-up prior to the start of spotlighting and the proper antenna pointing angle vs time curve is selected. This relationship is linear to a good approximation.

Spotlighting is started when the angle between the aircraft track and the aircraft-to-scattering area direction is 45° . This point is determined by the DME (distance measurement equipment) on board the aircraft. As the antenna is slewed, the angular pointing information from the antenna synchro is used to drive the y-axis on the chart recorder. The x-axis recorder drive is controlled by the recorder sweep speed, which is 10 seconds per inch. Since the slew rates are slow, the desired angle-time relationship, as plotted on the chart recorder, can be followed manually. Thus, a record of antenna pointing angle relative to the aircraft as a function of time is generated during each pass for the particular velocity during each pass. During each pass, the following reference points are "called out" on the air-to-ground communication channel and also recorded on tape:

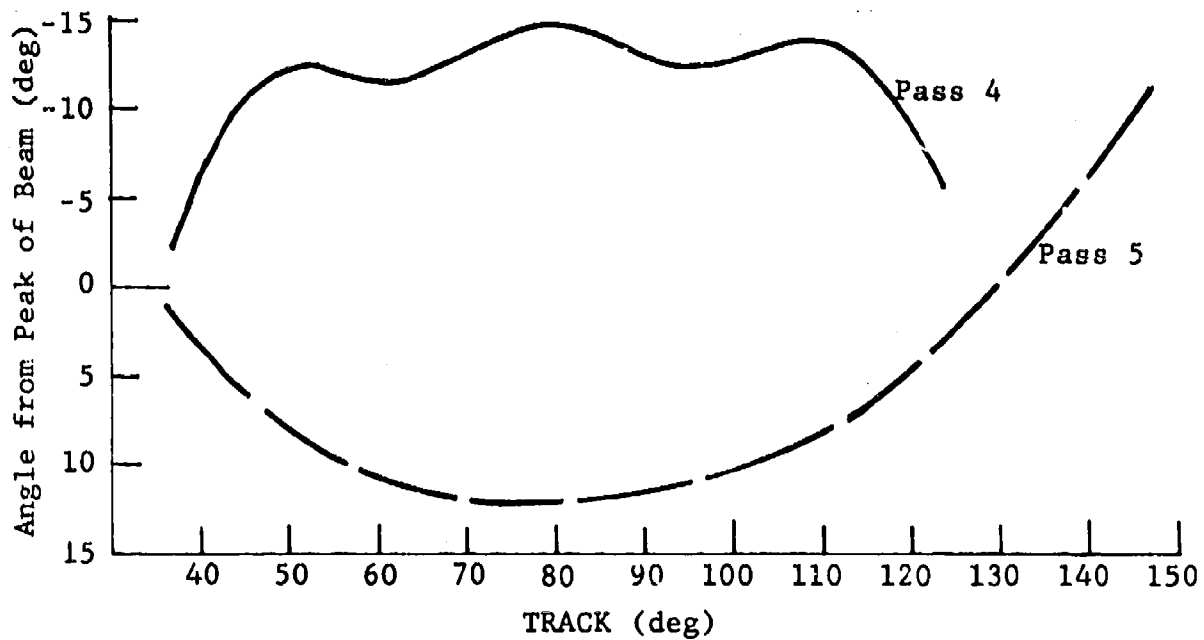
<u>ϕ_{TRANS}</u>	<u>LOCATION</u>
-45.0° (forward)	start of pass
-22.5°	1/2 point
0	mid-pass
+22.5° (aft)	3/4 point
+45.0°	end pass

Aerial vertical photography is also obtained during each pass.

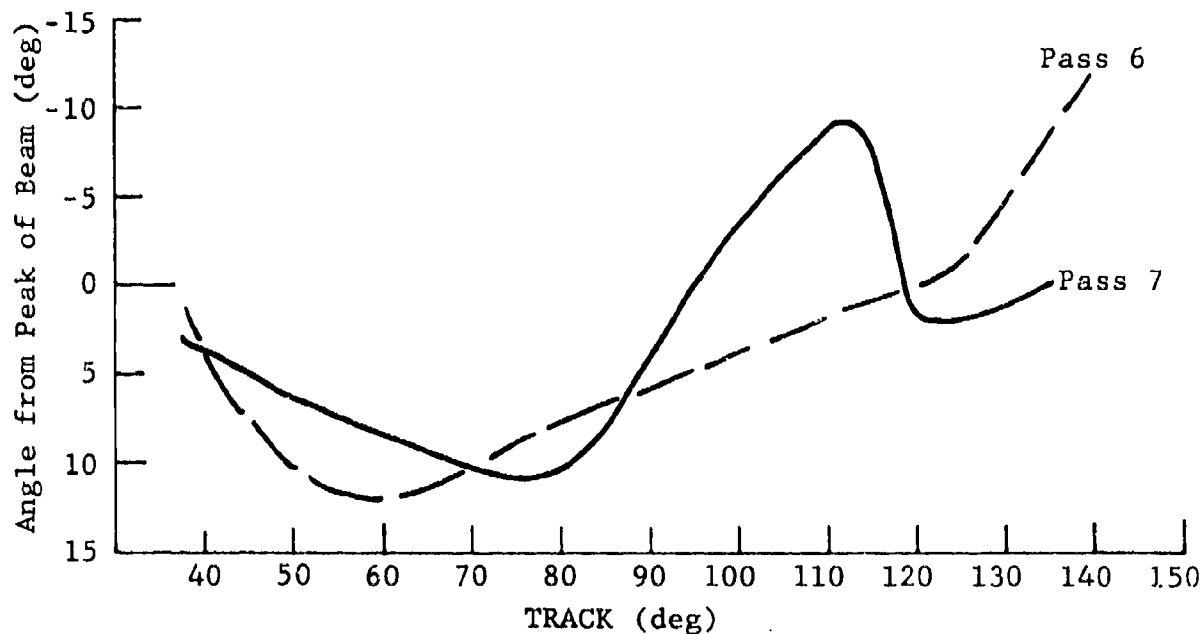
Values of ϕ_{TRANS} together with the corresponding values of TRACK as well as the time marks on both the ϕ_{TRANS} and TRACK records were used to calculate antenna pointing angles. Any deviation between the actual ground track, as determined from aerial photography, and the planned ground track produces a pointing error. Figure C-2 gives the calculated values of transmitting antenna pointing error; the negative angles are on the right while the positive angles are on the left. Using these values with the measured transmitting antenna radiation pattern, the proper correction for the transmitting antenna gain is determined.

C.2 CHECKLISTS AND LOG

This section presents three checklists and a log form used in the data collection program. These include (Figure C-3) the pre-flight calibration checklist, (Figure C-4) the ground check and operate checklist, (Figure C-5) the in-flight calibration checklist, and (Figure C-6) the measurement log form.

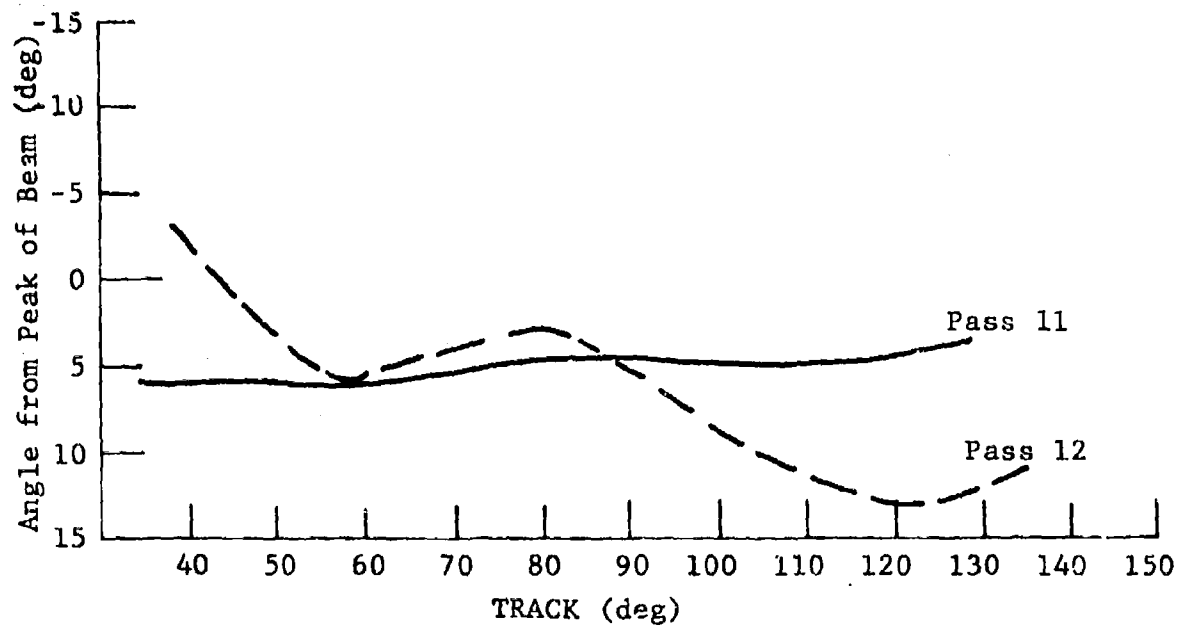


(a) Passes 4 and 5, Flight 7/17/76

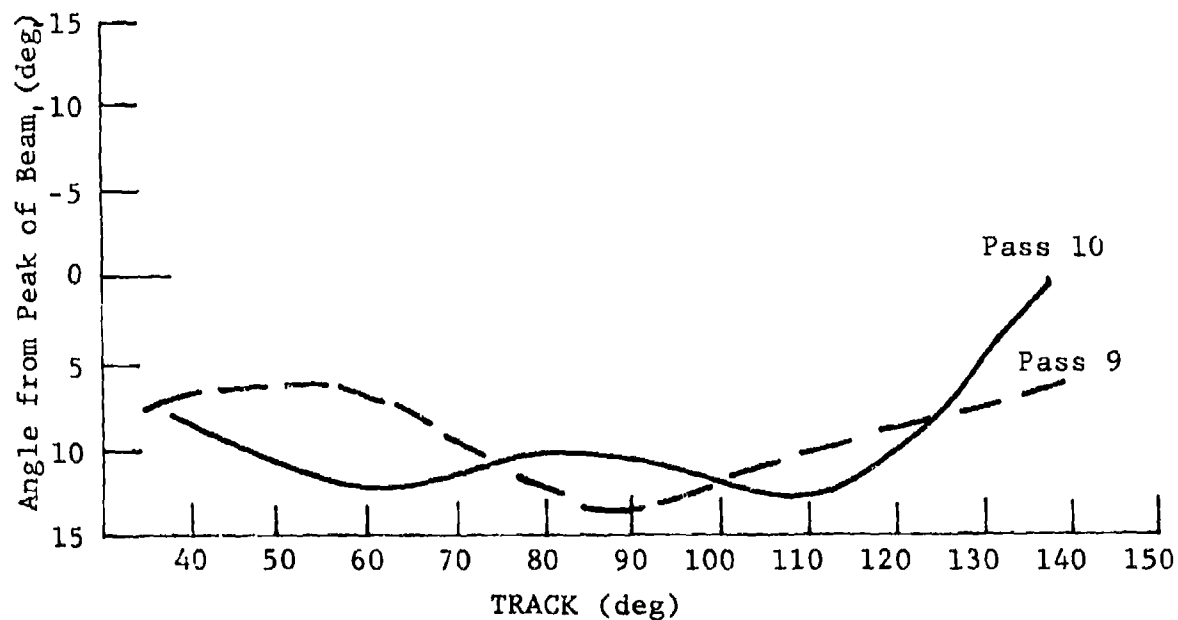


(b) Passes 6 and 7, Flight 7/17/76

Figure C-2. Calculated Transmitting Antenna Pointing Errors



(c) Passes 11 and 12, Flight 7/17/76



(d) Passes 9 and 10, Flight 7/17/76

Figure C-2. Calculated Transmitting Antenna Pointing Errors (concluded)

PPE-FLIGHT BISTATIC CALIBRATION-1

- Gunn attenuators Hi - 19.0 dB, Lo = 21.8 dB
- Crown attenuators disconnected
- 2 - 100 MHz multipliers offset (500 Hz) on
- Alfred 500 Hz on
- X-band calibration attenuator 0.0 dB
- L-band calibration attenuator 10.0 dB
- System in stand-by (Calibration light off, operate light off)
- Pulse - CW switch to pulse
- Measure azimuth voltage supply TP6-B6 18.0 V dc
- Measure tracker azimuth volts 9.0 V dc at 90°
(.050V/ $^{\circ}$) TP3 - B6
- Measure scanner azimuth volts 9.0 V dc at 90°
(.050V/ $^{\circ}$) TP8 - B6
- Set sync pulse (TP-1, B1) for 4850 nsec + ΔT with respect to scope trigger
- Look at boxcar video L-band TP2-B5 and adjust delay R-2. Adjust B-2 until video amplitude is peaked
- X-band L.O. calibration switch to LO.
- Check serrodyne amplitude (Alfred) for min. AM modulation (adjust Helix volts on Alfred) while viewing X-band L.O. on SA
- OP - CAL switch to calibrate
- Check delay time (ΔR) vs calibration steps. (Include ΔT before running)
- Use L-band cross video (raw), 1:1 - Toggle in 1:1 (UP) (B-2).
- Push calibration start - record video delay time for each step.

Figure C-3. Pre-Flight Calibration Checklist

PRE-FLIGHT BISTATIC CALIBRATION-2

<u>ΔR STEP</u>	<u>TIME (nsec)</u>	
ΔR-1	5695	T = 20 nsec (included) + July
ΔR-2	5780	1976 Add + 75 nsec (ramp sync
ΔR-3	5880	delay)
ΔR-4	5980	
ΔR-5	6080	ΔR = 5695 = 20 nsec
ΔR-6	6185	
ΔR-7	6295	
ΔR-8	6420	
ΔR-9	6545	
ΔR-10	6670	
ΔR-11	6810	
ΔR-12	6955	
ΔR-13	7040	

Check PRF for 8.0 KC; TP1 B1 (125 μsec ± 2 μsec)

Set park angle on bistatic antenna

Set scan limit on bistatic antenna

Set scan rate on bistatic antenna

Check "hold" slope on ΔR Board 3, TP-4 (blue).

Adjust R-1 if needed. Adjust @ ΔR min. range (system to standby) and measure voltage at TP4-B3. Adjust R2 B#3 for -1.3 V @ min. range.

Check TP4(blue) B#3 with min. and max. range = -1.3 V to + 1.4 V respectively.

Adjust R-3, B3 to obtain a total voltage output of 2.7 V between min. and max. ΔR range.

Readjust R-2, B3 if necessary to obtain a -1.3 V when ΔR is at its min. range.

Figure C-3. Pre-Flight Calibration Checklist (continued)

PRE-FLIGHT BISTATIC CALIBRATION-3

- ___ Operation-Calibrate switch to Calibrate
- ___ Toggle - 1:1 Switch (B-2) to toggle (down)
- ___ Gunn Attenuators Hi = 19 dB, Lo = 21.8 dB
- ___ Alfred input attenuator 4 dB
- ___ Alfred sawtooth generator 500 Hz
- ___ 2 - 100 MHz multiplier 500 Hz ON
- ___ X-band level set (input to W/J) Set to 13 dB*
- ___ Set S.A. input attenuator to 2W position
- ___ CW - Pulse Switch to CW
- ___ Check X-band LO on S.A.
- ___ X-band LO - Cal Switch to LO. Must measure +6 dBm on S.A. (This gives ~ 4.0 watts to LO line).
- ___ Check L-band LO, on S.A.
- ___ L-band LO - Cal switch to LO. Must measure +0.5 dBm (This gives +10.5 dBm to LO line).
- ___ Remove Crown attenuator cables
- ___ X-band LO-Cal switch to Cal.
- ___ L-band LO-Cal switch to Cal.
- ___ Set X & L-Band Calibrate attenuators to 0 dB
- ___ CW-pulse switch to CW
- ___ View L-band Cal. Sig. on S.A. Should be -39 dBm
- ___ View X-band Cal. Sig. on S.A. Should be -13 dBm
- ___ CW-pulse switch to pulse
- ___ X-band Cal. attenuator to max.
- ___ View X-band Parallel box car video TP2B4, on scope, and set X-band threshold for sample hold to just trigger on noise
- ___ L-band Cal. attenuator to 33.0 dB (-72 dBm to Rx).*

*Subject to change.

Figure C-3. Pre-Flight Calibration Checklist (continued)

PRE-FLIGHT BISTATIC CALIBRATION-4

- View L-band parallel video TP2-B5.
- Set L-band threshold for sample-hold to just trigger on signal
- Set X and L-band Cal. attenuators to 10.0 dB
- Check X and L-band box car video and measure sample-hold time $\approx 220 \mu\text{sec}$
- Connect cables to crown attenuators BNC 37 & 38
- Set X and L-band calibrate attenuators to 0.0 dB
- CW - pulse switch to pulse position
- FR-1300 ck tape recorder speed - 60 ips - ck plug-in filters 60 ips
- Start 8-channel chart recorder -- mm/sec
- Start FR-1300 60 ips
- Push Cal. Start Switch
- When Cal. is completed, stop 8-channel chart recorder
- Stop FR-1300

Figure C-3. Pre-Flight Calibration Checklist (concluded)

BISTATIC GROUND CHECK AND OPERATE-1

3. ☐ Cal. Switch - OFF
- ☐ Operate switch to operate
- ☐ Gunn attenuators Hi & Lo set to max.
- ☐ Check Alfred input attenuator to 4.0 dB
- ☐ 2 - 100 MHz multipliers (no offset) term. 50
- ☐ X-band level set (input W/J) 13 dB
- ☐ Connect tracker (LO antenna) to LO receiver input
- ☐ Position tracker antenna to approx. A/C position
- ☐ Instruct A/C to turn on 10 watt TWT
- ☐ Check LO and PRF lights on
- ☐ Instruct A/C to turn on X & L-band transmitters
- ☐ Position Bistatic antenna to approx. A/C position
- ☐ Check for X & L-band bistatic video (raw)
- ☐ If video is present and normal, notify A/C to prepare for takeoff.
- ☐ Set tracker tilt for pre-determined angle
- ☐ Position tracker to acquisition angle
- ☐ Position bistatic antenna to park angle (with theta dial)
- ☐ Set data start control for desired angle
- ☐ Set data alert control for desired angle, $\sim 5^\circ$ less than data start
- ☐ Start data indicator should be out
4. ☐ A/C will notify ground station when on-line and give ground speed - compute time to T_0 and notify A/C.
- ☐ When tracker error signal = 0, place auto-manual switch in auto track. Switch ON B-10 (UP).

Figure C-4. Ground Check and Operate Checklist

BISTATIC GROUND CHECK AND OPERATE-2

- P.A.I. to tracker position
- Switch Bistatic antenna to scan mode (switch ON B-11 (UP))
- Notify A/C at data start - 10°
- Call last 5° (1° steps) for A/C
- Start chart recorder
- Start FR-1300
- Start audio recorder
- Notify A/C at data start
- Monitor L-band raw video
- Monitor 1 video channel of repro on FR-1300
- Monitor chart recorder
- Notify A/C at end of pass
- Place manual tracker control near tracker angle
- Place tracker auto-manual switch to manual
- Place scanner - auto-manual switch to manual
- Prepare for calibration

After last calibration (end of flight):

- Record tracker and scanner angle voltage (chart and tape) for 10° steps from scan start to scan stop.

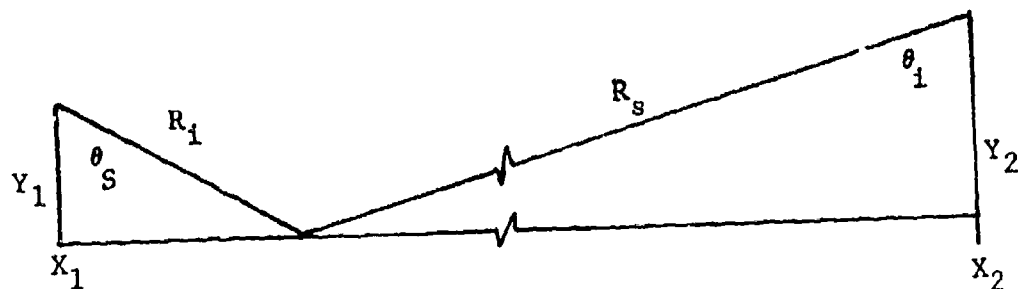
Figure C-4. Ground Check and Operate Checklist (concluded)

IN-FLIGHT BISTATIC CALIBRATION

- Operate switch OFF
- Calibrate switch to calibrate
- Toggle - 1:1 switch (B-2) to toggle (down)
- Gunn Attenuators Hi = 19 dB, Lo = 21.8 dB
- Check Alfred sawtooth generator. High voltage ON (red light on)
- 2 - 100 MHz multiplier 500 Hz ON
- CW - pulse switch to pulse position
- Monitor 1 video channel
- Start 8-channel chart recorder - mm/sec
- Start FR-1300 60 ips
- Push calibration start switch
- When calibration is completed, stop 8-channel chart recorder
- Stop FR-1300

- OFF sets removed from (2) 100 MHz multiplier - Term./51 ohm.
- Gunn attenuators: Hi and Lo to maximum
- Calibration switch OFF
- Place bistatic scanner auto-manual switch to auto (UP)
- Operate switch to operate
- Ready for operation--Go to Section 4 (bistatic ground check and operate sheet)

Figure C-5. In-Flight Calibration Checklist



BISTATIC MEASUREMENT:

DATE:

LOCATION:

PASS NO.:

PARAMETERS:

Y_1

(MSL - AGL)

Y_2

X_1

X_2

θ_S

THRESHOLD LEVEL:

X -

dBm

L -

dBm

DELAY SETTING:

T_{ON} - DIRECT -

N SEC

ANTENNA SCAN LIMITS:

$\leq \text{SCAN} \leq$

Figure C-6. Measurement Log Form

AIRCRAFT HEADING:	MAGNETIC (DEGREES)
DRIFT ANGLE:	DEGREES
TRANS. ANTENNA SCAN ANGLE:	
$\leq \phi \leq$ TRANS	
GROUND VELOCITY:	KTS
TRANSMITTED POWER:	
X -	
L -	
TRACKER ANGLE:	
$\leq \text{TRACK} \leq$	
ELEVATION ANGLE:	DEGREES
CALIBRATIONS:	
CHART RECORDER	
MAGNETIC TAPE	
DATA EVALUATION (ON SITE):	
X -	
L -	
TRACKER -	
L.O. POWER -	
WEATHER CONDITIONS:	

Figure C-6. Measurement Log Form (concluded)

APPENDIX D DATA PROCESSING

This appendix presents the details of the overall data processing procedure used to obtain values of σ_0 from the empirical data recorded during the data gathering flights. The information presented includes the digitization process (Section D.1), the calculation of video signal power (D.2), and the data reduction programs (D.3).

D.1 DIGITIZATION PROCESS

This section describes the computer program which controls the transfer of data from the analog tape record to digital magnetic tape. The program is run on a PDP 11/10 minicomputer with special peripherals configured as shown in Figure D-1. The Sample Command Generator is a custom-built piece of hardware which generates the six pulses needed during each complete PRF cycle to synchronize the data-sampling circuitry.

See Figure D-2 and note that a complete PRF cycle, including both a 3 cm and a 23 cm pulse, lasts 500 μ sec, reflecting the fact that the analog tape is played back at half speed. (During flight, this time is 250 μ sec.) Note also that, regardless of whether the sample command pulses are synchronized with the 3 cm or 23 cm part of the PRF, the four video channels are sampled at times when the video data are valid. (Samples occur during the high portion of a sample command pulse.)

The program consists of an interrupt handler and a main loop. The interrupt routine, activated by a sample command, first deposits the result from the last conversion into a buffer and increments a pointer which is used to step through the buffer. Then, it selects the correct

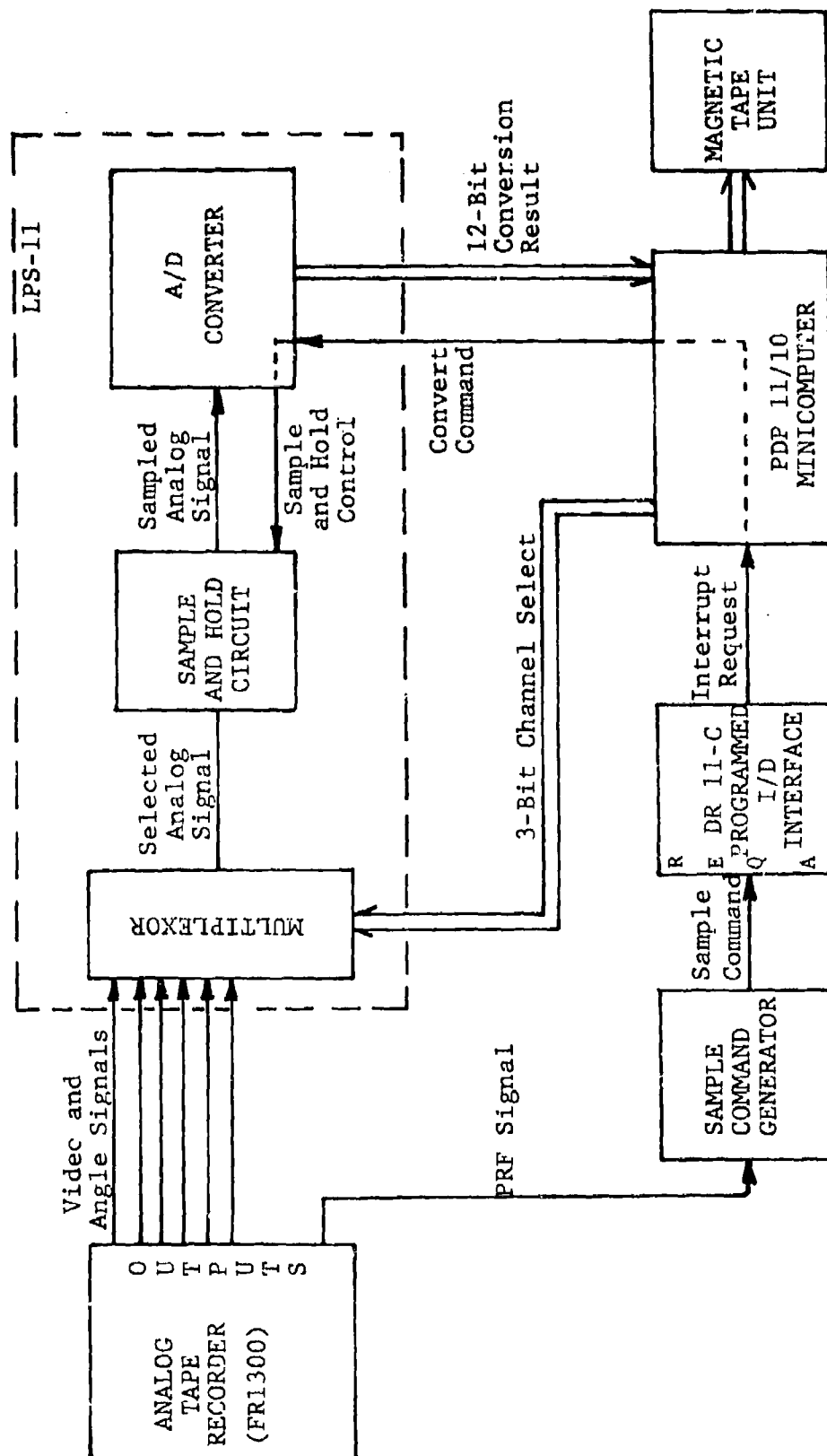


Figure D-1. Digitization System

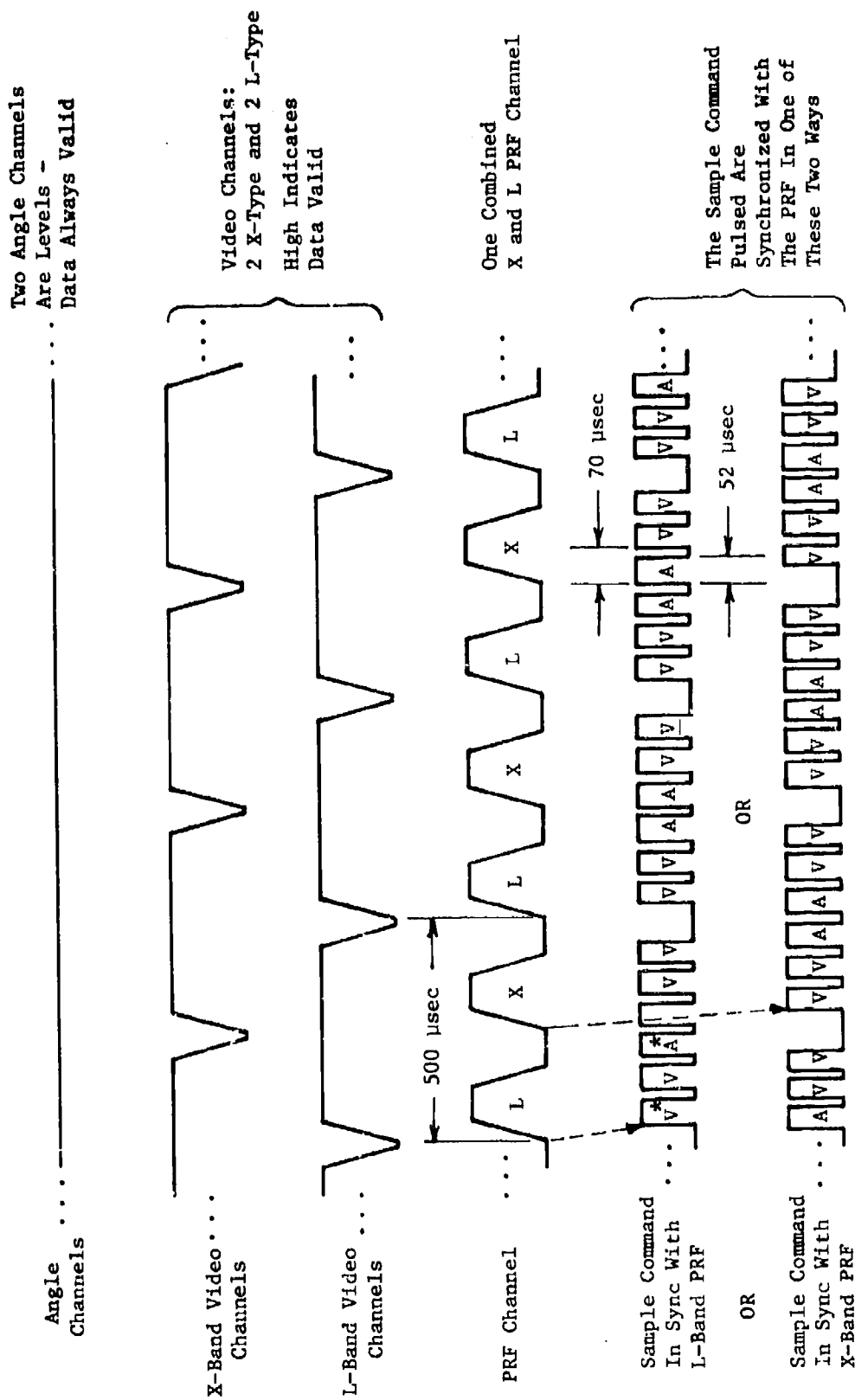


Figure D-2. Digitization Timing Diagram

multiplexer channel and initiates a convert command. The main loop monitors the buffer pointer. When a buffer is full, it writes an entire record to tape and sets up a new buffer pointer for the interrupt routine to use. Thus, there are two, 6000-word buffers and, at any given time, one is being filled with data by the interrupt routine and one is being emptied to the magnetic tape unit. Due to strict timing constraints, one group of six samples is missed when the buffer switch-over occurs.

D.2 CALCULATION OF VIDEO SIGNAL POWER

This section describes a program which calculates the power in each digitized video signal over a set of intervals determined by the angle information. The average power in any interval of N samples is calculated by

$$P = \frac{1}{N} \sum_{i=1}^N X_i^2, \quad (D-1)$$

where the X_i 's are the video samples. The summation intervals are defined by dividing the range of scan angle values into a number of equal divisions. In Figure D-3, for example, the scan angle range has been divided into five equal parts. With the data shown, this has resulted in twenty summation intervals. That is, twenty values of average power will be computed for each video channel. Note the (exaggerated) glitch between intervals thirteen and fourteen. Here, the scan angle jumped into division 2, jumped back into division 1, and then continued normally into division 2. Note that, under normal circumstances, this would produce two, small summation intervals between intervals thirteen and fourteen. To avoid this, the program has a user-input sample number threshold (That is, a threshold on N). If

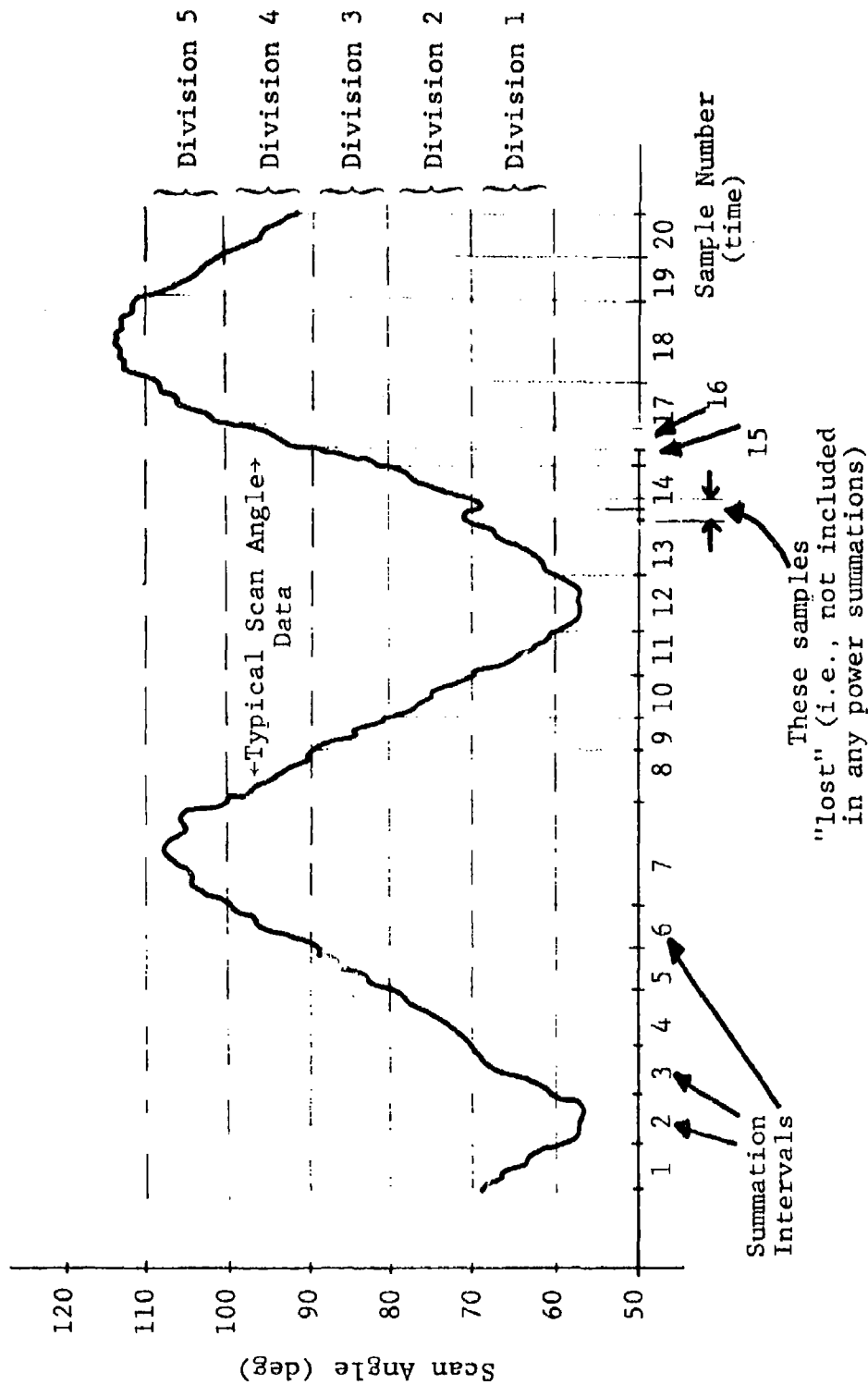


Figure D-3. Example of Scan Angle Divisions

the number of samples in a summation interval is less than this threshold, the interval is ignored and no power calculation is made.

The inputs to this program are the tapes created during the digitization process. Eight values are outputted for each summation interval: (1) the number of samples in the interval (N), (2) the division number, (3 and 4) two values of the tracker angle, one corresponding to the first sample in the interval and the other from the last sample in the interval, and (5 through 8) a value of average power for each of the four video channels. This output is printed on the terminal and also goes to magnetic tape (namely, the uncalibrated computer compatible tape referred to in Section D.3).

D.3 DATA REDUCTION PROGRAMS

Four programs, written in IBM Fortran IV and run on the Ann Arbor, Michigan MTS (Michigan Terminal System) computing facilities, are used to compute σ_o (radar cross section per unit area). These programs start from the uncalibrated CCT (computer compatible tape) with some user input and end by producing terminal and CALCOMP plots displaying σ_o versus ϕ_s (difference between scan and track angles).

The simulation program, BSMAIN, may be used in a stand-alone mode requiring only user response.

D.3.1 MAIN PROGRAM DESCRIPTIONS

The processing of data from the uncalibrated CCT to the actual plotting of results has been divided into three main procedures.

The first procedure applies calibration equations to

the data from the CCT and outputs the intermediate results to the second procedure.

The second procedure accepts the above results along with some positional dimensions and then calls the simulation program BSMAIN to obtain KI, the power weighting factor. Sigma naught (σ_0) is then computed and, along with ϕ_s , outputted to the third procedure.

The third procedure accepts the above results along with some labeling information and produces terminal and CALCOMP plots of the results.

D.3.1.1 Procedure FIRST (User Input)

This program (whose flow chart is shown in Figure D-4) is used to calibrate the data found on the CCT. The following questions require user response:

1. Scattering? Forward scattering assumes $\text{SCAN} = 0^\circ$ to be north, whereas back scattering assumes $\text{SCAN} = 0^\circ$ to be south.
2. Count Acceptance Threshold? A particular data point may be rejected if the number of samples from which it was obtained is less than some threshold.
3. Minimum Scan Angle? A data point may be rejected if its scan angle is less than some minimum.
4. Power Corrections? Power corrections, which are added to the incident power, are defined at three points over the scan angle range (see Section C.3). These points define equations which may be used to interpolate a power correction at any scan angle.
5. Scan and Track Equations? Point-slope form equations are entered to convert the CCT angle information into SCAN and TRACK in degrees.

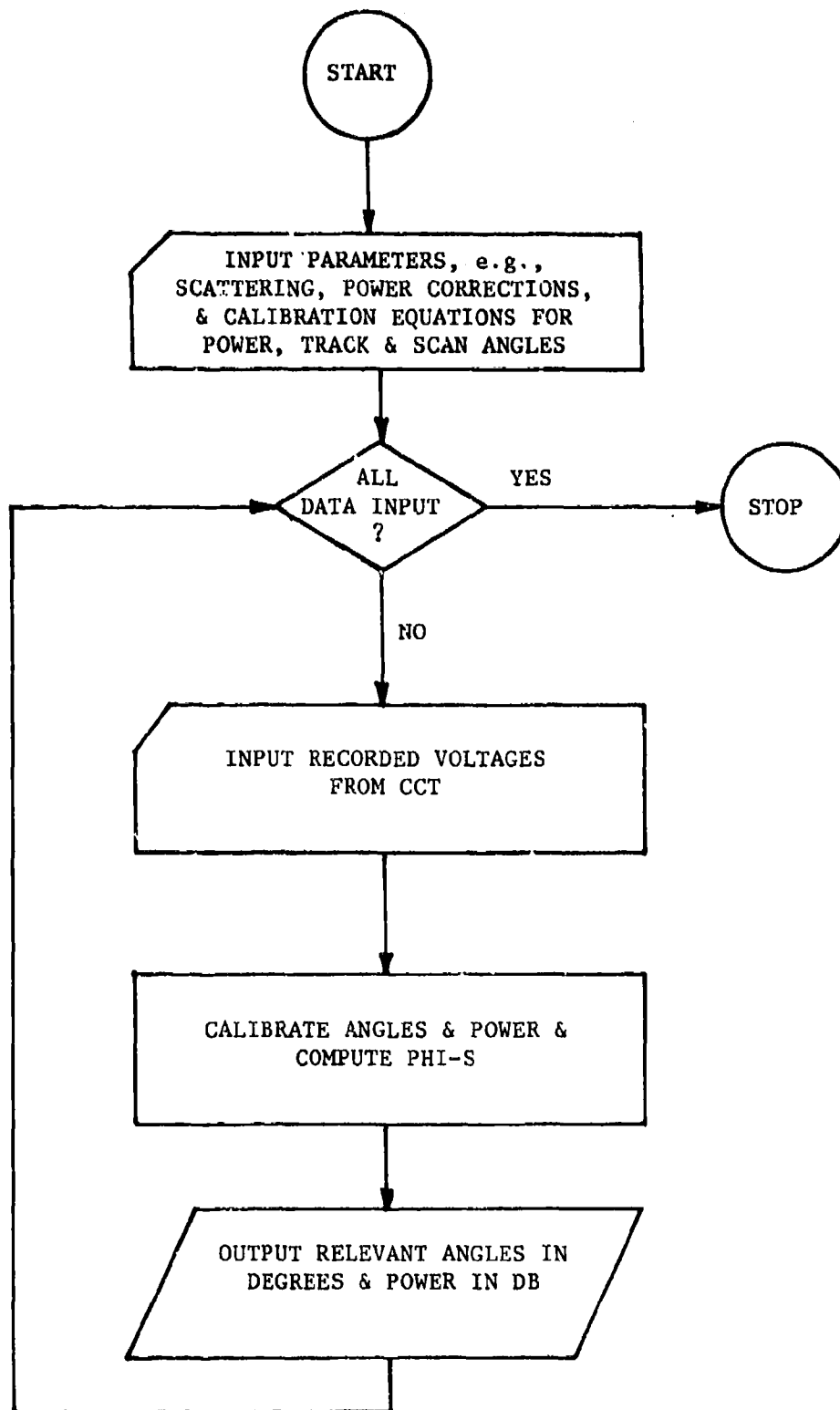


Figure D-4. Flow Chart for Procedure FIRST

6. Power Equations? Point-slope form equations are entered to convert the CCT power information into 3 cm and 23 cm (parallel and cross) power in dB.

D.3.1.2 Procedure FIRST (Data Input-Output)

The components of each line read from the CCT are calibrated using the proper above-mentioned equations unless certain conditions, also mentioned above, are not met, in which case the entire line is rejected. All angles (including ϕ_s which is calculated) and all powers (including power corrections) are then outputted in tabular form (see the example in Table D-1). The program listing for this procedure is shown in Figure D-5.

D.3.1.3 Procedure SECOND

This program (whose flow chart is shown in Figure D-6) calculates σ_o given the geometry of the flight and the simulated KI. The following parameters are required as inputs: (1) receiver depression angle and height, (2) transmitter height and range, and (3) whether to use 3 or 23 cm radar parameters. The results of procedure FIRST are then inputted, one data case at a time, to obtain the proper SCAN and TRACK angles. If the power is in the noise, it is rejected at this point.

After all other necessary parameters have been assigned, BSMAIN, the simulation program which (when given the proper geometry) will return the power weighting factor KI, is called. Sigma naught is then computed with the following equation:

$$\sigma_o = P_r - P_i - KI - \text{Correction (All values in dB)}.$$

The separate parts of this equation may be outputted, as shown in Table D-2. A source listing is presented in

BEST AVAILABLE COPY

TABLE D-1. PROCEDURE FIRST OUTPUT

SCA = 20,2000 +
INACA = 43,7000 +
X-RAY = 75,2000 +
L-BAND = 60,0000 +
THAT SHLD = 50

COUNT	SCAN	TRACK	PHI-S	DAT-A	DAT-B	DAT-C	DAT-D	CORRECTION
3526	64.4(4)	48.9(-214)	16.0	-104.6(0)	-104.6(0)	-62.3(7)	-61.9(8)	-6.5
1362	73.2(5)	45.7(-212)	24.5	-75.2(0)	-104.6(0)	-66.6(2)	-66.6(2)	-6.5
1200	82.0(6)	49.4(-208)	32.6	-104.6(0)	-104.6(0)	-69.0(1)	-66.6(2)	-6.4
2203	90.6(7)	50.4(-202)	40.4	-75.2(1)	-104.6(0)	-69.0(1)	-65.6(2)	-6.3
574	108.4(8)	53.5(-183)	54.9	-75.2(1)	-104.6(0)	-66.6(2)	-66.6(2)	-5.9
3417	122.0(9)	55.0(-174)	27.0	-75.2(1)	-104.6(0)	-66.6(2)	-66.6(2)	-5.7
3355	73.2(5)	55.8(-169)	17.4	-104.6(0)	-104.6(0)	-69.0(1)	-65.2(3)	-5.6
3219	64.4(4)	56.6(-164)	7.8	-104.6(0)	-104.6(0)	-62.3(7)	-50.8(199)	-5.4
3078	64.4(4)	58.4(-151)	5.6	-75.2(1)	-104.6(0)	-61.5(9)	-52.2(134)	-5.2
3766	73.2(5)	59.6(-146)	13.6	-104.6(0)	-104.6(0)	-66.6(2)	-64.2(4)	-5.1
3797	82.0(6)	60.3(-142)	21.7	-75.2(1)	-104.6(0)	-69.0(1)	-69.0(1)	-5.0
3501	90.6(7)	61.8(-133)	29.0	-69.0(1)	-75.2(1)	-69.0(1)	-69.0(1)	-4.8
3639	94.6(8)	62.9(-126)	36.7	-75.2(1)	-104.6(0)	-69.0(1)	-69.0(1)	-4.6
1870	108.4(8)	62.9(-126)	45.5	-75.2(1)	-104.6(0)	-69.0(1)	-69.0(1)	-4.5
503	117.2(10)	63.6(-122)	53.6	-72.2(1)	-104.6(0)	-60.2(13)	-58.1(24)	-4.3
1030	117.2(10)	65.4(-111)	51.8	-75.2(1)	-104.6(0)	-68.9(1)	-51.5(165)	-4.3
3678	108.4(8)	65.1(-113)	43.3	-72.2(1)	-75.2(1)	-69.0(1)	-65.0(1)	-4.3
2223	99.6(8)	66.0(-107)	33.6	-70.5(1)	-75.2(1)	-66.6(2)	-65.2(3)	-4.2
3064	99.6(8)	67.5(-98)	23.3	-75.2(1)	-104.6(0)	-66.6(2)	-65.2(3)	-4.0
3455	82.0(6)	69.3(-87)	12.7	-104.6(0)	-104.6(0)	-59.7(15)	-55.4(53)	-3.6
3090	73.2(5)	70.2(-82)	3.0	-104.6(0)	-75.2(1)	-51.0(191)	-46.5(700)	-3.6
2272	64.4(4)	70.4(-78)	6.4	-104.6(0)	-75.2(1)	-49.7(277)	-47.3(556)	-3.6
3602	64.4(4)	71.5(-74)	7.1	-75.2(1)	-104.6(0)	-47.9(464)	-47.2(560)	-3.5
3647	73.2(5)	72.5(-68)	0.7	-75.2(1)	-104.6(0)	-48.7(373)	-46.7(659)	-3.3
2167	82.0(6)	73.6(-61)	8.4	-104.6(0)	-104.6(0)	-60.3(11)	-57.6(26)	-3.2
3353	90.6(7)	74.8(-54)	16.0	-104.6(0)	-104.6(0)	-62.9(6)	-58.7(20)	-3.0
3405	94.6(8)	76.1(-46)	23.5	-104.6(0)	-104.6(0)	-64.2(4)	-59.3(17)	-3.0
3084	108.4(8)	77.1(-40)	31.3	-104.6(0)	-75.2(1)	-69.0(1)	-66.6(2)	-3.0
3305	117.2(10)	78.1(-34)	39.1	-104.6(0)	-75.2(1)	-57.6(28)	-57.8(26)	-3.0
3486	117.2(10)	79.2(-27)	38.0	-75.2(1)	-75.2(1)	-56.6(35)	-55.9(14)	-3.0
3337	108.4(8)	79.9(-23)	28.5	-75.2(1)	-75.2(1)	-65.2(3)	-65.2(3)	-3.0
3223	94.6(8)	80.9(-17)	18.7	-75.2(1)	-75.2(1)	-55.9(46)	-55.8(200)	-3.0
3314	90.6(7)	81.9(-11)	8.9	-104.6(0)	-75.2(1)	-55.1(58)	-44.5(1249)	-3.0
1952	82.0(6)	81.9(-11)	0.1	-75.2(1)	-75.2(1)	-46.0(805)	-44.2(1390)	-3.0
3462	64.4(4)	84.9(7)	20.5	-104.6(0)	-104.6(0)	-48.3(414)	-47.3(551)	-3.0
4172	64.4(4)	86.8(19)	22.4	-104.6(0)	-104.6(0)	-51.8(149)	-47.7(501)	-3.0
3056	73.2(5)	87.0(20)	13.8	-104.6(0)	-104.6(0)	-50.1(249)	-48.1(440)	-3.0
3783	82.0(6)	87.7(24)	5.7	-75.2(1)	-104.6(0)	-47.4(541)	-45.6(912)	-3.0
3404	90.6(7)	89.3(34)	1.5	-75.2(1)	-104.6(0)	-51.6(160)	-50.5(218)	-3.0
3726	94.6(8)	90.0(38)	9.6	-68.4(5)	-75.2(1)	-46.7(661)	-42.4(320)	-3.0
3706	108.4(8)	91.6(42)	16.6	-68.4(5)	-75.2(1)	-52.0(141)	-45.4(941)	-3.0
3207	117.2(10)	90.6(42)	26.6	-75.2(1)	-104.6(0)	-57.0(33)	-48.6(378)	-3.0
3452	117.2(10)	91.8(49)	25.4	-70.5(3)	-75.2(1)	-53.6(90)	-51.3(172)	-3.0
2171	108.4(8)	92.1(51)	16.3	-66.3(8)	-75.2(1)	-51.0(192)	-48.7(375)	-3.0
3750	99.6(8)	92.9(53)	6.7	-70.5(3)	-75.2(1)	-54.6(66)	-47.8(486)	-3.0
1452	90.6(7)	93.1(62)	3.1	-66.4(5)	-75.2(1)	-47.4(548)	-46.1(790)	-3.0
3633	64.4(4)	94.1(75)	31.7	-75.2(1)	-75.2(1)	-54.1(76)	-51.3(175)	-3.0
1819	64.4(4)	98.5(90)	34.1	-69.3(4)	-75.2(1)	-48.2(427)	-47.8(489)	-3.0
3757	73.2(5)	100.5(102)	27.3	-104.6(0)	-75.2(1)	-50.3(231)	-48.4(401)	-3.0
3401	82.0(6)	102.3(116)	20.8	-104.6(0)	-75.2(1)	-48.7(370)	-43.8(1571)	-3.0

```

22 INTEGER*2 RUF(6),BUF2(6)
23 LOGICAL*1 BACK,FRUC
24 REAL SCAN(2),TRACK(2),XB(2),LB(2),POW(4),PC(2,2)
25 CALL FCYTRN(1)
26 CALL FTRCND('OFFAULT RESPRINT')
27 CALL FTRCND('SET WARMUP=OFF')
28 CALL ENPYF(7)
29 WRITE(6,22)
30 FORMAT(' FORWARD OR BACK SCATTERED?')
31 READ(5,23) BACK
32 FORMAT(1)
33 IF (BACK) THEN
34   C20 FORMAT(' ENTER NUMBER OF SCAN DIVISIONS AND DIVISION ENDPOINTS')
35   READ(5,21) NOIV,DMIN,DMAX
36   C21 FORMAT(15,2F10.0)
37   SCAN(2)=(DMAX+DMIN)/FLOAT(NOIV-1)
38   C22 SCAN(1)=DMIN-SCAN(2)
39   C23 FORMAT(18)
40   WRITE(6,23)
41   C24 FORMAT(' ENTER COUNT ACCEPTANCE THRESHOLD')
42   READ(5,24) ITWRES
43   C25 WRITE(6,25)
44   C26 FORMAT(' ENTER MINIMUM SCAN ANGLE')
45   READ(5,26) SCNMTH
46   C27 WRITE(6,27)
47   C28 FORMAT(' ENTER CORRECTION START, MID AND END TRACK ANGLES')
48   READ(5,28) AS,AM,AE
49   C29 WRITE(6,29)
50   C30 FORMAT(' ENTER START, MID AND END TRANSMITTER POWER CORRECTIONS')
51   READ(5,30) PCS,PCM,PCE
52   C31 PC(2,1)=(PCM-PCS)/(AM-AS)
53   C32 PC(2,2)=(PCE-PCM)/(AE-AM)
54   C33 PC(1,1)=PCS-PC(2,1)*AS
55   C34 PC(1,2)=PCM-PC(2,2)*AM
56   C35 WRITE(6,31)
57   C36 FORMAT(' ENTER SCAN CONVERSION EQUATION')
58   READ(5,32) SCAN
59   C37 FORMAT(3F10.0)
60   C38 WRITE(6,33)
61   C39 FORMAT(' ENTER TRACK CONVERSION EQUATION')
62   READ(5,34) TRACK
63   C40 WRITE(6,35)
64   C41 FORMAT(' ENTER X-RAND POWER EQUATION')
65   READ(5,36) XR
66   C42 C43 XRAND(5,12) XR
67   C44 WRITE(6,37)
68   C45 FORMAT(' ENTER L-RAND POWER EQUATION')
69   READ(5,38) LR
70   C46 XB(1)=80.0
71   C47 XB(2)=90.0
72   C48 LB(1)=70.1
73   C49 LB(2)=80.0
74   C50 WRITE(6,39)
75   C51 FORMAT(1)
76   C52 810X,'SCAN =',F10.4,' +',F10.4,' X',/
77   C53 810X,'TRACK =',F10.4,' +',F10.4,' X',/
78   C54 810X,'XRAND =',F10.4,' +',F10.4,' X',/
79   C55 810X,'LRAND =',F10.4,' +',F10.4,' X',/
80   C56 810X,'THRESHOLD =',F10.4,' X',/
81   C57 WRITE(6,40)
82   C58 FORMAT(1)
83   C59 810X,'COUNT',5X,'SCAN',7X,'TRACK',5X,'PHI-S',5X,'DAT-A',8X,'DAT-B',8X,'DAT-C',8X,'DAT-D',7X,'CORRECTION',/1X)
84   C60 ENPYF(1)

```

Figure D-5. Program Listing for Procedure FIRST

BEST AVAILABLE COPY

```

8 READ(4,7,END=6) RUF
9 FORMAT(8A2)
IF (RUF(1),LT,ITRES) GO TO 8
IBUF=RUF(2)
S=SCAN(1)+SCAN(2)+FLOAT(IBUF)
IF(S,1,SCANIN) GO TO 8
ITRACK=(RUF(3)+RUF(4))/2
ITRACK(1)+ITRACK(2)+FLOAT(ITRACK)
PHIS=ARS(S-1)
IF (FOUC(RACK,IN)) PHIS=ARS(PHIS-180.)
R=RUF(5)
POX(1)=XR(1)+XR(2)*ALOG10(AMAX1(R,001))*10.
R=RUF(6)
POX(2)=XR(1)+XR(2)*ALOG10(AMAX1(R,001))*10.
R=RUF(7)
POX(3)=R(1)+R(2)*ALOG10(AMAX1(R,001))*10.
R=RUF(8)
POX(4)=R(1)+R(2)*ALOG10(AMAX1(R,001))*10.
I=1
IF(I,GT,4) I=2
COR=PC(1,1)+PC(2,1)*T
WRITE(7) T,PHIS,POW,COR
WRITE(8,9) RUF(1),S,RUF(2),T,ITRACK,PHIS,(POW(I-4),RUF(1),I=5,8),CDK
FORMAT(I8,F7.1,('12,1'),F7.1,('14,1'),F7.1,('16,1'),F10.1)
GO TO 8
6 STOP
END

```

Figure D-5. Program Listing for Procedure FIRST (concluded)

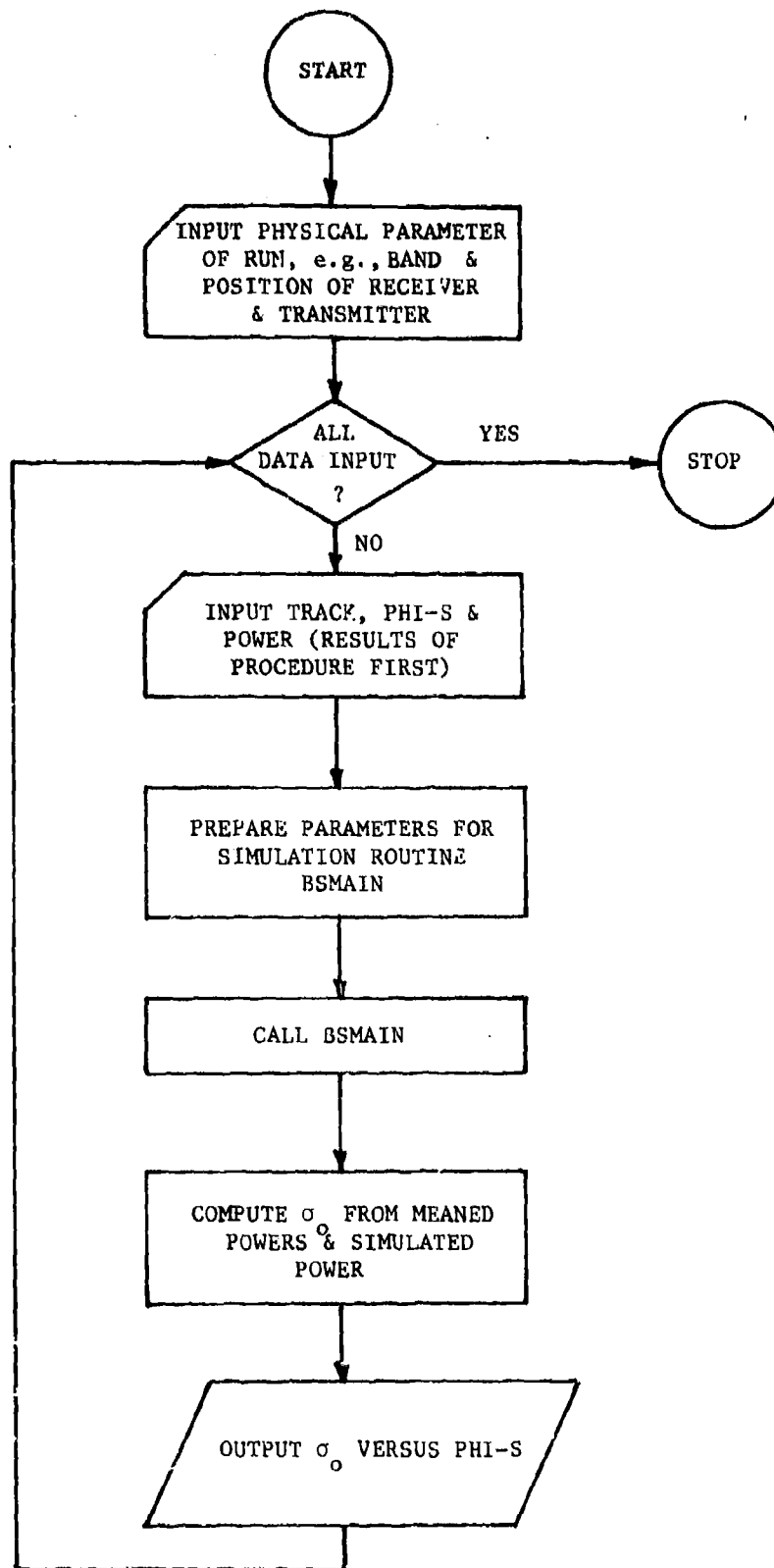


Figure D-6. Flow Chart for Procedure SECOND

BEST AVAILABLE COPY

TABLE D-2. PROCEDURE SECOND OUTPUT

PHIS	PI	PDW	KI	CON	SIGMA
10.8	57.0	-79.6	-82.9	-10.9	-42.8
11.4	57.0	-52.1	-82.6	-11.1	-15.5
2.0	57.0	-36.0	-86.4	-11.2	4.6
7.9	57.0	-36.0	-83.3	-11.3	1.6
17.9	57.0	15.5	-82.1	-11.3	51.9
27.7	57.0	-15.8	-82.9	-11.3	21.5
37.1	57.0	-15.8	-84.0	-11.5	22.8
46.6	57.0	-8.5	-85.2	-11.6	31.3
56.0	57.0	32.8	-86.3	-11.8	73.9
65.4	57.0	-15.8	-87.3	-11.9	26.4
75.1	57.0	19.0	-88.2	-12.0	62.2
78.6	57.0	7.6	-88.2	-12.1	50.9
64.6	57.0	-52.1	-87.3	-12.1	-9.7
54.3	57.0	-353.8	-86.3	-12.2	-312.3
44.4	57.0	-353.8	-85.2	-12.1	-313.9
34.3	57.0	-353.8	-84.0	-12.2	-314.6
23.7	57.0	25.1	-82.9	-12.3	63.4
13.4	57.0	-52.1	-82.1	-12.4	-14.6
3.0	57.0	22.2	-83.3	-12.5	61.0
7.3	57.0	22.2	-82.2	-12.6	59.9
17.7	57.0	49.1	-82.5	-12.7	86.3
18.5	57.0	15.5	-82.6	-12.9	54.0
9.0	57.0	-52.1	-81.9	-13.0	-14.3
0.9	57.0	-353.8	-83.3	-13.0	-314.5
11.0	57.0	-353.8	-82.1	-13.0	-315.8
20.7	57.0	-353.8	-82.9	-13.0	-314.9
30.1	57.0	-353.8	-84.0	-13.1	-313.8
39.8	57.0	-353.8	-85.2	-13.1	-312.5
49.2	57.0	-353.8	-86.3	-13.1	-311.4
58.7	57.0	-353.8	-87.3	-13.2	-310.4
68.7	57.0	-353.8	-88.2	-13.2	-309.5
68.1	57.0	30.9	-88.2	-13.2	74.8
57.9	57.0	-8.5	-87.3	-13.2	35.0
47.9	57.0	2.9	-86.3	-13.2	45.4
37.8	57.0	2.9	-85.2	-13.2	44.4
27.3	57.0	-8.5	-84.0	-13.2	31.8
17.0	57.0	-79.6	-82.9	-13.3	-40.5
6.5	57.0	-79.6	-82.1	-13.3	-41.3
3.9	57.0	-353.8	-81.9	-13.3	-315.7
13.9	57.0	-353.8	-82.7	-13.3	-314.8
24.1	57.0	-353.8	-83.8	-13.3	-313.7
25.2	57.0	-353.8	-84.1	-13.4	-313.4
15.8	57.0	-353.8	-83.1	-13.5	-314.2
6.1	57.0	-353.8	-82.2	-13.5	-315.1
4.1	57.0	-353.8	-82.1	-13.5	-315.3
13.9	57.0	-353.8	-82.9	-13.5	-314.5
23.6	57.0	-79.6	-84.0	-13.5	-39.1
33.1	57.0	-52.1	-85.2	-13.5	-19.4
42.5	57.0	-8.5	-86.3	-13.6	34.4
52.5	57.0	-8.5	-87.3	-13.6	35.3
61.6	57.0	7.6	-88.2	-13.6	52.4
70.8	57.0	-8.5	-86.3	-13.7	34.5
80.0	57.0	-79.6	-85.2	-13.7	-37.7
20.5	57.0	-353.8	-84.0	-13.7	-313.1
10.2	57.0	-353.8	-82.9	-13.7	-314.2
0.1	57.0	-353.8	-82.1	-13.7	-315.0
10.9	57.0	-353.8	-83.2	-13.8	-313.9

Figure D-7.

D.3.1.4 Procedure THIRD

This program (whose flow chart is shown in Figure D-8) computes averages over a ϕ_s increment and plots the results. Axis labels and an angular averaging increment are required inputs from the user along with some scaling information. Three pairs of terminal plots are then produced from the results of the second procedure for each pass. Each pair of plots (an example of which is shown in Figure D-9) consists of (1) an unaveraged graph and (2) the average of that graph. The first pair of plots uses all the data from the particular pass, the second uses the first half of the data, and the third uses the last half.

These results are also outputted in tabular form so that canned MTS programs may CALCOMP-plot selected graphs. A source listing for this program is presented in Figure D-10.

D.3.2 SIMULATION DESCRIPTION

The simulation program BSMAIN, which is called by the second procedure, may also be run as a stand-alone main program. Given the proper geometry and radar parameters, BSMAIN computes a power weighting (KI) over a calculated area.

The program's first action, after all necessary parameters have been entered via Namelist input, is to draw the scene on a graphics display terminal. Anything drawn on the screen may also be reproduced as a CALCOMP plot, as shown in Figure 33, for example.

Given the receiver height, depression angle, scan angle, and beamwidth, an elliptical receiver footprint may

BEST AVAILABLE COPY

```

REAL R(6),T(6),QZ(9),POM(4),KON,KI
LOGICAL PLINT,ORAN,REPEAT,PAUSE
COMMON /RI/ R,T,QZ,DX,DX2,SCALE,PLINT,ORAN,REPEAT,PAUSE,SPENT,AREA,KI,AREAR,TRACK,KON,DLANDA
LOGICAL A1,KL,EQUCLAR(Q1),YES,AUX
INTEGER IZ,LEN
INTEGER COST
ICECHST(0)
CALL FCUTMR(1)
CALL ENDTYF(R)
:PATH=1
CALL BSMAIN(PATH)
CALL Q(USE X OR L BAND?)
READ(5,1) XL,AUX
FORMAT(2A1)
CALL Q(ENTER RECEIVER DEPRESSION ANGLE?)
READ(5,2) R(5)
FORMAT(F10.0)
CALL Q(ENTER RECEIVER HEIGHT?)
READ(5,2) R(2)
CALL Q(ENTER TRANSMITTER HEIGHT?)
READ(5,2) T(2)
CALL Q(ENTER TRANSMITTER DISTANCE?)
READ(5,2) T(1)
R(1)=0.
R(3)=0.
IXL=2
IF(LOC(XL,'X')) IXL=0
IF(LOC(XL,'X')) GO TO 3
R(4)=9.36
KONS=.667
DLANDA=13.36
PI=57.
GO TO 4
R(4)=8.7
KONS=.037
DLANDA=14.02
PI=57.
WRITE(6,7) R(4),DLANDA,PI,KON
FORMAT('08= ',F5.2, ' DLANDA = ',F6.2, ' PI = ',F5.1, ' K = ',F6.3/)
WRITE(6,8) R(4),DLANDA,PI,KON
FORMAT('08= ',F5.2, ' DLANDA = ',F6.2, ' PI = ',F5.1, ' K = ',F6.3/)
CALL Q(ARE ANY OTHER PARAMETERS TO BE CHANGED?)
READ(5,1) YES
:PATH=2
IF(LOC(YES,'Y')) :PATH=3
READ(7,END=9) TR,PHIS,POM,COR
TR=90.-PI
T(3)=T(1)+ATAN(TW/57.296)
P(6)=TR-PHIS
IF(POM(1)) LT=-74..AND..IXL.EQ.0) GO TO 5
IF(POM(3)) LT=-64..AND..IXL.EQ.2) GO TO 5
CALL BSMAIN(IPATH)
:PATH=1
SIG1=POM(1)+IXL-.01-KI-COR
SIG2=POM(2)+IXL-.01-KI-COR
WRITE(8,9) PHIS,SIG1,SIG2
FORMAT(F10.1)
IF(LOC(AUX,'Y')) WRITE(19,8) PHIS,PI,POM(1+IXL),KI,COR,SIG1
GO TO 5

```

Figure D-7. Source Listing for Procedure SECOND

BEST AVAILABLE COPY

```

9  CONTINUE
   PCOST=FLRAT((COST(0)-IC)/100)/100.
   WRITE(6,10) PCOST
10  FORMAT('TOTAL COST =',F6.2)
   STOP
   END

C
C  SUBROUTINE Q(Q)
   LOGICAL R(1)
   INTEGER I2 LEN
   CALL FINDST(R,120,'',1,1,TFND)
   IF (IFND.EQ.0) IFND=6
   LEN=TFND-1
   CALL SERCUM(R,LEN,0)
   RETURN
   END

```

Figure D-7. Source Listing for Procedure SECOND (concluded)

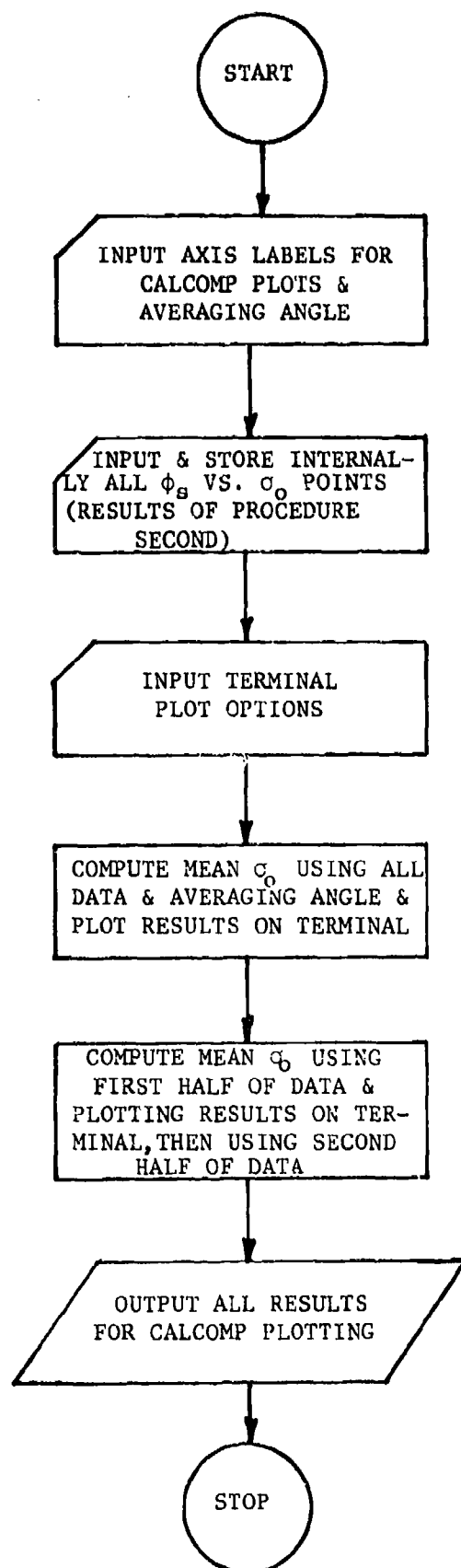


Figure D-8. Flow Chart for Procedure THIRD

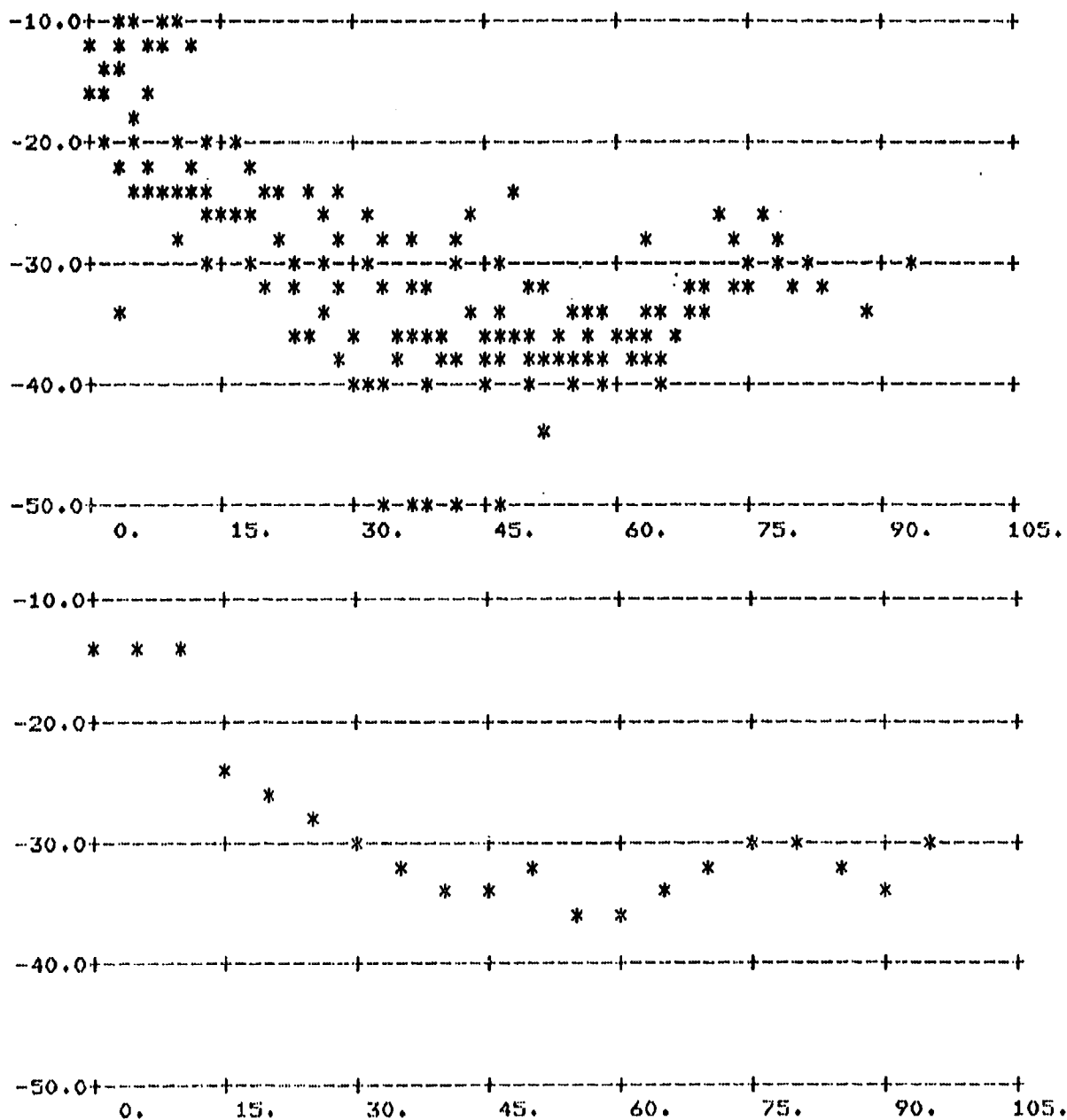


Figure D-9. Example Output Plots from Procedure THIRD

BEST AVAILABLE COPY

```

LOGICAL A1 LAR(50)
REAL SIG1(1000), SIG2(1000), PHIS(1000)
INTEGER ITAG(1000)
LOGICAL A1 FMT(1)/'A'/
REAL MT(2,1001), MT2(2,1001)
CALL FCVTHR(1)
CALL EMPTYF(0)
CALL EMPTYF(1)
CALL EMPTYF(2)
WRITE(0,14)
WRITE(1,14)
WRITE(2,14)
14 FORMAT(' (F10.0,F10.0)')
C CALL Q('INSERT PARALLEL X-AXIS LABEL;')
C CALL READ(LAR,LEN,0,IN,5)
C CALL WRITE(LAR,LEN,0,LN,0)
C CALL Q('INSERT PARALLEL Y-AXIS LABEL;')
C CALL READ(LAR,LEN,0,IN,5)
C CALL WRITE(LAR,LEN,0,LN,0)
C CALL Q('INSERT CROSS X-AXIS LABEL;')
C CALL READ(LAR,LEN,0,IN,5)
C CALL WRITE(LAR,LEN,0,LN,1)
C CALL Q('INSERT CROSS Y-AXIS LABEL;')
C CALL READ(LAR,LEN,0,IN,5)
C CALL WRITE(LAR,LEN,0,LN,1)
WRITE(0,A)
8 FORMAT(' ENTER AVERAGING ANGLE')
READ(5,9) HANG
9 FORMAT(F10.0)
DO 1 J=1,1000
READ(8,2,END=6) PHIS(J), SIG1(J), SIG2(J)
2 FORMAT(3F10.1)
ITAG(J)=J
1 NCC=J
6 CONTINUE
WRITE(0,10)
10 FORMAT(' X-AXIS OPTIONS?')
READ(5,11) L1,XN,XX
WRITE(0,12)
12 FORMAT(' Y-AXIS OPTIONS?')
READ(5,11) L2,YN,YX
11 FORMAT(15,2F10.0)
HANG=HANG/2.
CALL Q('ALIGN TOP OF FORM;')
READ(5,2) ?
DO 13 JJJ=1,3
IS=IE+1
IF(JJJ.NF.3) IS=1
IE=NCC/2
IF(JJJ.NF.2) IE=NCC
NC=IE-IS+1
CALL SORT3('S=FL,A,,4 END ',PHIS(IS),PHIS(IE),4,ITAG(IS),4)
M=0
K=IS-1
ANG=0.
4 S1=0.
S2=0.
N=0
3 IF(PHIS(K+1).GT.ANG+HANG) GO TO 5
N=N+1

```

Figure D-10. Source Listing for Procedure THIRD

BEST AVAILABLE COPY

```

K=K+1
S1=S1+10.+(SIG1(ITAG(K))/10.)
S2=S2+10.+(SIG2(ITAG(K))/10.)
IF(K.LT.1E) GO TO 3
5 IF(N.EQ.0) GO TO 7
S1=10.*ALOG10(S1/FLOAT(N))
S2=10.*ALOG10(S2/FLOAT(N))
M=M+1
IO=JJJ-1
WRITE(10,2) ANG,S1
MT2(1,M)=ANG
MT2(2,M)=S1
7 ANG=ANG+MANG*2.
IF(K.LT.1E) GO TO 4
I=0
DO 15 J=15,IF
I=I+1
MT(1,I)=PHIS(J)
15 MT(2,I)=SIG1(ITAG(J))
CALL PLOTT(MT,NC,L1,XN,XX,L2,YN,YX)
WRITE(6,16)
16 FORMAT('1')
CALL PLOTT(MT2,M,L1,XN,XX,L2,YN,YX)
WRITE(6,16)
WRITE(6,17)
17 FORMAT('01')
IF(JJJ.NE.3) CALL SORT3('3=FI,A,,4 END ',ITAG(1S),ITAG(1E),4,PHIS(1S),4)
13 CONTINUE
STOP
END

C
C
SUBROUTINE R(FB)
LOGICAL A1 R(1)
INTEGER A2 LEN
CALL FINDST(R,120,' ',1,1,IFND)
IF(IFND.EQ.0) IFND=6
LEN=IFND-1
CALL SERCOM(R,LEN,0)
RETURN
END

C
C
C
SUBROUTINE PLOTT(MT,NP,L1,XN,XX,L2,YN,YX)
LOGICAL A1 D/'-','/','P/'/'/
LOGICAL A1 MAT(64,21),S/'A'/'/','B/' '/'
REAL YM(9),X(8),MT(2,NP)
ALN10=ALOG(10.)
XMAX=-1.E70
YMAX=-1.E70
XMIN=1.E70
YMIN=1.E70
DO 1 K=1,NP
IF(MT(1,K).GT.XMAX) XMAX=MT(1,K)
IF(MT(1,K).LT.XMIN) XMIN=MT(1,K)
IF(MT(2,K).GT.YMAX) YMAX=MT(2,K)
IF(MT(2,K).LT.YMIN) YMIN=MT(2,K)
1 CONTINUE
IF(XN.EQ.XX) GO TO 20

```

Figure D-10. Source Listing for Procedure THIRD (continued)

BEST AVAILABLE COPY

```

XMIN=XN
XMAX=XX
20 IF(YN.EQ.YX) GO TO 21
YMIN=YN
YMAX=YX
21 CONTINUE
IF(I.1.EQ.1.AND.XMIN.LT.0) GO TO 102
IF(I.2.EQ.1.AND.YMIN.LT.0) GO TO 102
IF(I.1.NE.1) GO TO 2
XMIN=ALOG10(XMIN)
XMAX=ALOG10(XMAX)
2 IF(I.2.NE.1) GO TO 3
YMIN=ALOG10(YMIN)
YMAX=ALOG10(YMAX)
3 DO 4 K=1,64
DO 4 M=1,21
4 MAT(K,M)=8
DO 6 K=1,64
DO 6 M=1,21,5
6 MAT(K,M)=0
DO 5 K=1,64,9
DO 5 M=1,21,5
5 MAT(K,M)=P
YMM=XMAX-XMIN
YMM=YMAX-YMIN
YFUJ=20./YMM
YFUJ=63./XMM
DO 7 K=1,NP
MT(1,K)=AMIN1(MT(1,K),XMAX)
MT(1,K)=AMAX1(MT(1,K),XMIN)
MT(2,K)=AMIN1(MT(2,K),YMAX)
MT(2,K)=AMAX1(MT(2,K),YMIN)
IF(I.1.NE.1) MT(1,K)=(MT(1,K)-XMIN)*YFUJ
IF(I.1.EQ.1) MT(1,K)=(ALOG10(MT(1,K))-XMIN)*YFUJ
IF(I.2.NE.1) MT(2,K)=(MT(2,K)-YMIN)*YFUJ
IF(I.2.EQ.1) MT(2,K)=(ALOG10(MT(2,K))-YMIN)*YFUJ
7 CONTINUE
DO 8 K=1,NP
8 MAT(1FIX(MT(1,K)+.5)+1,1FIX(MT(2,K)+.5)+1)=8
WRITE(6,53)
FORMAT(' ')
53 YFUJY=YMM/20.
YFUJY=XMM/63.
DO 54 K=1,5
54 YH(K)=YMAX-FLOAT(K-1)*5.*YFUJY
IF(I.2.NE.1) GO TO 56
DO 55 K=1,5
55 YH(K)=EXP(YH(K)*ALN10)
56 NL=0
DO 9 K=1,5
NL=NL+1
WRITE(6,50)YH(K),(MAT(M,22-NL),M=1,64)
IF(NL.EQ.21) GO TO 10
DO 9 L=1,4
NL=NL+1
9 WRITE(6,51)(MAT(M,22-NL),M=1,64)
10 DO 11 K=1,8
11 X(K)=XMIN+FLOAT(K-1)*9.*YFUJY
IF(I.1.NE.1) GO TO 13
DO 12 K=1,8

```

Figure D-10. Source Listing for Procedure THIRD (continued)

BEST AVAILABLE COPY

```
12 X(K)=EXP(X(K)*ALN10)  
13 WRITE(6,14) X  
50 FORMAT(1X,F6.1-64A1)  
51 FORMAT(7X,64A1)  
14 FORMAT(2X,A(F9.0))  
RETURN  
102 WRITE(1,60)  
60 FORMAT(' NEGATIVE ARG FOR LOG')  
CALL ERRHIN  
END
```

Figure D-10. Source Listing for Procedure THIRD (concluded)

be calculated and drawn where it intersects the flat earth. Range ellipses may also be drawn if the transmitter position is known. One range ellipse is designed to pass through the point defined by the center of the receiver beam intersecting the earth, unless specifically offset. The second range ellipse is found by increasing the size of the first ellipse by some fixed amount. A transmitter footprint may also be drawn upon request.

The area of interest is then found by dividing the receiver footprint into many small square areas dA and then asking the following two questions: (1) is this dA outside the inner range ellipse and (2) is this dA inside the outer range ellipse? If both conditions are not met, the area is rejected. If not rejected, the dA is multiplied by the transmitter and receiver power patterns as well as an experimentally-derived weight function and divided by the distances squared from the integration point to both the transmitter and receiver. The entire receiver footprint is integrated in this manner, producing KI .

These runs may be mass-produced and the results outputted in tabular form (an example is shown in Table D-3). A source listing of the main program and its subroutines is presented in Figure D-11.

TABLE D-3. BSMAN PROGRAM OUTPUT

RECEIVER				TRANSMITTER				AREA	AREA/R	KI(08)
Y	DEP	ANT	X	Y	Z	TRACK	QSPEC			
100.0	80.0	-30.0	20060.0	6000.0	34744.9	60.0	40581.1	701.9	-98.29	-102.80
100.0	80.0	0.0	20060.0	6000.0	34744.9	60.0	40581.1	1433.0	-95.19	-99.87
100.0	80.0	30.0	20060.0	6000.0	34744.9	60.0	40581.1	4006.6	-91.35	-96.29
100.0	85.0	-30.0	20060.0	6000.0	34744.9	60.0	40581.1	1463.2	-100.67	-108.13
100.0	85.0	0.0	20060.0	6000.0	34744.9	60.0	40581.1	3658.0	-96.78	-102.39
100.0	85.0	30.0	20060.0	6000.0	34744.9	60.0	40581.1	-10974.1	-92.47	-97.87
100.0	80.0	-30.0	20060.0	6000.0	11581.6	30.0	23953.0	1374.5	-90.75	-95.38
100.0	80.0	0.0	20060.0	6000.0	11581.6	30.0	23953.0	3655.7	-86.90	-91.80
100.0	80.0	30.0	20060.0	6000.0	11581.6	30.0	23953.0	5293.4	-86.08	-97.28
100.0	85.0	-30.0	20060.0	6000.0	11581.6	30.0	23953.0	3658.0	-92.12	-97.96
100.0	85.0	0.0	20060.0	6000.0	11581.6	30.0	23953.0	9510.9	-86.14	-93.67
100.0	85.0	30.0	20060.0	6000.0	11581.6	30.0	23953.0	59260.3	-82.89	-88.99
100.0	80.0	-30.0	20060.0	6000.0	0.0	0.0	20967.0	3567.9	-85.77	-90.73
100.0	80.0	0.0	20060.0	6000.0	0.0	0.0	20967.0	5325.6	-84.63	-95.18
100.0	80.0	30.0	20060.0	6000.0	0.0	0.0	20967.0	3567.9	-85.77	-90.72
100.0	85.0	-30.0	20060.0	6000.0	0.0	0.0	20967.0	8087.7	-87.62	-92.72
100.0	85.0	0.0	20060.0	6000.0	0.0	0.0	20967.0	38083.7	-82.34	-87.47
100.0	85.0	30.0	20060.0	6000.0	0.0	0.0	20967.0	8779.3	-87.48	-91.98
100.0	80.0	-30.0	20060.0	6000.0	-11581.6	-30.0	23953.0	5293.4	-86.08	-97.28
100.0	80.0	0.0	20060.0	6000.0	-11581.6	-30.0	23953.0	3714.2	-86.86	-91.80
100.0	80.0	30.0	20060.0	6000.0	-11581.6	-30.0	23953.0	1491.5	-90.35	-95.29
100.0	85.0	-30.0	20060.0	6000.0	-11581.6	-30.0	23953.0	59260.3	-82.89	-86.99
100.0	85.0	0.0	20060.0	6000.0	-11581.6	-30.0	23953.0	8779.3	-86.69	-92.80
100.0	85.0	30.0	20060.0	6000.0	-11581.6	-30.0	23953.0	2108.8	-92.63	-98.51
100.0	60.0	-30.0	20060.0	6000.0	-34744.9	-60.0	40581.1	4006.6	-91.35	-96.26
100.0	60.0	0.0	20060.0	6000.0	-34744.9	-60.0	40581.1	1520.8	-94.92	-99.89
100.0	60.0	30.0	20060.0	6000.0	-34744.9	-60.0	40581.1	818.9	-97.65	-102.72
100.0	85.0	-30.0	20060.0	6000.0	-34744.9	-60.0	40581.1	10282.5	-92.56	-97.00
100.0	85.0	0.0	20060.0	6000.0	-34744.9	-60.0	40581.1	2198.8	-99.29	-102.38
100.0	85.0	30.0	20060.0	6000.0	-34744.9	-60.0	40581.1	1463.2	-100.87	-109.81

281STAT
 R=0.100.0.9.36.85.30.1.20060.0.6000.0.-34744.92.12.71.5.30.1. TRACK=60.0. DX=3. DX2=88.74.104. KONE=867.
 DRAWING=40581.1.4. CDT=0. AREA=1463.2. AREAS=100.8699. KI=-104.81. QSPEC=40581.06. NCNT=41729.61. SCALE=1.5. PLOT=F. DRAW=F. REPEAT=F.
 PAUSE=F. SPENT=1.37. OLAMDA=13.36. BUG=F. PULSE=90.0. PUFF=0.0. MT=1. MT=F. N8INS=2.
 KEND

BEST AVAILABLE COPY

[illegible]

Figure D-11. Source Listing for BSMMAIN Program and Its Subroutines

```

119 C
120 C
121 C
122 C
123 C
124 C
125 C
126 C
127 C
128 C
129 C
130 C
131 C
132 C
133 C
134 C
135 C
136 C
137 C
138 C
139 C
140 C
141 C
142 C
143 C
144 C
145 C
146 C
147 C
148 C
149 C
150 C
151 C
152 C
153 C
154 C
155 C
156 C
157 C
158 C
159 C
160 C
161 C
162 C
163 C
164 C
165 C
166 C
167 C
168 C
169 C
170 C
171 C
172 C
173 C
174 C
175 C
176 C
177 C
178 C
179 C
180 C
181 C
182 C
183 C
184 C
185 C
186 C
187 C
188 C
189 C
190 C
191 C
192 C
193 C
194 C
195 C
196 C
197 C
198 C
199 C
200 C
201 C
202 C
203 C
204 C
205 C
206 C
207 C
208 C
209 C
210 C
211 C
212 C
213 C
214 C
215 C
216 C
217 C
218 C
219 C
220 C
221 C
222 C
223 C
224 C
225 C
226 C
227 C
228 C
229 C
230 C
231 C
232 C
233 C
234 C
235 C
236 C
237 C
238 C
239 C
240 C
241 C
242 C
243 C
244 C
245 C
246 C
247 C
248 C
249 C
250 C
251 C
252 C
253 C
254 C
255 C
256 C
257 C
258 C
259 C
260 C
261 C
262 C
263 C
264 C
265 C
266 C
267 C
268 C
269 C
270 C
271 C
272 C
273 C
274 C
275 C
276 C
277 C
278 C
279 C
280 C
281 C
282 C
283 C
284 C
285 C
286 C
287 C
288 C
289 C
290 C
291 C
292 C
293 C
294 C
295 C
296 C
297 C
298 C
299 C
300 C
301 C
302 C
303 C
304 C
305 C
306 C
307 C
308 C
309 C
310 C
311 C
312 C
313 C
314 C
315 C
316 C
317 C
318 C
319 C
320 C
321 C
322 C
323 C
324 C
325 C
326 C
327 C
328 C
329 C
330 C
331 C
332 C
333 C
334 C
335 C
336 C
337 C
338 C
339 C
340 C
341 C
342 C
343 C
344 C
345 C
346 C
347 C
348 C
349 C
350 C
351 C
352 C
353 C
354 C
355 C
356 C
357 C
358 C
359 C
360 C
361 C
362 C
363 C
364 C
365 C
366 C
367 C
368 C
369 C
370 C
371 C
372 C
373 C
374 C
375 C
376 C
377 C
378 C
379 C
380 C
381 C
382 C
383 C
384 C
385 C
386 C
387 C
388 C
389 C
390 C
391 C
392 C
393 C
394 C
395 C
396 C
397 C
398 C
399 C
400 C
401 C
402 C
403 C
404 C
405 C
406 C
407 C
408 C
409 C
410 C
411 C
412 C
413 C
414 C
415 C
416 C
417 C
418 C
419 C
420 C
421 C
422 C
423 C
424 C
425 C
426 C
427 C
428 C
429 C
430 C
431 C
432 C
433 C
434 C
435 C
436 C
437 C
438 C
439 C
440 C
441 C
442 C
443 C
444 C
445 C
446 C
447 C
448 C
449 C
450 C
451 C
452 C
453 C
454 C
455 C
456 C
457 C
458 C
459 C
460 C
461 C
462 C
463 C
464 C
465 C
466 C
467 C
468 C
469 C
470 C
471 C
472 C
473 C
474 C
475 C
476 C
477 C
478 C
479 C
480 C
481 C
482 C
483 C
484 C
485 C
486 C
487 C
488 C
489 C
490 C
491 C
492 C
493 C
494 C
495 C
496 C
497 C
498 C
499 C
500 C
501 C
502 C
503 C
504 C
505 C
506 C
507 C
508 C
509 C
510 C
511 C
512 C
513 C
514 C
515 C
516 C
517 C
518 C
519 C
520 C
521 C
522 C
523 C
524 C
525 C
526 C
527 C
528 C
529 C
530 C
531 C
532 C
533 C
534 C
535 C
536 C
537 C
538 C
539 C
540 C
541 C
542 C
543 C
544 C
545 C
546 C
547 C
548 C
549 C
550 C
551 C
552 C
553 C
554 C
555 C
556 C
557 C
558 C
559 C
560 C
561 C
562 C
563 C
564 C
565 C
566 C
567 C
568 C
569 C
570 C
571 C
572 C
573 C
574 C
575 C
576 C
577 C
578 C
579 C
580 C
581 C
582 C
583 C
584 C
585 C
586 C
587 C
588 C
589 C
590 C
591 C
592 C
593 C
594 C
595 C
596 C
597 C
598 C
599 C
600 C
601 C
602 C
603 C
604 C
605 C
606 C
607 C
608 C
609 C
610 C
611 C
612 C
613 C
614 C
615 C
616 C
617 C
618 C
619 C
620 C
621 C
622 C
623 C
624 C
625 C
626 C
627 C
628 C
629 C
630 C
631 C
632 C
633 C
634 C
635 C
636 C
637 C
638 C
639 C
640 C
641 C
642 C
643 C
644 C
645 C
646 C
647 C
648 C
649 C
650 C
651 C
652 C
653 C
654 C
655 C
656 C
657 C
658 C
659 C
660 C
661 C
662 C
663 C
664 C
665 C
666 C
667 C
668 C
669 C
670 C
671 C
672 C
673 C
674 C
675 C
676 C
677 C
678 C
679 C
680 C
681 C
682 C
683 C
684 C
685 C
686 C
687 C
688 C
689 C
690 C
691 C
692 C
693 C
694 C
695 C
696 C
697 C
698 C
699 C
700 C
701 C
702 C
703 C
704 C
705 C
706 C
707 C
708 C
709 C
710 C
711 C
712 C
713 C
714 C
715 C
716 C
717 C
718 C
719 C
720 C
721 C
722 C
723 C
724 C
725 C
726 C
727 C
728 C
729 C
730 C
731 C
732 C
733 C
734 C
735 C
736 C
737 C
738 C
739 C
740 C
741 C
742 C
743 C
744 C
745 C
746 C
747 C
748 C
749 C
750 C
751 C
752 C
753 C
754 C
755 C
756 C
757 C
758 C
759 C
760 C
761 C
762 C
763 C
764 C
765 C
766 C
767 C
768 C
769 C
770 C
771 C
772 C
773 C
774 C
775 C
776 C
777 C
778 C
779 C
780 C
781 C
782 C
783 C
784 C
785 C
786 C
787 C
788 C
789 C
790 C
791 C
792 C
793 C
794 C
795 C
796 C
797 C
798 C
799 C
800 C
801 C
802 C
803 C
804 C
805 C
806 C
807 C
808 C
809 C
810 C
811 C
812 C
813 C
814 C
815 C
816 C
817 C
818 C
819 C
820 C
821 C
822 C
823 C
824 C
825 C
826 C
827 C
828 C
829 C
830 C
831 C
832 C
833 C
834 C
835 C
836 C
837 C
838 C
839 C
840 C
841 C
842 C
843 C
844 C
845 C
846 C
847 C
848 C
849 C
850 C
851 C
852 C
853 C
854 C
855 C
856 C
857 C
858 C
859 C
860 C
861 C
862 C
863 C
864 C
865 C
866 C
867 C
868 C
869 C
870 C
871 C
872 C
873 C
874 C
875 C
876 C
877 C
878 C
879 C
880 C
881 C
882 C
883 C
884 C
885 C
886 C
887 C
888 C
889 C
890 C
891 C
892 C
893 C
894 C
895 C
896 C
897 C
898 C
899 C
900 C
901 C
902 C
903 C
904 C
905 C
906 C
907 C
908 C
909 C
910 C
911 C
912 C
913 C
914 C
915 C
916 C
917 C
918 C
919 C
920 C
921 C
922 C
923 C
924 C
925 C
926 C
927 C
928 C
929 C
930 C
931 C
932 C
933 C
934 C
935 C
936 C
937 C
938 C
939 C
940 C
941 C
942 C
943 C
944 C
945 C
946 C
947 C
948 C
949 C
950 C
951 C
952 C
953 C
954 C
955 C
956 C
957 C
958 C
959 C
960 C
961 C
962 C
963 C
964 C
965 C
966 C
967 C
968 C
969 C
970 C
971 C
972 C
973 C
974 C
975 C
976 C
977 C
978 C
979 C
980 C
981 C
982 C
983 C
984 C
985 C
986 C
987 C
988 C
989 C
990 C
991 C
992 C
993 C
994 C
995 C
996 C
997 C
998 C
999 C
1000 C

```

Figure D-11. Source Listing for BSMAN Program and Its Subroutines (continued)

BEST AVAILABLE COPY

```

C      CALL IGCN('A')
C
C      ORAN TRANSMITTER FOOT PRINT
C
C      CALL GETELL('FPCNT,FPMAJ,TFPMIN,TOA,EX,EZ,DUM,DUM,DUM,DUM')
C      DO 24 J=1,401
C      EX(J)=X(J)+T(1)
C      EZ(J)=Z(J)+T(3)
C      CONTINUE
C24
C      CALL IGVEC(40),FX,EZ
C      CALL IGENDS('ELL1')
C      IF(ORAN) CALL IGDROM('TERMINAL')
C
C      FIND RANGE ELLIPSES IN ZERO COORDINATES
C
C      TTSQRT(T(1)+T(1)+T(3)+T(3))
C      RSQ=1+T(2)+T(2)
C      YR2=9.44R2+T(2)+T(2)
C      INC=9
C      IF(MT) INC=1
C      DO 5 J=1,9,INC
C      CSR=0(J)+2
C      CX=OSQ-TT+T
C      CR2=OSQ-RSQ
C      RCH(J)=TT+(CR+RM2)/(2.*RQ)
C      RMAJ(J)=(QSQ/RQ)*T(CR-RM2)+2-YR2)/(QX+RQ)
C      IF(RMAJ(J).LE.0.) GO TO 90
C      RMAJ(J)=SQRT(RMAJ(J))
C      RMN(J)=((CR-RM2)+2-YR2)/(QX+RQ)
C      IF(RMN(J).LE.0.) GO TO 90
C      RMN(J)=SQRT(RMN(J))
C      CONTINUE
C      IF(.NOT.(ORAN.OR.PLOT)) GO TO 23
C      CALL GETELL('PCNT(1),RMAJ(1),RMN(1),RTOA,EX,EZ,DUM,DUM,DUM,DUM')
C      CALL IGCN('ELL1')
C      CALL IGVFC(40),FX,EZ
C      CALL IGENDS('ELL1')
C      IF(ORAN) CALL IGDROM('TERMINAL')
C      CALL GETELL('PCNT(9),RMAJ(9),RMN(9),RTOA,EX,EZ,DUM,DUM,DUM,DUM')
C      CALL IGCN('ELL1')
C      CALL IGVFC(40),FX,EZ
C      CALL IGENDS('ELL1')
C      IF(ORAN) CALL IGDROM('TERMINAL')
C
C      START SCAN
C
C      DX2=DX
C      IF(DX.EQ.0.) DX=-19.
C      IF(DX.LT.0.) DX2=FPMIN/ARS(DX)
C      IF(ORAN.OR.PLOT) CALL IGCN('ELL1')
C      XS=FPCNT+FPMAJ-DX2/2.
C      XE=FPCNT+FPMAJ
C      KING=0
C      N=0.
C      AR=0.
C      PDL=PI*DLAND
C      XSE=X+DX2
C      E=ATY.E.TRUE.
C      IF(XS.GE.XE) GO TO 13

```

Figure D-11. Source Listing for BSMAIN Program
and Its Subroutines (continued)

BEST AVAILABLE COPY

Figure D-11. Source Listing for BSMAIN Program
and Its Subroutines (continued)

[illegible]

BEST AVAILABLE COPY

```

3 IF(ORAW) CALL ICDROM('TERMINAL')
  IF(REPEAT,AND,PAUSE,AND,ORAW) READ(5,3) 3
  FORMAT(11)
4 IF(ORAW) CALL ICDTRL('TERMINAL','POSN',-1,1,5)
  IF(.NOT.REPEAT) ICOST=COST(0)
  IF(PLOT) CALL ICDROM('CALCOMP')
  IF(.NOT.REPEAT) PLOT=-.FALSE.
  IF(REPEAT) GO TO 4
  IF(SUB) WRITE(6,PERUG)
  IF(MAIN,OR,IPATH,EQ,2,OR,IPATH,EQ,3) WRITE(4,B1STAT)
  IF(.NOT.MAIN) RETURN
  GO TO 2
90 WRITE(6,91)
91 FORMAT(100 100 SMALL'/IX)
  GO TO 4
92 WRITE(6,93)
93 FORMATTORFAM TOR HIGH:/IX)
  GO TO 4
99 CONTINUE
  RETURN
100 CALL MTS
  MTS=.FALSE.
  IF(.NOT.MAIN) RETURN
  GO TO 2
  END

C
C
C
SURROUTINE MUX(QS,QCNT,ICOST,JUTLST,*)
  REAL R(6),T(6),Q(9),Y1(10),X2(10),Y2(10),Z2(10),TS(10),FA(10),KI
  COMMON /R1/ R,T,Q,X,Y,Z,SCALE,PLOT,ORAW,REPEAT,PAUSE,SPENT,AREA,KI,AREAR,TRACK
  LOGICAL EMPTY,PLOT,ORAW,PRINT,REPEAT,PAUSE,REPEAT/F,JUTLST
  INTEGER RUN/0/,COST
  IF(RUN,GF,1) GO TO 10
  TY1=1
  TX2=1
  TY2=1
  TZ2=1
  IT5=1
  IFAZ=1
  WRITE(6,1)
  FORMAT('RECEIVER HEIGHTS?')
  CALL RARRAY(Y1,10,TY1,5,812)
  WRITE(6,2)
  FORMAT('RECEIVER DEPRESSION ANGLES?')
  CALL RARRAY(TS,10,ITS,5,812)
  WRITE(6,3)
  FORMAT('RECEIVER ORIENTATION ANGLES?')
  CALL RARRAY(FA,10,IFAT,5,812)
  WRITE(6,4)
  FORMAT('TRANSMITTER X POSITIONS?')
  CALL RARRAY(X2,10,IX2,5,812)
  WRITE(6,5)
  FORMAT('TRANSMITTER Y POSITIONS?')
  CALL RARRAY(Y2,10,IY2,5,812)
  WRITE(6,6)
  FORMAT('TRANSMITTER TRACKS?')
  CALL RARRAY(Z2,10,IZ2,5,812)
  WRITE(7,8)
  GO TO 1
  C
  C1
  C
  2
  3
  4
  5
  6

```

Figure D-11. Source Listing for BSMA IN Program and Its Subroutines (continued)

Figure D-11. Source Listing for BSMAIN Program
and Its Subroutines (continued)

BEST AVAILABLE COPY

```

4      YX=-1.E50
      ZX=-1.E50
      YN=1.F50
      ZN=1.F50
      DO 4 J=1,N01
      CALL ROT(EX(J),EZ(J),0A,EX(J),EZ(J))
      XN=AMAX1(XN,EX(J))
      YN=AMIN1(YN,EX(J))
      ZX=AMAX1(ZX,FZ(J))
      ZN=AMIN1(ZN,FZ(J))
      CONTINUE
      RETURN
      END
      C C C

      SUBROUTINE ROT(X,Y,A,XX,YY)
      XX=XACOS(A)-YASIN(A)
      YY=XASIN(A)+YACOS(A)
      RETURN
      END
      C C C

      FUNCTION FIND(X,Z,C,FJ,FN,A)
      CALL ROT(X,Z,-A,XX,ZZ)
      FIND=((XX-C)/FJ)+A*2*(ZZ/FN)+A*2
      RETURN
      END
      C C C

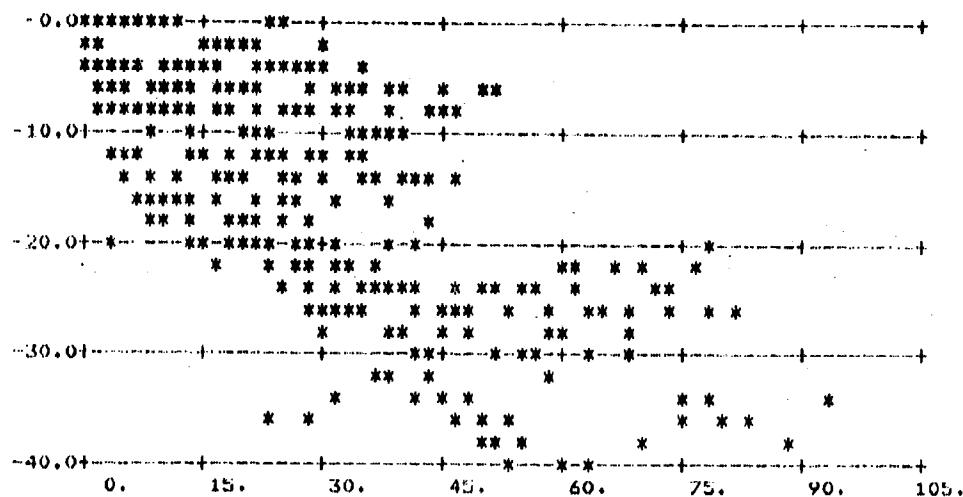
      SUBROUTINE RARRAY(ARRAY,N,H,IO,*)
      REAL ARRAY(N)
      EQUIVALENCE (ICORE,CORE)
      CALL FCYTHR(1)
      CALL FCNDR('SET MINUSZERO=DN',16)
      READ(10,1,FND=4) (ARRAY(I),I=1,N)
      DO 2 J=1,N
      CORE=ARRAY(J)
      IF(ICORE.LF.IC) GO TO 3
      CONTINUE
      M=N
      RETURN
      M=N-1
      RETURN
      RETURN 1
      END
      1
      2
      3
      4

```

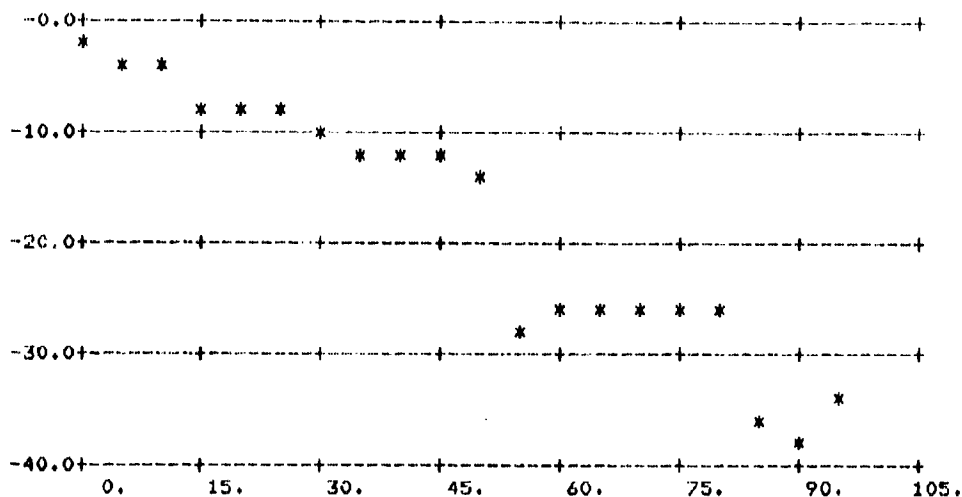
Figure D-11. Source Listing for BSMMAIN Program
and Its Subroutines (concluded)

APPENDIX E COMPLETE RECORD OF RESULTS

The data shown in Section 5 are averages of the total number of data samples obtained for each bistatic angle set. This appendix includes results from all final computer runs made to obtain σ_0 values. The data here are given for each pass that was processed for each data gathering period. All data are for horizontal polarization, both transmitted and received. The data sets for each pass consist of two graphs; the top graph gives the computed value for each data point calculated while the lower curve gives averaged values.

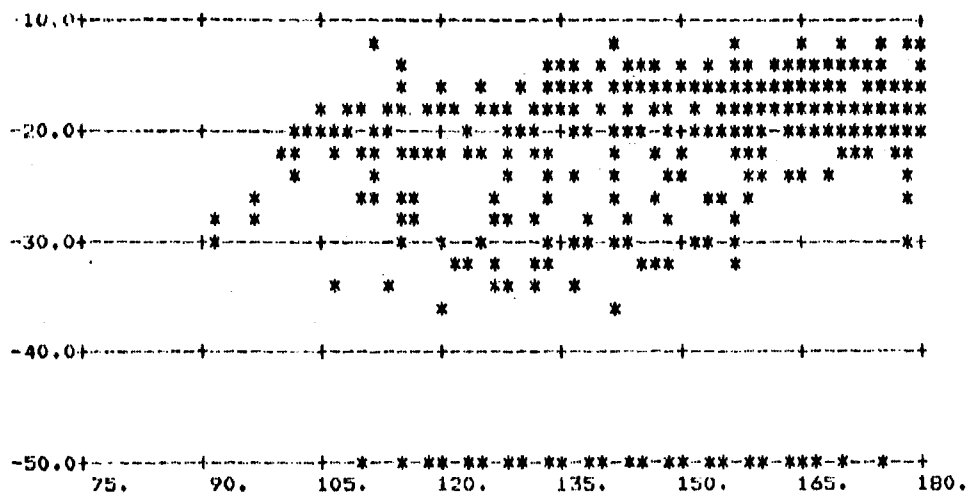


(a) All Points

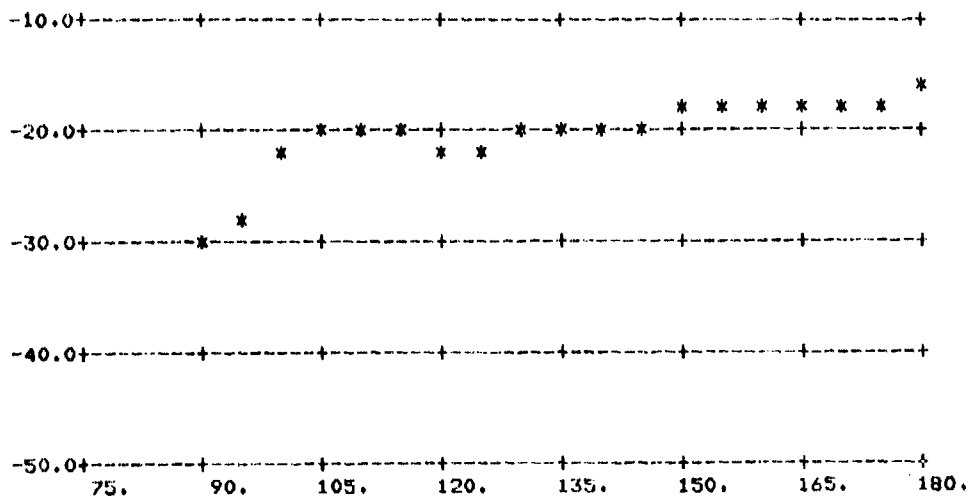


(b) Averages

Figure E-1. σ_0 vs ϕ_s for Pass 3, Flight 7/17/76
at 23 cm Wavelength, Horizontal Polarization
($\theta_s = 80^\circ$, $\theta_i = 80^\circ$, $y_1 = 100$ ft, $x_2 = 21220$ ft,
 $y_2 = 4000$ ft; data taken from entire pass)

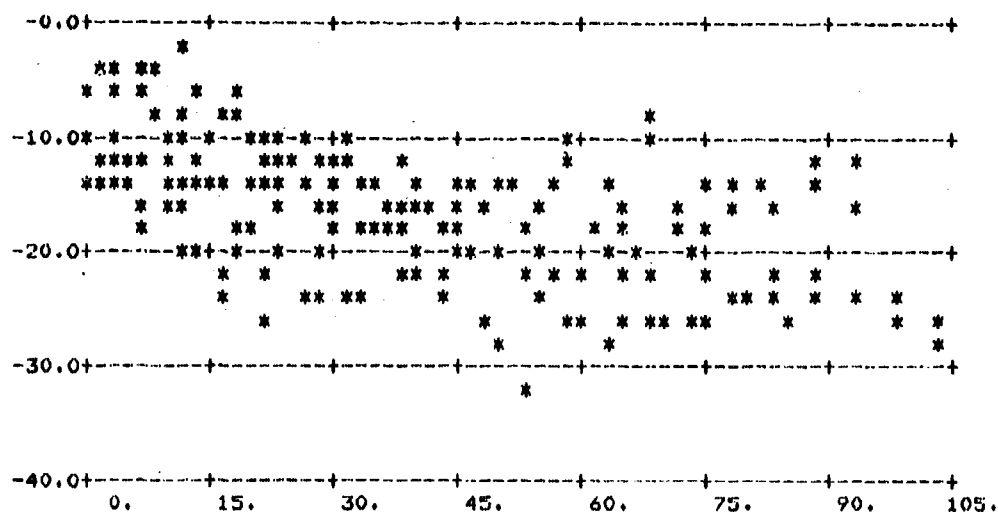


(a) All Points

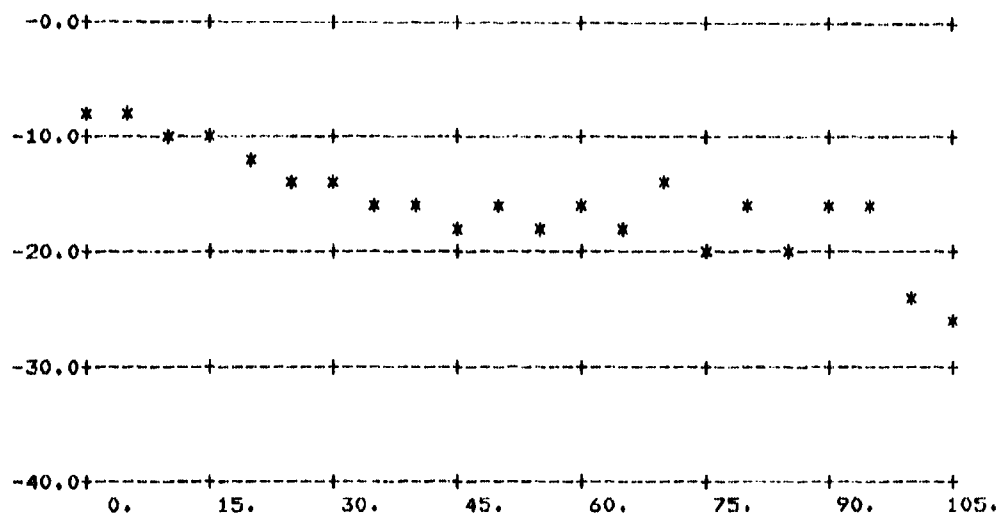


(b) Averages

Figure E-2. σ_0 vs ϕ_s for Pass 9, Flight 7/17/76
at 23 cm Wavelength, Horizontal Polarization
($\theta_s = 80^\circ$, $\theta_i = 80^\circ$, $y_1 = 100$ ft, $x_2 = 18480$ ft,
 $y_2 = 4000$ ft; data taken from entire pass)

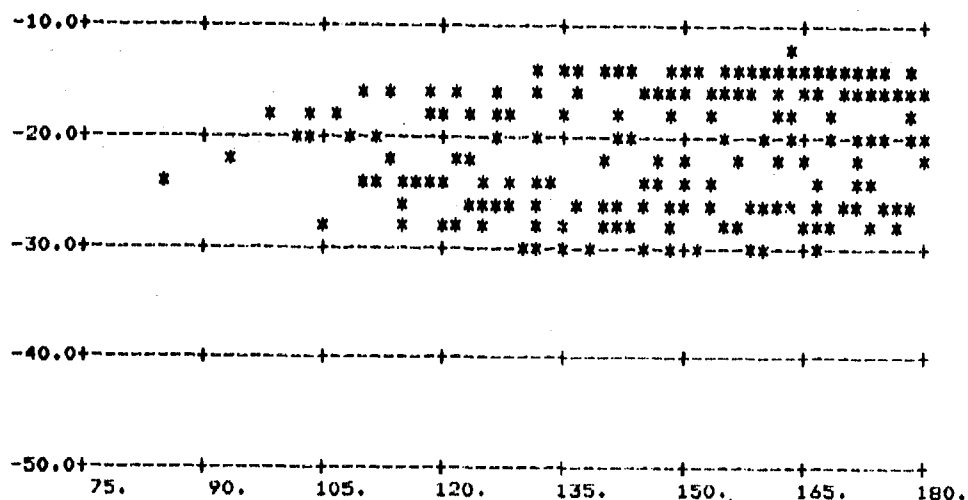


(a) All Points

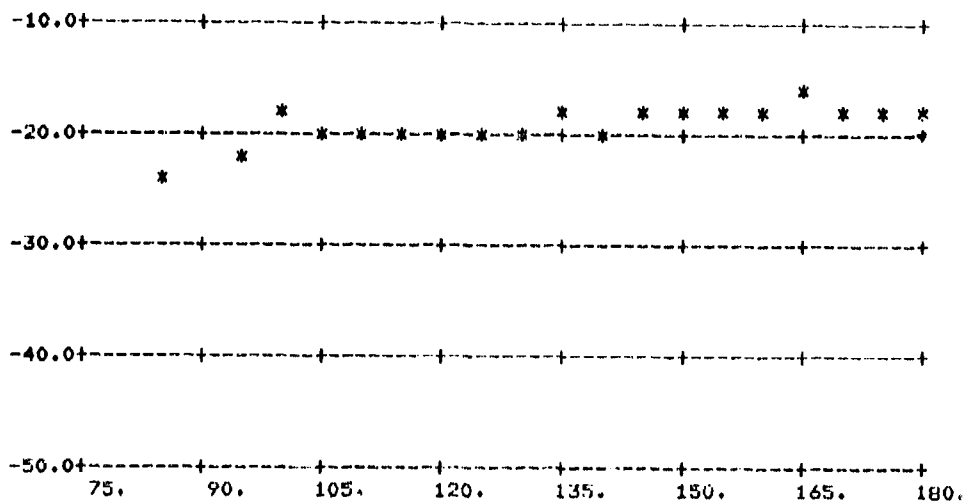


(b) Averages

Figure E-3. σ_O vs ϕ_s for Pass 4, Flight 7/17/76
at 23 cm Wavelength, Horizontal Polarization
($\theta_s = 80^\circ$, $\theta_i = 75^\circ$, $y_1 = 100$ ft, $x_2 = 20060$ ft,
 $y_2 = 6000$ ft; data taken from entire pass)

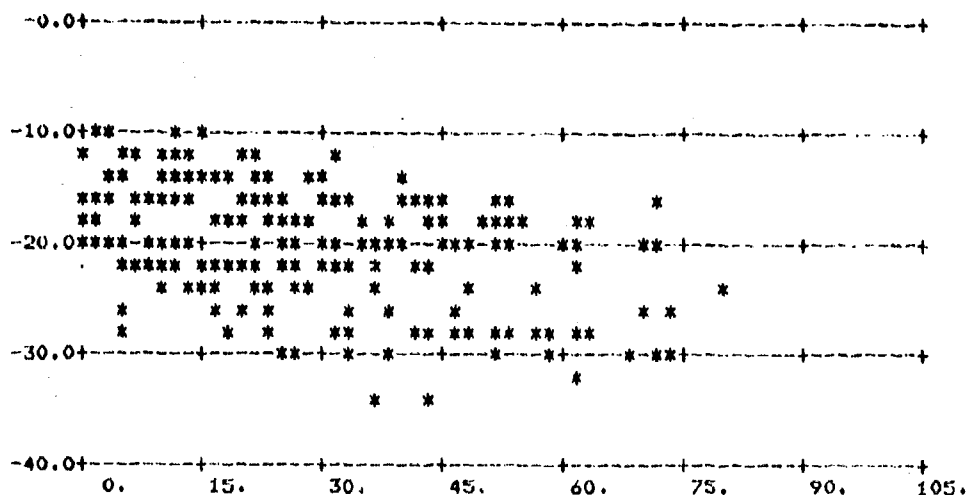


(a) All Points

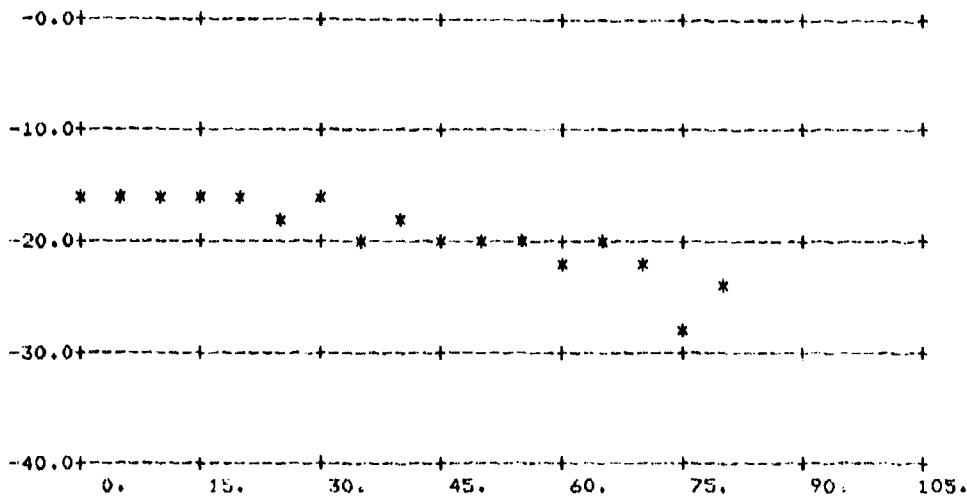


(b) Averages

Figure E-4. σ_0 vs ϕ_s for Pass 7, Flight 7/17/76
at 23 cm Wavelength, Horizontal Polarization
($\theta_s = 80^\circ$, $\theta_1 = 75^\circ$, $y_1 = 100$ ft, $x_2 = 18740$ ft,
 $y_2 = 6000$ ft; data taken from entire pass)

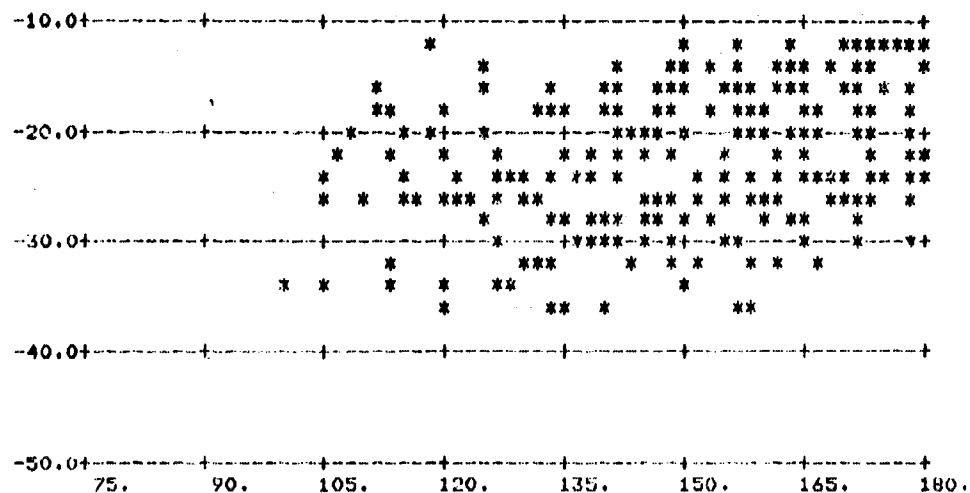


(a) All Points

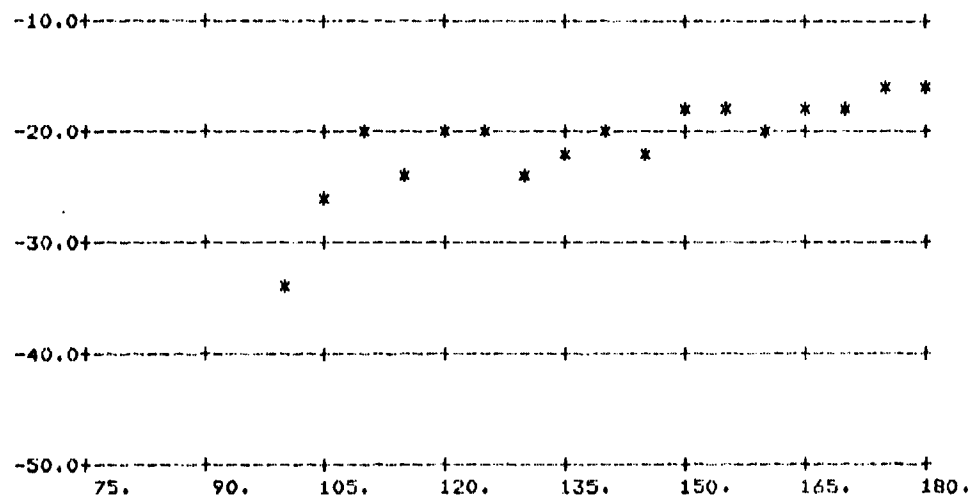


(b) Averages

Figure E-5. σ_0 vs ϕ_s for Pass 5, Flight 7/17/76
 at 23 cm Wavelength, Horizontal Polarization
 ($\theta_s = 80^\circ$, $\theta_i = 70^\circ$, $y_1 = 100$ ft, $x_2 = 18480$ ft,
 $y_2 = 8000$ ft; data taken from entire pass)

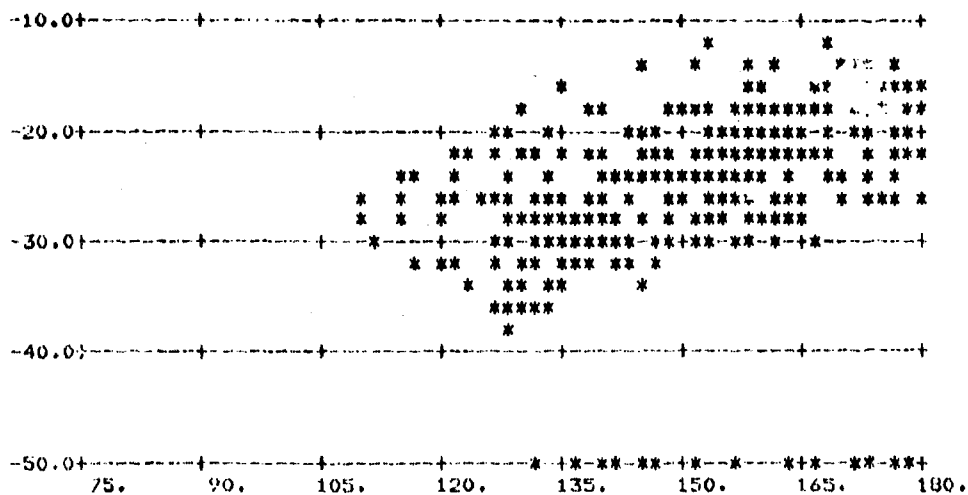


(a) All Points

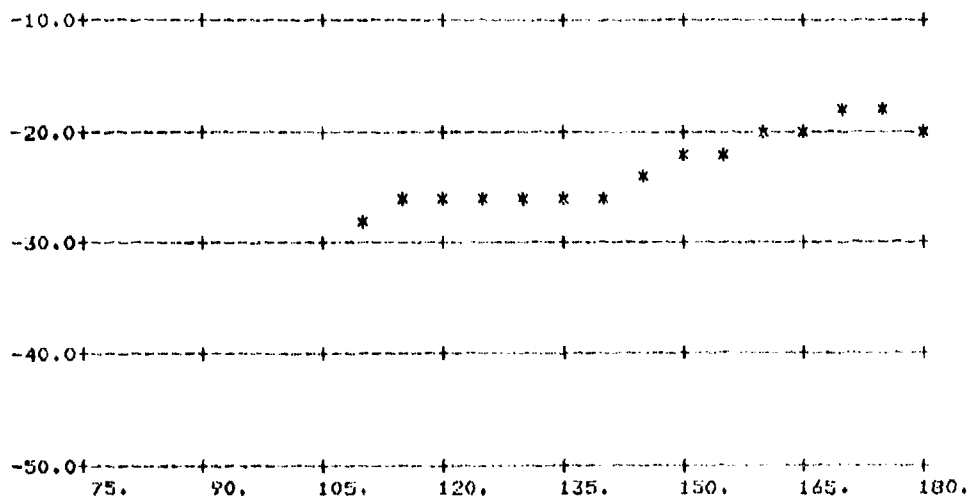


(b) Averages

Figure E-6. σ_O vs ϕ_S for Pass 6, Flight 7/17/76
 at 23 cm Wavelength, Horizontal Polarization
 $(\theta_s = 80^\circ, \theta_i = 70^\circ, y_1 = 100 \text{ ft}, x_2 = 18480 \text{ ft},$
 $y_2 = 8000 \text{ ft; data taken from entire pass})$

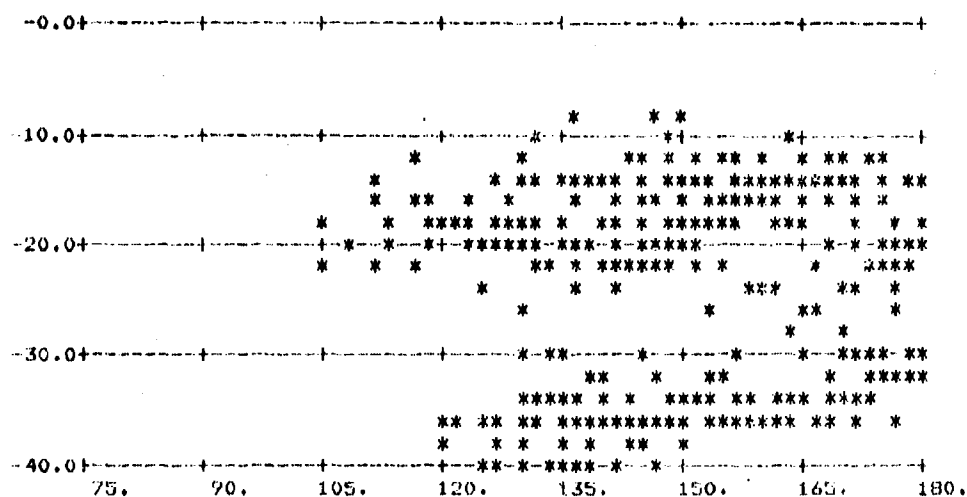


(a) All Points

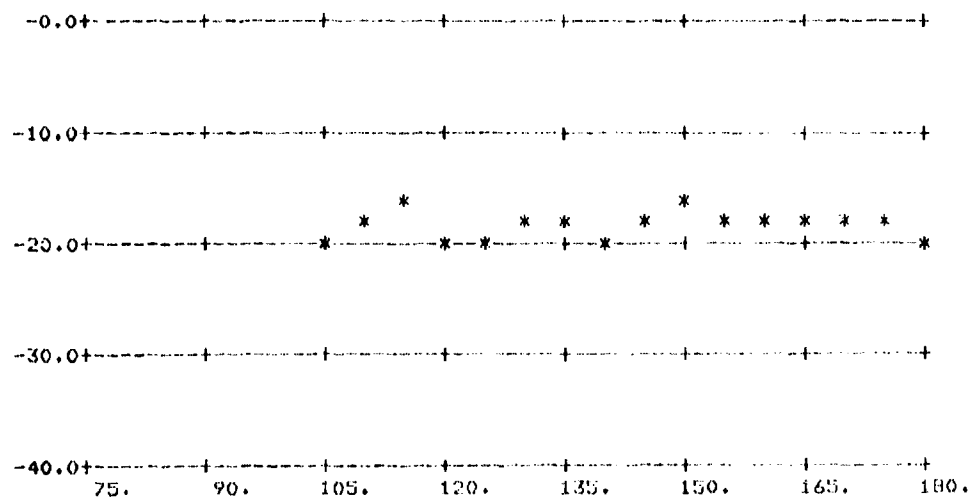


(b) Averages

Figure E-7. σ_0 vs ψ_s for Pass 10, Flight 7/17/76
 at 23 cm Wavelength, Horizontal Polarization
 $(\theta_s = 70^\circ, \theta_i = 80^\circ, y_1 = 100 \text{ ft}, x_2 = 18740 \text{ ft},$
 $y_2 = 4000 \text{ ft; data taken from entire pass})$

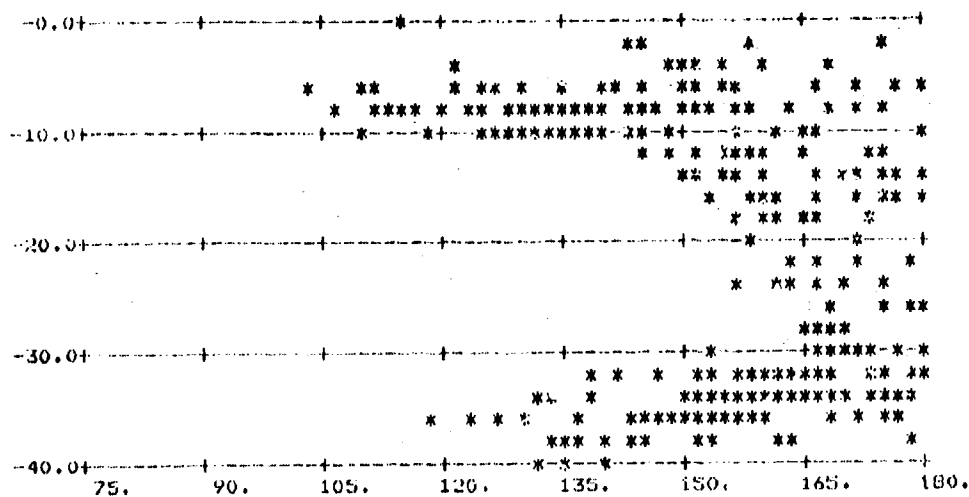


(a) All Points

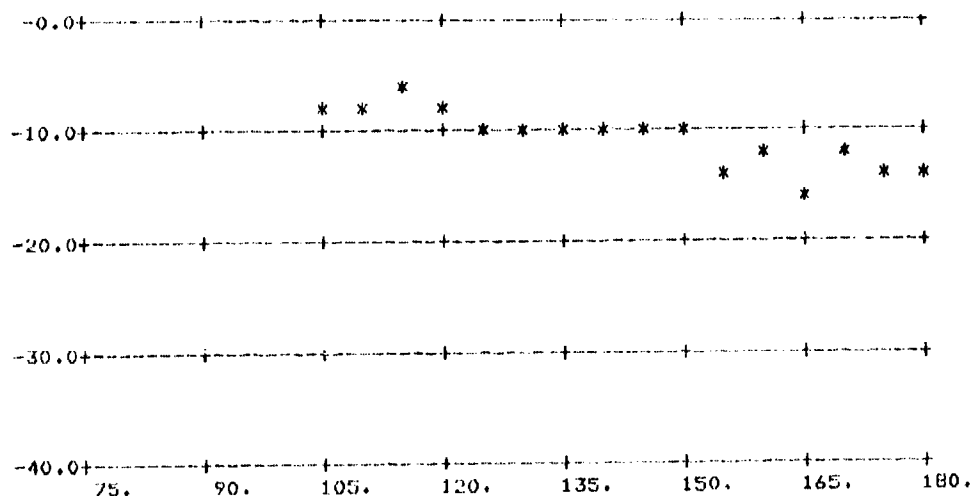


(b) Averages

Figure E-8. σ_0 vs ϕ_s for Pass 11, Flight 7/17/76
 at 23 cm Wavelength, Horizontal Polarization
 $(\theta_s = 70^\circ, \theta_i = 75^\circ, y_1 = 100 \text{ ft}, x_2 = 18480 \text{ ft},$
 $y_2 = 6000 \text{ ft; data taken from entire pass})$

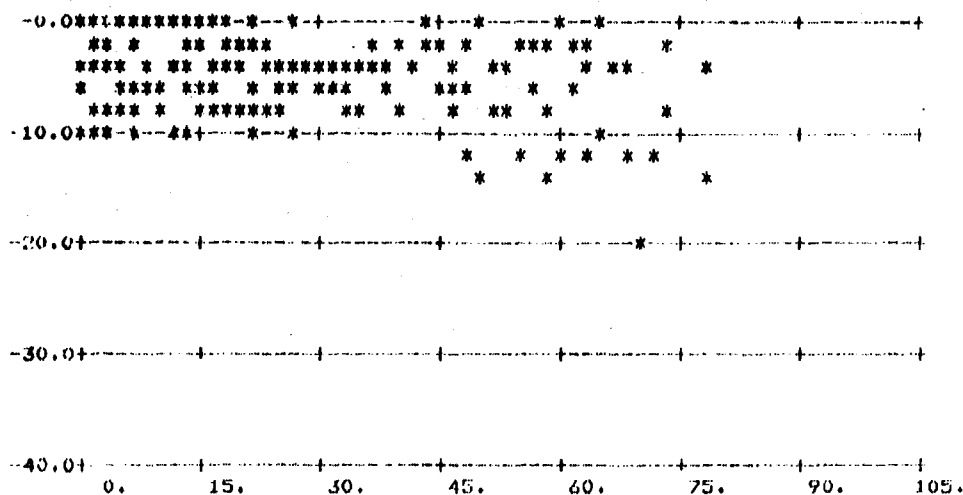


(a) All Points

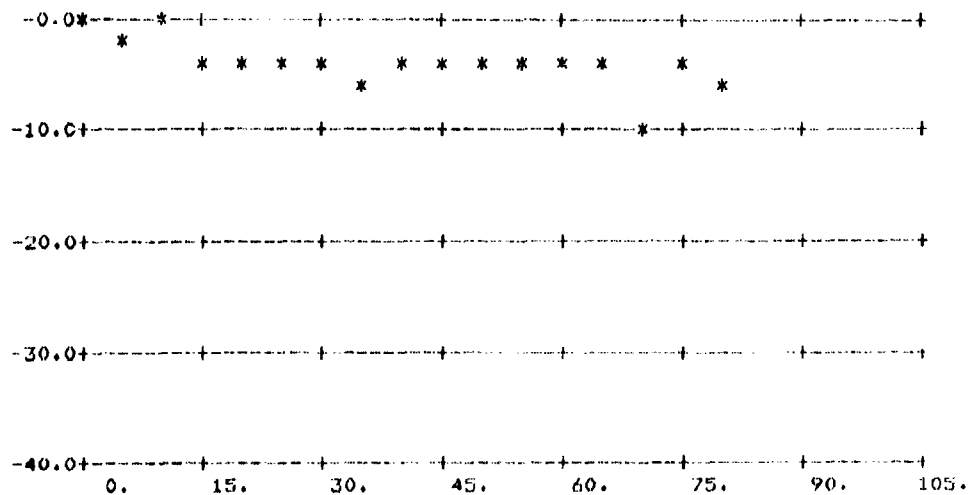


(b) Averages

Figure E-9. σ_0 vs ϕ_s for Pass 12, Flight 7/17/76
 at 23 cm Wavelength, Horizontal Polarization
 ($\theta_s = 70^\circ$, $\theta_i = 70^\circ$, $y_1 = 100$ ft, $x_2 = 18480$ ft,
 $y_2 = 8000$ ft; data taken from entire pass)

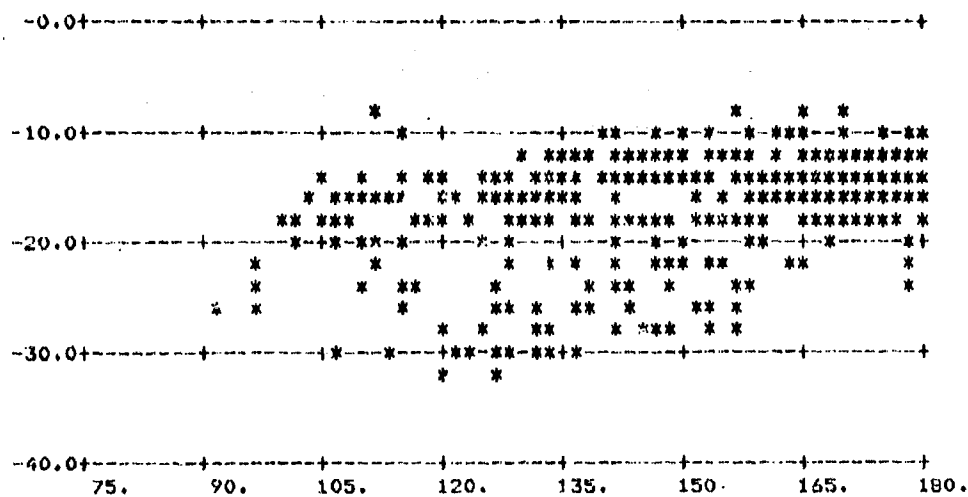


(a) All Points

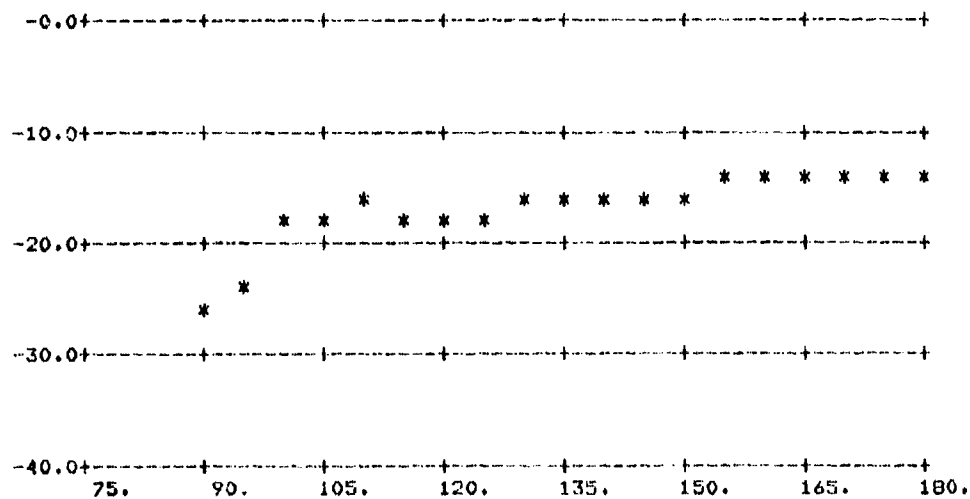


(b) Averages

Figure E-10. σ_0 vs ϕ_s for Pass 3, Flight 7/17/76
 at 3 cm Wavelength, Horizontal Polarization
 $(\theta_s = 80^\circ, \theta_i = 80^\circ, y_1 = 100 \text{ ft}, x_2 = 21120 \text{ ft},$
 $y_2 = 4000 \text{ ft; data taken from entire pass})$

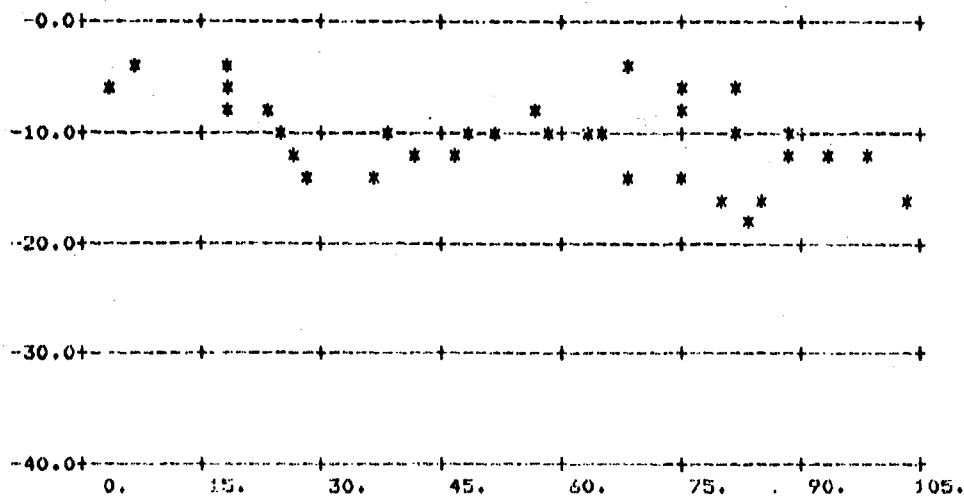


(a) All Points

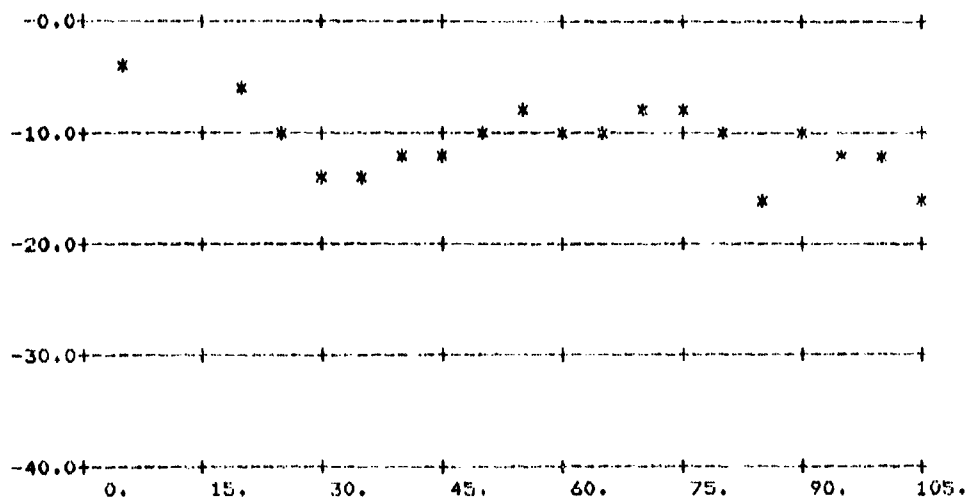


(b) Averages

Figure E-11. σ_0 vs ϕ_s for Pass 9, Flight 7/17/76
 at 3 cm Wavelength, Horizontal Polarization
 ($\theta_s = 80^\circ$, $\theta_1 = 80^\circ$, $y_1 = 100$ ft, $x_2 = 18480$ ft,
 $y_2 = 4000$ ft; data taken from entire pass)

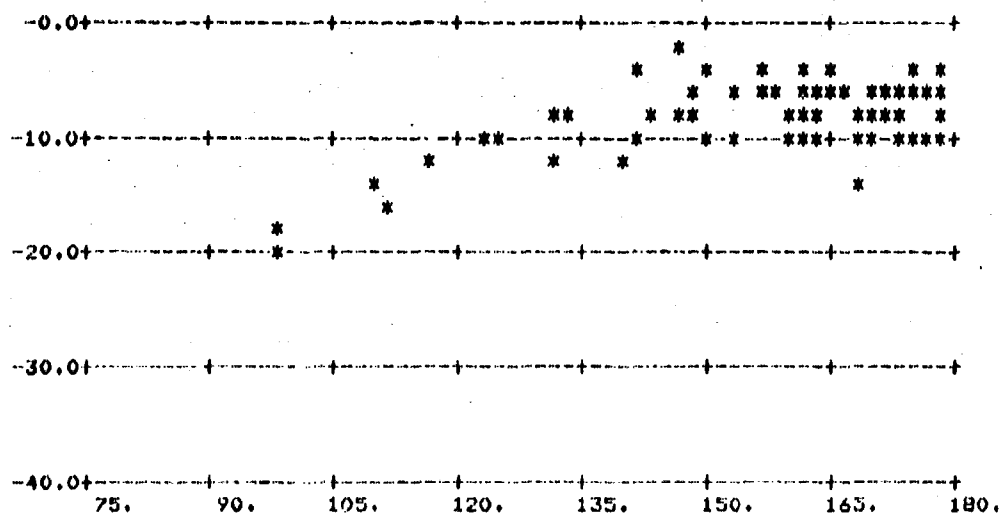


(a) All Points

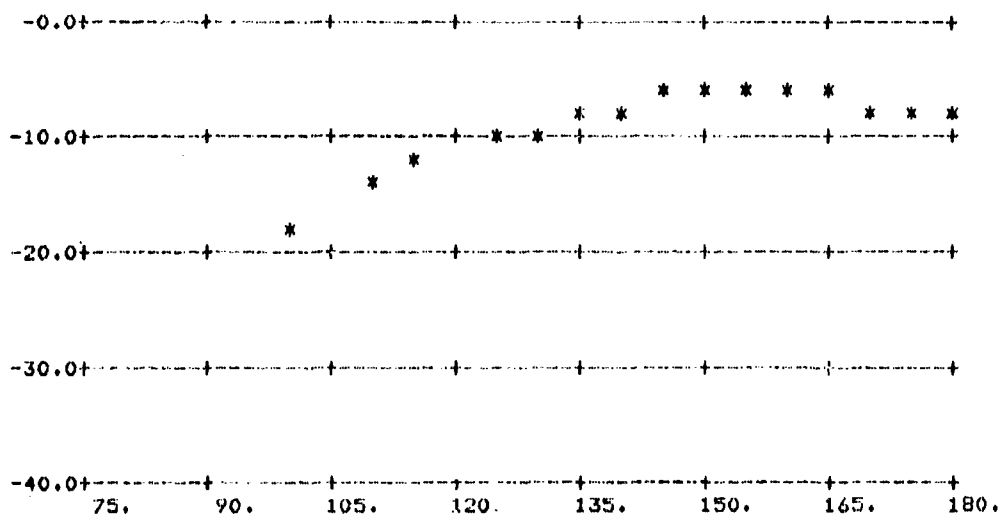


(b) Averages

Figure E-12. σ_0 vs ϕ_s for Pass 4, Flight 7/17/76
 at 3 cm Wavelength, Horizontal Polarization
 ($\theta_s = 80^\circ$, $\theta_1 = 75^\circ$, $y_1 = 100$ ft, $x_2 = 20060$ ft,
 $y_2 = 6000$ ft; data taken from entire pass)

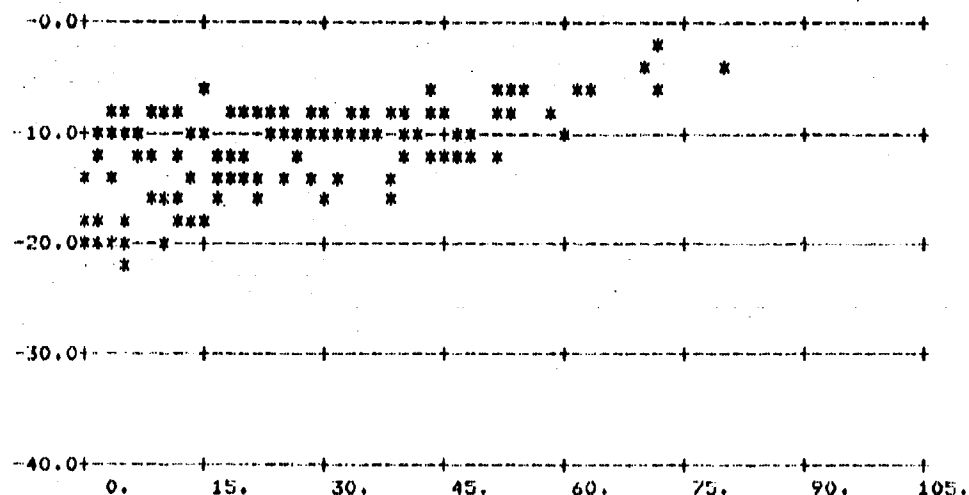


(a) All Points

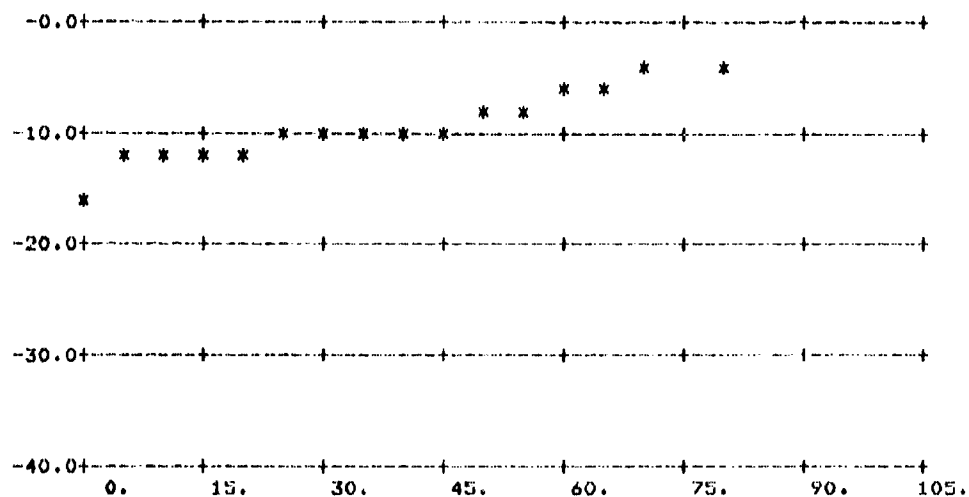


(b) Averages

Figure E-13. σ_0 vs ϕ_s for Pass 7, Flight 7/17/76
 at 3 cm Wavelength, Horizontal Polarization
 $(\theta_s = 80^\circ, \theta_i = 75^\circ, y_1 = 100 \text{ ft}, x_2 = 18740 \text{ ft},$
 $y_2 = 6000 \text{ ft; data taken from entire pass})$

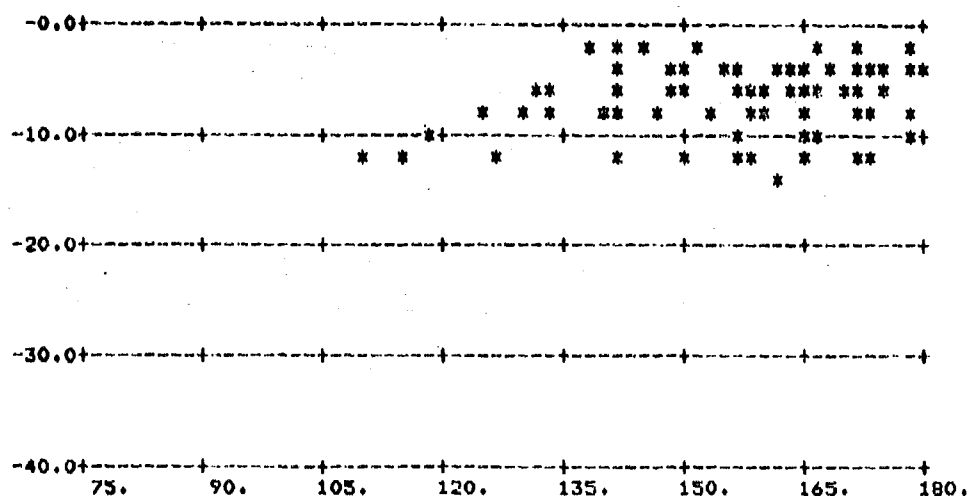


(a) All Points

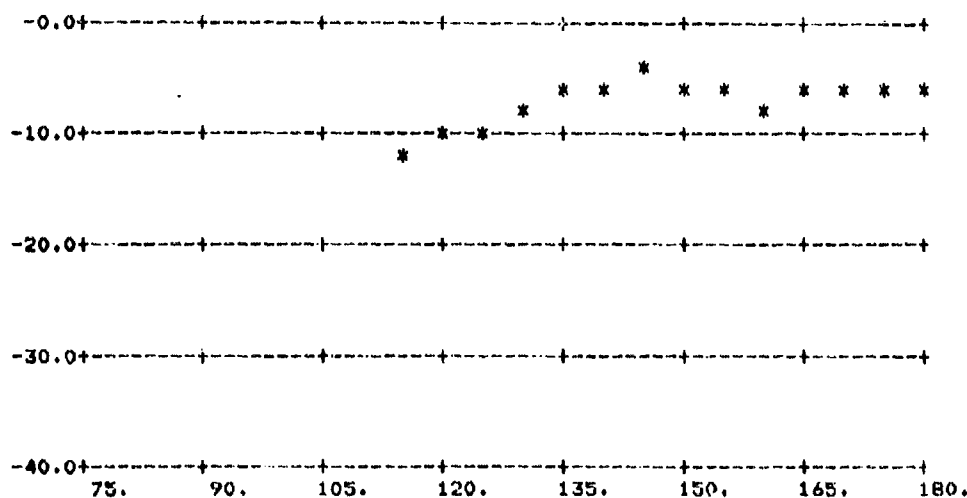


(b) Averages

Figure E-14. σ_0 vs ϕ_s for Pass 5, Flight 7/17/76
at 3 cm Wavelength, Horizontal Polarization
($\theta_s = 80^\circ$, $\theta_1 = 70^\circ$, $y_1 = 100$ ft, $x_2 = 18480$ ft,
 $y_2 = 8000$ ft; data taken from entire pass)

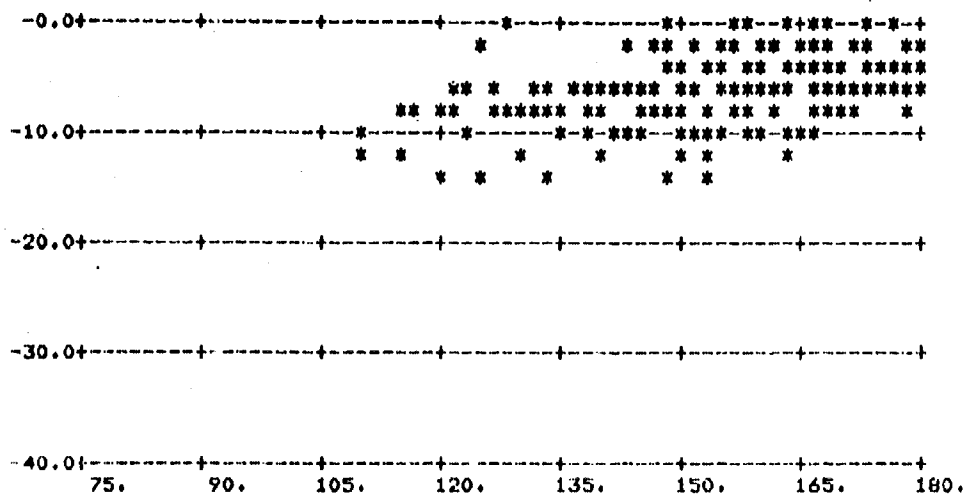


(a) All Points

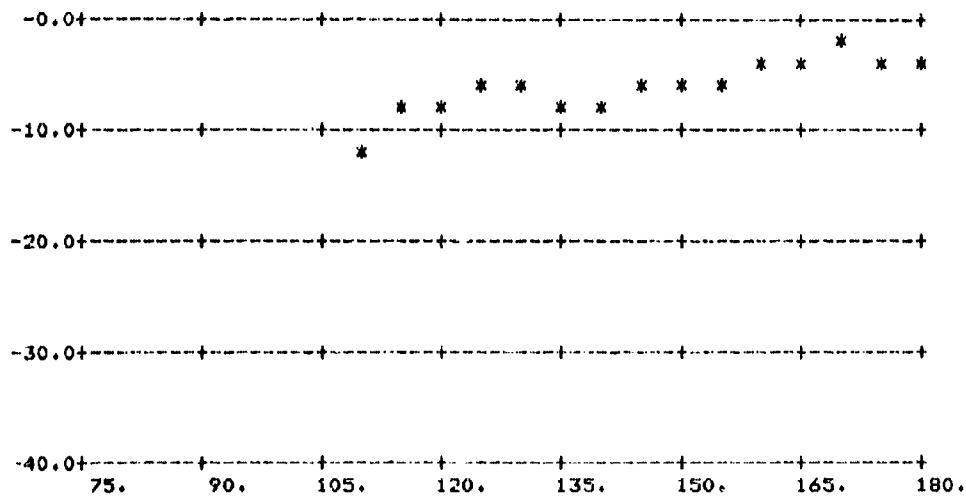


(b) Averages

Figure E-15. σ_0 vs ϕ_s for Pass 6, Flight 7/17/76
 at 3 cm Wavelength, Horizontal Polarization
 ($\theta_s = 80^\circ$, $\theta_i = 70^\circ$, $y_1 = 100$ ft, $x_2 = 18480$ ft,
 $y_2 = 8000$ ft; data taken from entire pass)

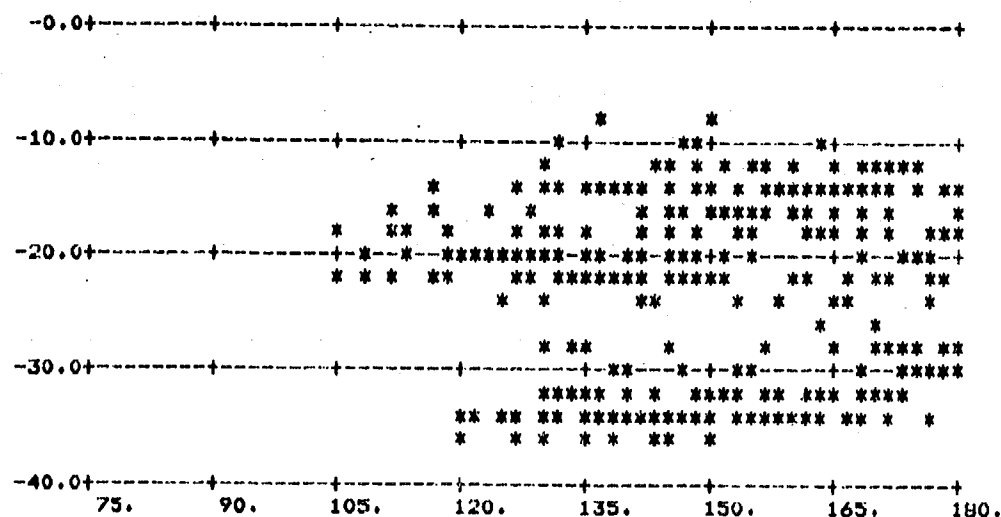


(a) All Points

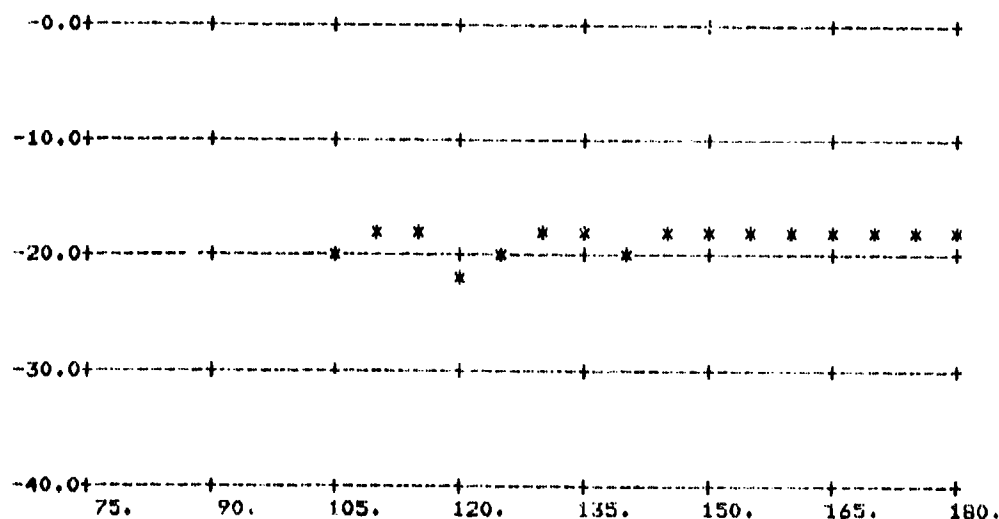


(b) Averages

Figure E-16. σ_O vs ϕ_S for Pass 10, Flight 7/17/76
at 3 cm Wavelength, Horizontal Polarization
($\theta_S = 70^\circ$, $\theta_I = 80^\circ$, $y_1 = 100$ ft, $x_2 = 18740$ ft,
 $y_2 = 4000$ ft; data taken from entire pass)

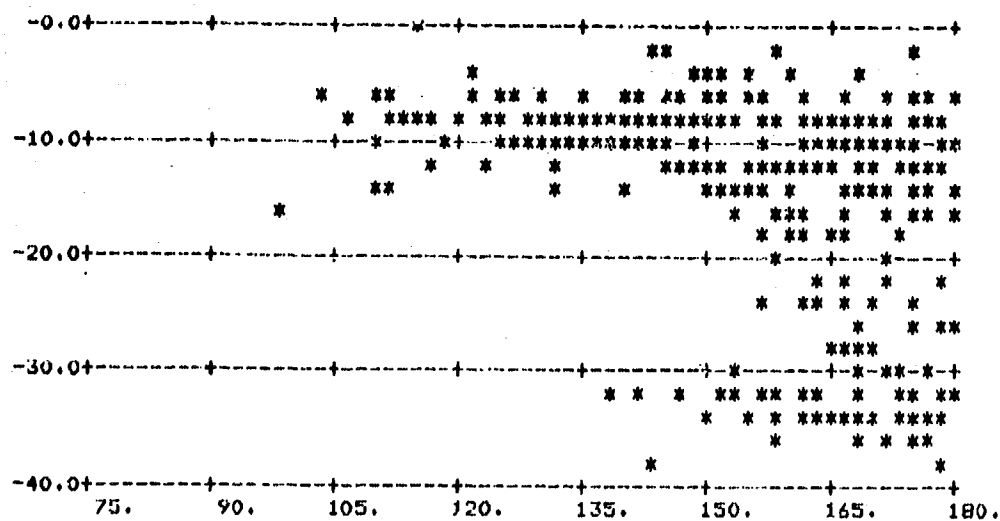


(a) All Points

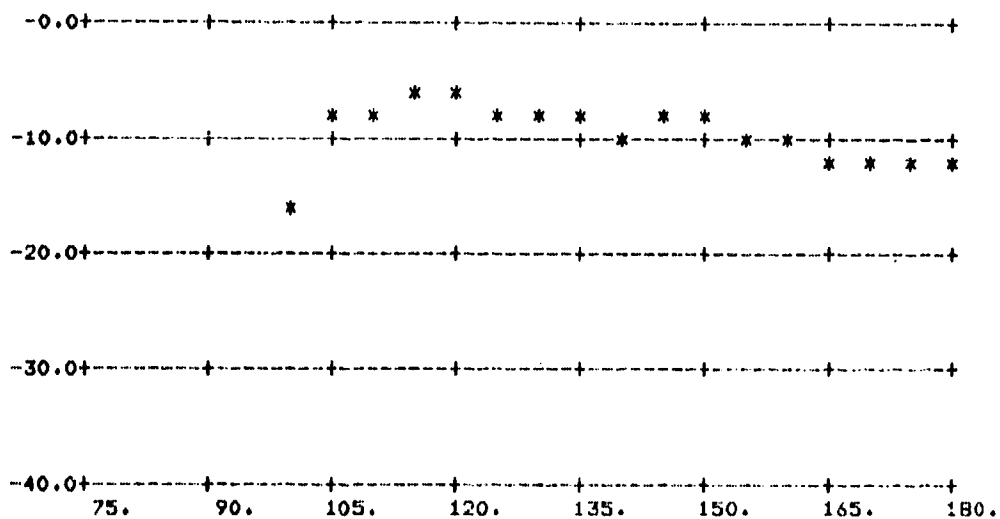


(b) Averages

Figure E-17. σ_0 vs ϕ_s for Pass 11, Flight 7/17/76
at 3 cm Wavelength, Horizontal Polarization
($\theta_s = 70^\circ$, $\theta_i = 75^\circ$, $y_1 = 100$ ft, $x_2 = 18480$ ft,
 $y_2 = 6000$ ft; data taken from entire pass)

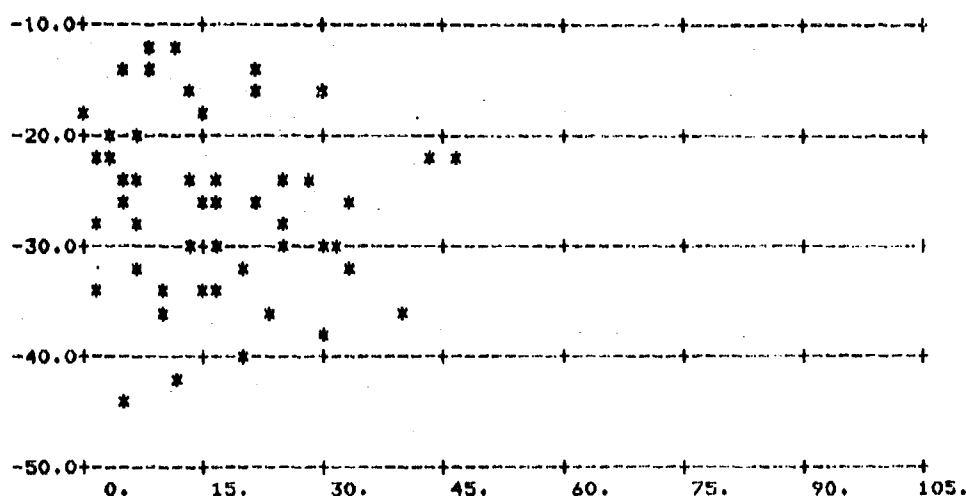


(a) All Points

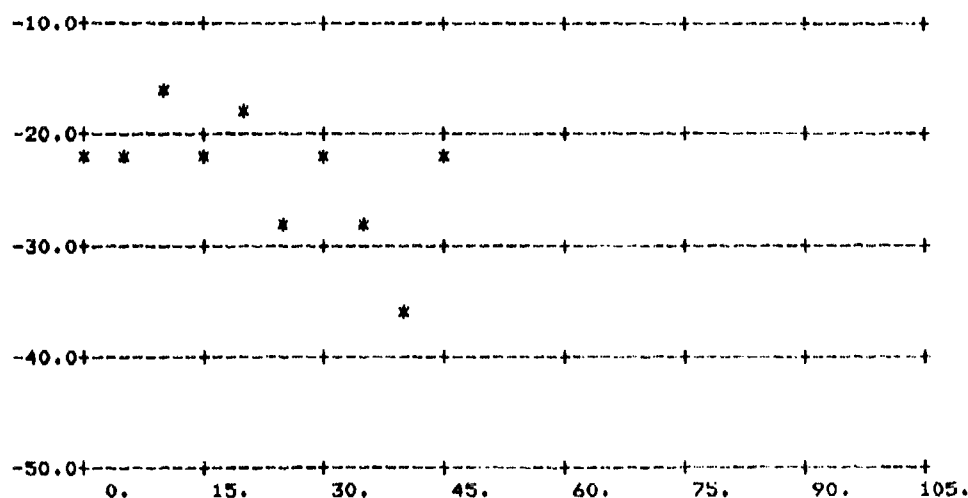


(b) Averages

Figure E-18. σ_0 vs ϕ_s for Pass 12, Flight 7/17/76
 at 3 cm Wavelength, Horizontal Polarization
 $(\theta_s = 70^\circ, \theta_i = 70^\circ, y_1 = 100 \text{ ft}, x_2 = 18480 \text{ ft},$
 $y_2 = 8000 \text{ ft; data taken from entire pass})$

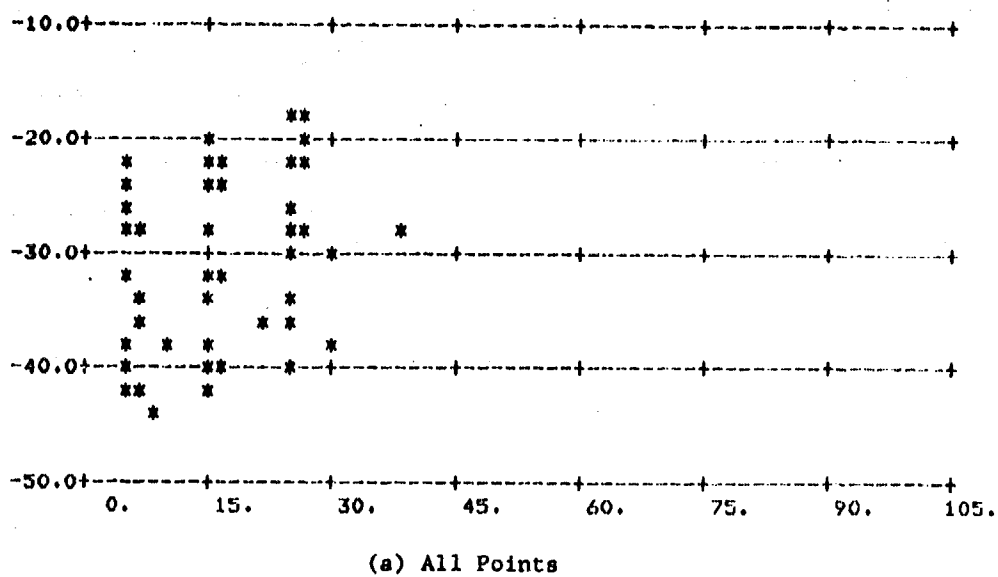


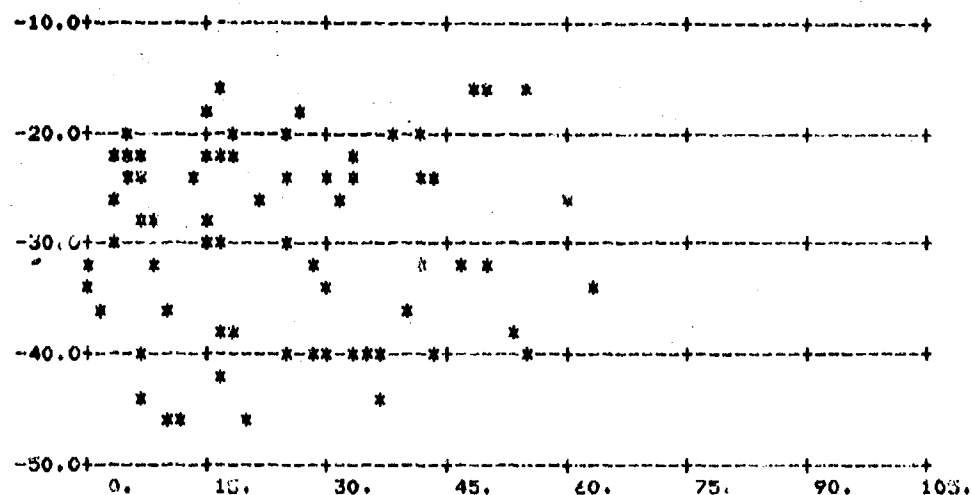
(a) All Points



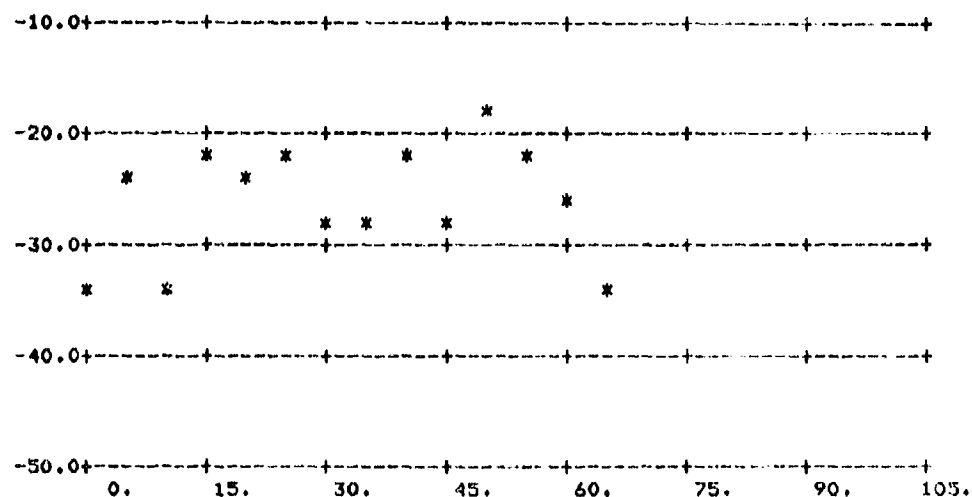
(b) Averages

Figure E-19. σ_O vs ϕ_s for Pass 2, Flight 7/9/76
 at 23 cm Wavelength, Horizontal Polarization
 $(\theta_s = 85^\circ, \theta_1 = 80^\circ, y_1 = 45 \text{ ft}, x_2 = 14700 \text{ ft},$
 $y_2 = 3200 \text{ ft; data taken from entire pass})$



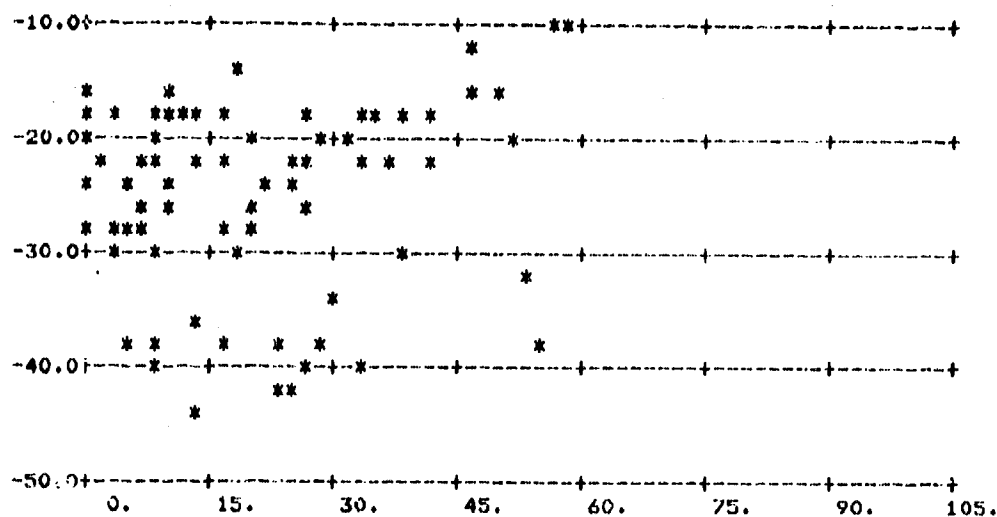


(a) All Points

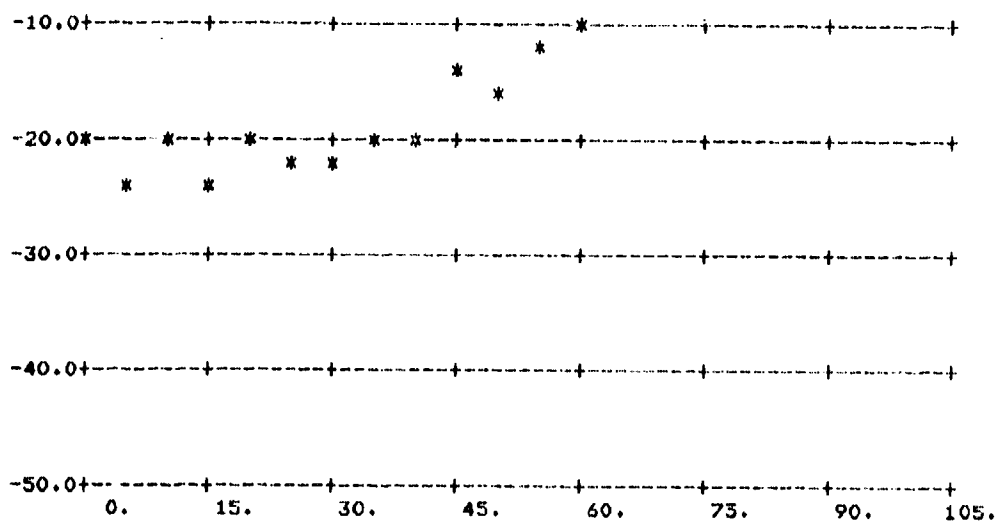


(b) Averages

Figure E-21. σ_0 vs ϕ_s for Pass 6, Flight 7/9/76
at 23 cm Wavelength, Horizontal Polarization
($\theta_s = 85^\circ$, $\theta_1 = 80^\circ$, $y_1 = 45$ ft, $x_2 = 14850$ ft,
 $y_2 = 3400$ ft; data taken from entire pass)

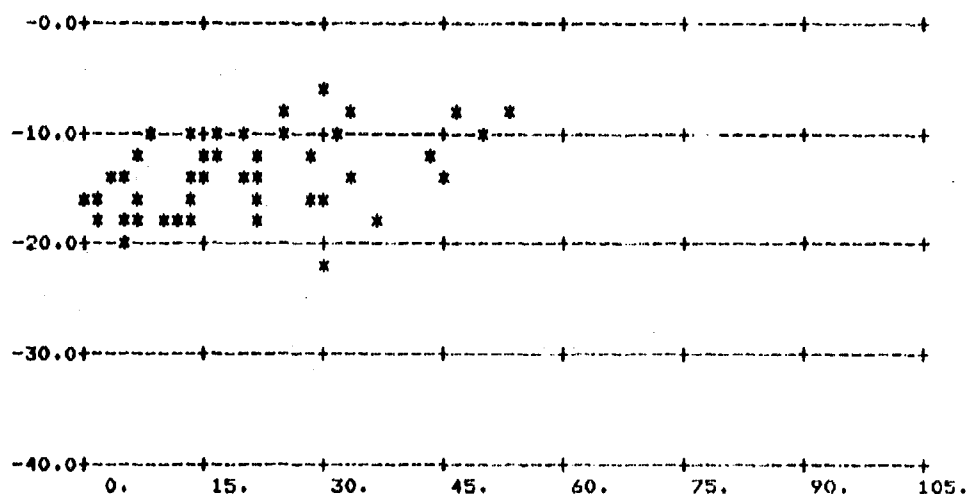


(a) All Points

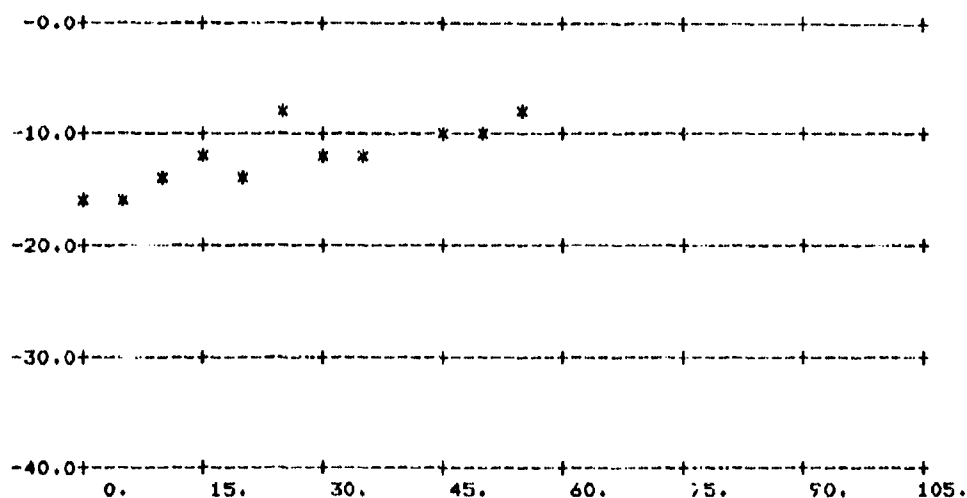


(b) Averages

Figure E-22. σ_0 vs ϕ_s for Pass 7, Flight 7/9/76
at 23 cm Wavelength, Horizontal Polarization
($\theta_s = 85^\circ$, $\theta_1 = 80^\circ$, $y_1 = 45$ ft, $x_2 = 16400$ ft,
 $y_2 = 2200$ ft; data taken from entire pass)

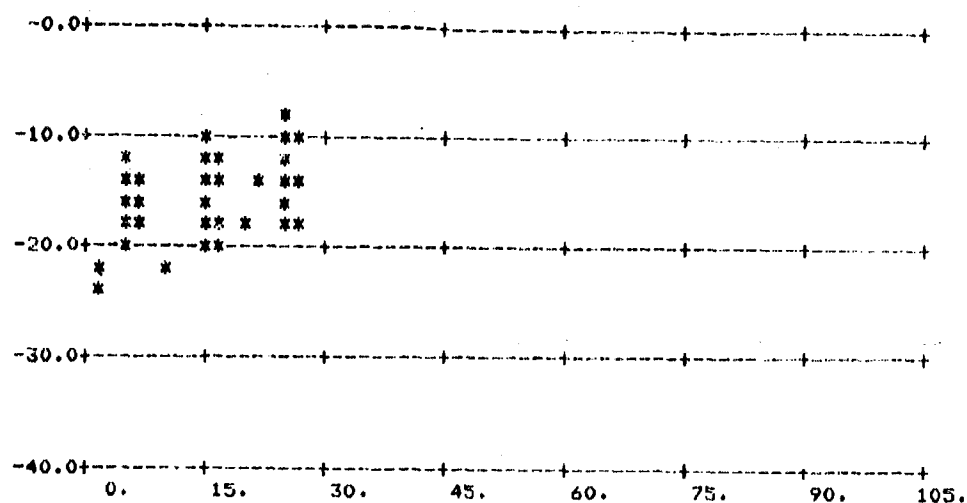


(a) All Points

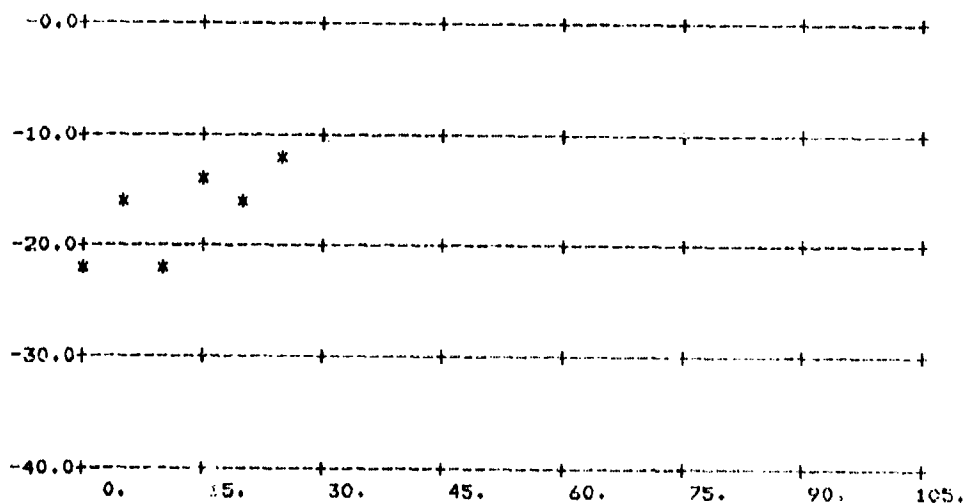


(b) Averages

Figure E-23. σ_0 vs ϕ_s for Pass 2, Flight 7/9/76
at 3 cm Wavelength, Horizontal Polarization
($\theta_s = 85^\circ$, $\theta_i = 80^\circ$, $y_1 = 45$ ft, $x_2 = 14700$ ft,
 $y_2 = 3200$ ft; data taken from entire pass)

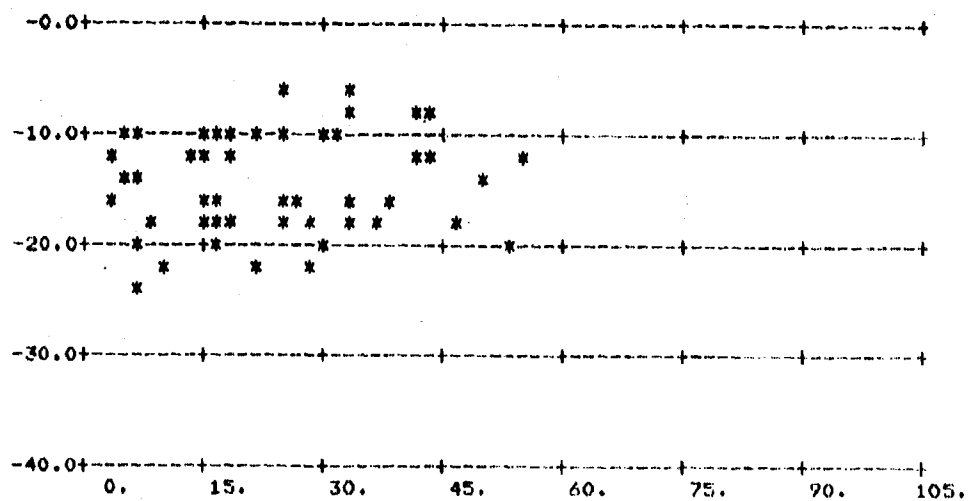


(a) All Points

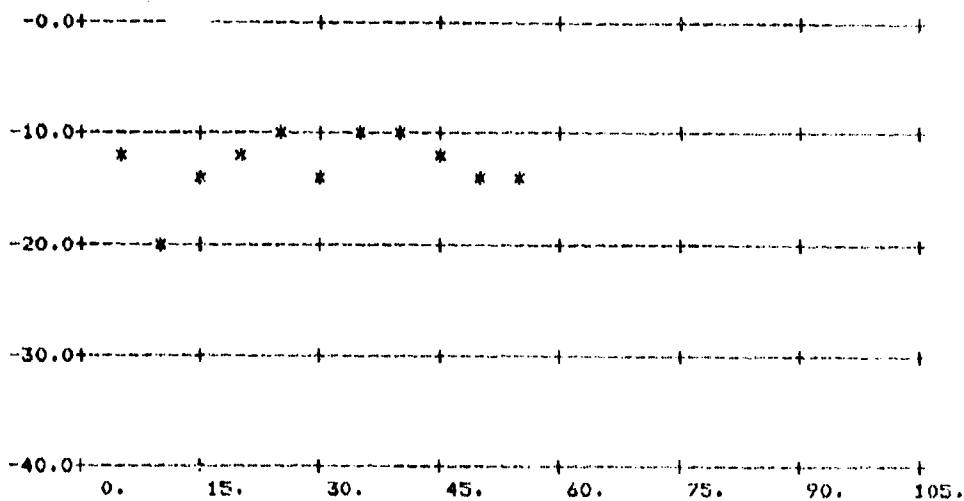


(b) Averages

Figure E-24. c_o vs ϕ_s for Pass 5, Flight 7/9/76
at 3 cm Wavelength, Horizontal Polarization
($\theta_s = 85^\circ$, $\theta_i = 80^\circ$, $y_1 = 45$ ft, $x_2 = 15500$ ft,
 $y_2 = 3200$ ft; data taken from entire pass)

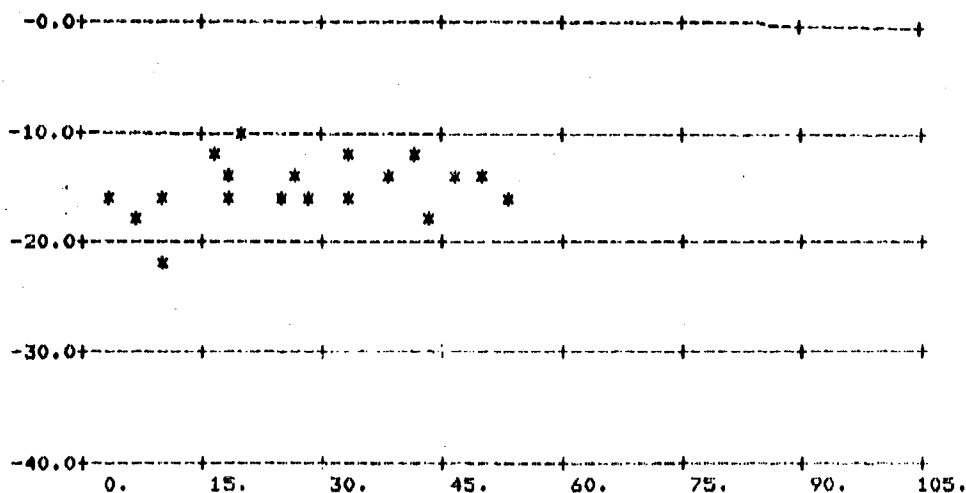


(a) All Points

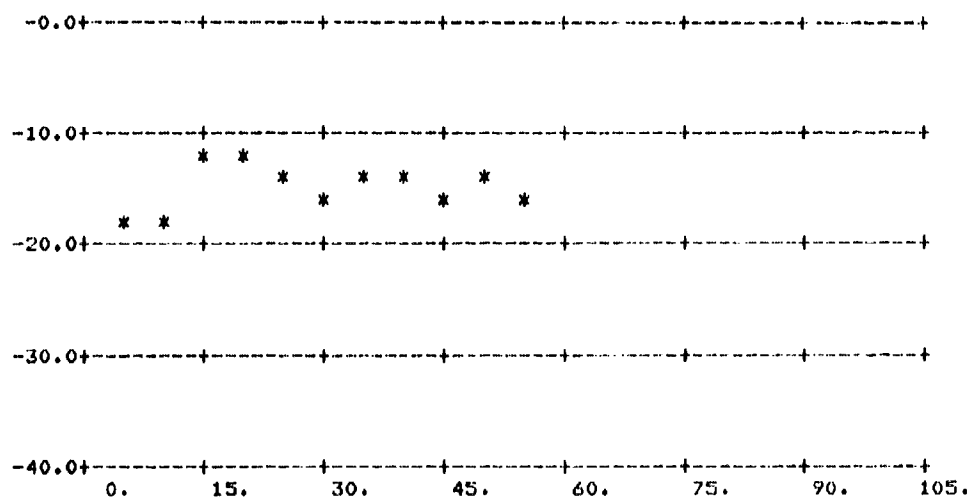


(b) Averages

Figure E-25. σ_0 vs ϕ_s for Pass 6, Flight 7/9/76
 at 3 cm Wavelength, Horizontal Polarization
 ($\theta_s = 85^\circ$, $\theta_1 = 80^\circ$, $y_1 = 45$ ft, $x_2 = 14850$ ft,
 $y_2 = 3400$ ft; data taken from entire pass)



(a) All Points



(b) Averages

Figure E-26. σ_0 vs ϕ_s for Pass 7, Flight 7/9/76
 at 3 cm Wavelength, Horizontal Polarization
 $(\theta_s = 85^\circ, \theta_i = 80^\circ, y_1 = 45 \text{ ft}, x_2 = 16400 \text{ ft},$
 $y_2 = 2200 \text{ ft; data taken from entire pass})$

MISSION of Rome Air Development Center

RADC plans and conducts research, exploratory and advanced development programs in command, control, and communications (C³) activities, and in the C³ areas of information sciences and intelligence. The principal technical mission areas are communications, electromagnetic guidance and control, surveillance of ground and aerospace objects, intelligence data collection and handling, information system technology, ionospheric propagation, solid state sciences, microwave physics and electronic reliability, maintainability and compatibility.

